Organometallic Science
https://www.sciltp.com/journals/os

Review

Organometallic Complexes and Macromolecules: Evolving Roles in Biomedical and Pharmaceutical Sciences

Ahmad Abd-El-Aziz [1,2], Zexuan Li [1,2], Amal M. Youssef [3], Ning Ma [1,2,*] and Alaa S. Abd-El-Aziz [1,2,*]

[1] College of Materials Science and Chemical Engineering, Harbin Engineering University, Harbin 150001, China
[2] Qingdao Innovation and Development Center, Harbin Engineering University, Qingdao 266000, China
[3] Department of Pharmaceutical Chemistry, Faculty of Pharmacy, Alexandria University, Alexandria 21521, Egypt
* Correspondence: nma@hrbeu.edu.cn (N.M.); aabdelaziz@hrbeu.edu.cn (A.S.A.-E.-A)

How To Cite: Abd-El-Aziz, A.; Li, Z.; Youssef, A.M.; et al. Organometallic Complexes and Macromolecules: Evolving Roles in Biomedical and Pharmaceutical Sciences. *Organometallic Science* **2027**, *1*(1), 4. https://doi.org/10.53941/os.2027.100004

Received: 12 June 2026
Revised: 7 August 2026
Accepted: 1 September 2026
Published: 15 September 2026

Abstract: Biomedical and pharmaceutical research and development continues to face many challenges in terms of efficacy, cost-effective manufacturing, and sustainability. More efforts need to be devoted to the discovery and testing of new effective and commercially viable biomedical and pharmaceutical materials. Organometallic complexes play an important role in the search for the most effective drugs with fewer side effects. The vast array of metallic moieties provides tremendous opportunities for drug design and imaging due to exhibiting a range of physiological effects. Since the development of the organometallic chemistry field in the mid-twentieth century, there has been a great deal of research into the biomedical and pharmaceutical applications of these complexes, which has only accelerated due to the design of organometallic macromolecules such as polymers and dendrimers. The aim of this review article is to focus on the most recent developments in the search for effective organometallic complexes, dendrimers and polymers for biomedical and pharmaceutical applications. Synthetic methodologies for these classes of molecules will be described and connected with examining their biomedical activities. The article will be divided into bioimaging, phototherapeutic, antimicrobial, anticancer, antiparasitic, antiviral, anti-inflammatory and anti-neurodegenerative applications, with representative organometallic examples, including both homo- and heterometallic moieties. Various optimization strategies for the complexes will be outlined, including strengthening antibiofilm performance and utilizing multivalency to enhance the targeting ability. The design of stimuli-responsive theranostic platforms derived from functional materials containing highly active organometallic moieties will also be illustrated. The past decade has seen continuous discoveries of new complexes with potential biomedical activities, and it is clear that this is an area of growth in light of the potential synergistic activities of the vast arrays of organic ligands and metallic moieties.

Keywords: organometallic complexes; antimicrobial; anticancer; antiparasitic; antiviral; bioimaging

1. Introduction

This review article is dedicated to the role of organometallic complexes, dendrimers and polymers in biomedical and pharmaceutical applications. Organometallic complexes are defined by the bonding of metallic moieties to individual carbon atoms of organic ligands, such as alkyl or aryl groups, or to multiple carbon centers, such as bonding with alkenes, alkynes, cyclopentadienyl or arenes [1–4]. Since the middle of the twentieth century,

Copyright: © 2026 by the authors. This is an open access article under the terms and conditions of the Creative Commons Attribution (CC BY) license (https://creativecommons.org/licenses/by/4.0/).
Publisher's Note: Scilight stays neutral with regard to jurisdictional claims in published maps and institutional affiliations.

the chemistry of organometallic complexes has been widely studied for a range of applications, including but not limited to the synthesis of organic compounds [5–8] and polymeric materials [9–13], organic light-emitting diodes (OLEDs) [14–17], catalysis [18–22], biomedical imaging [23–27], and drug design [28–37]. The interactions between the metal moieties of organometallic complexes and specific amino acid residues of proteins is key to their biological activities, and has therefore been studied for drug design [37,38]. These interactions can be modified by the charges and polarity of the organic ligands [39,40]. It is noteworthy to mention that there is a vast array of coordination complexes and macromolecules that have been well examined for their biomedical applications, including organometallic complexes and macromolecules [29,41–48]. In this review, the focus will be on the biomedical and pharmaceutical applications of organometallic complexes and macromolecules.

The fluorescence or magnetic properties of metals are valuable for bioimaging applications. Bioimaging, a non-invasive process that allows for visualization of biological activity *in vivo* in real time, has great value for medical diagnoses as well as scientific study of biological and pathological processes in living organisms. Organometallic compounds enhance these properties as well as reducing toxicity, allowing for improved visualization of cells and tissues [49–51]. The multifunctional characteristics of organometallic bioimaging agents also show potential in the field of theranostics, i.e., diagnostic approaches used to guide therapeutic interventions, as they can be used for imaging while exhibiting anticancer or antibacterial activities. A recent review by Tang and coworkers outlined several theranostic strategies using AIE of organic and organometallic complexes [52]. One of the most common applications of this strategy is the use of imaging-guided phototherapies, which use photosensitizing agents that can be activated by lasers of specific wavelengths to kill cancer cells [53], and can even target specific organelles within cells [54].

Another major area of interest for organometallic complexes is as a strategy for combating antimicrobial resistance (AMR). The escalating global health crisis of AMR has been predicted to cause ten million deaths per year by 2050 [55]. In 2024, a systematic analysis by Naghavi et al. published in The Lancet estimated that 1.14 million deaths in 2021 were directly attributable to bacterial AMR, with a total of 4.71 million deaths associated with bacterial AMR [56]. As a result, new and diverse antimicrobial agents are necessary for preventing the spread of resistance and treating resistant strains. Organometallic complexes have already been proven as a promising platform in this field, as they have demonstrated broad-spectrum efficacy against diverse microorganisms including Gram-positive and Gram-negative bacteria, fungi, and bacterial biofilms that are highly resistant to conventional antibiotics [57–64]. The combination between the natural antimicrobial properties of the metal moieties and the unique structural advantages of the organic moiety can improve the activity of the resulting complex, including optimized architecture, multivalency, and tunable functionalities. Complexes of various metals have been investigated for their antimicrobial properties including copper, zinc, silver, ruthenium, iron, and other transition metals. The antimicrobial mechanisms of the metal complexes include diverse mechanisms, such as generation of reactive oxygen species (ROS) and damage to the cell wall [65,66]. Additionally, organometallic macromolecular materials not only allow for the development of antimicrobial drugs but can also be expanded to designing functionalized materials such as textiles and hydrogels that can prevent infections, as well as potentially inhibiting the production of biofilms.

Another biomedical application of organometallic complexes is cancer, which remains a major cause of global mortality. Based on the Cancer Atlas Fourth Edition launched by the International Agency for Research on Cancer (IARC) and the American Cancer Society (ACS), cancer is in the “top 3” causes of mortality for 151 nations. By 2050, it is expected that 35 million new cancer cases will be added per year due to a combination of population growth and aging, with a disproportional burden placed on low- and middle-income countries [67]. This highlights the urgent demand for developing novel therapeutic strategies, of which metal-based agents have shown promise in combating cancer. An early example of this was cisplatin, which was discovered in 1965, and made significant progress in cancer treatment, beginning a new era of metal-based anticancer drugs. In 1971, clinical trials were conducted for cisplatin, and by 1979 it had been authorized for the treatment of testicular and ovarian carcinoma in the USA and Europe [68–70]. However, traditional chemical treatments face the challenges of developing resistance, host cytotoxicity and off-target effects. In this situation, the class of organometallic agents (compounds/dendrimers/polymers) is a novel platform that has attracted a great deal of attention due to their tunable activities and ability to reduce cytotoxicity. Starting from the 1980s, research into the biomedical applications of metal-based macromolecules has steadily increased, in light of their highly adjustable architecture and multifunction. These macromolecules enhance anticancer efficiency thanks to the combination of the pharmacokinetic advantages of the organic ligand with the bioactivity of the metallic moieties [71,72]. Despite the progress that has already been achieved, the vast combinatorial potential of organometallic complexes, dendrimers and polymers remains underexplored, offering diverse opportunities to address existing challenges for cancer treatment. Although antimicrobial and anticancer agents have received a great deal of research attention, given

their high burdens on healthcare, the wide variety of metals and organic ligands that comprise organometallic structures have many other potential therapeutic applications. Several areas of interest include anti-inflammatory agents, antiviral and antiparasitic therapies, and treatment of neurodegenerative diseases.

While there are a number of reviews covering various applications of organometallic and coordination complexes in the biomedical field, this review intends to give a comprehensive overview focusing on synthesis and biomedical applications of organometallic molecules and macromolecules. The synthetic methodologies for organometallic complexes, including dendrimeric and polymeric materials, with metallic moieties either integrated into the backbone or pendent to the backbone or side chain of the material, will be highlighted. This review will demonstrate current advances across the biomedical applications of organometallic compounds containing various transition metals, with focus on their mechanisms, structure-activity relationships, and potential to overcome drug resistance while minimizing off-target effects. These applications include bioimaging, phototherapy, antimicrobial, antiparasitic, anticancer, anti-inflammatory, antiviral and anti-neurodegenerative agents, as outlined in Figure 1. The unique advantages of macromolecular scaffolds such as polymers and dendrimers in comparison to simple organometallic compounds will also be examined. The development of organometallic complexes, dendrimers and polymers as imaging and therapeutic agents integrates inorganic and organic chemistry to create next-generation agents with enhanced selectivity and multifunctional capabilities.

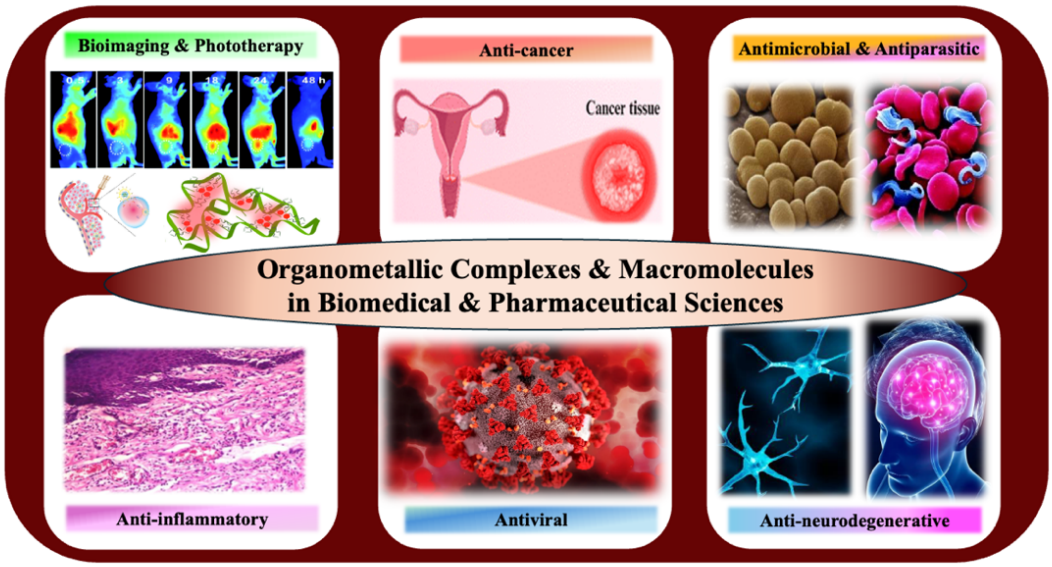

Figure 1. Applications of organometallic complexes and macromolecules in biomedical and pharmaceutical fields.

2. Bioimaging and Phototherapy

Bioimaging is a technique used to gather data and generate images of biological activity in living organisms with minimal disruption of normal function [73]. Methodologies for bioimaging include computed tomography (CT), magnetic resonance imaging (MRI), and positron emission tomography (PET), all of which use agents to enhance image contrast in clinical use, with the disadvantage of adverse reactions in the body away from the site of imaging. CT scans produce cross-sections based on computer algorithms that reconstruct three-dimensional images from X-ray attenuation produced by a rotating X-ray tube [74]. On the other hand, MRI detects resonance emission from the nuclei of hydrogen atoms found within water molecules in tissues of the body via application of magnetic fields [75]. Unlike X-rays, MRI can image soft tissues and organs, and does not expose tissues to potentially harmful ionizing radiation, which is why it has become a key diagnostic imaging methodology. PET detects gamma ray pairs indirectly emitted by a radionuclide that emits positrons. This technique allows for study of altered metabolic processes in addition to structural details, although the radionuclide tracer employed must be specific to the process of interest [76]. Additionally, fluorescent labels can be used to track the movement of molecules within organelles or cells, allowing for visualization of cellular localization. The optical and electronic properties of metals in organometallic complexes and macromolecules allow them to be used for more efficient fluorescence or contrast agents. Furthermore, organometallic complexes provide potential tunability as well as decreased toxicity in comparison with free metals or metal ions. As an example, Gupta et al. showed the fluorescence enhancement by an iridium probe for detection of RNA sequences of SARS-CoV-2 (the virus responsible for COVID-19) via aggregation-induced emission (AIE), as described in Figure 2 [77]. Organometallic

polymers can increase the number of active moieties involved in imaging, increasing their local concentration without increasing the overall dose required, while the three-dimensional architectures of dendrimers can enhance their activity and solubility in aqueous environments, while decreasing toxicity. Additionally, bioimaging can be used to guide the application of phototherapy, and by addition of moieties with different functions, organometallic compounds can act as both the label for imaging as well as the photosensitizing agents. Phototherapy uses lasers of specific wavelengths to activate photosensitizing compounds and can be divided into photodynamic therapy (PDT), which releases reactive oxygen species (ROS) [78], and PTT, which generates extreme heat that can kill cells [79]. The photosensitizers can be modified with fluorescent moieties in order to precisely target the area to which the photosensitizers were localized, avoiding unnecessary and damaging exposure of the surrounding tissue to the laser treatment.

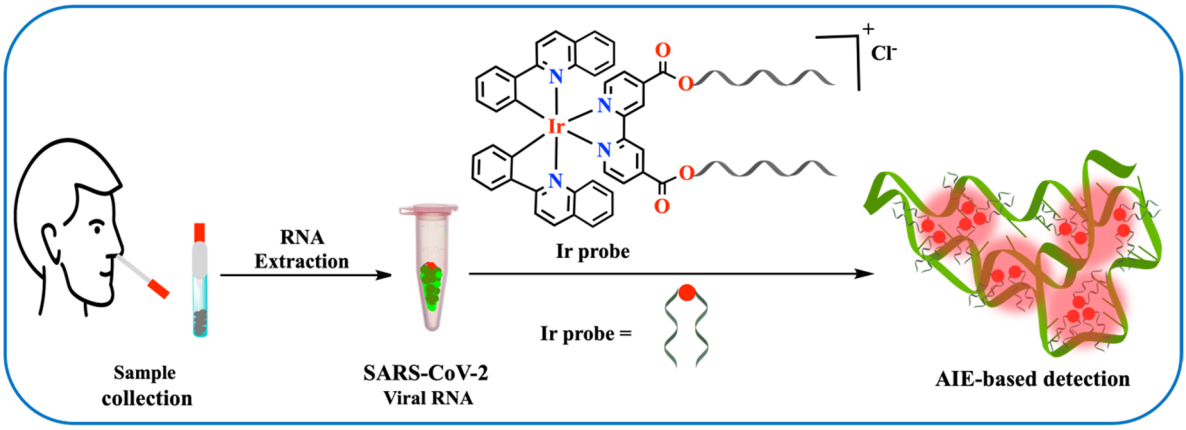

Figure 2. Fluorescence detection by an organometallic iridium-based probe for AIE-based detection of SARS-CoV-2 virus [77].

Considering the overlap between the development of organometallic bioimaging and phototherapeutic agents, this section will highlight some examples based on the nature of the metallic moieties as well as their functional behaviours.

2.1. Technetium and Rhenium Complexes

Technetium and rhenium complexes have demonstrated abilities for imaging and radionuclide therapy. For example, Pitchumony et al. prepared organometallic Tc(I) complexes based on Re(I) luminescent probes, as shown in Figure 3 [80]. These complexes contained the metastable ^{99m}Tc radionuclide used for emission of gamma rays in medical imaging, as it has a short half-life that prevents harmful long-term radiation exposure, but also reduces its stability for use *in vivo*. Reaction of *fac*-$[M(OH_2)_3(CO)_3]^+$ **(1)**, where the metallic moiety was Re or Tc, with bipyridine allowed for the isolation of the *fac*-$[M(OH_2)(bipy)(CO)_3]^+$ complex **(2)** which was then reacted with cyclohexylnicotinate **(3)** to yield the desired *fac*-$[Re(CO)_3(bipy)(cyclohexylnicotinate)]^+$ complex **(4)** where the counteranion was chloride, as shown in Figure 3. The effect on stability of the ^{99m}Tc was dependent on the nature of the monodentate pyridyl ligand. Confocal microscopy of the MCF-7 breast cancer cells incubated with 100 µg/mL of the Re(I) complex, shown in Figure 3, showed the uptake of the luminescent complex. Cell uptake of the ^{99m}Tc(I) complex by MCF-7 cells was then evaluated using a gamma counter to measure gamma ray emission. As shown by the graph in Figure 3, the Tc(I) complex alone (in the blue bar in the graph) showed increased uptake after 30 and 120 minutes of incubation. Co-incubation of the Tc(I) and the Re(I) complex with the cells increased uptake of Tc(I) complex for 30 minutes of incubation. On the other hand, this effect was reduced after 120 minutes, indicating that the Tc(I) uptake was still effective, just slower.

Hungnes et al. designed Re and ^{99m}Tc-labelled complexes containing cyclic Arg-Gly-Asp-DPhe-Lys (RGD) peptides for single photon emission CT (SPECT) [81]. This was achieved via the reaction of 2,3-bis(diphenylphosphino)maleic anhydride (**5**) with the cyclic peptide, Arg-Gly-Asp-DPhe-Lys (RGD) (**6**) to produce the racemic mixture of complexes **7** and **8**, $[MO_2(DP\text{-}RGD)_2]^+$ (M = Re, ^{99m}Tc) as shown in Scheme 1. These complexes were found to be excreted without digestion, meaning they were highly stable in the body with no toxic byproducts.

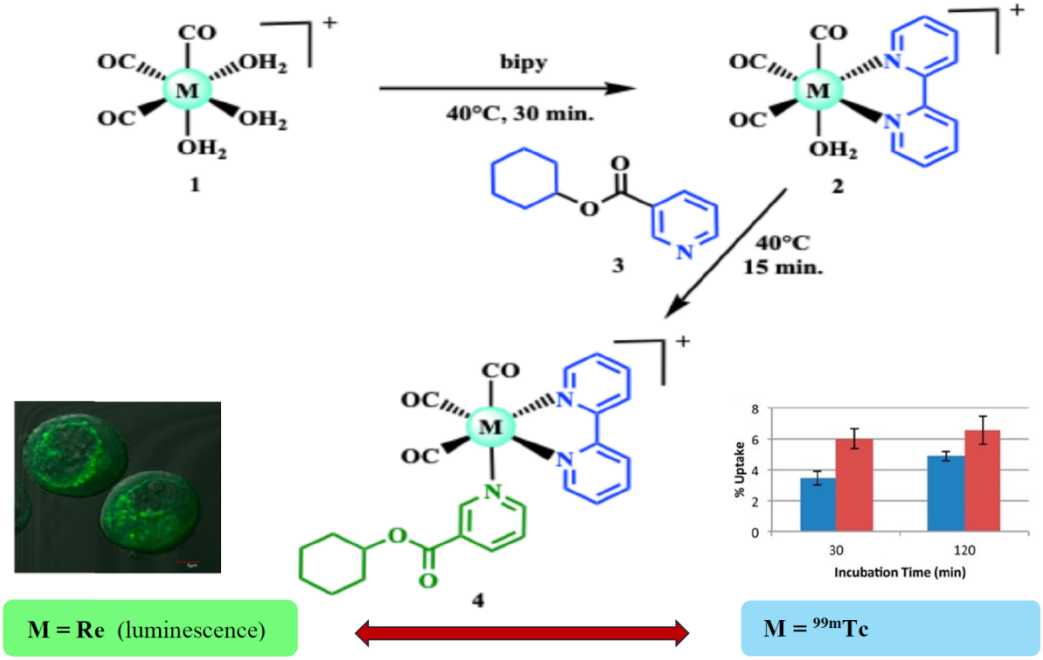

Figure 3. Synthesis of complex **4** containing either rhenium or technetium, with the confocal micrographs of MCF-7 cells stained with the Re(I) complex and graph of the uptake for Tc(I) complex with and without the presence of the Re(I) complex (blue and red bars, respectively). Adapted with permission from Ref. [80], Copyright © 2013, American Chemical Society.

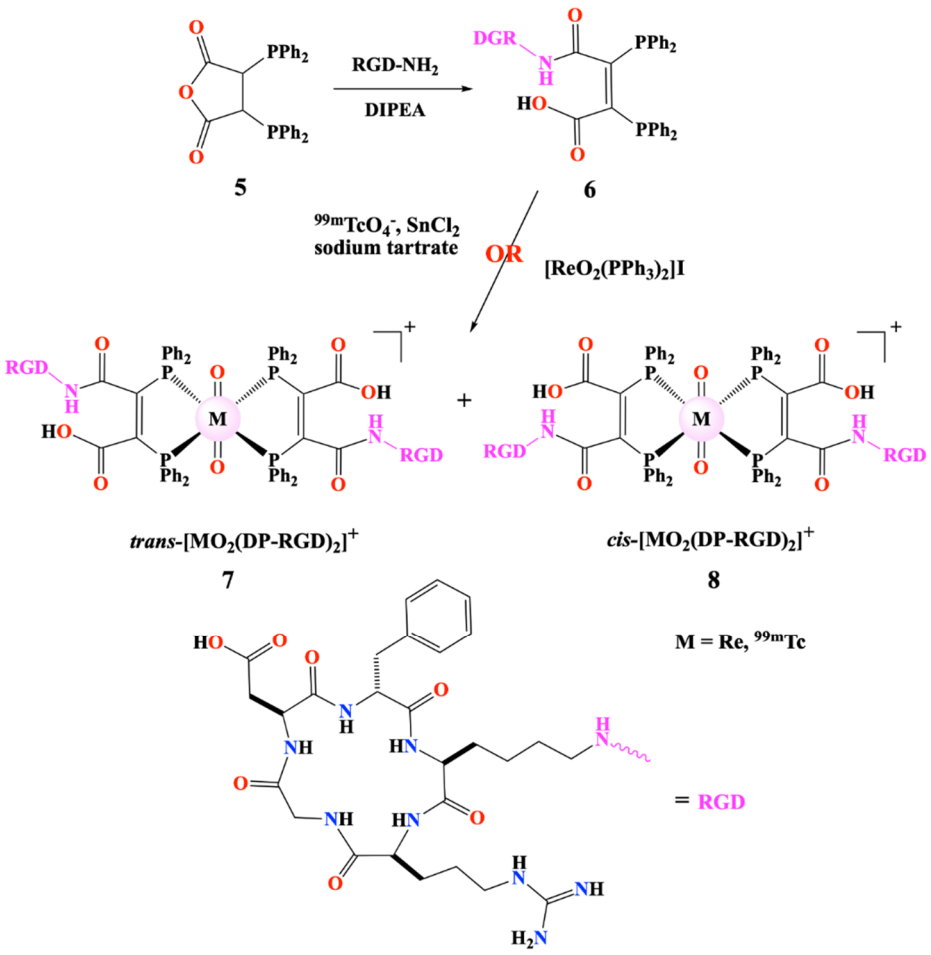

Scheme 1. Synthesis of *trans*- (**7**) and *cis*-$[MO_2(DP\text{-}RGD)_2]^+$ (**8**).

The mixture of complexes **7** and **8** was able to target $\alpha_v\beta_3$-integrin receptors, which are overexpressed during inflammation and in cancer cells in vitro. An example of SPECT imaging was evaluated for an *in vivo* mouse

model of rheumatoid arthritis using an injection of serum from arthritic individuals into the hind paw. As can be seen in the quantitative analysis shown in Figure 4A, the ankle (i.e., hind paw, RA) exhibited more extreme swelling than the wrist (i.e., front paw), which correlated with dose uptake of the radioactive imaging complexes. The complexes were also detected in kidneys and bladder due to being removed from circulation for excretion, as seen in the minimum intensity projection in Figure 4B, as well as the thyroid, due to the ability for Tc to act as a mimic of iodide.

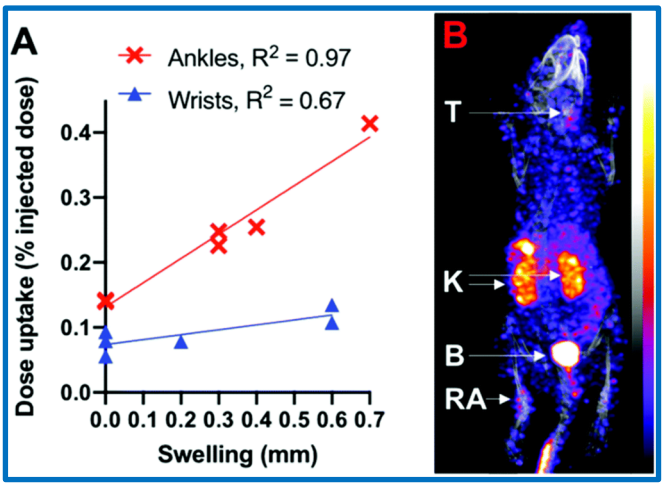

Figure 4. SPECT imaging using the racemic mixture of complexes **7** and **8** for a mouse model of rheumatoid arthritis represented by (**A**) quantitative analysis of dose uptake vs. swelling for the ankles (front paws) and wrists (rear paws) and (**B**) minimum intensity projection (T = thyroid, K = kidney, B = bladder, RA = rheumatoid arthritic "ankle". Reproduced with permission from Ref. [81], https://doi.org/10.1039/D1DT03177E (accessed on 14 April 2026), under the terms of the CC BY 4.0 license, https://creativecommons.org/licenses/by/4.0/.

It has also been reported that rhenium complexes could be linked to collagen, through hydrogen bonding or electrostatic interactions with the positively charged side chains of amino acid residues, in order to visualize oxygen concentration via phosphorescence lifetime imaging microscopy (PLIM) [82]. Two examples of the rhenium complexes, namely [Re(phen)$(CO)_3$(TPPTS)Na_2] (**11**) and [Re(phen)$(CO)_3$$(TPPTS)_2Na_5$] (**12**), were prepared as illustrated in Scheme 2. The reaction of *fac*-[Re$(CO)_3$(phen)Cl] (**9**) with acetonitrile and silver(I) trifluoromethanesulfonate gave rise to complex **10** as the $CF_3SO_3^-$ salt, which was then reacted with the sodium salt of *tris*-(3-sulfophenyl)phosphine (TPPTS) to produce the desired complexes **11** and **12** [82,83].

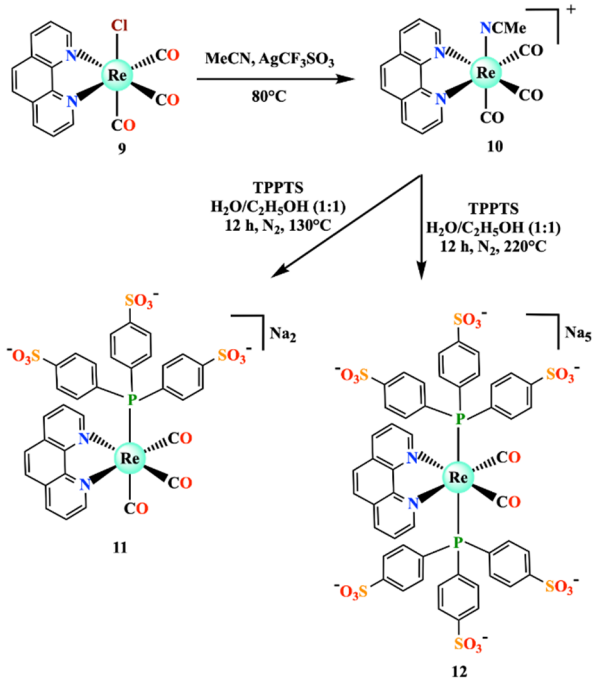

Scheme 2. Synthesis of [Re(phen)$(CO)_3$(TPPTS)Na_2] (**11**) and [Re(phen)$(CO)_3$$(TPPTS)_2Na_5$] (**12**).

The T_1-S_0 phosphorescence transition at the metal center can be quenched by the presence of oxygen, so an increase in phosphorescence lifetime is inversely proportional to oxygen concentration. This mechanism can therefore be useful for imaging of low oxygen levels (hypoxia) in tumours or tissue ischemia. In an *in vivo* melanoma model in mice, the oxygen concentration measured by complex **12** was shown to be lower at the center of the tumor compared to 5 mm away from the center, as shown in Figure 5a, which is consistent with the process of tumour development. The complex detected the lower oxygen concentration at the center by exhibiting longer phosphorescence lifetimes, as can be observed by the normalized intensity graphs in Figure 5b. The binding of complex to collagen fibers in the extracellular matrix is described in Figure 5c, which shows the stabilizing hydrogen bonding interactions between the positively charged histidine and arginine residues with the negatively charged sulfophenyl groups of the rhenium complex.

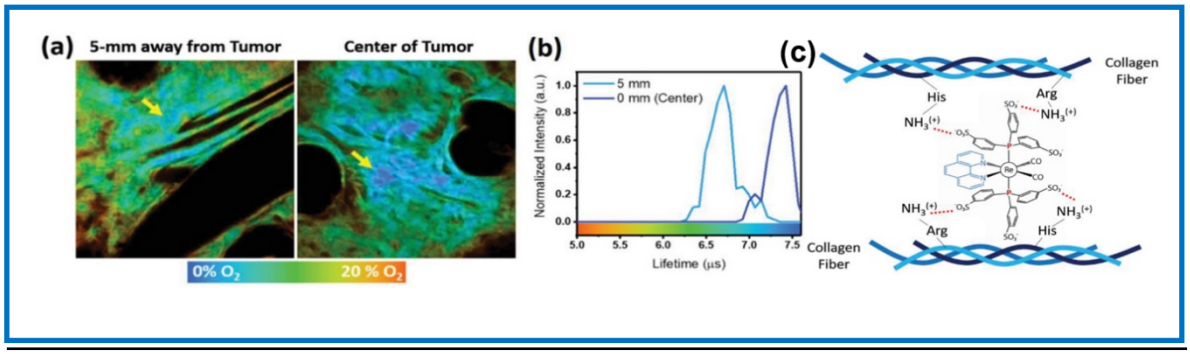

Figure 5. (**a**) Imaging of hypoxia and (**b**) lifetime phosphorescence of complex **12** at 5 mm away from and at the centre of a melanoma tumour in an *in vivo* mouse model. (**c**) Schematic illustration of the interactions between the anionic groups of complex **12** with the cationic side chains of histidine and arginine residues in collagen. Adapted with permission from Ref. [82], https://doi.org/10.1002/advs.202102788, under the terms of the CC BY 4.0 license, https://creativecommons.org/licenses/by/4.0/.

2.2. Iron and Ruthenium Complexes

Iron complexes have also been shown to be effective in the development of imaging and phototherapeutic agents. For example, ferrocene complexes can activate the ferroptosis pathway, an iron-dependent cell death pathway involving ROS production that is distinct from apoptosis. While there is a range of factors that can initiate the pathway, photoactivated ferroptosis has been investigated for its use in PDT for cancer therapy [84]. It should be noted that these ferrocene complexes may also have other anticancer mechanisms, including apoptosis or involvement of the immune response [85]. A simple ferrocene complex that showed efficacy as a PDT agent was 2-nitroethenyl ferrocene (NVFc), which was prepared from the condensation of ferrocene carboxaldehyde with nitromethane [86]. NVFc was found to undergo photocatalysis to produce ROS, primarily singlet oxygen. After irradiation for 10 min with visible light, phototoxicity was observed for both HeLa cells (IC_{50} = 3.52 μM for irradiation at 520 nm) and HepG2 liver cancer cells (IC_{50} = 2.81 μM for irradiation at 620 nm). In HeLa cells, NVFc decreased membrane potential for mitochondria, which suggested that the ROS production may result in mitochondrial dysfunction as part of its cytotoxic mechanism. The gene expression of lipid peroxidase enzymes GPX4 and SLC7A11 was also observed to decrease, demonstrating induction of the ferroptosis pathway by NVFc. Critically, the cytotoxicity against cancer cells was only observed after light irradiation, with low toxicity in dark conditions. Furthermore, NVFc could induce ferroptosis against two different cancer cell lines, showing its broad-spectrum activity.

In order to target the mitochondria for improved anticancer activity by photoinduction of ferroptosis, ferrocene complexes were conjugated to several N-alkylpyridinium salts, of which the most active complex was (E)-N-(n-butyltriphenylphosphonium bromide)-4-[2-(ferrocenyl)vinyl]-pyridinium bromide **(13)**, as shown in Figure 6 [87]. The triphenylphosphonium moiety is known to promote localization of these complexes to the mitochondria over the nucleus. The cation disperses the charge across a larger surface, increasing the lipophilicity for crossing lipid membranes while maintaining the overall positive charge. Preferential photocytotoxicity was exhibited for HeLa cancer cells at 568 nm compared to healthy NIH-3T3 cells, with IC_{50} values of 1.3 and 27.7 μM, respectively. By contrast, an organic analogue containing the 4-methoxyphenyl moiety substituted for ferrocene was inactive, showing that the ferrocene was necessary for the photocytotoxicity. Induction of ROS, especially type I photocatalysis producing hydroxyl radicals, resulted in apoptotic cell death, shown using the annexin/propidium iodide (annexin/PI) assay, as well as DNA cleavage. The disruption of the mitochondrial

membrane was evaluated using a JC-1 dye (5,5,6,6-tetrachloro-1,1,3,3-tetraethylbenzimidazolylcarbocyanine iodide) assay to measure the mitochondrial membrane potential. Alone, the JC-1 monomer emits green fluorescence (529 nm), while aggregation causes the fluorescence to redshift (590 nm). JC-1 can aggregate in healthy mitochondria with high membrane potentials, but the aggregation is inhibited if the membrane potential is lowered in mitochondria in apoptotic cells, the ratio of green to red emission can be used as a measure of membrane potential. As would be expected, the cells treated with complex **13** in the dark showed low ratios of green/red fluorescence (<1.0), representative of high membrane potential, as can be seen in Figure 6. On the other hand, the cells treated with complex **13** with visible light displayed high ratios above 2.0, comparable to the reference drug valinomycin, indicating that disruption of the mitochondria was involved in the apoptotic mechanism.

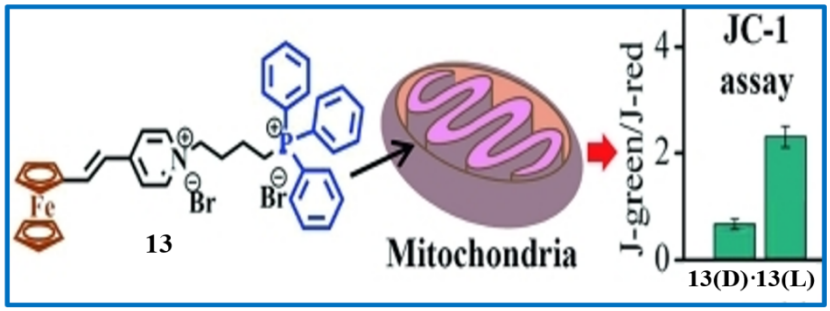

Figure 6. Structure of ferrocene-based complex **13**, its ability to be localized to mitochondria, and disruption of mitochondrial membrane potential measured by the JC-1 assay. Reproduced from Ref. [87] with permission from John Wiley & Sons, Copyright © 2015, Wiley-VCH Verlag GmbH & Co. KgaA, Weinheim, Germany.

In addition to ferrocene complexes, polymeric materials containing ferrocene moieties have been found to be effective candidates as phototherapeutic agents. A copolymer of poly (ethylene glycol) methyl ether methacrylate (PPEGMMA, **14**) and ferrocenylmethyl methacrylate (FMMA, **15**) referred to as PPEGMA-*b*-PFMMA (**16**), was prepared by Lin et al., with ferrocene as an oxidation-responsive moiety [88]. Nanoparticles of PPEGMA-*b*-PFMMA (**16)** then self-assembled with docetaxel as a chemotherapy agent and IR808 as a photosensitizer, as shown in Figure 7a. The polymer could be degraded to release docetaxel by redox reactions of the ferrocene with hydrogen peroxide in the tumour. As shown in Figure 7b, the mechanism began with the application of the laser to trigger the PTT/PDT effects, to generate heat and ROS that enhance this release mechanism. The combined effects of docetaxel, phototherapy, and ferroptosis led to cell death and membrane rupture. The release of antigens from the cancer cell was then detected and caused migration of immune dendritic cells (DCs), which stimulated the antitumour immune response via presentation to $CD8^+$ cells at the lymph node. The immune system could not only target the tumour cells but allowed for recognition of the tumour for immunological memory, which was demonstrated in an *in vivo* mouse model. The synergistic mechanism of copolymer **16** was therefore both effective at killing tumour cells, as well as inhibiting the growth of tumours away from the active site and inhibiting recurrence via the adaptive immune response.

A number of ruthenium-containing coordination complexes, including organometallic complexes, have been widely investigated for their phototherapeutic and antiproliferative activities [89–93]. These range from simple complexes to polymeric and dendrimeric materials. Ruthenium complexes tend to be less cytotoxic than well-recognized platinum complexes. The diamagnetic Ru(II) and the paramagnetic Ru(III) have both been found to be effective for targeting cancer cells [94,95]. Additionally, certain ruthenium compounds have been demonstrated to have higher selectivity for cancer cells, due to Ru mimicking the uptake of Fe by binding to serum proteins [96,97].

For example, Patra and coworkers prepared two piano-stool complexes with three ligands as the “legs” and a *p*-cymene moiety on “top” in a pseudooctahedral geometry, [Ru^{II}(η^6-p-cymene)(N-(2-morpholinoethyl)-4-(2-aminoethyl)amino-naphthalimide)Cl_2] (**17**) and [Ru^{II}(η^6-p-cymene)(N-(2-morpholinoethyl)-4-(2-aminoethyl)amino-naphthalimide)(PTA)Cl]PF_6 (**18)** (Figure 8), where PTA represents 1,3,5-triaza-7-phosphatricyclo-[3.3.1.1]decane [98]. The morpholine moiety (labelled in green) was used to target lysosomes, while the ruthenium(II) centre and the amino-naphthalimide moiety (labelled in blue) provided the luminescence and photosensitizing activities of these complexes. Both complexes exhibited photocytotoxicity on exposure to blue light irradiation at 448 nm via PDT, specifically producing singlet oxygen. The chloro complex **17** was more lipophilic, which increased internalization by MCF-7 cells, thereby improving the activity. Confocal fluorescent microscopy showed that both complexes were localized to the nucleus and lysosomes in order to target nuclear DNA and disrupt lysosomal integrity, resulting in a synergistic cytotoxic mechanism.

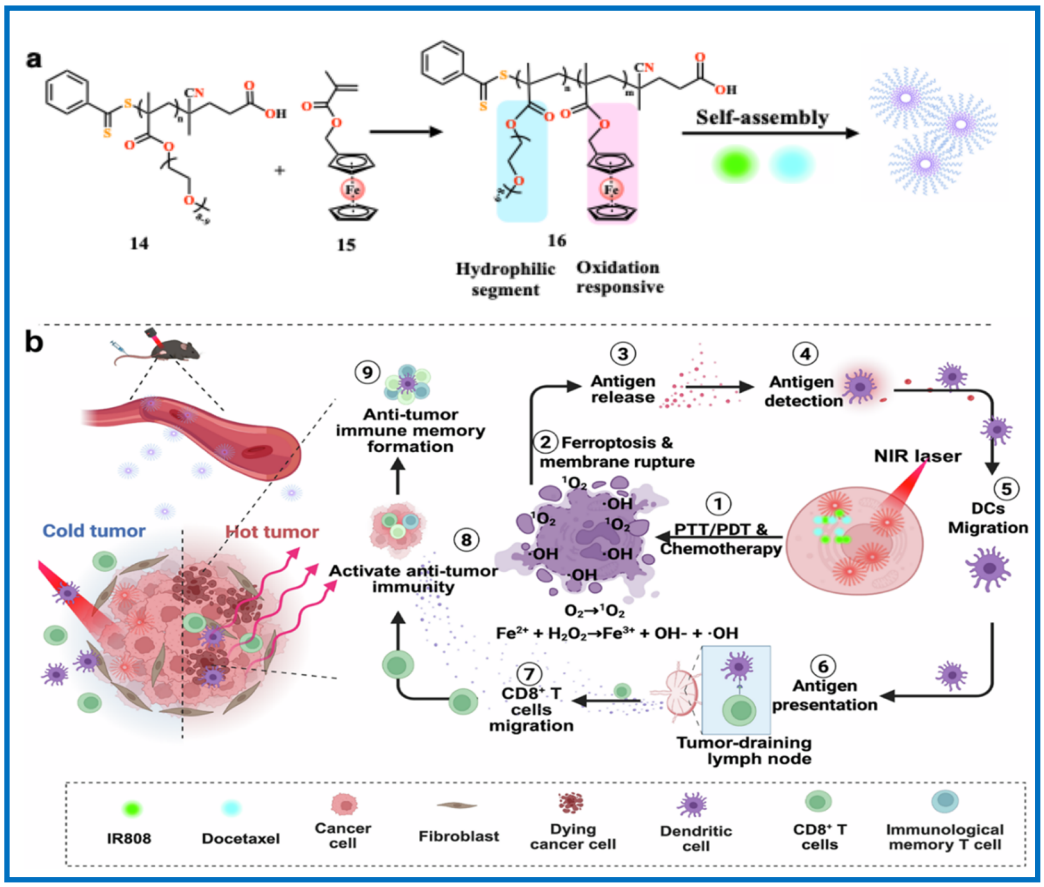

Figure 7. (**a**) Synthesis of PPEGMA-*b*-PFMMA copolymer **16** and self-assembly into nanoparticles with docetaxel and IR808. (**b**) Mechanisms of antiproliferative activity and immunological memory caused by the synergistic phototherapeutic and chemotherapeutic effects of copolymer **16**. Reproduced from Ref. [88], https://doi.org/10.1038/s41392-026-02608-5, under the terms of the CC BY NC ND 4.0 license, http://creativecommons.org/licenses/by-nc-nd/4.0/.

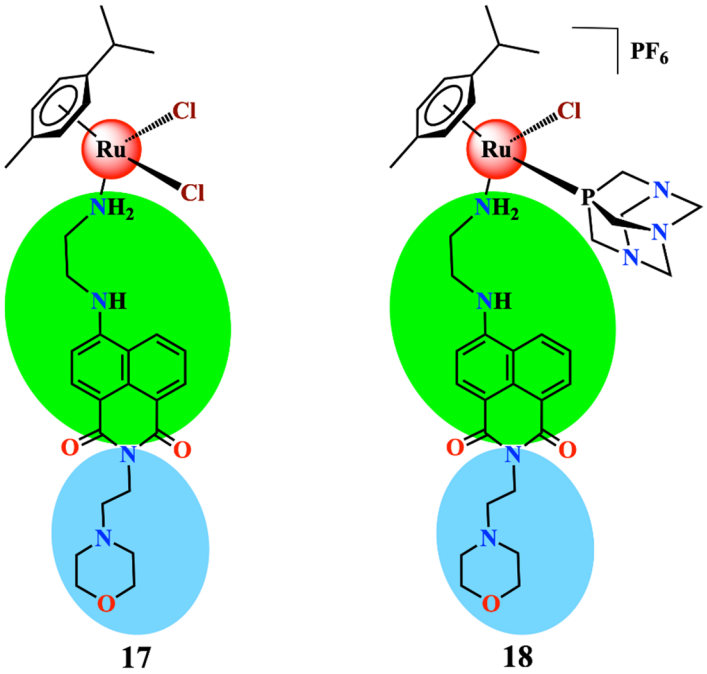

Figure 8. Structures of ruthenium complexes **17** and **18**.

The transport of ruthenium complexes is generally accomplished by the protein transferrin, which can bind to metals to result in endocytosis mediated by transferrin receptors on the cell membrane. Docking calculations were therefore performed for human transferrin (hTf), as either the protein alone (PDB ID: 2HAV) or the protein-iron(III) complex (3QYT), for both complexes **17** and **18**. Five binding sites were selected based on nearby histidine residues. The resulting docked conformations indicated that the most favourable sites were around His207 and His242 for both complexes. While complex **17** was more lipophilic, PTA-containing complex **18** containing had stronger binding affinities, in particular at the His242 site, where the binding cavity could enhance interactions of the Ru(II) complex with the histidine residues. Additionally, the improved binding affinity in the transferrin containing iron indicated cooperation by the Fe(III) group.

Another example of a "piano-stool" Ru(II)-η^6-*p*-cymene complex was prepared by Bisceglie et al. [99]. Generally, the pyridyl ligand of the complex was modified with a naphthalimide group to act as an antenna that could capture the energy of the photon irradiation and transfer it to the Ru(II) centre. Upon irradiation at 420 nm, complexes **19-21** dissolved in dimethyl sulfoxide (DMSO) would undergo a substitution reaction with the solvent, releasing the DMSO-substituted Ru(II) complex (**22**) and the pyridine-naphthalimide product (**R1-3**), as outlined in Scheme 3. This caused a change in the emission profile from blue emission by the full complex to a combination of green light by the DMSO-substituted complex and red by the pyridine-naphthalimide product. Complex **21** was the only one to exhibit cytotoxicity after exposure to blue light, with an IC_{50} of 10.55 μM, although all showed no toxicity for A549 cells in the dark. This finding is supported by the almost total dissociation of the naphthalimide ligand after 3 hours of blue light irradiation, compared to only ~50% dissociation for the other two complexes.

In addition to these complexes alone, polymeric structures could be used to improve their photoactivity. One example of this approach was the self-assembly of nanoparticles of complex **23** (Figure 9) encapsulated with pluronic F127, a triblock copolymer composed of two polyethylene oxide (PEO) chains connected by polypropylene oxide (PPO) [100]. The polymeric nanoparticles were then used for PDT/PTT using a NIR laser (808 nm) to generate ROS, especially singlet oxygen, as well as heat. The addition of pluronic F127 to the nanoparticles increased biocompatibility to ensure greater accumulation at the tumour.

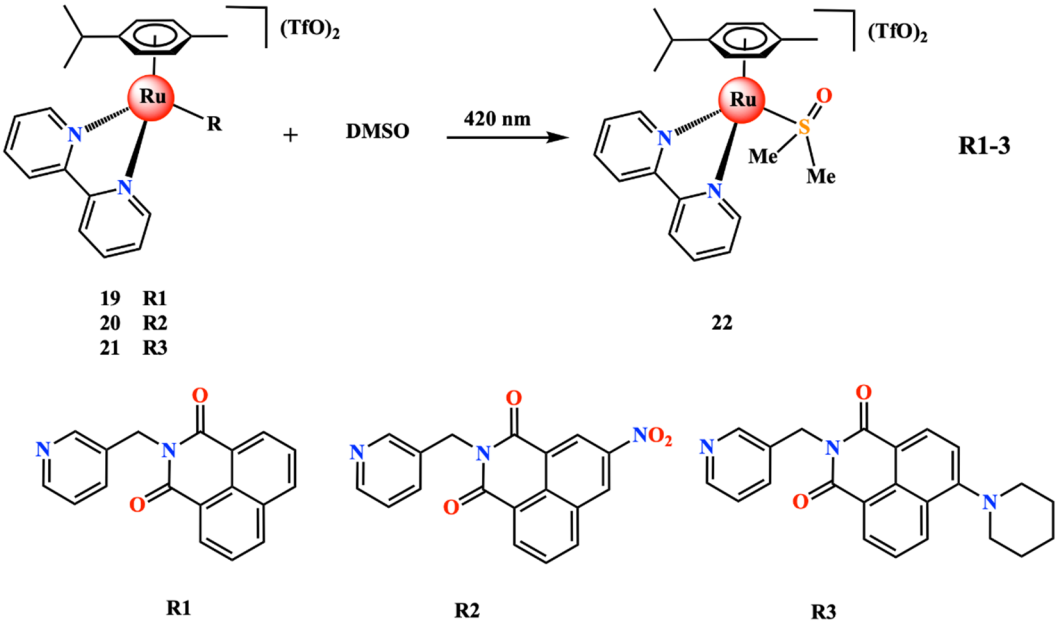

Scheme 3. Degradation by 420 nm irradiation for complexes **19-21** to produce the DMSO-conjugated complex **22** and compounds **R1-R3**, respectively.

Treatment with complex **23** and the complex/pluronic F127 nanoparticles, with and without irradiation at 808 nm, were evaluated in an *in vivo* model of triple negative breast cancer using MDA-MB-231 cells in nude mice. Figure 10A demonstrated the enhanced heating at the tumour for the nanoparticles containing complex **23** compared to the complex alone or saline as a negative control. The photothermal conversion efficiency of the complex was also found to be superior to commercially available gold nanorods (24% and 21%, respectively). No toxicity was detected for either the complex or NPs without the laser, but significant decrease in tumour volume (Figure 10B) and weight (Figure 10C) was exhibited for both with addition of the laser treatment. Furthermore, tumours from mice treated with the nanoparticles containing complex **23** and laser irradiation were significantly lower in both volume and weight. The biocompatibility of the nanoparticles allowed them to accumulate at the

tumour, resulting in a 95.2% decrease in tumour volume. No change in total body weight of the subjects was observed for any of the conditions, so neither complex **23** nor the nanoparticles affected overall health over the course of the study, with or without the laser irradiation, as shown in Figure 10D. This was confirmed by the histology results in Figure 10E, as the hematoxylin and eosin (H&E) stained tissue slices showed healthy tissue except for the tumours treated with laser irradiation and either complex **23** or the nanoparticles.

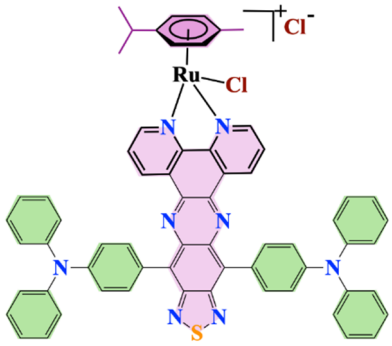

23

Figure 9. Structure of ruthenium complex **23**.

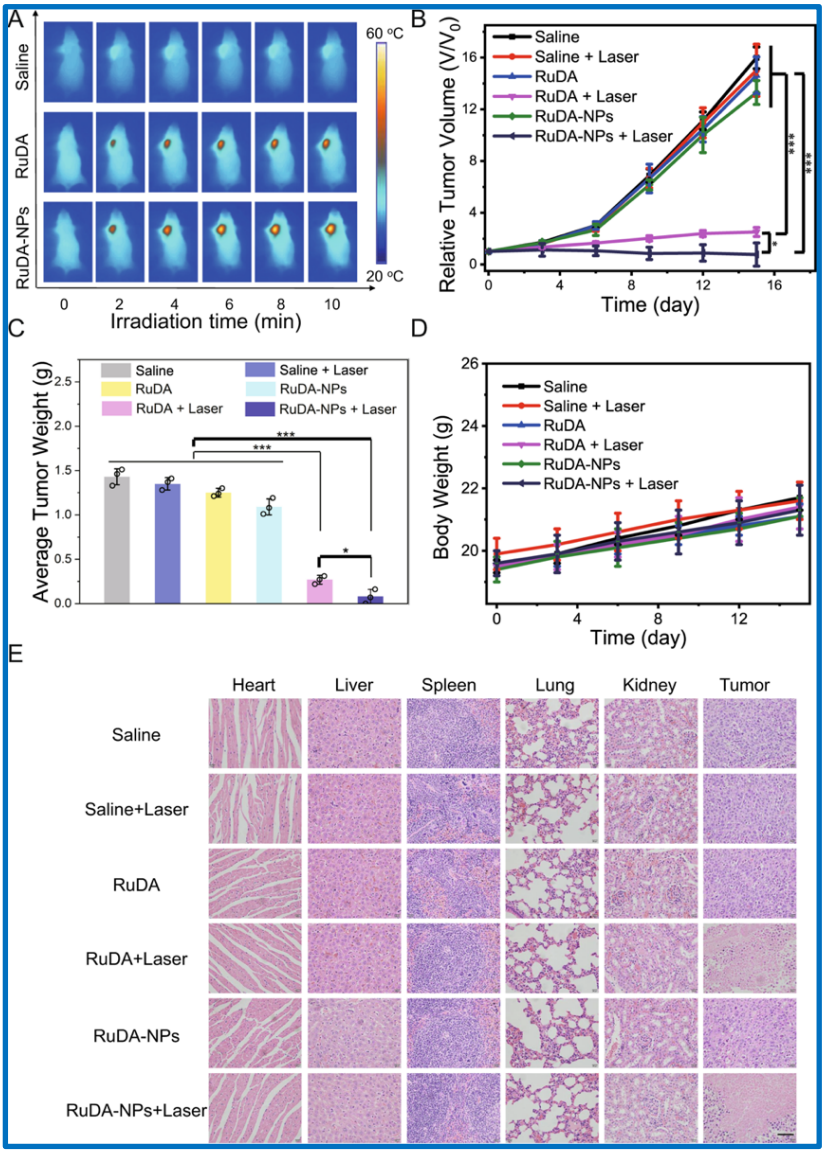

Figure 10. Phototherapy of mice bearing MDA-MB-231 tumours and treated with saline, complex **23** (RuDA), or the complex **23**/pluronic F127 nanoparticles. (**A**) Infrared images of mice 8h post-injection after various durations

of irradiation with an 808 nm laser. (**B**) The relative volume and (**C**) average weight of the tumours from each treatment group. (**D**) Total body weight of the mice over the experimental period (* $p < 0.05$, and *** $p < 0.001$). (**E**) Micrographs of heart, liver, spleen, lung, kidney, and tumour tissues stained with H&E (scale bars = 60 μm). Reproduced from Ref. [100], https://doi.org/10.1038/s41467-022-30721-w (accessed 7 May 2026), under the terms of the CC BY 4.0 license, https://creativecommons.org/licenses/by/4.0/.

Transition-metal containing dendrimers have been utilized in bioimaging and phototherapeutic applications. However, the majority of metallodendrimers coordinated through the nitrogen or oxygen atoms of the organic ligands rather than the carbon atoms. There are a few examples where the metallic moieties of the dendrimers are coordinated to carbon atoms. For example, Michlewska et al. synthesized ruthenium-containing dendrimers for anticancer applications that were labelled with fluorescein isothiocyanate (FITC) as a fluorescent probe [101]. This research group prepared carbosilane dendrimers decorated with Ru(η^6-*p*-cymene) groups at the periphery of the dendrimeric material, as shown in Scheme 4. The carbosilane dendrimer **24** with amino groups in the periphery was reacted with picolinaldehyde to produce the corresponding dendrimer with a 3:1 ratio of terminal iminopyridine to amino groups (**25**), followed by reaction with [Ru(η^6-*p*-cymene)Cl_2]$_2$ (**26**) to yield the dendrimer with terminal ruthenium moieties and a free amino group (**27**). The amino group was then reacted with FITC to produce the desired dendrimeric material labelled with FITC (**28**).

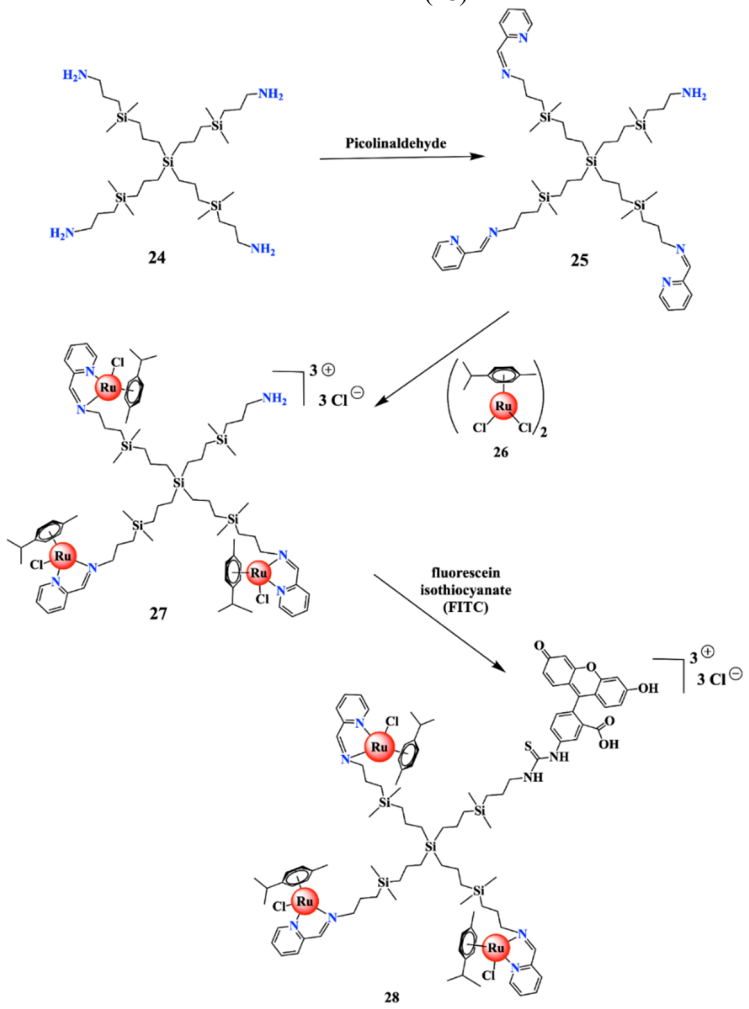

Scheme 4. Preparation of FITC-labelled carbosilane dendrimer **28**.

The Ru(II) moieties provided the dendrimer anticancer activity by inhibiting nucleic acid synthesis and induction of apoptosis, while the FITC moiety acted as a fluorescent label in the imaging of cellular localization of the dendrimers. Notably, the addition of FITC in dendrimer **28** did not inhibit the uptake of the dendrimer by cancer cells, which demonstrated the use of this probe for fluorescence was not detrimental to its application as an anticancer agent. Confocal micrographs of the leukemia cell line HL-60 incubated with 2.5 μM (Figure 11B) and 5 μM (Figure 11C) of the dendrimer showed uptake by the cells compared to the untreated negative control (Figure 11A). The dendrimers were visualized in yellow, while the nuclei were stained with 4′,6-diamidino-2-phenylindole (DAPI, blue) and the cytoskeletal protein actin stained with Texas Red X-phalloidin (red). The fluorescent imaging yielded by the FITC

label could therefore allow this dendrimer system to be further investigated for use in clinical diagnostic imaging or laboratory bioimaging studies of anticancer dendrimer development.

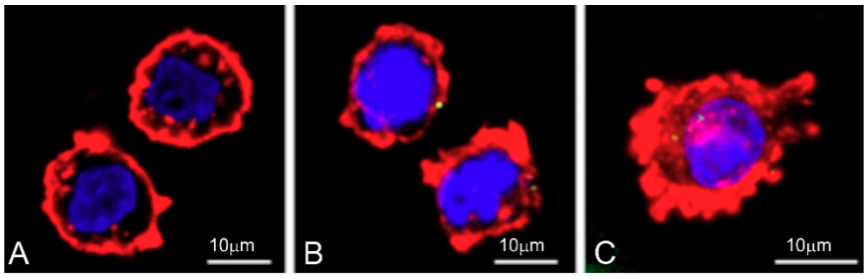

Figure 11. HL-60 cells treated with (**A**) 0 μM, (**B**) 2.5 μM or (**C**) 5μM dendrimer **28** stained with DAPI and Texas Red-X Phalloidin and imaged with confocal microscopy. Reproduced with permission from Ref. [101], https://doi.org/10.3390/biom9090411, under the terms of the CC BY 4.0 license, https://creativecommons.org/licenses/by/4.0/.

2.3. Iridium Complexes

Iridium(III) complexes emit near-infrared (NIR) radiation, rather than UV fluorescence, allowing them to be used for imaging applications as well as PDT and PTT. The general structure of these Ir(III) complexes is an iridium center with at least two cyclometallated C^N ligands and one N^N ligand [102]. The C^N ligands have been found to provide the major contributions to the photophysical properties. Despite the advantages provided by Ir(III) complexes, research into their phototherapeutic applications remains ongoing because of issues with efficiency. One of the main limiting factors is PDT mechanisms reliant on generating singlet oxygen, which is inhibited by the low oxygen concentrations found in tumours, particularly at the centre.

As an example of Ir(III) complexes with this structure, two fluorescent probes were designed for imaging of SARS-CoV-2 enhanced by AIE [77]. The fluorescent probes **29** and **30** consisted of an Ir(III) complex, responsible for the AIE activity, connected to a targeting moiety containing a short oligonucleotide of single stranded DNA complementary to specific viral RNA sequences (Figure 12). The probes could therefore bind to RNA via base pairing hydrogen bonds, causing aggregation and therefore AIE. The AIE mechanism was validated by addition of viral RNA amplified using quantitative polymerase chain reaction (qPCR) assays, which resulted in increased fluorescence intensity for the probes. The probes were examined for their activity against clinical isolates of SARS-CoV-2 RNA at room temperature. Within 10 minutes, a sensitive and specific fluorescence response was detected, with a limit of detection (LOD) of 1.84 RNA copies per reaction.

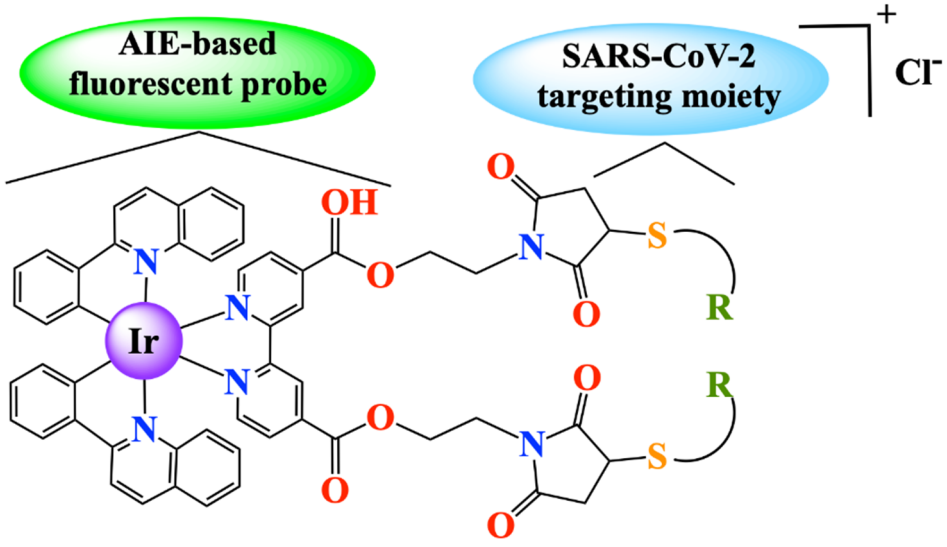

Figure 12. Structures of iridium complexes **29** and **30**.

Photostable and tunable luminescent Ru(II) complexes have been used for the development of DNA probes [103]. Although charged complexes increase aqueous solubility and interaction with the DNA, hydrophobicity is more desirable for cellular imaging studies, as the molecule needs to be able to cross the phospholipid cell membrane. As a result, amphiphilic complexes **42-46** were prepared containing hydrophobic dipyridophenazine moieties and a hydrophilic ethylene diamine ligand. The ligands **31-35** were reacted with $IrCl_3 \cdot xH_2O$ (**36**) to form the dichloro-bridged dimers **37-41**, which gave the mononuclear cationic complexes **42-46** by reaction with excess ethylene diamine (Scheme 5).

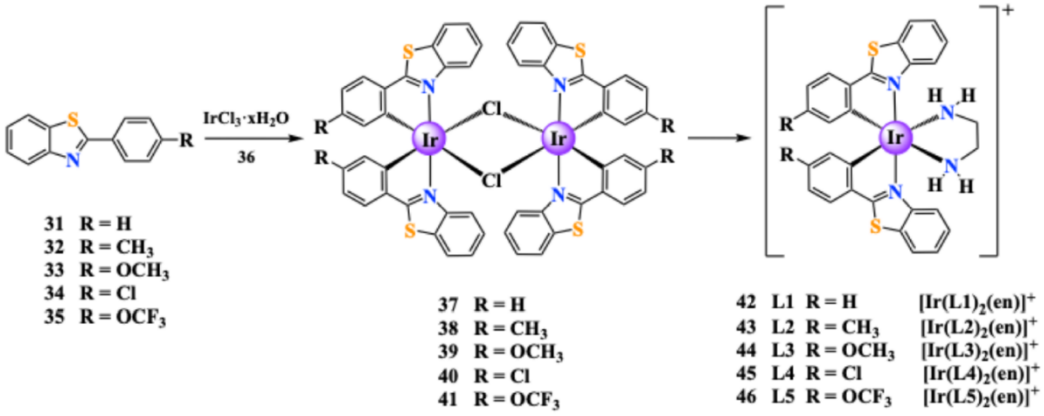

Scheme 5. Synthesis of complexes **42-46**.

Docking studies were performed with X-ray crystal structures of complexes **42**, **43** and **45** with a segment of double stranded DNA, namely $d(ATCGAGACGTCTCGAT)_2$, which contained a gap suitable for intercalation. It is important to note that the authors used the analogous complexes containing Co for docking instead of Ir, due to issues with parameterization. On the other hand, the coordination environment around the metal was kept rigid to maintain the structure of the complex, so the overall structure should not have significantly impacted the outcome of the simulations. The Ir(III) complexes were observed to bind to DNA without intercalating, as can be seen in Figure 13, instead interacting with the DNA groove via electrostatic or hydrogen bonding interactions. Further study using isothermal titration calorimetry (ITC) confirmed that complexes **42** and **43**, as well as complex **44**, were all found binding to DNA in two binding sites: one with specific major or minor DNA groove binding with high binding affinity (10^7–10^8 M^{-1}) and a second non-specific binding with the negatively charged DNA backbone with lower binding affinity (10^5 M^{-1}).

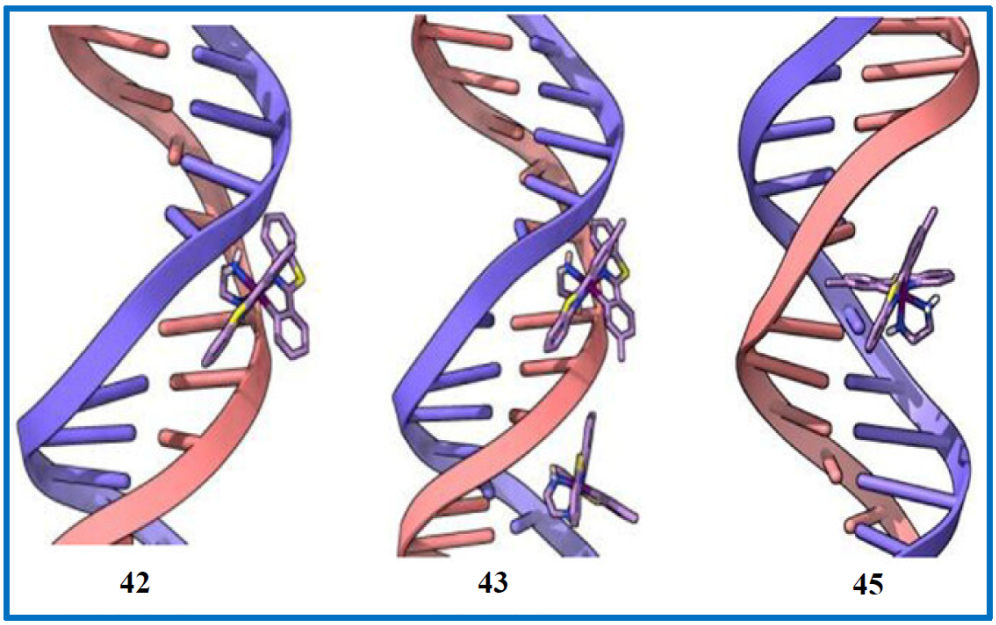

Figure 13. DNA binding to complexes **42**, **43** and **45**. Reproduced with permission from Ref. [103], https://doi.org/10.1002/chem.202500290, under the terms of the CC BY 4.0 license, https://creativecommons.org/licenses/by/4.0/.

As an example of Ir(III) complexes with phototherapeutic applications, Das et al. designed ER-targeting complexes for both fluorescent imaging and PDT [104]. The iridium complexes **47** and **50**, were ground with 2-aminothiophenol and *p*-toluene sulfonic acid (PTSA) for 10 minutes to yield complexes **48** and **51**, followed by reaction with $[Cp^*IrCl_2]_2$, where Cp* = 1,2,3,4,5-pentamethylcyclopentadiene, and sodium acetate in methanol at 50 ºC for six hours to produce the trinuclear complexes **49** and **52**, as shown in Scheme 6. Complexes **48**, **49**, **51**, and **52** were all non-toxic against MCF-7 cells in the dark, with IC_{50} values of 24.50, 27.25, 24.54 and 28.65 μM, respectively. On the other hand, photoexcitation at 390 nm resulted in apoptosis via ROS production, with IC_{50} values of 0.79, 0.51, 0.50 and 0.11 μM, respectively. Trinuclear complexes **49** and **52** localized in the nucleus, while the smaller mononuclear complexes **48** and **51** accumulated in the endoplasmic reticulum. The authors concluded that this was due to the differences in charge distribution, with the trinuclear complexes being able to distribute the charge over a larger surface area. This effect could therefore be used to target different organelles.

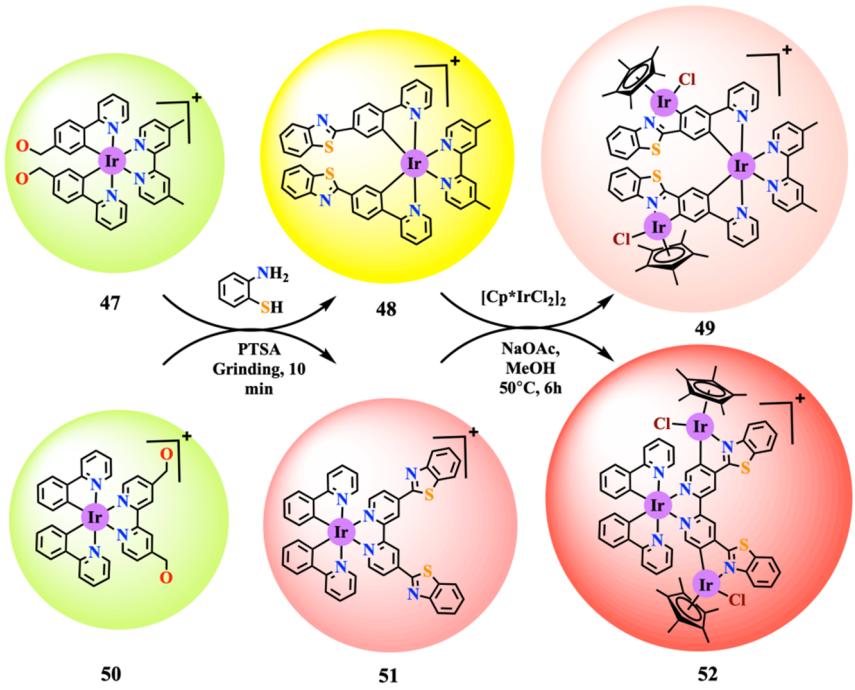

Scheme 6. Preparation of mononuclear Ir(III) complexes **48** and **51** and trinuclear complexes **49** and **52**.

Zhou et al. used a rhodamine moiety to enhance the ROS generation of a fluorescent Ir(III) complex by PDT [105]. The rhodamine-decorated complex **53** was composed of the phosphorescent Ir(III) complex (in blue) and fluorescent rhodamine (in red) as shown in Figure 14. The cyclometallated 2,3-diphenylquinoxaline ligands of the complex enhanced ER targeting, while the rhodamine moiety captured energy from photons and transferred it to the iridium centre.

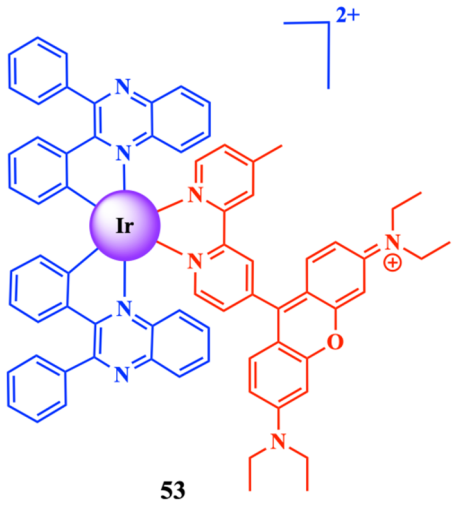

Figure 14. Structure of iridium complex **53**.

The NIR spectra of the complex showed an absorption peak at 578 nm and weak fluorescence at 635 nm. NIR fluorescence imaging using complex **53** was examined in an *in vivo* mouse model bearing MCF-7 tumours. As can be seen by the fluorescence image in Figure 15a and graph of fluorescence intensity in Figure 15b, the fluorescence signal migrated from circulation to the tumour tissue, reaching a maximum at 24 hours post-injection before being cleared. The ex vivo organs and tissues of these animals were also analyzed, as shown in the fluorescence image in Figure 15c and graph of intensity in Figure 15d, which showed that complex **53** primarily accumulated at the tumour, with some found in lung and liver tissues. Despite the fluorescence detected in these tissues, however, no abnormalities were observed, showing that the complex was not significantly toxic without exposure to irradiation. The photoactivity for PDT was due to complex **53** targeting the ER and generating singlet oxygen to induce apoptosis. The quantum yield of singlet oxygen produced by complex **53** was 1.6x greater than the positive control Rose Bengal in acetonitrile solution, confirming its efficacy at generating ROS. PDT experiments *in vivo* were performed on mice given complex **53** with application of irradiation by a xenon lamp. As in the imaging experiments, there were no abnormalities observed in the organs after irradiation, but a significant decrease in tumour volume as measured, in addition to a 100% survival rate for all mice in the complex **53**-treated group.

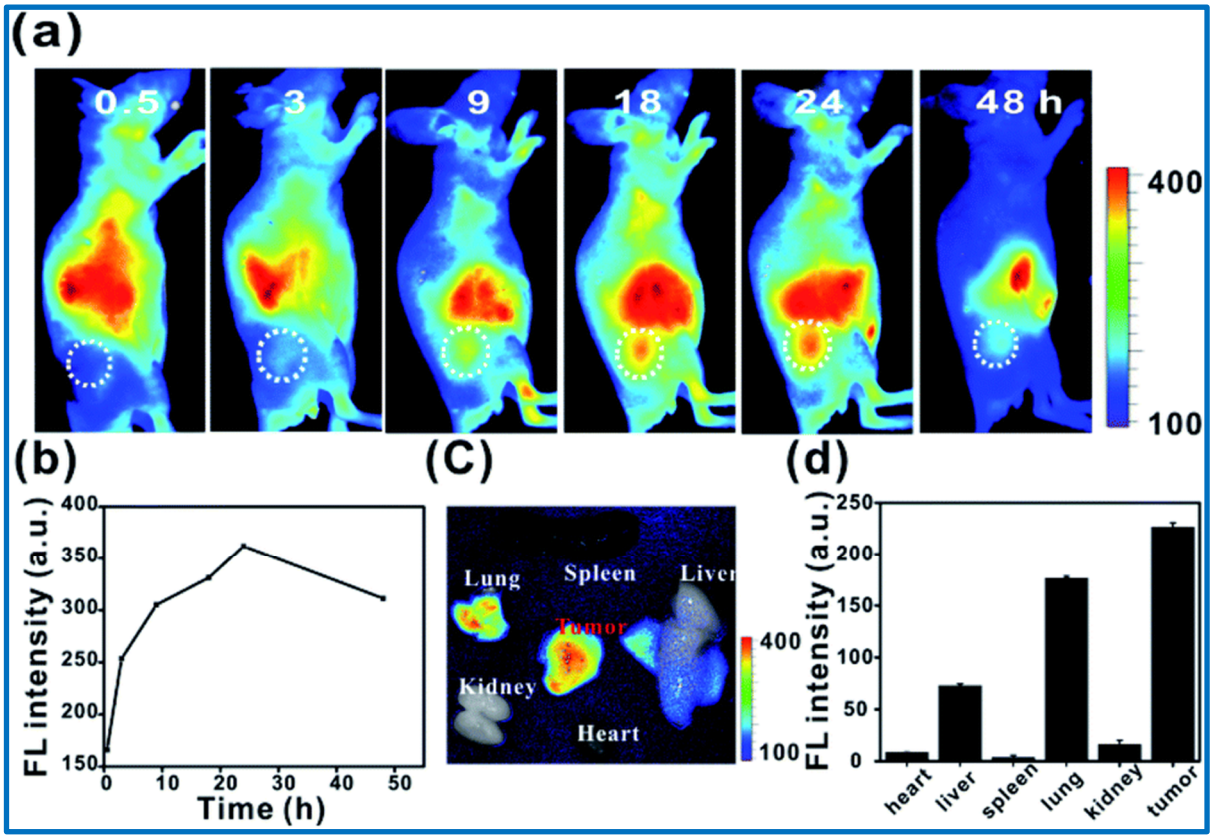

Figure 15. NIR fluorescence imaging for nude mice bearing MCF-7 tumours using complex **53**. (**a**) NIR fluorescence image and (**b**) intensity from the mice as well as (**c**) NIR fluorescence image and (**d**) intensity ex vivo organs and tumours taken after the end of the experiment. Reproduced with permission from Ref. [105], https://doi.org/10.1039/D0SC04751A, under the terms of the CC BY 4.0 license, https://creativecommons.org/licenses/by/4.0/.

Two Ir(III) complexes, **54** and **55** (Figure 16), were designed by Liu et al. for PDT to produce ROS while also depleting antioxidant glutathione (GSH) in the mitochondria of cancer cells [106]. The α,β-unsaturated ketone moiety in both complexes oxidizes the thiol group in GSH, preventing its use for protection against ROS-induced apoptosis.

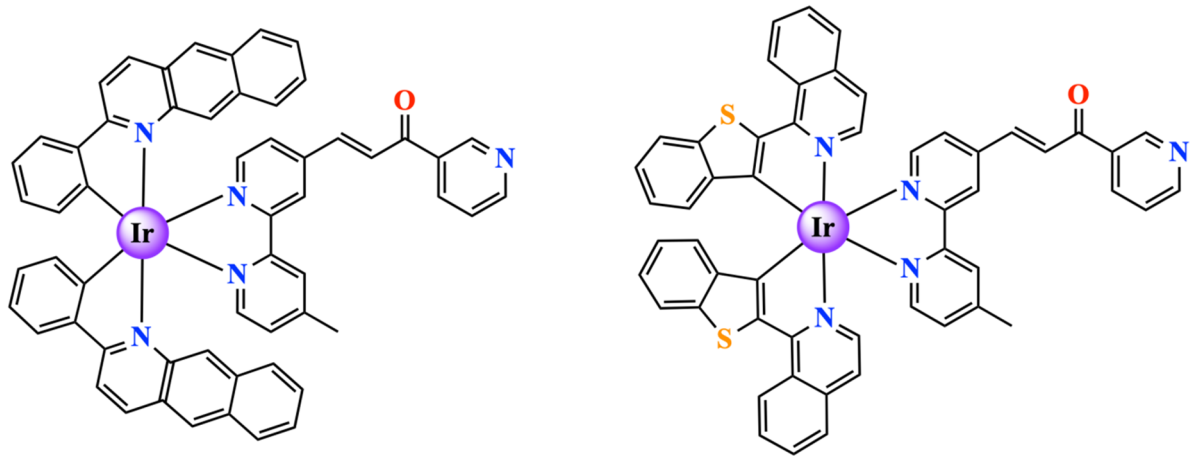

Figure 16. Structures of iridium complexes **54** and **55**.

Both complexes contributed towards ROS induction of apoptosis through a combination of type I photocatalysis, which produces superoxide and hydroxyl radicals, and type II photocatalysis, which produces singlet oxygen, as outlined in Figure 17. This allows them to be active even under low oxygen conditions in the tumour. Also, the AIE properties enhanced emission of fluorescence for imaging of the aggregates at the tumour. Additionally, the positive charge on the complexes gives them the ability to target mitochondria, where the complexes could then deplete GSH, which was confirmed by colocalization experiments that showed predominant association of both complexes with the mitochondria. The induction of ROS and depletion of GSH mechanism resulted in low cytotoxicity in the dark with IC_{50} values of 18.24 μM for complex **54** and 15.21 μM for complex **55**, but efficient photocytotoxicity with IC_{50} values of 0.69 μM for complex **54** and 1.47 μM for complex **55**.

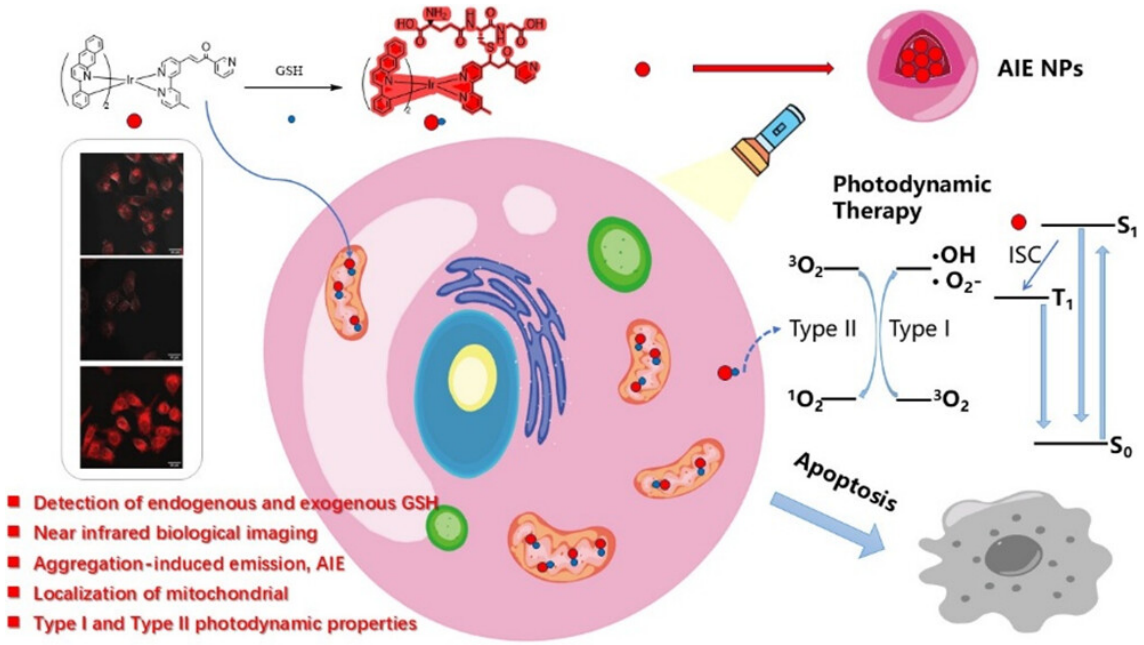

Figure 17. Schematic illustration of PDT using complexes **54** and **55**. Reproduced with permission from Ref. [106], Copyright © 2026, American Chemical Society.

Another example of Ir(III) complexes designed to target mitochondria is the approach used by Gupta et al. [107]. The di-iridium complex **56** containing 2-phenylquinoline ligands was reacted with five different ligands to yield the cyclometallated iridium complexes **57**–**61** containing various 4,4′-dimethyl-2,2′-bipyridine moieties (Scheme 7). Complex **57** was unsubstituted, while complex **58** contained a carboxylic acid group. Complexes **59**, **60**, and **61** were all esters, functionalized with a PEG chain, an alkyl triphenylphosphonium (TPP) moiety, and biotin (vitamin B7), respectively.

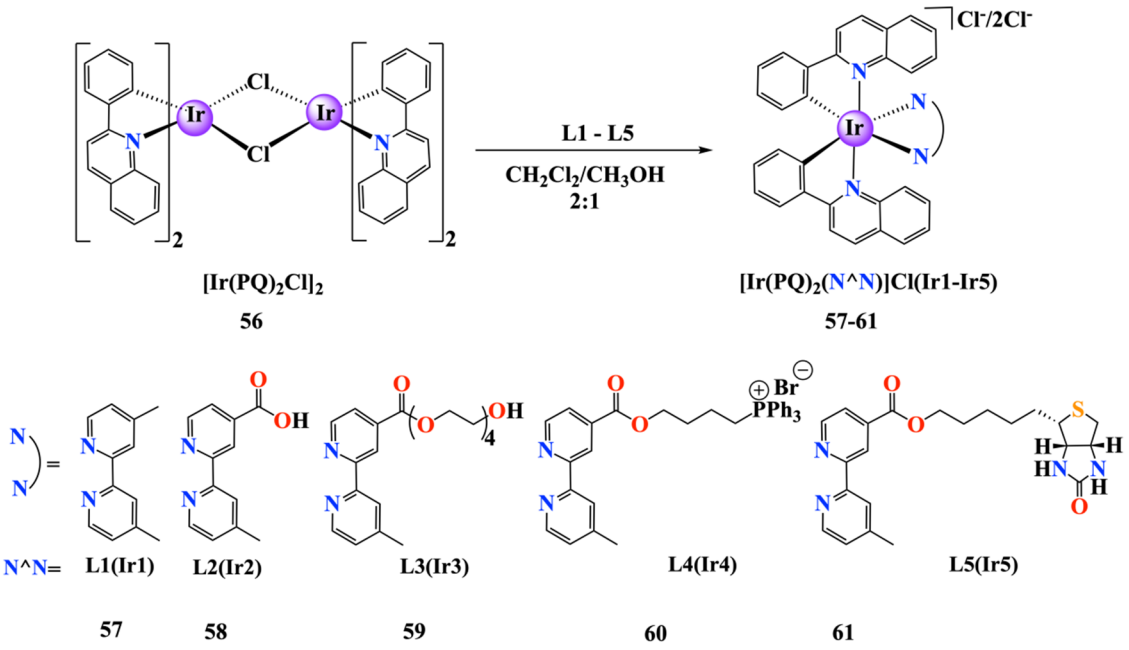

Scheme 7. Preparation of complexes **57-61** with various 4,4′-dimethyl-2,2′-bipyridine ligands (**L1-L5**).

A2780 cisplatin-sensitive ovarian cancer, A2780cisR cisplatin-resistant ovarian cancer, A549 lung cancer, and MCF-7 breast cancer cells, as well as healthy HEK293 embryonic kidney cells, were used to examine the photocytotoxicity of complexes **57-61** in vitro. The only complex containing a cationic ligand was complex **60** with a PPh_3 moiety, which was also the most phototoxic as well as exhibiting the greatest localization to mitochondria (Figure 18). The IC_{50} values with and without irradiation at 405 nm for complex **60** were 4.14 and 0.22 μM against A2780, 3.84 and 0.06 μM against A2780cisR, 4.84 and 0.07 μM against A549, and 3.43 and 0.09 against MCF-7. This showed that PDT using complex **60** was effective against all the cancer cell lines, including the antibiotic-resistant A2780cisR cells. Although HEK293 still showed cytotoxicity, both with or without irradiation, they displayed higher IC_{50} values than cancer cells (7.27 and 0.93 μM, respectively), demonstrating that complex **60** was more active against cancer cells than healthy cells. This complex was also evaluated against A549 multicellular tumour spheroids (MCTSs), which are used as an in vitro model of tumours to mimic their three-dimensional structure. Complex **60** exhibited an IC_{50} value of 0.9 μM, indicating potent photocytotoxicity against the MCTSs.

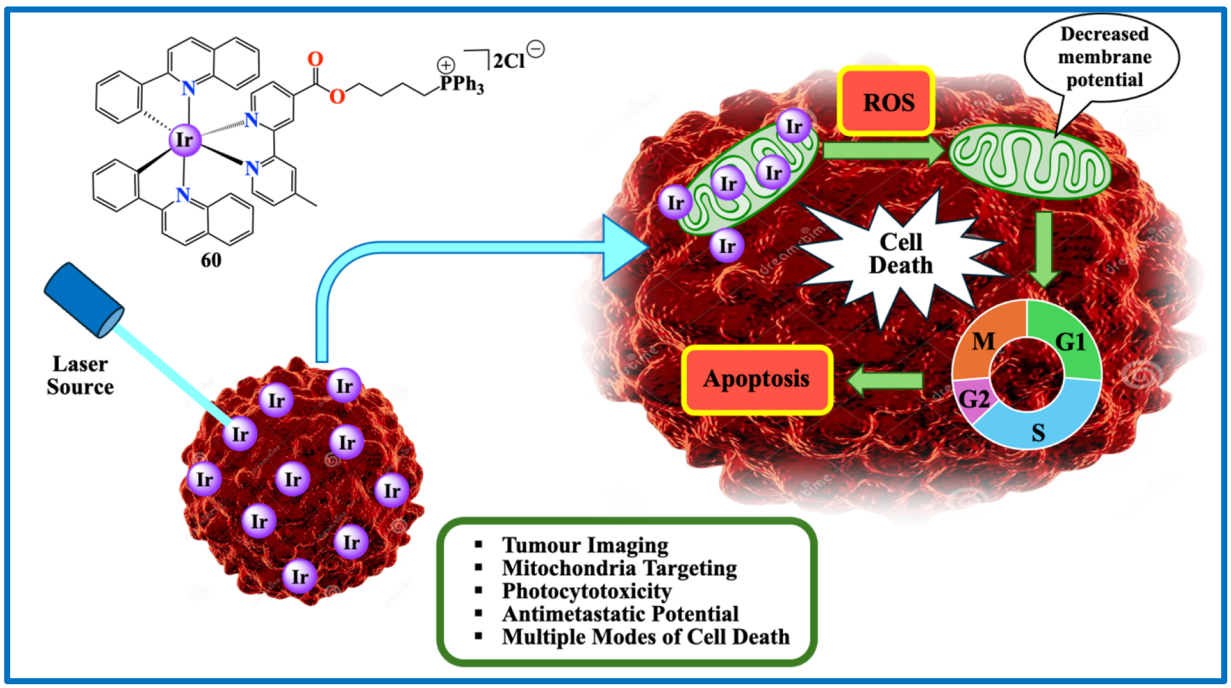

Figure 18. The phototherapeutic mechanism and applications of complex **60**.

Jones et al. prepared the cyclometallated Ir(III) complex **64** with 2-thienyl pyridine and 2,2′-bis-benzimidazole ligands as a photosensitizer for a range of cancer cells [108]. Complex **64** was synthesized from the reaction of the dichloro-bridged Ir(III) dimer **62** with 2,2′-bis-benzimidazole (**63**) as shown in Scheme 8. The phosphorescence of complex **64** was measured to determine its uptake for bladder (EJ), malignant melanoma (A375), and oropharyngeal (OPSCC72) cancer cells. In all three cell lines, the complex was detected in the cytoplasm up to 24 hours after incubation with 20 μM complex **64**. Photoirradiation of cells treated with the complex (at 405 or 455 nm) resulted in a significant increase in cytotoxicity against all three cancer cell lines, compared to the lack of cell death observed for cells treated with the complex in the dark. The cytotoxic mechanism acted via induction of ROS, primarily singlet oxygen. PDT using complex **64** was also effective against 3D spheroids of A375 cells, resulting in a 40% decrease in surface area 72 hours post-irradiation.

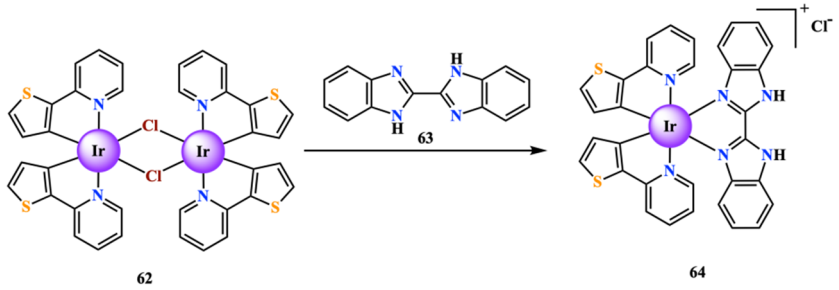

Scheme 8. Synthesis of cyclometallated Ir(III) complex **64** with 2-thienyl pyridine and 2,2′-bis-benzimidazole ligands.

To determine the subcellular localization of complex **64**, EJ bladder cells were treated with fluorescently labelled antibodies against the ER, Golgi apparatus and mitochondria. Utilizing both the fluorescence for each antibody and the phosphorescence emitted by the complex, confocal fluorescence microscopy produced the micrographs in Figure 19. The merged images showed the greatest colocalization of the complex in the Golgi apparatus, although it was present in all three organelles. Oxidative damage to these three organelles is known to be involved in autophagy and apoptosis induced by irradiation and was therefore concluded to be involved in the photocytotoxic mechanism of complex **64**.

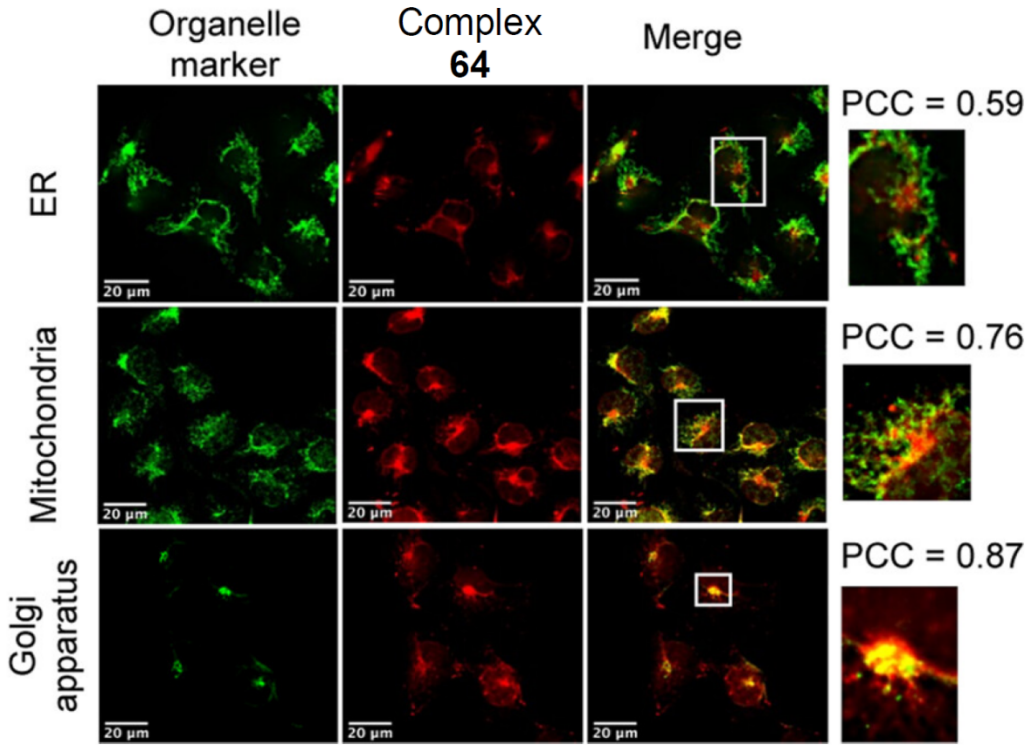

Figure 19. Organelle-specific antibody labelling of EJ cells incubated with complex **64**. Reproduced from Ref. [108], https://doi.org/10.1021/acs.jmedchem.4c00869, under the terms of the CC BY 4.0 license, https://creativecommons.org/licenses/by/4.0/.

Iridium(III) complexes with the general structure of two C^N and one N^N ligand, utilizing 2-(2′-benzothiazolyl)-benzimidazole ligands, were examined for imaging via AIE-induced emission and for PDT [109]. Induction of ROS was not reliant on singlet oxygen due to increased activity of type I photocatalysis, maintaining its efficacy against the tumour cells despite hypoxia in the centre of tumours. These complexes were found to be phototoxic after irradiation with blue light (405 nm) in A549 lung cancer cells, as well as tumour tissue models constructed from spheroids of HCC827 lung cancer cells (a different cell line used due to the inability of A549 to form spheroids). Another complex with this structure was prepared by Shee et al., where the cyclometallated Ir complex was conjugated with biotin [110]. The mechanism was a combination of chelation of copper ions to disrupt homeostasis and PDT increasing ROS production and lipid peroxidation, resulting in induction of apoptosis and ferroptosis.

While there are many examples of phototherapeutic applications for organoiridium complexes, there are also a few examples of organoiridium-containing polymers utilized in the development of phototherapeutic agents. To use Ir(III) complexes to generate singlet oxygen for PDT by exposure to NIR (980 nm) irradiation, Zhao et al. prepared polymeric micelles using a combination of the iridium complex **65** for its PDT activity and the antineoplastic agent lapatinib (**66**) for synergistic anticancer activity, connected via polyethylene glycol (PEG) spacers [111]. These polymeric materials were then self-assembled using ultrasonic treatment with upconversion nanoparticles ($NaYF_4$:Yb/Tm@$NaYF_4$) to capture and transfer energy from NIR irradiation to the iridium centres. The structure of the polymeric micelles consisted of upconversion nanoparticles in the center, which were connected to units of Ir(III) complex **65**, with lapatinib on the surface, as illustrated in Figure 20.

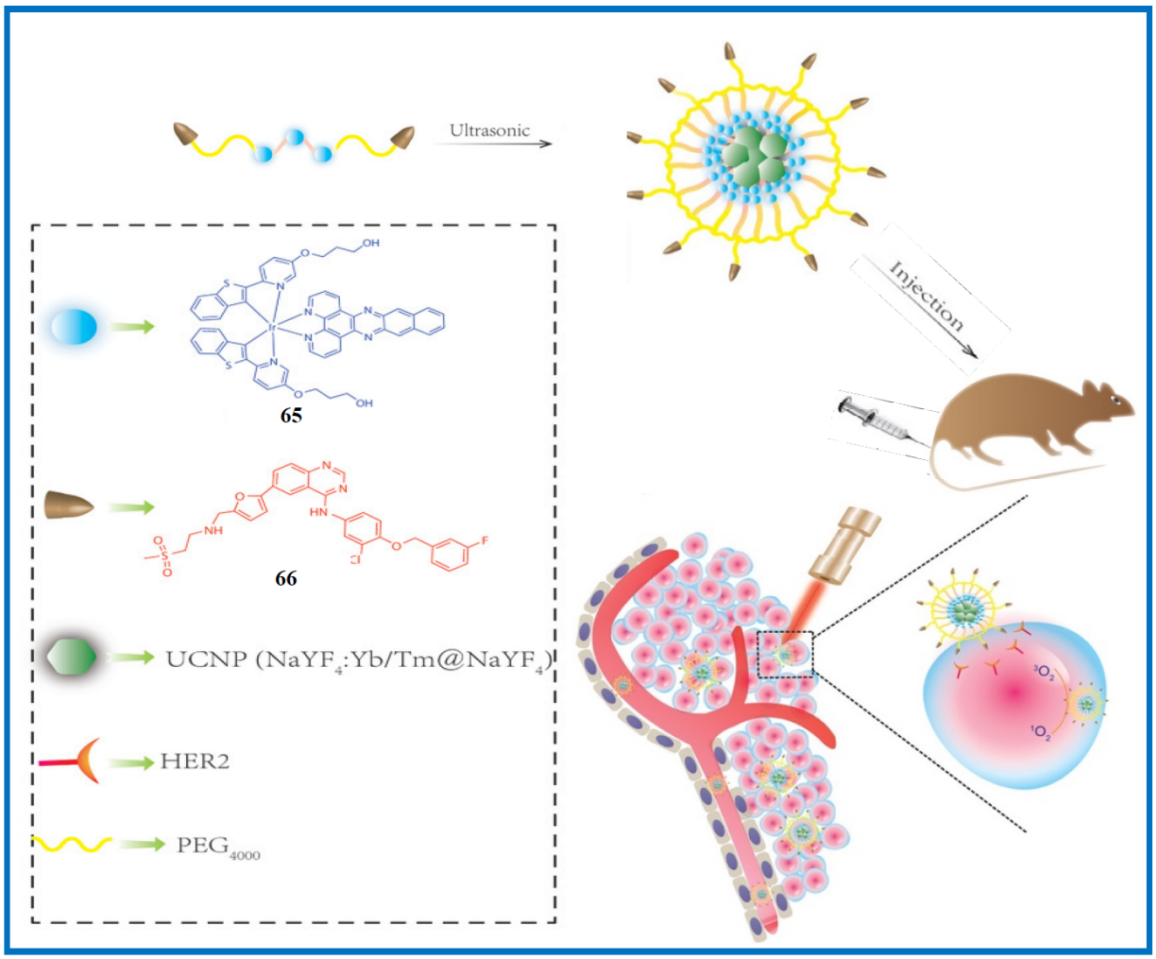

Figure 20. Self-assembly and phototherapeutic application of polymeric micelles containing complex **65** and lapatinib **66**. Reproduced from Ref. [111] with permission from John Wiley & Sons, Copyright © 2020, Wiley-VCH Verlag GmbH & Co. KgaA, Weinheim, Germany.

The cytotoxicity of the polymeric micelles with both complex **65** and lapatinib was evaluated in vitro against SKOV3 cancer cells, and they were shown to inhibit the growth of cancer cells, with an IC_{50} of 0.89 μg/mL after irradiation at 460 nm, in comparison with polymeric micelles without lapatinib (IC_{50} = 1.32 μg/mL). It should be noted that this effect was only present for SKOV3 cancer cells, which have HER2 proteins expressed on the

surface, and the HER2-negative MCF-7 cells showed no significant difference for inhibition by micelles decorated with or lacking lapatinib (IC_{50} = 1.60 μg/mL and 1.50 μg/mL, respectively). The interaction of lapatinib with HER2 on the cell membrane was therefore concluded to be responsible for the increase in the photocytotoxicity. The cytotoxic mechanism was confirmed to be generation of ROS by staining with DCFH-DA. Other desirable properties of these micelles included their ability to increase local concentration at the tumour, ability to penetrate tissue, biocompatibility due to low cytotoxicity in the dark (i.e., without irradiation), and aqueous solubility. Together, these characteristics made the micelles containing complex **65** and lapatinib more effective than existing cyclometallated Ir(III) complexes, however, a high-intensity laser was still required due to low upconversion efficiency. Therefore, further research would be required to develop micelles that could be excited in a one-photon process.

Another example of a polymeric nanoparticle structure was composed of several units of a cyclometallated Ir(III) complex with terminal thiol groups **67**, which was joined by a disulfide bond in the polymer **68**, as shown in Figure 21 [112]. These polymers could then self-assemble into nanoparticles which can be modified by the addition of PEG, to enhance solubility, and biotin, for its ability to target cancer cells. Not only could the disulfide bond be broken by GSH in the tumour cells to release the photoactive metal complexes, which induces oxidative stress by PDT, the depletion of GSH would prevent it from acting as an antioxidant. As a result, not only was GSH unable to reduce ROS that induce apoptosis, GSH also caused increased ROS levels by inhibiting lipid peroxidation, thereby triggering the ferroptotic pathway, as shown in Figure 21. This polymer therefore caused cell death by a multimodal approach that induced both apoptosis and ferroptosis.

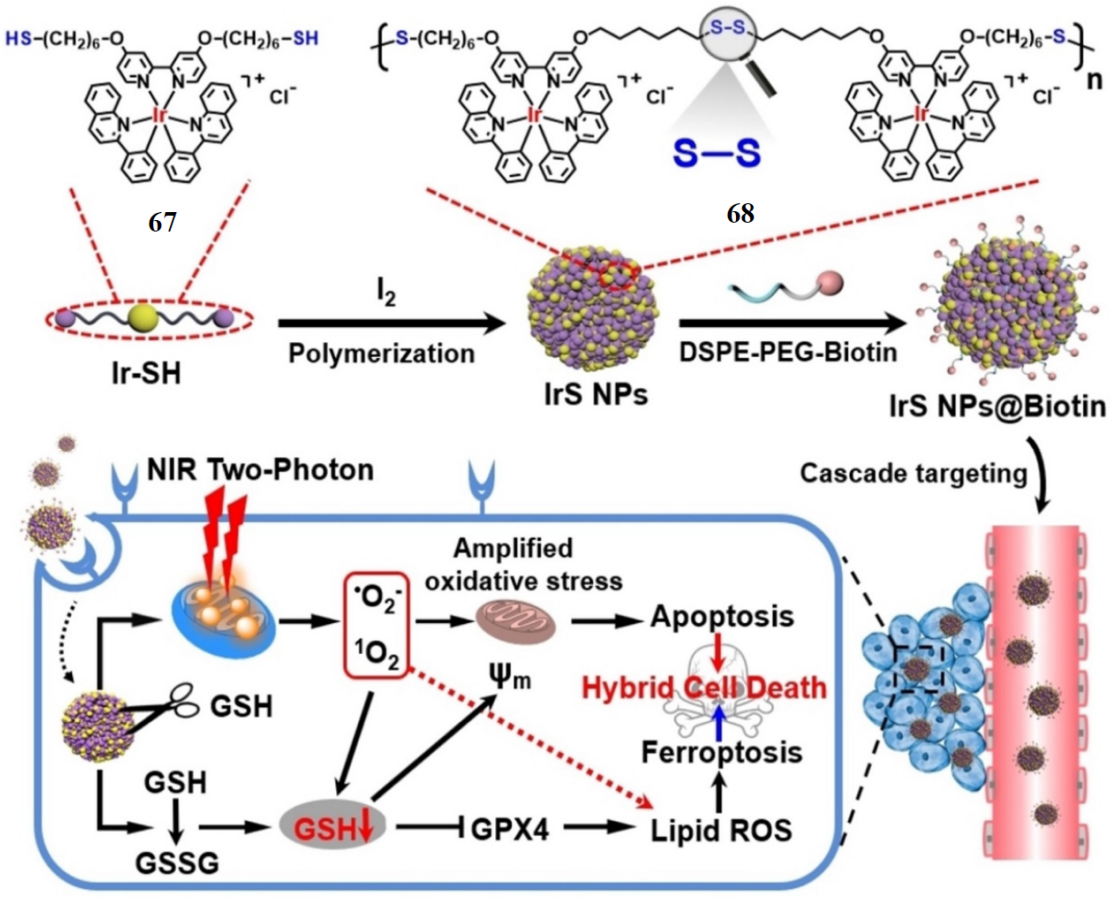

Figure 21. Preparation of nanoparticles of Ir(III)-containing polymer **68** coated with PEG and biotin. Reproduced from Ref. [112] with permission from John Wiley & Sons, Copyright © 2022, Wiley-VCH Verlag GmbH & Co. KgaA, Weinheim, Germany.

2.4. Gold Complexes

Although gold complexes are not commonly used for their phototherapeutic activity, Dyson and coworkers investigated the use of gold(I)-azide complexes **69-76** as chemotherapeutic and phototherapeutic agents (Figure 22) [113]. The cytotoxicity of all gold(I) complexes was evaluated against A549 cells and MRC-5 fibroblasts and exhibited IC_{50} values in the range of 12–15 μM, which was similar to cisplatin (16.7 μM), except for complexes **72** and **76**, with IC_{50} values of 39.1 and 38.0 μM, respectively. Additionally, increased water solubility was

observed for complexes **72** and **73**. The PTA-containing complex **74** was amphiphilic and displayed greater selectivity with an IC_{50} of 15.0 μM for A549 cancer cells compared to 26.3 μM for MRC-5 cells. Importantly, all complexes except **72** and **74** were roughly twice as cytotoxic for the fibroblast cells compared to the cancer cells, and due to the lower activity of **72**, complex **74** appeared to be the most promising candidate without irradiation.

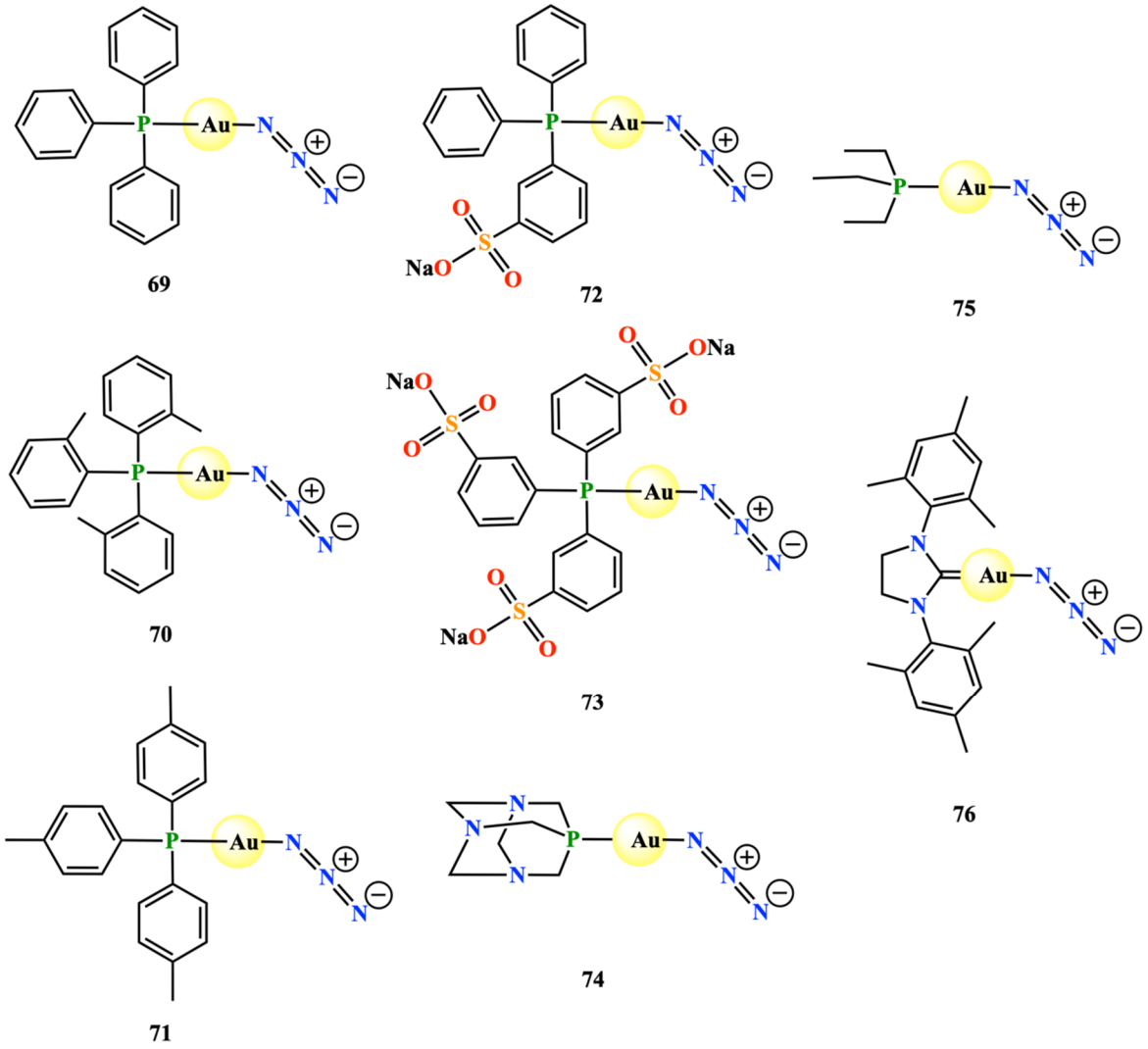

Figure 22. Structure of gold(I)-azide complexes **69-76**.

Complexes **73** and **76** showed increased cytotoxicity after irradiation at 450 nm for 8 minutes. The weakening of the Au(I)-azide bond in complex **73** may result in the release of the azide ligand from the gold complex. However, due to the presence of an NHC ligand instead of a phosphine complex **76**, the complex was shown not to decompose upon irradiation, suggesting a separate mechanism. The photocytotoxicity of **76**, in addition to its lower toxicity in the dark, indicates that this complex may have potential for further development for phototherapeutic applications.

2.5. Heterometallic Complexes

2.5.1. Ruthenium and Zinc

Massoud et al. prepared two arene-ruthenium compounds containing porphyrin moieties, one with zinc (Zn-TPyP-Ru, complex **77**) and one without (TPyP-Ru, complex **78**), for phototherapy targeting colorectal cancers, as illustrated in Figure 23 [114]. While the porphyrin moieties acted as photosensitizers, the ruthenium moieties enhanced the solubility in water to enhance internalization into the cells.

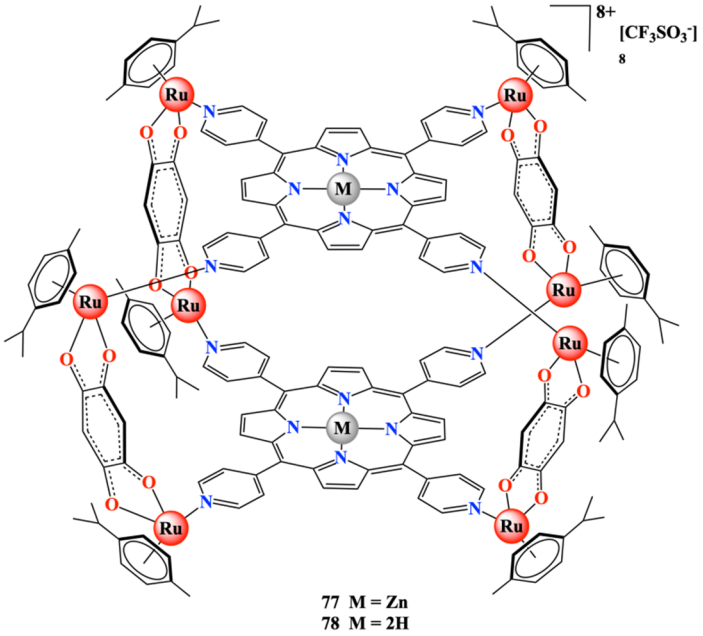

Figure 23. Structures of ruthenium/zinc complexes **77** and **78**.

The phototherapeutic activity of complexes **77** and **78** were evaluated against the two colorectal cancer cell lines HT-29 and HCT116. Without irradiation, neither complex showed significant inhibitory activity against either cell line. At 48 hours after irradiation (630–660 nm), complex **77** with Zn-porphyrin complexes was less toxic than complex **78** with uncomplexed porphyrin moieties, with IC_{50} values of 394 nM and 54.1 nM against HT-29 cells and 207 nM and 35.2 nM against HCT116 cells. It was observed, however, that both induced apoptosis in the cancer cell lines. Despite the arene-Ru moieties having minimal effects on the overall photocytotoxicity, these moieties were necessary for the activity as they provided the aqueous solubility that improved the uptake into cells. The generation of ROS activated caspase-3 and caspase-7 in the apoptotic caspase pathway in mitochondria, which inhibit poly ADP-ribose polymerase (PARP) enzymes that repair DNA. The inhibition of PARP and exposure to ROS result in DNA fragmentation, leading to a buildup of cells arrested in S phase as well as apoptosis. The uptake and photocytotoxic mechanisms of both complexes are shown in Figure 24.

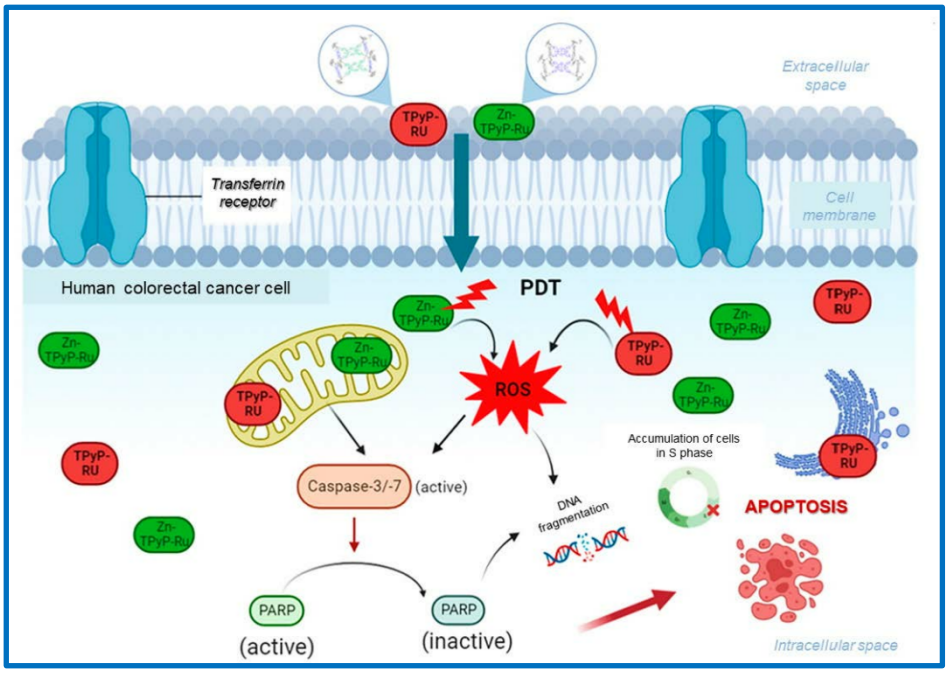

Figure 24. Uptake and photocytotoxic mechanism of complexes **77** (Zn-TPyP-Ru) and **78** (TPyP-Ru). Reproduced from Ref. [114], https://doi.org/10.3390/inorganics11120451 (accessed on 28 April 2026), under the terms of the CC BY 4.0 license, https://creativecommons.org/licenses/by/4.0/.

2.5.2. Iridium and Platinum

In comparison with homometallic iridium complexes, heterometallic complexes could be multifunctionalized, as the combination between different metal center complexes may cause synergistic effects. In 2024, Shi et al. combined the *trans, trans, trans*-[$Pt(N_3)_2(OH)_2(py)_2$] complex (**79**) with a cyclo-metalated iridium(III) polypyridine complex (**80**) to generate a new heterometallic Pt-Ir complex (**81**) as illustrated in Scheme 9 [115]. The Pt-Ir heteronuclear complex **81** achieves anticancer effects through synergistic PDT and photoactivated chemotherapy, where the Ir(III) moiety generates singlet oxygen ($^1O_2$) that oxidizes NADH to NAD radicals under blue light irradiation, while the Pt(IV) moiety undergoes photoreduction to release azidyl radicals ($\cdot N_3$) and the DNA-binding Pt(II) species. Intramolecular charge transfer from the Ir(III) donor to the Pt(IV) acceptor significantly accelerates photodecomposition by six times faster than mononuclear Pt-OH, and redshifts absorption to 500 nm, enabling activation at longer wavelengths. Upon irradiation, the heterometallic complex **81** was distributed throughout cells, damaging nuclei and releasing chromosomes via $^1O_2$/radical-induced oxidative stress and Pt(II)-DNA adduct formation. This dual-mode mechanism confers potent photocytotoxicity for A2780 ovarian cancer, A549 lung cancer and PC3 prostate cancer cells after 60 min of irradiation at 465 nm, far exceeding that of the individual mononuclear complexes or their mixtures. For example, for A549 cells, the heterometallic complex **81** had an IC_{50} of 3.5 μM. The individual platinum (**79**) and iridium (**80**) complexes exhibited IC_{50} values of 51.9 and 20.2 μM, respectively, and a 1:1 mixture of the two mononuclear complexes only achieved a IC_{50} of 19.2 μM, while cisplatin as a reference drug required a concentration >100 μM.

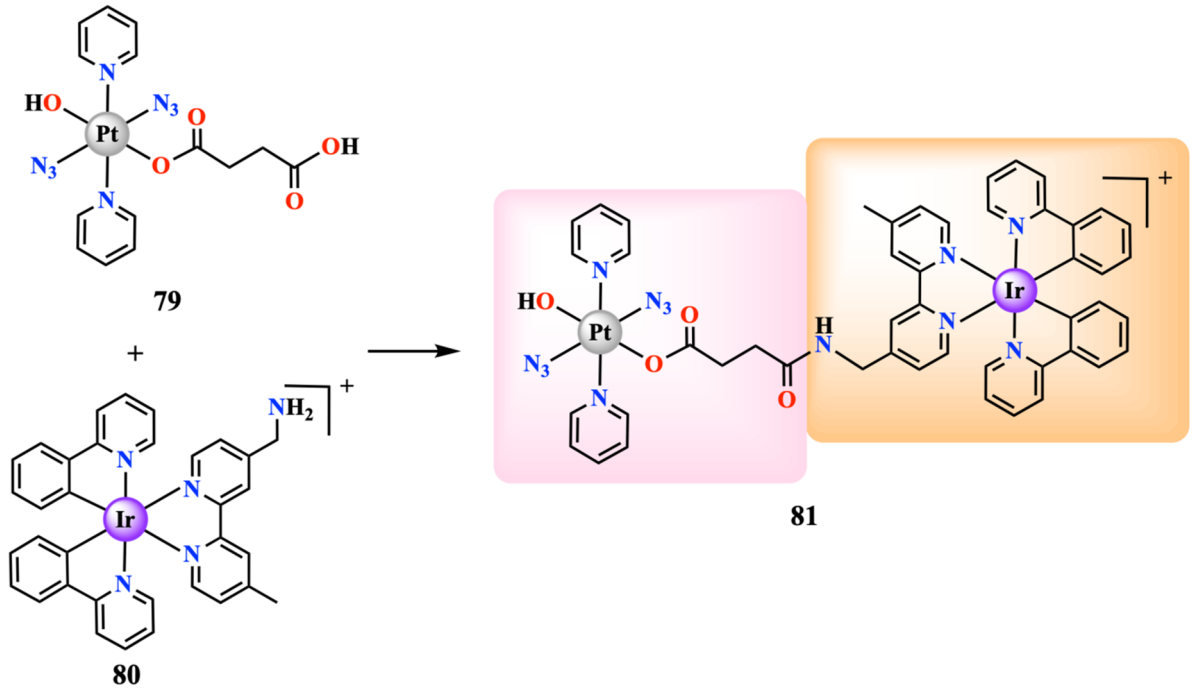

Scheme 9. Formation of heterometallic complex **81** from platinum complex **79** and iridium complex **80**.

Cellular studies revealed heterometallic complex **81** accumulates twice as much platinum in the cells compared to the mononuclear platinum complex **79** due to an increase in positive charge and lipophilicity, with intracellular levels of platinum being four times greater than iridium under dark conditions. Further, the iridium localizes in small vesicles, suggesting complex cleavage via lysosomal digestion. The confocal micrographs in Figure 25a show colocalization of complex **81** (Pt-Ir) with different organelles in A549 cells, which were stained with SYTO™ for nuclei, LysoTracker™ Deep Red for lysosomes, and MitoTracker™ Red for mitochondria. The complex was distributed throughout the cells, while the nuclei were disrupted after irradiation. The levels of ROS were also measured, using fluorescent 2′,7′-dichlorodihydrofluorescein diacetate (DCFH-DA) as a general probe for ROS (Figure 25b) and Singlet Oxygen Sensor Green (SOSG) reagent as a probe for singlet oxygen (Figure 25c), both of which only showed high levels in the cells after irradiation and treatment with complex **81**. Additionally, the addition of 10 mM of the antioxidant compound N-acetyl-L-cysteine (NAC) to the irradiated cells given complex **81** scavenged ROS, preventing any DCFH-DA fluorescence, as shown in Figure 25b.

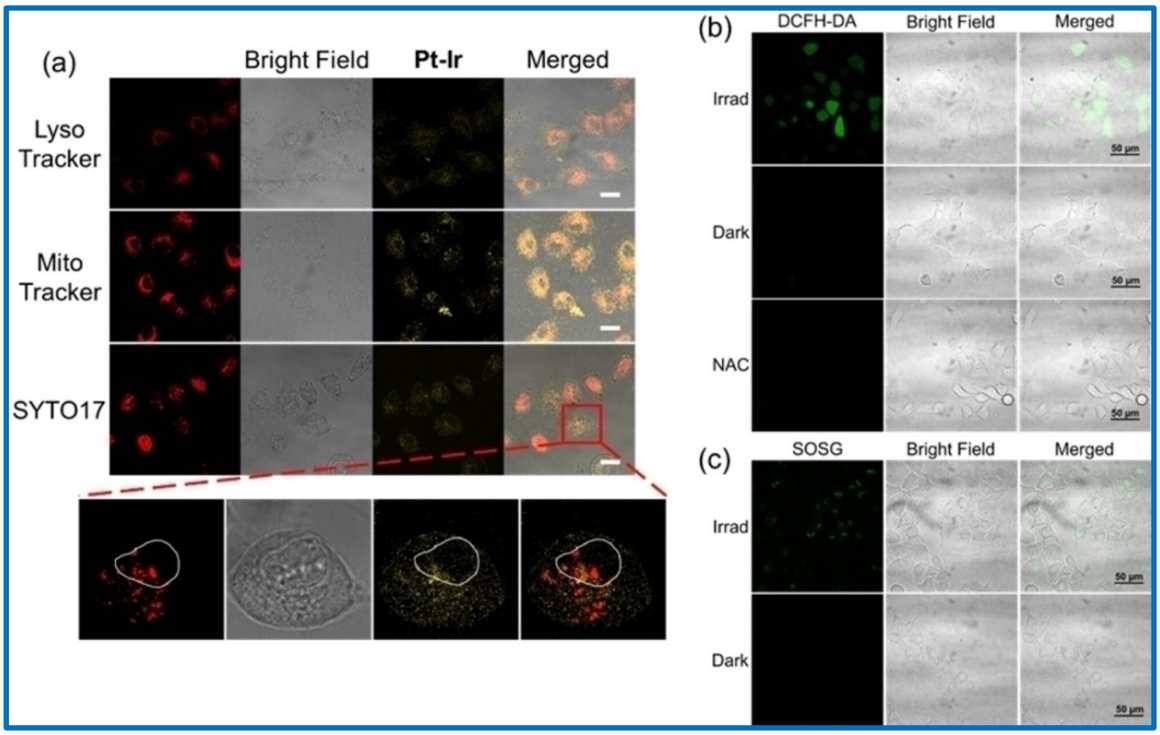

Figure 25. Confocal microscopy of A549 cells showing (**a**) colocalization of Pt-Ir (complex **81**) with three organelle-specific stains (inset: closeup of SYTO17-stained cells to display nuclear disruption) or (**b**) DCFH-DA for detection of ROS (NAC = N-acetyl-L-cysteine) and (**c**) SOSG for detection of singlet oxygen. Reproduced with permission from Ref. [115], https://doi.org/10.1002/anie.202400476 (accessed on 21 April 2026), under the terms of the CC BY 4.0 license, https://creativecommons.org/licenses/by/4.0/.

This section highlighted the advances in the use of organometallic molecules and macromolecules in bioimaging and phototherapeutic applications. The selected examples from the past decade clearly demonstrate the versatility of organometallic systems and, while they covered several transition metallic moieties, Ir(III) particularly demonstrated its utility in photodynamic therapy due to its tunable photophysical properties and high quantum yield. It is worth noting that a number of limitations remain to be overcome in cancer treatment using PDT and PTT, including low levels of ROS generation, specific targeting of tumours and inefficient photothermal conversion. While phototherapy has emerged as an important methodology for the treatment of cancer, there are several other mechanisms that can be utilized with different advantages. The next section will be devoted to research progress in combating cancer using organometallic complexes, polymers and dendrimers with different mechanisms than phototherapy.

3. Antiproliferative Drug Design

Cancer is one of the most feared diseases that continues to be among the leading causes of death globally [116]. In early 2026, a survey of the WHO's global cancer database (GLOBOCAN) and reported that 40% of cancers could be prevented by controlling the causes of cancers such as alcohol, tobacco, obesity, air pollution and ultraviolet radiation [117,118]. However, there is still an urgent need to develop new and more effective antiproliferative drugs. Organometallic complexes offer potential solutions for the design of antiproliferative drugs in light of their diverse structures and geometries [119]. A recent review by Hartinger highlighted the structures of some organometallic complexes as potential anticancer metallodrugs as well as their modes of action [120]. In the search for potential organometallic complexes as effective drugs, several characteristics must be considered, including the specific cytotoxicity of the complex for cancer cells, potential mechanisms of antiproliferative activity, routes of administration of the drug and the design of the complex for drug delivery.

In the 1970's, one example of anticancer activity was reported by Köpf and Köpf-Maier for the titanocene dichloride complex ($Ti(\eta^5\text{-}C_5H_5)_2Cl_2$) that was also shown to target DNA [121]. Another class of organometallic complexes, namely ferrocene derivatives, were also reported around the same time to show antitumour activities by Yashchenko et al. and Wenzel et al. [122,123]. In the early 1980's, Köpf-Maier, Köpf, and Neuse described the antitumour activity of ferrocenium complexes [124]. Over the past three decades, there has been tremendous research into the development of organometallic complexes for their potential as antiproliferative drugs [34]. In

this section, we will cover some recent examples of transition and main group organometallic complexes and macromolecules for their antiproliferative activities. While the previous section dealt mainly with the phototherapeutic anticancer applications of organometallic complexes, this section will primarily discuss the antiproliferative activities of organometallic complexes without irradiation.

3.1. Titanium, Zirconium and Hafnium Complexes

One example of a titanium-containing organometallic complex involved modification of titanocene by conjugation with non-steroidal anti-inflammatory drugs (NSAIDs) for their antitumour activity [125]. Titanocene dichloride (**82**) was reacted with the sodium salts of NSAIDs flurbiprofen (**83**), naproxen (**84**), ibuprofen (**85**) or diclofenac (**86**) to produce the corresponding titanocene conjugates (**87-90**), as outlined in Scheme 10. The cytotoxicity of the complexes was evaluated against A2780 ovarian cancer cells, and ibuprofen-containing complex **89** displayed the lowest IC_{50} of 116 μM compared with titanocene dichloride (IC_{50} = 180 μM). Unfortunately, this increase in cytotoxicity was also observed against human pulmonary fibroblasts (HPF), while the titanocene dichloride and other titanocene complexes **87**, **88**, and **90** were non-toxic for the non-cancerous cell line (IC_{50} >400 μM). On the other hand, the resulting IC_{50} of 179 μM against HPF indicated there was still some selectivity against the cancer cells. It should be noted that even the lower IC_{50} value for complex **89** was not comparable to reference drugs cisplatin or auranofin, which was determined to have IC_{50} values of 0.55 μM and 0.70 μM, respectively [126,127]. The authors also noted that complex **89** exhibited the highest lipophilicity of all the complexes in addition to stability in aqueous solutions, suggesting the increased cytotoxicity may be due to increased uptake by the cells. Other studies by Guk et al. examined a series of titanocene dicarboxylates against malignant MCF-7 and non-malignant MCF-10A breast cancer cells, which showed low activities with IC_{50} values ≥ 100 μM [128].

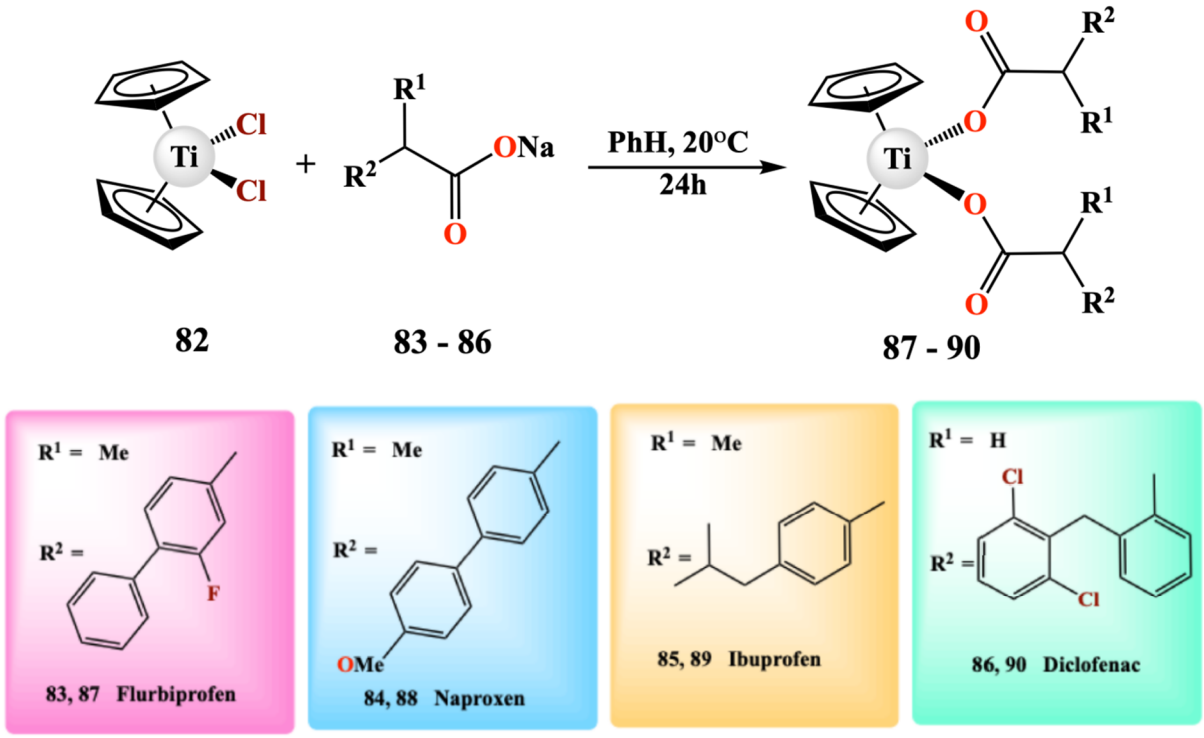

Scheme 10. Design of NSAID-conjugated titanocene complexes **87-90**.

The antitumour activities of a series of enantiopure cyclopentadienyl Ti(IV) oximato complexes were investigated by de la Cueva-Alique et al. [129]. Reaction of the oxime-containing ligands **91-93** with [(η^5-C_5H_5)$TiCl_3$] (**94**) gave rise to (*S*,*R*)-[(η^5-C_5H_5)Ti(κ^2NO,(R)NH·HCl)Cl_2] (R = phenyl **95**, benzyl **96**, 2-picolyl **97**), as shown in Scheme 11. However, reaction of the ligands **91-93** with [(η^5-C_5H_5)$_2TiCl_2$] (**82**) led to the formation of (*S*,*R*)-[(η^5-C_5H_5)$_2$Ti(κ^2NO,(R)NH)Cl] (R = phenyl **98**, benzyl **99**, 2-picolyl **100**).

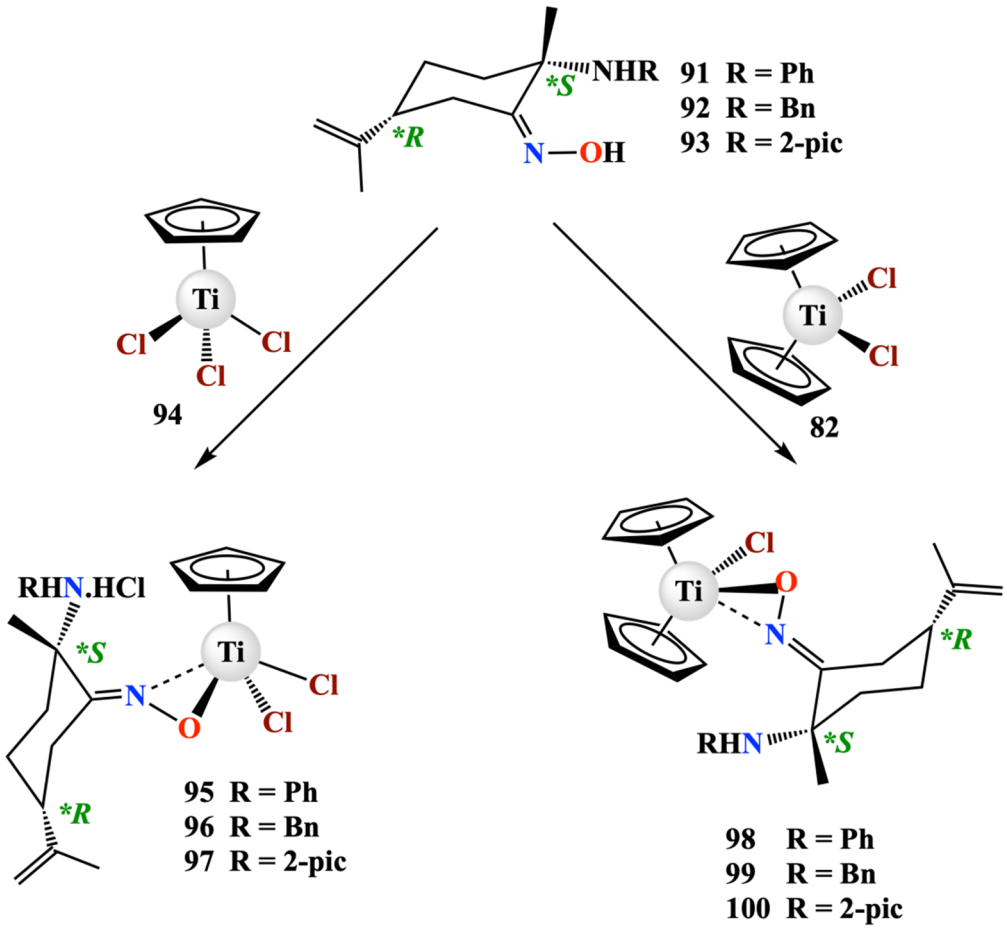

Scheme 11. Preparation of cyclopentadienyl titanium complexes **95-97** and titanocene complexes **98-100**.

The antiproliferative activity of complexes **95-100** against the PC-3 prostate cancer cell line was measured, and the highest activity was identified for complexes **97**, **99** and **100**, with IC_{50} values of 25.7 μM, 59.3 μM and 17.3 μM, respectively. All three were significantly improved compared to the free ligands **91**, **92**, and **93**, which had IC_{50} values of 201.7 μM, 177.0 μM and 204.7 μM, respectively. Complexes **99** and **100** were also evaluated against Caki-1 renal cancer, DLD-1 colon cancer and MDA-MB-231 triple-negative breast cancer cell lines as well as the healthy HEK-293T human renal cell line. While the complexes were less selective for the colon cancer compared to the healthy renal cells, they did exhibit higher selectivity for the renal cancer cells. The calculated IC_{50} values were 8.55 μM for complex **99** and 4.51 μM for complex **100** for Caki-1, compared to 50.99 μM for complex **99** and 70.22 μM for complex **100** for HEK-293T. The complexes were also more active than two reference drugs against Caki-1 cells, namely titanocene Y (IC_{50} = 29.42 μM) or cisplatin (IC_{50} = 29.42 μM). The mechanism of cell death was investigated, and it was observed that the main mode of cell death was apoptosis for both complexes. Complex **100** resulted in the largest decrease in viable cells down to 16%, as well as the largest proportion of apoptotic cells at 76%.

Polymeric materials containing titanocene that demonstrated their potential as anticancer candidates were reported earlier by Carraher and coworkers [130,131]. In their studies, they prepared polymers of titanocene, zirconocene and hafnocene through the condensation reaction of the corresponding metallocene dichlorides (**82**, **101**, **102**) with α-cyano-4-hydroxycinnamic acid (**103**) as illustrated in Scheme 12. The metallocene containing-polymers (**104-106**) were evaluated for their anticancer activities against two human cancer cell lines, pancreatic adenocarcinoma cells (AsPC-1) and pancreatic epithelioid duct carcinoma cells (PANC-1), as well as the healthy mouse fibroblast cell line (NIH/3T3). All the polymeric materials were more effective for specific inhibition of the cancer cells compared to the reference drug cisplatin, with the hafnocene-containing polymer **106** displaying the highest activity, followed by the zirconocene-containing polymer **105**, then titanocene-containing polymer **104**.

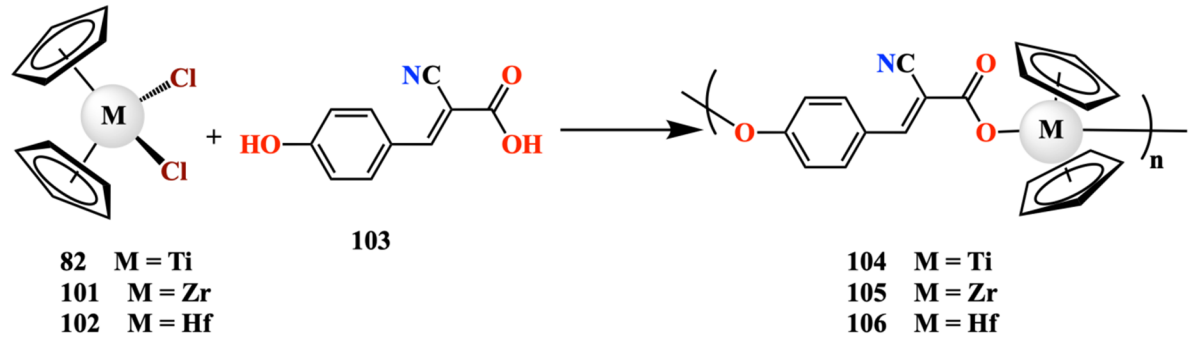

Scheme 12. Preparation of metallocene-containing polymers **104-106**.

3.2. Manganese and Rhenium Complexes

First-, second- and third-generation dendrimers of diaminobutane poly(propylenimine) (DAB/PPI) containing peripheral manganese or rhenium moieties were designed by Hu et al. (**110-115**) [132]. First-generation DAB/PPI (**107**) was reacted with the tricarbonyl half-sandwich complexes of Mn (**108**) and Re (**109**) to produce the metal-containing dendrimers **110** and **111**, as illustrated in Scheme 13. This process was repeated with second-generation and third-generation DAB/PPI dendrimers to yield dendrimers **112-115** as shown in Figure 26. A resazurin assay was used to determine the anticancer activity of dendrimers **110-115** against the MCF-7 breast cancer cell line, and it was observed that the first-generation dendrimers **110** and **111** were the most effective. The cytotoxicity did not increase with an increase in generation, suggesting that a larger number of metallic moieties did not improve the activity. The authors theorized that, instead of increasing the concentration of metal moieties, the dendrimer increased cytotoxicity by improving cellular uptake, likely due to increased lipophilicity. This was validated by a comparison with a poly(amidoamine) (PAMAM) dendrimer modified with the same manganese complexes, which exhibited lower activity due to the lower lipophilicity of the organic dendrimer.

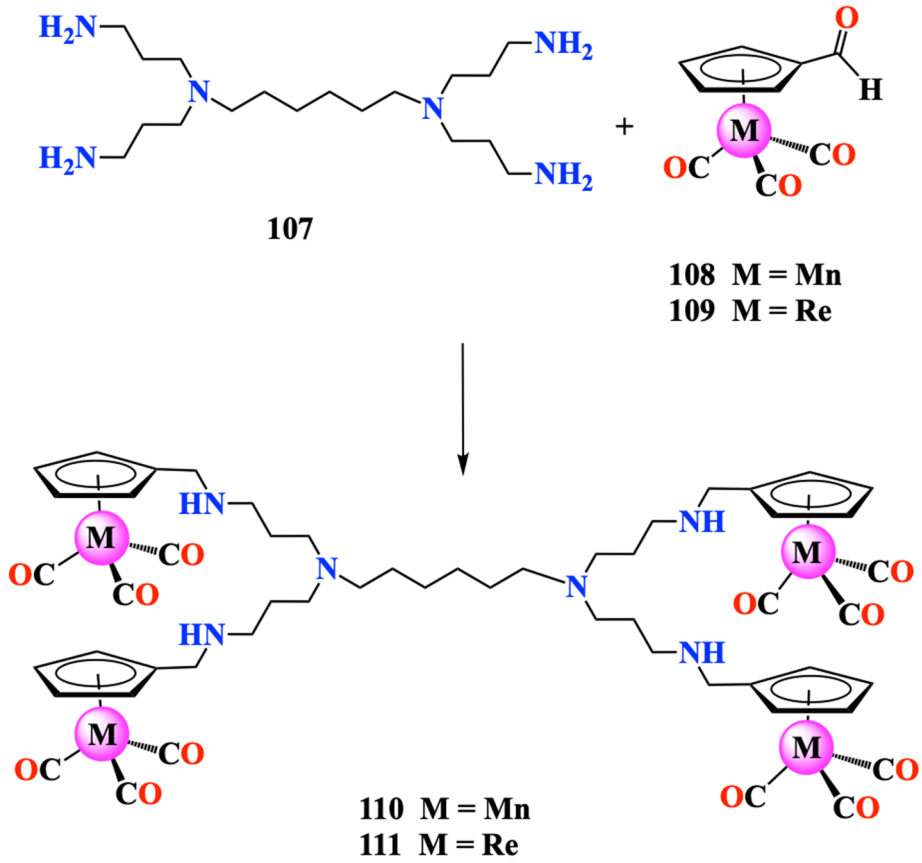

Scheme 13. Synthesis of first-generation dendrimers **110** and **111** containing manganese or rhenium moieties.

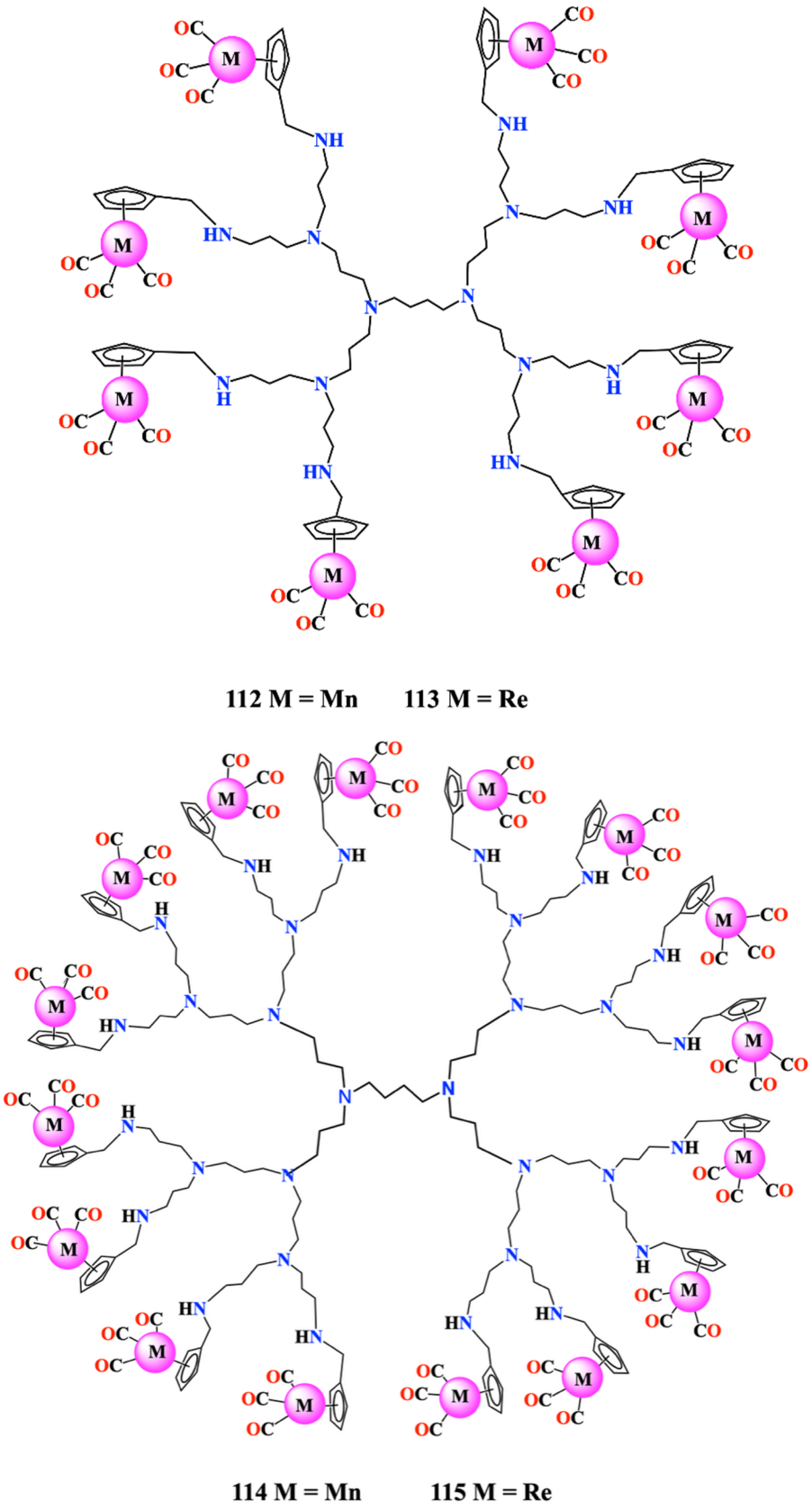

Figure 26. Structures of second-generation dendrimers **112** and **113** as well as third-generation dendrimers **114** and **115** containing manganese or rhenium moieties, respectively.

Rhenium complexes with the facial octahedral structure *fac*-$Re(CO)_3L_{1-3}$ have shown great potential as anticancer candidates [133–138]. Herein, we will highlight some examples that demonstrate the great promise of these complexes. Konkankit et al. synthesized the rhenium complex *fac*-[$Re(CO)_3$(2,9-dimethyl-1,10-phenanthroline)(OH_2)]$^+$ (**116**), as illustrated in Figure 27, to overcome cancer cell resistance to conventional

platinum-based drugs [139]. The uptake of the complex by cisplatin-sensitive A2780 and cisplatin-resistant A2780CP70 ovarian cancer cells was examined and both cell lines showed comparable rhenium content, suggesting that, unlike cisplatin, uptake of complex **116** was not significantly inhibited in the resistant cell line. An *in vivo* experiment using a xenograft with MDA-MB-231 breast cancer tumours in mice was also conducted. The tumour volume decreased significantly for mice treated with 10 mg/kg of complex **116** by approximately 60% compared to the negative control using the injection vehicle alone, as shown in Figure 27. It was also observed that increasing the concentration to 20 or 40 mg/kg did not increase the activity. Furthermore, the body weight of the mice was not significantly affected, demonstrating the minimal effect of the complex on overall health of the mice. Despite the high levels of Re found in the kidneys (6.0 pg Re/mg tissue) and the liver (10.7 pg Re/mg tissue), no notable organ toxicity was observed with H&E staining, as shown by an example of kidney tissue in Figure 27. Conversely, the tumours showed necrosis, even though the Re content detected within the tumours was lower (1.0 pg Re/mg tissue).

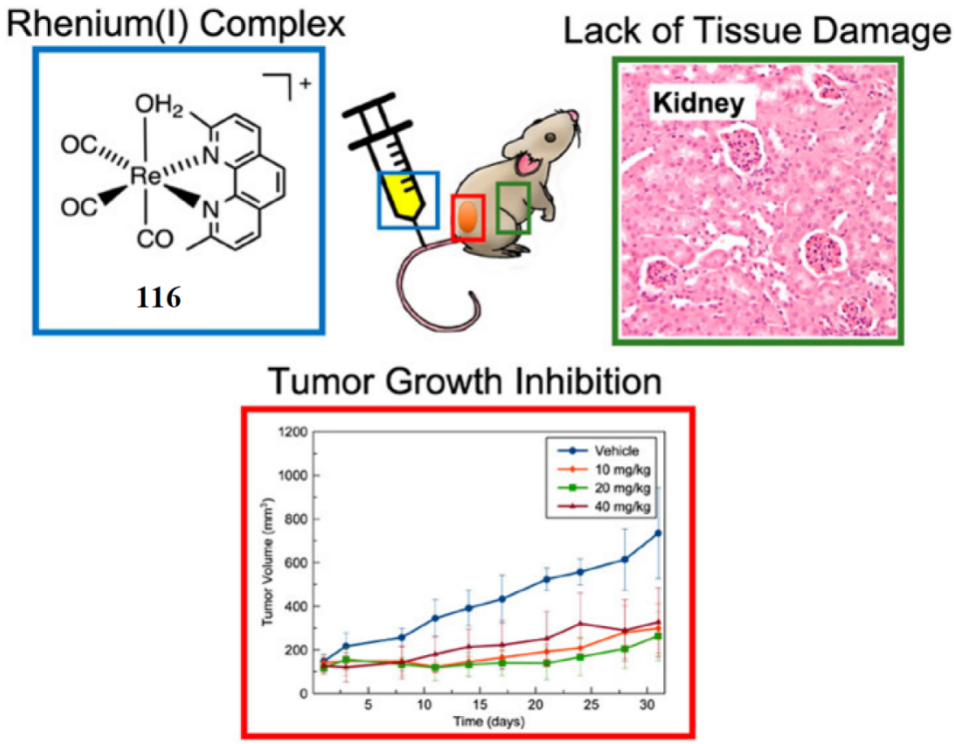

Figure 27. Summary of structure and *in vivo* anticancer activity of Re(I) complex **116**, showing its inhibition of tumour growth and micrographs of undamaged kidney tissue stained with H&E. Adapted with permission from Ref. [139] with permission from American Chemical Society, Copyright © 2019.

A series of tricarbonyl rhenium isonitrile polypyridyl (TRIP) complexes were prepared for their ability to induce ER stress by activating the unfolded protein response (UPR) pathway [140]. The UPR pathway involves misfolding of cellular proteins, resulting in stress that triggers apoptotic pathways of cell death. A general trend of increased cytotoxicity was observed for TRIP complexes with hydrophobic ligands with electron-donating properties and the greatest antiproliferative activity was observed for complex **117** (TRIP-1a) containing a monodentate *para*-tolyl isonitrile ligand and a bidentate 2,9-dimethyl-1,10-phenanthroline ligand. The IC_{50} of complex **117** was 1.4 μM against HeLa ovarian cancer cells, which was lower than cisplatin with an IC_{50} of 6.6 μM. Additionally, this complex was shown to induce protein aggregation due to misfolding within 30 minutes of treatment in HeLa cells, confirming the UPR activation mechanism. In light of these findings, complex **117** (Figure 28) was also evaluated in an *in vivo* model using mice bearing A2780 xenografts with the delivery vehicle alone as a negative control. The cohort of mice given 20 mg/kg of complex **117** twice weekly resulted in significantly inhibited tumour volume to less than half of the negative control and increased survival by 150%. The inhibition of tumour growth was also visible in magnetic resonance images of the mice, as the tumour (highlighted in red) was notably smaller at 1, 7 and 14 days in mice from the 20 mg/kg treatment cohort compared to the vehicle control cohort. However, mice treated with 5 mg/kg or 10 mg/kg of complex **117** did not show any improvements in tumour inhibition or survival due to the doses being insufficient for anticancer activity. Fortunately, the highest dose of 20 mg/kg still resulted in minimal side effects that led to no significant effect on body weight of the mice.

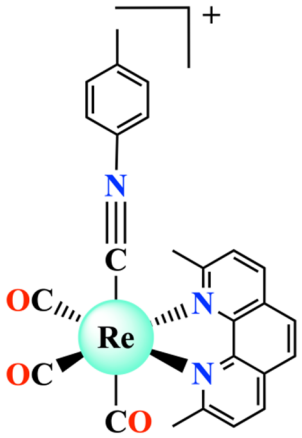

117
TRIP-1a

Figure 28. Structure of tricarbonyl rhenium isonitrile polypyridyl complex (TRIP-1a, **117**).

Padariya et al. prepared tricarbonyl rhenium(I) complexes with substituted phenyl(2-(thiazol-4-yl)-1H-benzo[d]imidazol-1-yl)methanone ligands and investigated their biological characteristics, including anticancer activity [141]. After 4-(1H-benzo[d]imidazole-2-yl)thiazole **118** was reacted with sodium hydride at low temperature (0–5 °C), the substituted benzoyl chlorides **119-124** were added to the solution to yield compounds **125-130**. The organic compounds were then reacted with the pentacarbonylchlororhenium(I) complex $ReCO_5Cl$, giving rise to complexes **131-136**, as outlined in Scheme 14.

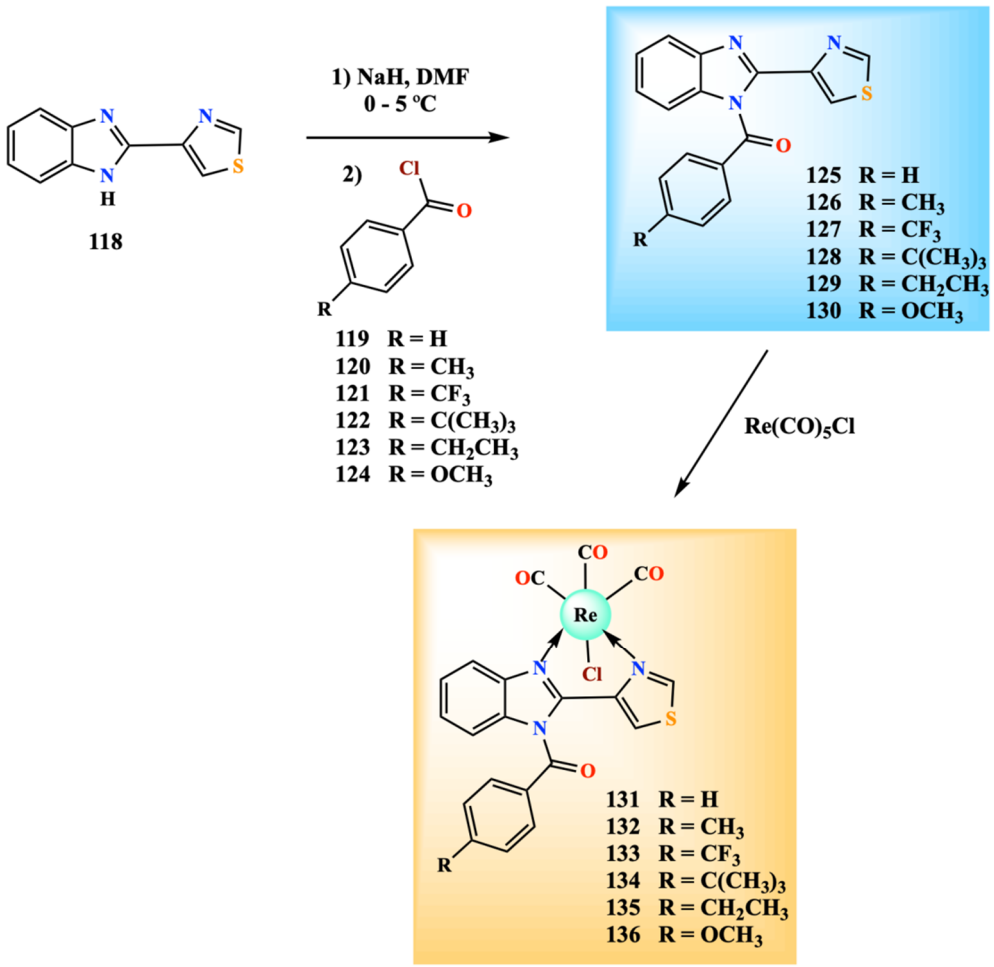

Scheme 14. Synthesis of substituted phenyl(2-(thiazol-4-yl)-1H-benzo[d]imidazol-1-yl)methanone ligands **125-130** and their Re complexes **131-136**.

The in vitro antiproliferative activity of compounds **125-136** was tested for the MCF-7 breast cancer cell line. The rhenium-containing complexes **131-136** exhibited IC_{50} values ranging from 91.72 to 120.40 µg/mL. On the other hand, the IC_{50} values of the organic compounds **125-130** ranged from 150.54 to 181.50 µg/mL, with the Re complexes showing greater activity than their corresponding organic compounds. For example, the Re complex **131** showed an IC_{50} of 120.40 µg/mL, while organic compound **125** showed an IC_{50} of 180.40 µg/mL. The complexes **131-136** were also concluded to exhibit excellent activity that was between the IC_{50} values of two platinum-containing reference drugs for the same cell line, namely cisplatin (80.00 µg/mL) and carboplatin (165.28 µg/mL). For the Re complexes, the highest activity, and therefore lowest IC_{50}, was observed for complex **134**, with a value of 91.72 µg/mL.

3.3. Iron and Ruthenium Complexes and Macromolecules

There have been a number of organometallic iron complexes and macromolecules that have shown potential anticancer activity. Ferrocene and ferrocenium derivatives have been examined for their ability to induce apoptosis and ferroptosis in cancer cells [142]. One recent example is a series of ferrocene-containing pyrazolo [1,5-a]pyrimidine complexes that showed potent anticancer activity against the oral squamous cell carcinoma (OSCC) cell line CAL27 [143]. Reaction of ferrocene carboxaldehyde (**137**) with substituted ketones (**138**) and 3-amino-pyrazoles (**139**) gave rise to the 7-ferrocenyl-substituted pyrazolopyrimidines (**140-147**), as shown in Scheme 15, while reaction of acetylferrocene (**148**) with (furan-2-yl)ethan-1-one (**149**) allowed for the formation of ferrocenyl-3-(furan-2-yl)prop-2-en-1-one (**150**) followed by reaction with 1H-pyrozol-3-amine (**151**) to give 5-ferrocenyl-7-furylpyrazolo [1,5-a]-pyrimidine (**152**) (Scheme 16).

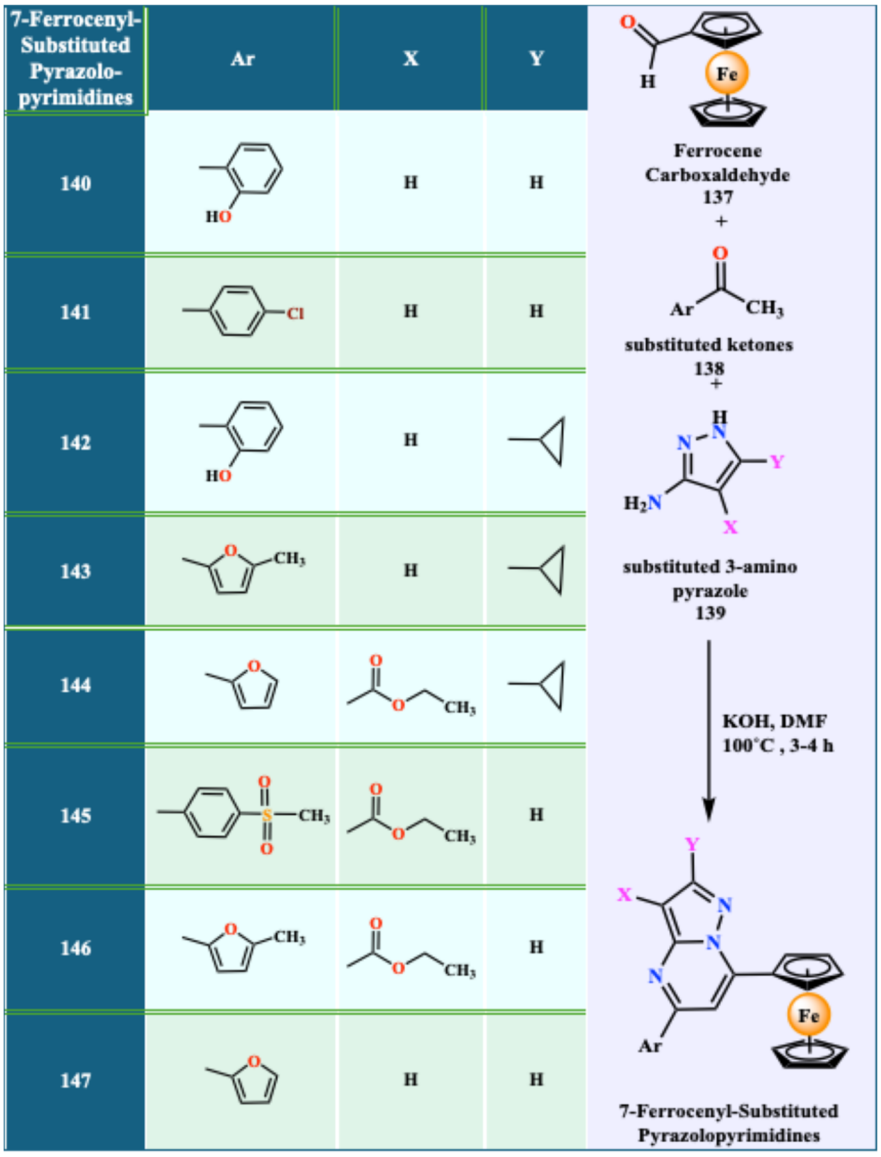

Scheme 15. Preparation and substitution of ferrocene-containing complexes **140-147**.

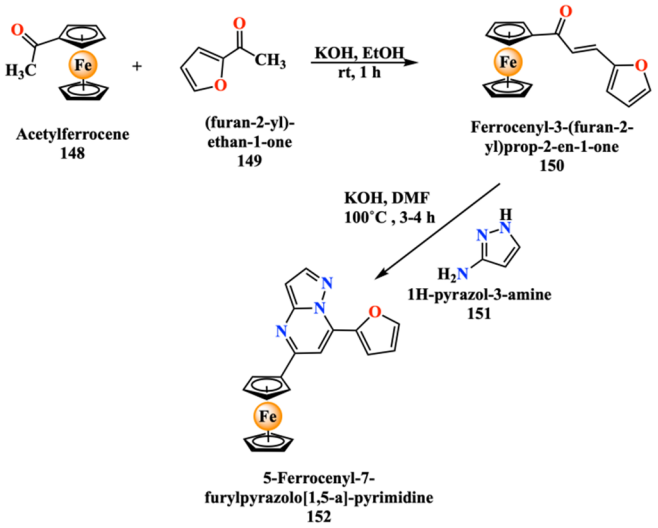

Scheme 16. Preparation of 5-ferrocenyl-7-furylpyrazolo [1,5-a]-pyrimidine (**152**).

The inhibition of CAL27 cells was evaluated by a colourimetric assay using Alamar Blue, which showed the concentration-dependent growth inhibition (by decrease in fluorescence emission) for the most active complex **147** (Figure 29a) as well as the remaining complexes (Figure 29b). An IC_{50} value of 7.49 µM was calculated for complex **147**, which was lower than the 9.50 µM for cisplatin against the same cell line. The mode of cell death caused by complex **147** was demonstrated to be primarily through apoptosis rather than necrosis. Further, the complexes generally showed higher specificity for cancer cells compared to normal oral epithelial (NOE) cells, as can be observed in Figure 29c, with complex **147** also exhibiting the greatest specificity, with the largest IC_{50} of 15.87 µM against NOE cells. Docking analysis also showed that this complex exhibited high binding affinity for DASA-58 binding site of the pyruvate kinase enzyme PKM2, which is upregulated in OSCC cancer cells and is involved in glycolysis.

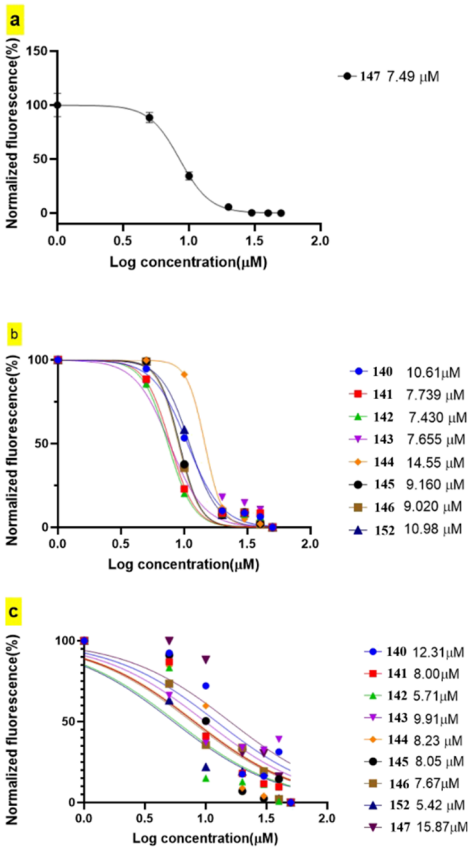

Figure 29. Cytotoxicity of (**a**) complex **147** and (**b**) complexes **140-146** and **152** against CAL27 cells and (**c**) complexes **140-147** and **152** against NOE cells**.** Reproduced with permission from Ref. [143], Copyright © 2022, American Chemical Society.

Saviozzi et al. synthesized multiple redox-active tri-iron complexes for use as anticancer agents, of which the most active was complex **158** [144]. As illustrated in Scheme 17, aminoferrocene (**153**) was reacted with phenyl formate to form ferrocenyl formamide (**154**), which was then reacted with $POCl_3$ and diisopropylamine to produce isocyanoferrocene (**155**), followed by reaction with the diiron complex **156** to yield the tri-iron complex **157**. The aminocarbyne moiety of complex **157** underwent reaction with methyl triflate, yielding methylated complex **158**. The methyl stabilizes the structure as well as improving the π-electron acceptor behaviour of the complex. Electrochemical studies of the tri-iron complex **158** confirmed the two redox centers could undergo different redox processes: an oxidation at the ferrocenyl moiety and a reduction at the bridging di-iron complex. The oxidation of the ferrocenyl was favoured under biological conditions, resulting in a positively charged complex.

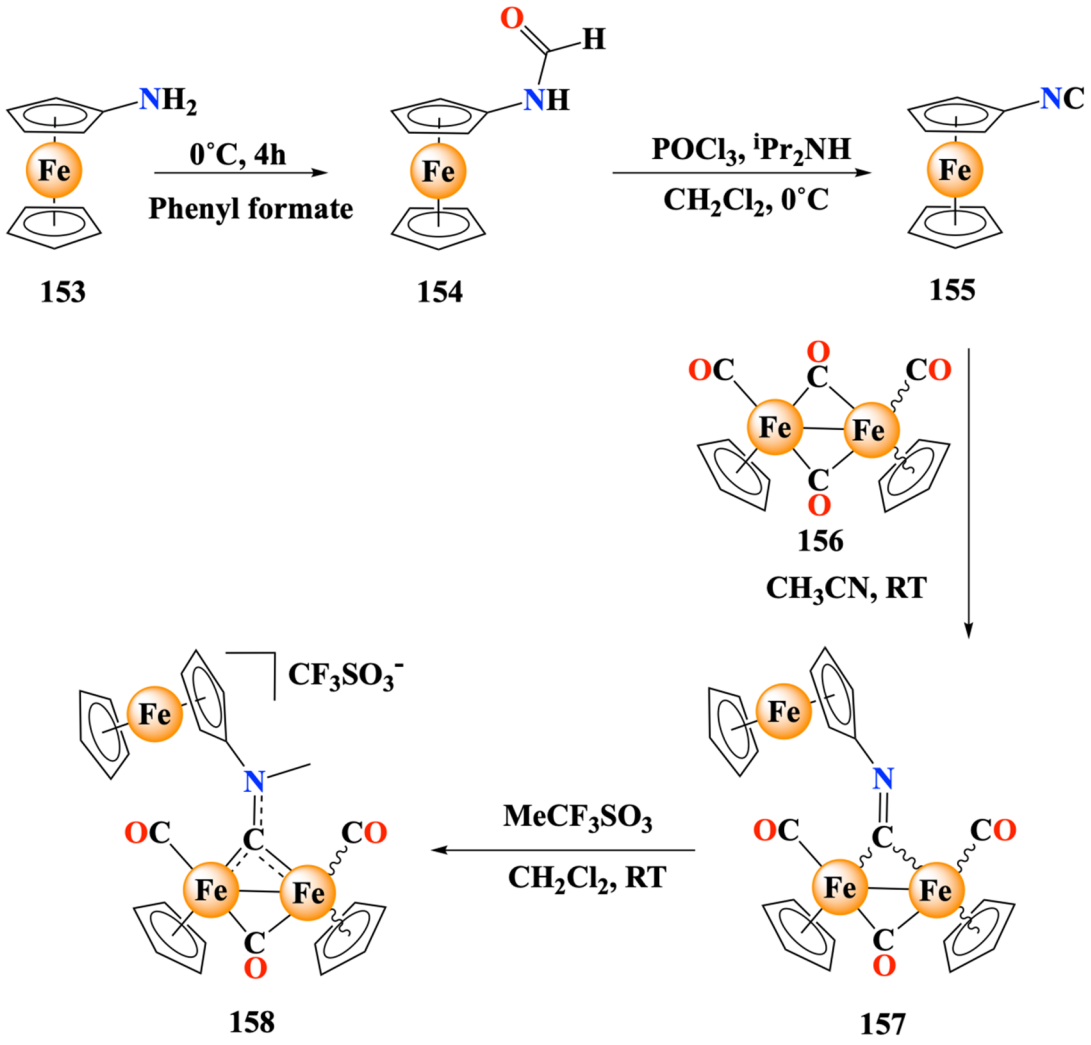

Scheme 17. Synthesis of tri-iron complex **158**.

Complex **158** showed antiproliferative activity against human epidermoid carcinoma A431, colon cancer HCT-15, pancreatic cancer PSN-1, ovarian cancer 2008, and small cell lung cancer U1285 cell lines, with IC_{50} values ranging between 16.0–60.0 μM compared to 1.7–13.9 μM for cisplatin. While the inhibition was only moderate for cells in the 2D in vitro experiment, complex **158** was more toxic than cisplatin in a 3D model of U1285 spheroids, with IC_{50} values of 51.3 μM and 65.4 μM, respectively. This finding demonstrates the enhanced ability of the tri-iron complex to penetrate tumour tissue and inhibit its growth. In terms of its antiproliferative mechanism, under physiological conditions, this complex becomes positively charged and generates ROS. ROS production by complex **158** was shown to be comparable to that caused by the reference drug antimycin, which inhibits mitochondrial respiration.

Woo et al. designed a copolymer coating for implantable device to release anticancer drugs such as paclitaxel using redox activity of ferrocene, with a polymeric structure that also inhibits biofilm formation by bacteria adhering to the device [145]. The coating consisted of alternating layers of the negatively charged copolymer Poly(FMMA-*r*-PEGMA-*r*-MA) (**163**) and the positively charged copolymer Poly(FMMA-*r*-PEGMA-*r*-DMAEMA) (**164**). These copolymers were prepared by reaction of ferrocenylmethyl methacrylate (FMMA, **159**) with poly(ethylene glycol)

methacrylate (PEGMA, **160**) and either methacrylate (MA, **161**), to yield copolymer **163**, or 2-(dimethylamino)-ethylmethacrylate (DMAEMA, **162**), to yield copolymer **164**, with AIBN in THF at 70 °C, as seen in Scheme 18.

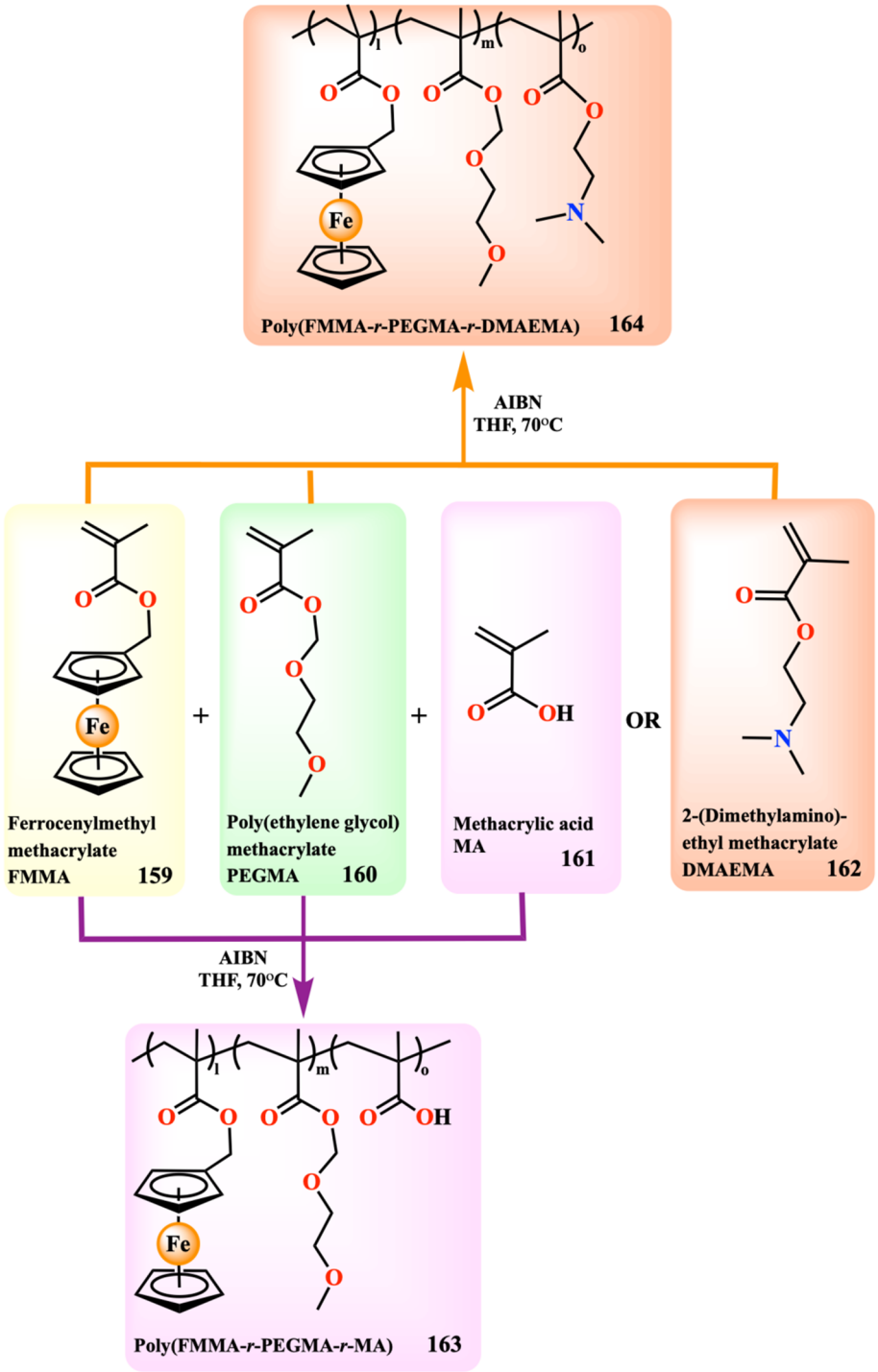

Scheme 18. Design of negatively charged copolymer Poly(FMMA-*r*-PEGMA-*r*-MA) (**163**) and the positively charged copolymer Poly(FMMA-*r*-PEGMA-*r*-DMAEMA) (**164**).

The ferrocene moieties allowed for loading of and redox-mediated release of paclitaxel from the film**.** The release profile of paclitaxel was dependent on pH and the redox environment, which was modelled by controlled addition of H_2O_2. The ideal conditions for drug release were found to be pH 5.5 and 0.1% H_2O_2, which are consistent with the acidic and oxidative environment of tumours. The film without paclitaxel-loading exhibited no significant cytotoxicity, indicating that the film was nontoxic to human cells. When the film was loaded with 500 μg/mL paclitaxel, however, antiproliferative activity was observed against MCF-7 cells. The antiproliferative activity increased with the number of layers in the film, with the 10-layer film loaded with paclitaxel resulting in <40% remaining viable cancer cells.

An example of ferrocene-containing polymers for anticancer drug delivery was reported by Qiu et al., who designed the amphiphilic polynorbornene copolymers with ferrocene and triethylene glycol (TEG) side chains described in Schemes 19 and 20 [146]. The amphiphilic copolymers could form micelles used to load doxorubicin for improved cell uptake and redox-mediated release at tumour cells. The preparation of random copolymer **167** involved ROMP of the ferrocene- and TEG-containing monomers **165** and **166** in a single step, while block copolymer **169** was formed by ROMP of the ferrocene-containing monomer **165** to form homopolymer **168** followed by reaction with the TEG-containing monomer **166**. The block copolymer **169** achieved 66.8% efficiency for doxorubicin encapsulation, which is higher than 21.1% for the random copolymer **167**. Doxorubicin release was dependent on the redox environment and could be modulated by altering the concentration of the oxidant $FeCl_3$, with the fastest rate of release being displayed at the highest tested concentration of 2 mg/mL $FeCl_3$. The in vitro biocompatibility of the copolymers was evaluated for L929 mouse fibroblast cells, and both copolymers were shown to be nontoxic even at the 8 mg/mL concentration. The copolymers also exhibited no effect on organ development for zebrafish embryos as an *in vivo* model.

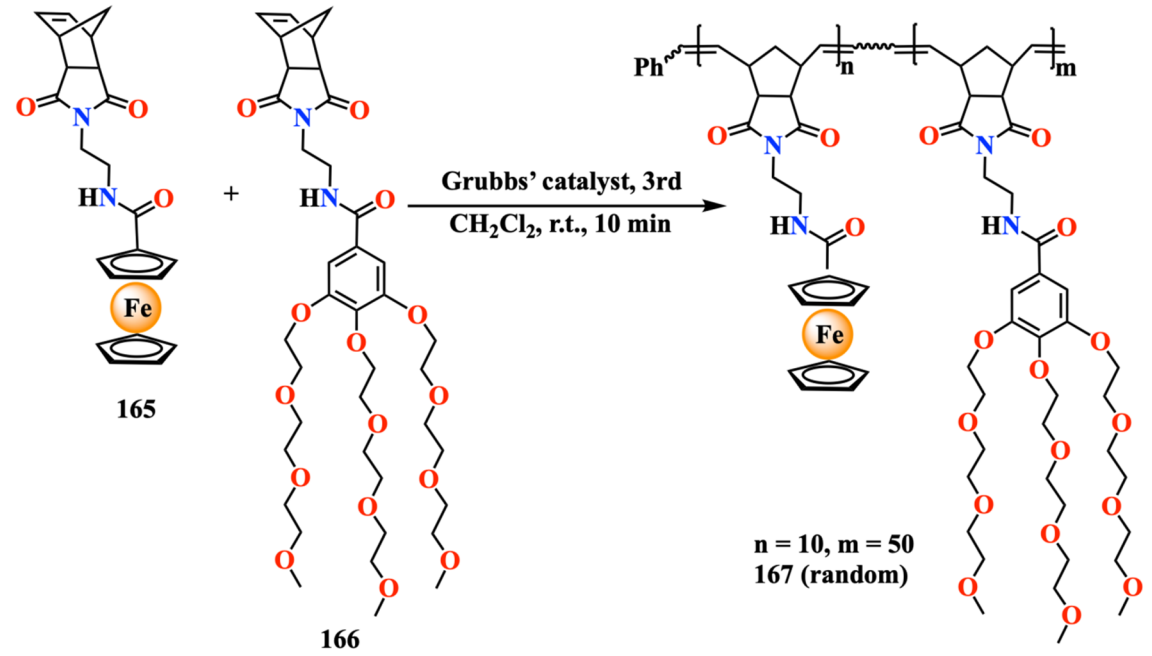

Scheme 19. Preparation of random polynorbornene copolymers containing ferrocene and TEG side chains **(167)**.

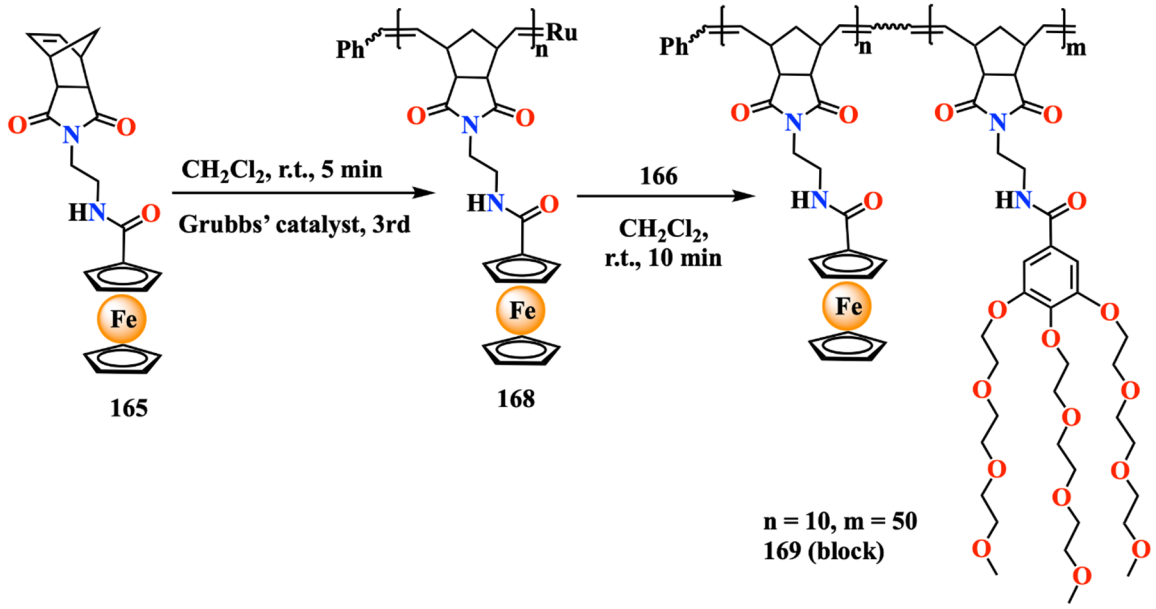

Scheme 20. Preparation of block polynorbornene copolymers containing ferrocene and TEG side chains **(169)**.

Ornelas and coworkers designed a polyamide dendrimer **174** decorated with ferrocene in the form of terminal triazolylferrocenyl moieties (Scheme 21) [147]. The reaction of polyamide dendrimer **170** with glutamate γ-ferrocene (**172**), using 1-[bis(dimethylamino)methylene]-1H-1,2,3-triazolo [4,5-b]pyridinium 3-oxide hexafluorophosphate **(171)** as a coupling agent, gave rise to the dendrimer **173** with trimethylsilyl protecting groups, which were removed to form the functional dendrimer **174**. The ferrocene moieties could undergo redox reactions to produce ROS, while the added triazole groups acted as electron donors and facilitated π-π conjugation with ferrocene, which lowered redox potential and increased the antiproliferative activity.

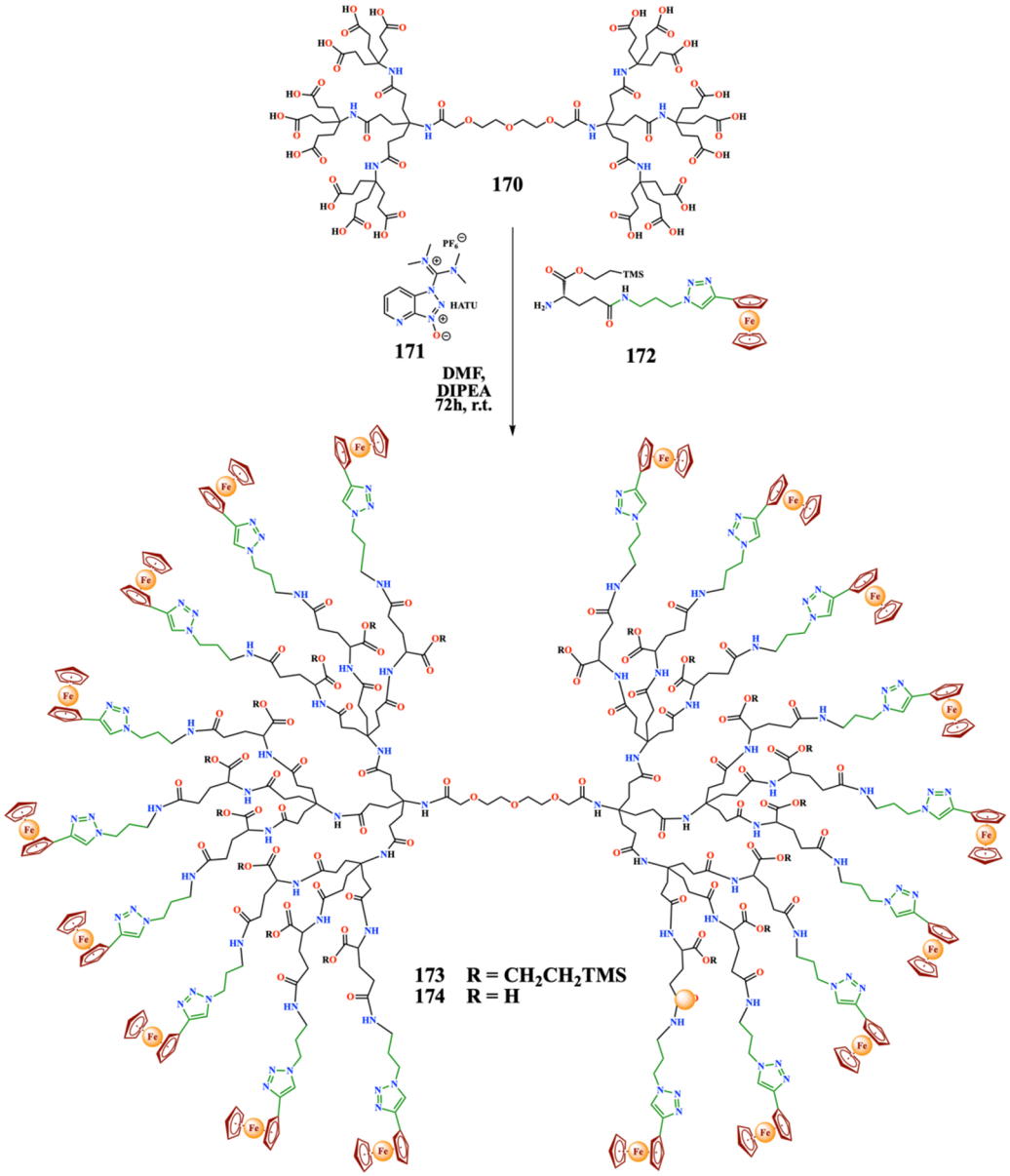

Scheme 21. Preparation of ferrocene-decorated dendrimer **174**.

Dendrimer **174** was evaluated for its antiproliferative activity against MCF-7, HeLa, Caco-2 and PC-3 cancer and healthy prostate tissue (PNT2) cell lines. Significant reductions in cell viability were observed for all the cancer cell lines, although the dendrimer was most active against HeLa cells, with an IC_{50} of 5.4 μM, followed by MCF-7 (16.2 μM), then Caco-2 (52.2 μM), as shown in Figure 30. For PC-3 cells, the IC_{50} could not be calculated as even the highest tested concentration of dendrimer **174** (55.6 μM) could not achieve <50% cell viability. Dendrimer **174** also displayed no significant cytotoxicity against the PNT2 cells, indicating its selectivity for the cancer cells. It was also observed that while the IC_{50} values of dendrimer **174** were moderate (in the micromolar range) for HeLa and MCF-7, the concentration of ferrocenyl groups was much higher than would be present for an equivalent concentration of a ferrocene-containing complex. For instance, the HeLa cells showed an IC_{50} of 5.4 μM for dendrimer **174**, which was equivalent to a concentration of 97.7 μM for the ferrocenyl groups. The

dendrimer could therefore increase the local concentration of the active ferrocenyl moieties with a lower concentration, which could reduce harmful side effects caused at higher concentrations.

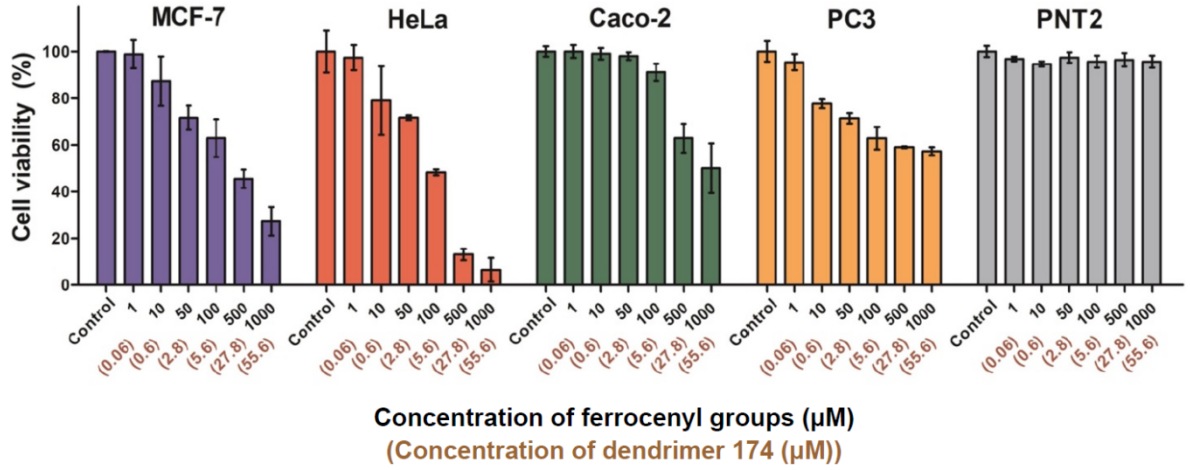

Figure 30. Concentration-dependent cytotoxicity of dendrimer **174** against four cancer cell lines (MCF-7, HeLa, Caco-2, PC-3) and one non-cancer cell line (PNT2). The concentrations of the dendrimer are shown in brown and the corresponding concentrations of the ferrocenyl groups within the dendrimer are shown in black. Adapted from Ref. [147] with permission from John Wiley & Sons, Copyright © 2022 Wiley-VCH GmbH.

Abd-El-Aziz and coworkers prepared cationic iron-containing oligomers and dendrimers. Dendrimeric materials capped with piperazines showed higher activities when compared to oligomeric organoiron materials [148,149]. Herein, the design and anticancer activities of three generations of dendrimers with a melamine core and capped with chloro, piperazine and hydroxyl groups will be described, as shown in Figure 31 [149]. This group of dendrimers was examined for their antitumour activities against two breast cancer cell lines HTB-26 and MCF-7 with doxorubicin as a positive control. Table 1 reported the activities against the two cancer cell lines. While the second-generation dendrimer **179** capped with piperazine moieties showed an increase in activity compared to the first-generation dendrimer **176**, with IC_{50} values against MCF-7 cells of 9.9 μM and 18.1 μM, respectively, the corresponding dendrimers with hydroxyl groups **180** and **177** showed less of an increase, with IC_{50} values of 27.8 μM and 36.7 μM, respectively. It is also clear that the dendrimers **175**, **178** and **181** with chloro groups were clearly inactive at all tested concentrations. The most effective dendrimer was the third-generation dendrimer with piperazine groups (**182**), which showed IC_{50} values of 3.6 μM against HTB-26 cells and 2.5 μM against MCF-7, which was slightly higher than the doxorubicin control with IC_{50} values of 0.6 μM and 0.4 μM, respectively.

Table 1. Inhibition of HTB-26 and MCF-7 cancer cells by dendrimers **175-182**.

Dendrimer	HTB-26		MCF-7	
	IC_{50} (μM)	MIC (μM)	IC_{50} (μM)	MIC (μM)
175	>75	>75	>75	>75
176	>75	>75	18.1 ± 0.5	>75
177	>75	>75	36.7 ± 0.5	>75
178	>75	>75	>75	>75
179	6.2 ± 0.3	12.3	9.9 ± 0.2	12.3
180	>75	>75	27.8 ± 0.4	>75
181	>75	>75	>75	>75
182	3.6 ± 0.1	5.26	2.5 ± 0.1	1.3
Doxorubicin	0.6 ± 0.1	3.7	0.4 ± 0.0	3.7

Organometallic ruthenium complexes have been well known as active materials for the treatment of cancer [150–153]. In a recent review by Domínguez-Jurado et al., they described the utility of organometallic ruthenium complexes in the treatment of breast cancer and their advantages over conventional platinum complexes [154]. One recent example by Kavukcu et al. examined naphthyl-substituted Ru(II)-*p*-cymene complexes against a breast cancer cell line (MCF-7) as well as colon cancer (Caco-2) and liver cancer (HepG2) cell lines [155]. Complex **184** was prepared via the reaction of *N*1-(naphthalen-1-yl)ethane-1,2-diamine (**183**) and $(RuCl_2[p\text{-cymene}])_2$ (**26**), as shown in Scheme 22. However, complex **186** was prepared via the reaction of $(RuCl_2[p\text{-cymene}])_2$ (**26**) and 4-methyl-*N*-(2-(naphthalen-1-ylamino)ethyl)benzenesulfonamide (**185**), as illustrated in Scheme 23. They also

prepared the bimetallic neutral dimeric complex **188** through the reaction of $(RuCl_2[p\text{-cymene}])_2$ (**26**) with 2-mercapto-N-(naphthalen-2-yl)acetamide (**187)** (Scheme 24).

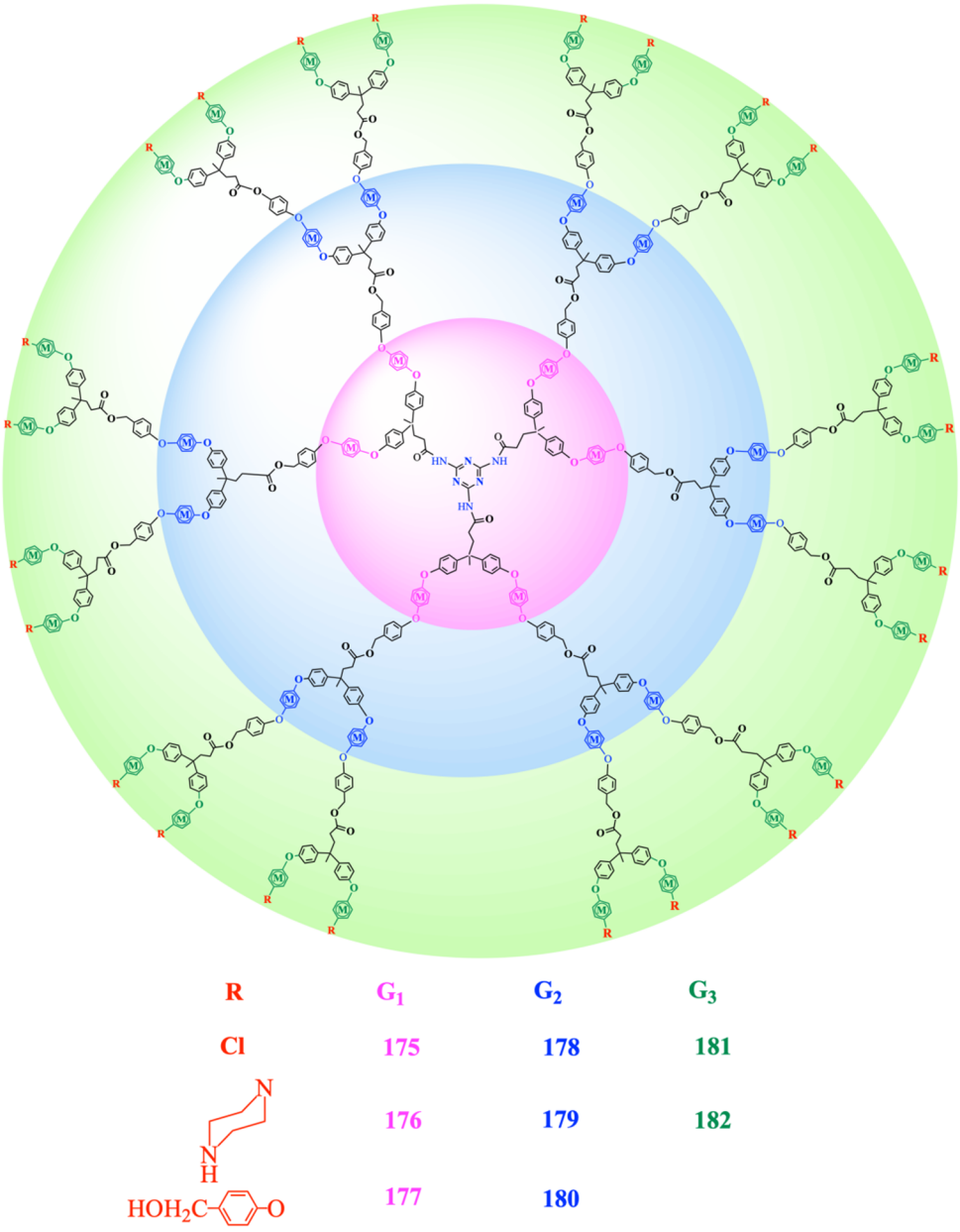

Figure 31. Structures of three generations of cationic iron-containing dendrimers with different peripheral groups **175-182**.

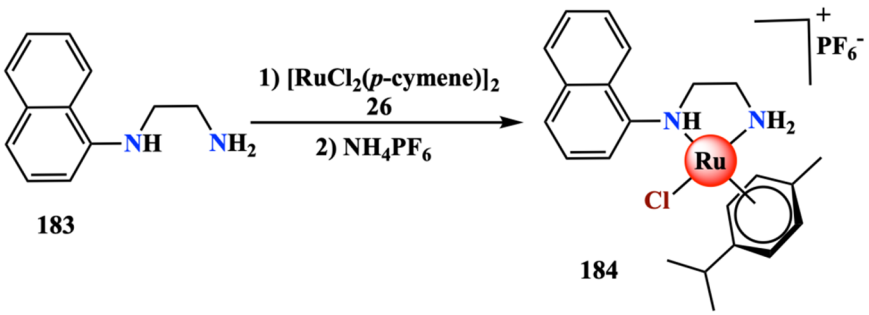

Scheme 22. Preparation of cationic naphthyl-substituted Ru(II)-*p*-cymene complex **184.**

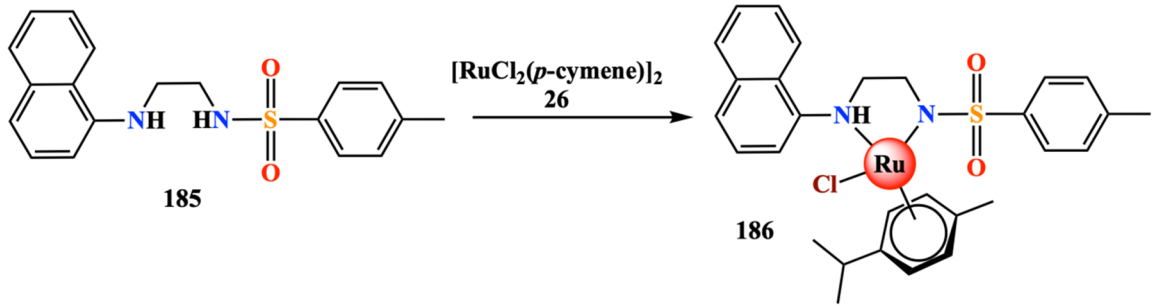

Scheme 23. Preparation of naphthyl-substituted Ru(II)-*p*-cymene complex **186.**

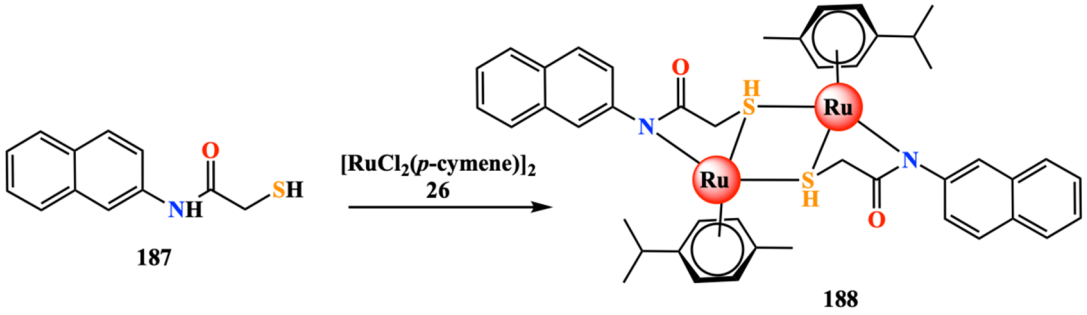

Scheme 24. Design of Ru(II)-*p*-cymene dimeric complex **188**.

The anticancer activity was assessed by treatment of MCF-7, Caco-2, HepG2 and the Vero cell line (kidney cells from African green monkey used as a model of healthy mammalian cells) with complexes **184**, **186** and **188** for 24 or 48 hours. The calculated IC_{50} values listed in Table 2 showed that the complexes tended to show the strongest inhibition for Caco-2 cells. The mononuclear complex **186** with a tosyl group demonstrated the greatest selectivity for cancer cells over Vero cells at 24h and increased selectivity at 48h, unlike complexes **184** or **188**. For example, complex **186** displayed an IC_{50} of 2.81 μM against MCF-7 cells after 24 hours of incubation, but 7.80 μM for the Vero cells. Furthermore, at 48 hours, the selectivity of complex **186** for cancer cells increased, with the IC_{50} values increasing to 8.75 μM against MCF-7 cells and 38.34 μM for Vero cells.

Table 2. Cytotoxicity of complexes **184**, **186** and **188** after 24 or 48 hours of incubation.

Complex	MCF-7 (μM)	Caco-2(μM)	HepG2 (μM)	Vero (μM)
184 (24 h)	**3.99**	**9.22**	**5.50**	**7.84**
184 (48 h)	**11.69**	**3.83**	**6.00**	**9.38**
186 (24 h)	**2.81**	**1.39**	**4.72**	**7.80**
186 (48 h)	**8.75**	**3.39**	**8.8**	**38.34**
188 (24 h)	**5.18**	**5.88**	**10.89**	**5.92**
188 (48 h)	**8.09**	**1.81**	**10.22**	**6.55**

Docking simulations of complex **188** to two forms of the epidermal growth factor regulator (EGFR) protein, namely the wild type EGFRWT and the mutant form EGFRT790M, were also performed. EGFR is used as a therapeutic target for the class of anticancer EGFR inhibitor drugs. Stronger binding affinities were observed for complex **188** to both EGFRWT and the mutant form (−204.437 kcal/mol and −176.946 kcal/mol, respectively) compared to the reference drug erlotinib (−179.941 kcal/mol and −150.700 kcal/mol, respectively). Unlike the reference drug, the complex bound to EGFRWT showed no hydrogen bonding interactions with the binding site in the protein, but strong hydrophobic and van der Waals interactions were instead detected. The absence of hydrogen bonding with the bound Ru complex suggests that it may exhibit an alternative mechanism of inhibition for EGFR. Additionally, while complex **188** exhibited superior binding affinity for EGFRWT compared to the mutant form, the complex still shows excellent binding affinity for the mutant form. The stability of complex **188** binding to the EGFRT790M mutant (Figure 32) is key, as this mutation is a common mechanism of cancer cells in the development of resistance to EGFR inhibitor drugs.



Figure 32. Complex **188** docked with 3D structure of mutant protein EGFRT790M (PDB ID: 3W20). Reproduced from Ref. [155], https://doi.org/10.1155/bca/5556956, under the terms of the CC BY 4.0 license, https://creativecommons.org/licenses/by/4.0/.

Welsh et al. designed three trinuclear ruthenium-arene complexes for their anticancer efficacy and found that they exhibited the greatest activity against two cell lines of rhabdomyosarcoma, a form of cancer that affects development of striated muscle [156]. The three trinuclear arene complexes were prepared from addition of Ru(II)-arene complexes to tris-2-quinolylbenzimidazole (**189**) to yield complex **190** with a *p*-cymene ligand, complex **191** with a hexamethylbenzene ligand, and complex **192** with a benzene ligand, as illustrated in Scheme 25.

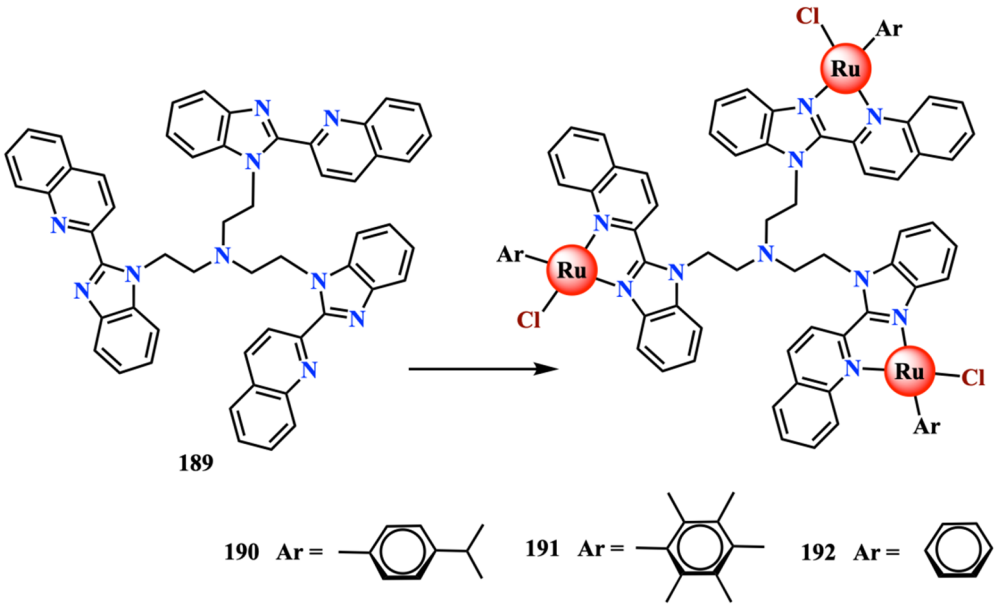

Scheme 25. Design of trinuclear Ru(II)-arene complexes **190-192**.

The *p*-cymene-containing complex **190** exhibited the greatest anticancer activity against two rhabdomyosarcoma cell lines: the less aggressive RD cell line, with an IC_{50} of 17.64 μM compared to 29.51 μM for cisplatin, and the metastatic RH-30 cell line, with an IC_{50} of 17.02 μM compared to 36.73 μM for cisplatin. The complex was also active against pancreatic cancer PANC-1 cells, with an IC_{50} of 19.28 μM compared to 31.08 μM for cisplatin but was less effective against metastatic pancreatic cancer CFPAC-1 cells than cisplatin, with IC_{50} values of 26.71 μM and 18.85 μM, respectively. Additionally, 3D spheroids of both rhabdomyosarcoma cell lines were used as a model of tumour structure, and the resulting micrographs and graphs of surface area are shown in Figure 33. For spheroids of the RD cell line (Figure 33a), complex **190** was more effective than cisplatin at half IC_{50}, IC_{50}, and double IC_{50} concentrations. On the other hand, the same complex was less effective at half IC_{50} or IC_{50} than cisplatin against the RH-30 cell line (Figure 33b), but the double IC_{50} concentration significantly reduced spheroid area compared to cisplatin, leading to almost complete elimination by day 6. The RH-30 cell line is aggressive and metastatic, suggesting that despite the higher concentration required to inhibit growth, the cytotoxic effects of complex **190** may be capable of not just inhibiting growth of metastatic tumours but eradicating them entirely. Mechanistic studies indicated that the anticancer activity of complex **190** was due to DNA damage, which was observed by upregulation of the protein γH2AX, a protein in the DNA repair pathway that acts as a marker of double stranded DNA breaks. This damage led to initiation of autophagy and apoptotic pathways, resulting in cancer cell death.

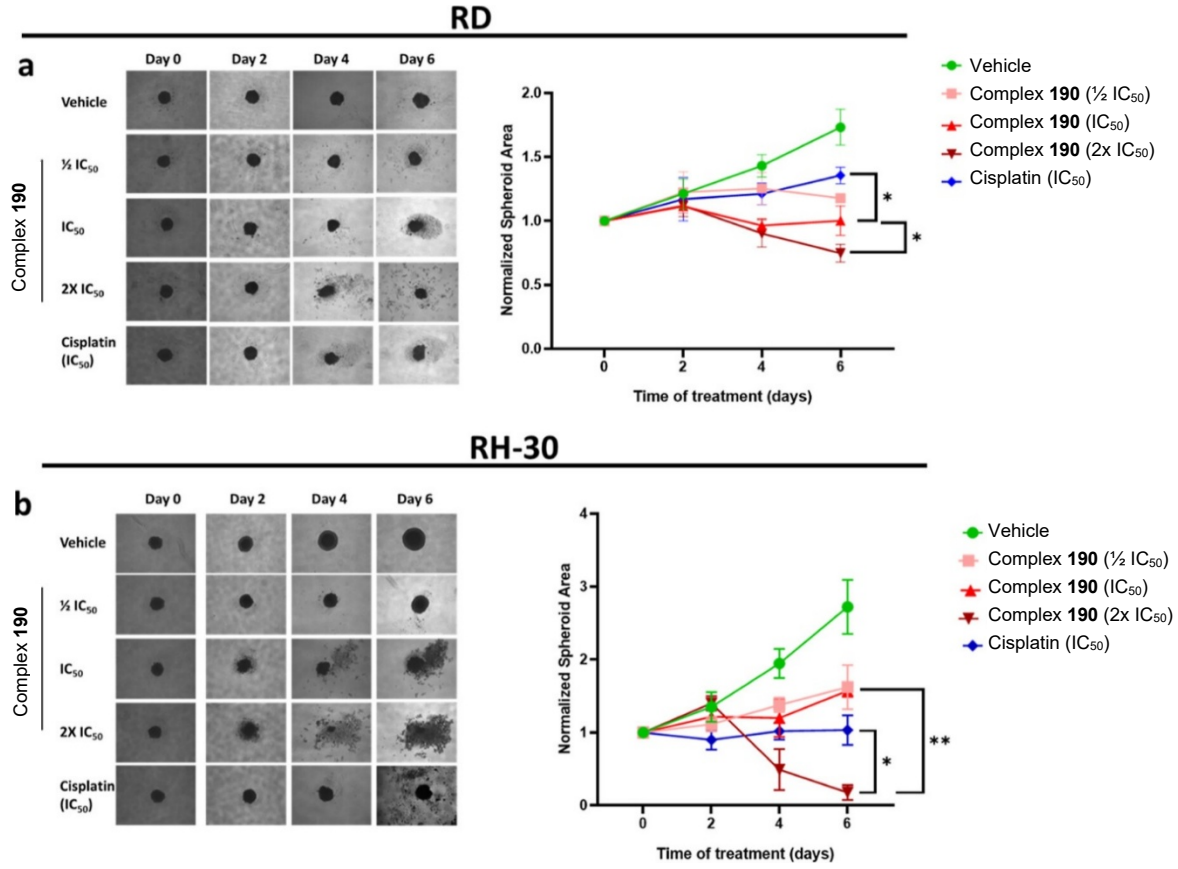

Figure 33. Optical micrographs and graphs of normalized area for spheroid models of rhabdomyosarcoma treated with complex **190**, specifically the cell lines (**a**) RD and (**b**) RH-30. Reproduced from Ref. [156], https://doi.org/10.1021/acs.jmedchem.4c00256, under the terms of the CC BY 4.0 license, https://creativecommons.org/licenses/by/4.0/.

Arunachalam et al. synthesized a series of biphenyl benzhydrazone arene Ru(II) complexes (**194-199**) through the reactions of biphenyl benzhydrazones with ruthenium arenes as shown in Scheme 26 [157]. The substituted biphenyl benzhydrazone **193** was utilized as a starting material for dimeric Ru(II) complexes containing benzene or *p*-cymene to yield complexes **194-196** or **197-199**, respectively.

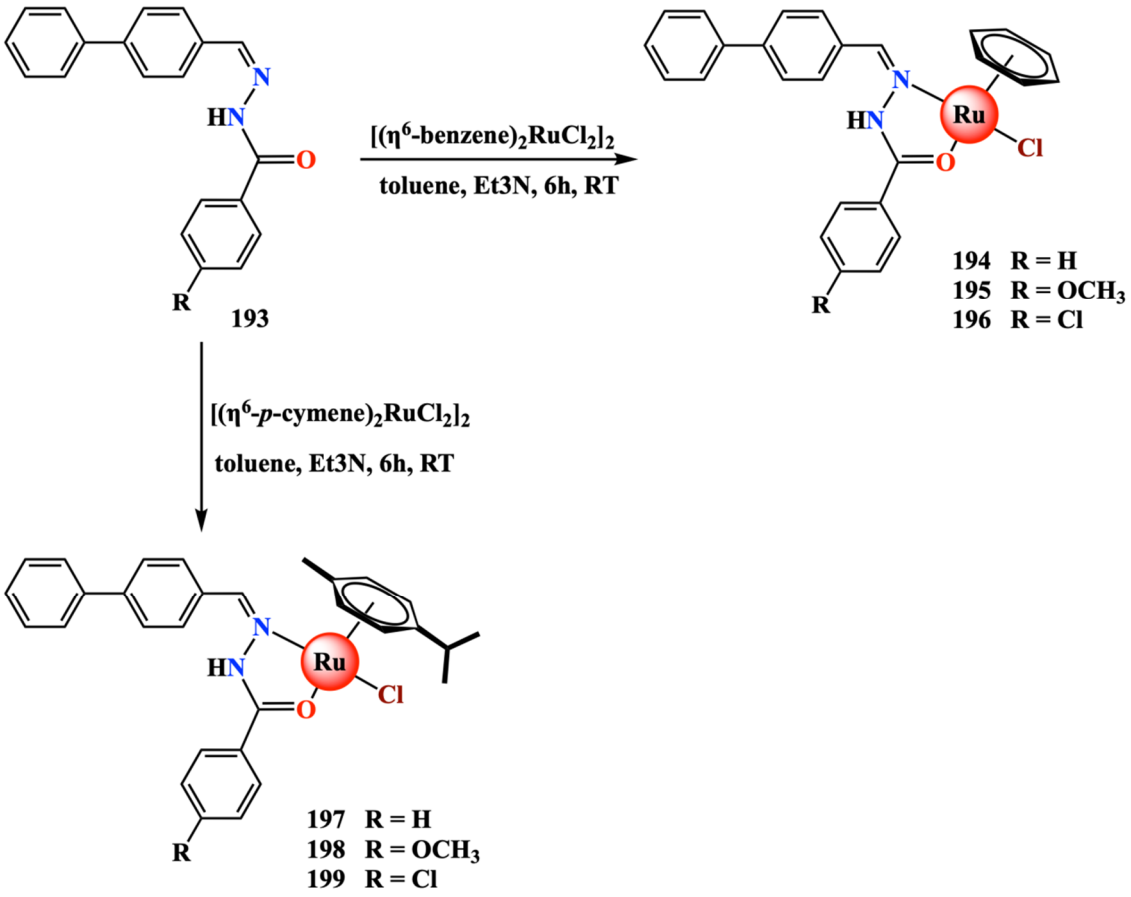

Scheme 26. Synthesis of biphenyl benzhydrazone Ru(II)-arene complexes **194-199**.

Complexes **194-199** all demonstrated potent cytotoxicity against A549, MDA-MB-231 and HepG2 cells. The highest efficacy and selectivity were shown for complex **198** with IC_{50} values of 7.36 μM for A549 cells, 9.53 μM for MDA-MB-231 cells and 10.83 μM for HepG2 cells, with low cytotoxicity (IC_{50} = 297.8 μM) for the non-cancerous HEK-293 cell line. This complex was also more effective than cisplatin, which was shown by IC_{50} values of 12.45 μM for A549 cells, 12.10 μM for MDA-MB-231 cells and 19.31 μM for HepG2 cells, as well as higher cytotoxicity (IC_{50} = 84.0 μM) for HEK-293 cells. The mechanism of these complexes was determined to be the generation of ROS and disruption of the mitochondrial membrane, resulting in oxidative stress that led to apoptotic cell death pathways. To examine the morphological changes associated with apoptotic cells, A549 cells were treated with complexes **194-199** for 48 hours and stained with acridine orange and ethidium bromide (AO-EB). Viable cells stained with AO-EB exhibited green fluorescence, necrotic cells were coloured reddish orange with no changes to the shape of the nuclei, and apoptotic cells showed some green fluorescence as well as developing orange patches due to membrane damage. The resulting confocal fluorescence micrographs of the cells shown in Figure 34 showed that, in comparison with the green fluorescence in the negative control cells, all the complexes resulted in membrane blebbing and cell death with apoptotic morphology. As expected, the largest proportion of apoptotic cells was observed for the most active complex **198**.

3.4. Iridium Complexes

In addition to the utilization of organometallic iridium complexes for phototherapy which was described earlier in this review, they have also been investigated for their inherent anticancer activities [158–166]. The role of iridium(III) triazole complexes for their antiproliferative activity has been investigated by Mondal et al. [167]. Reaction of substituted phenylacetylene (**200-202**) with 2-azidopyridine (**203**) allowed for the isolation of the triazole ligands **204-206**, which were reacted with [Ir(2-phenylpyridine)$_2$Cl]$_2$ to form the Ir(III) complexes **207-209**, as shown in Scheme 27.

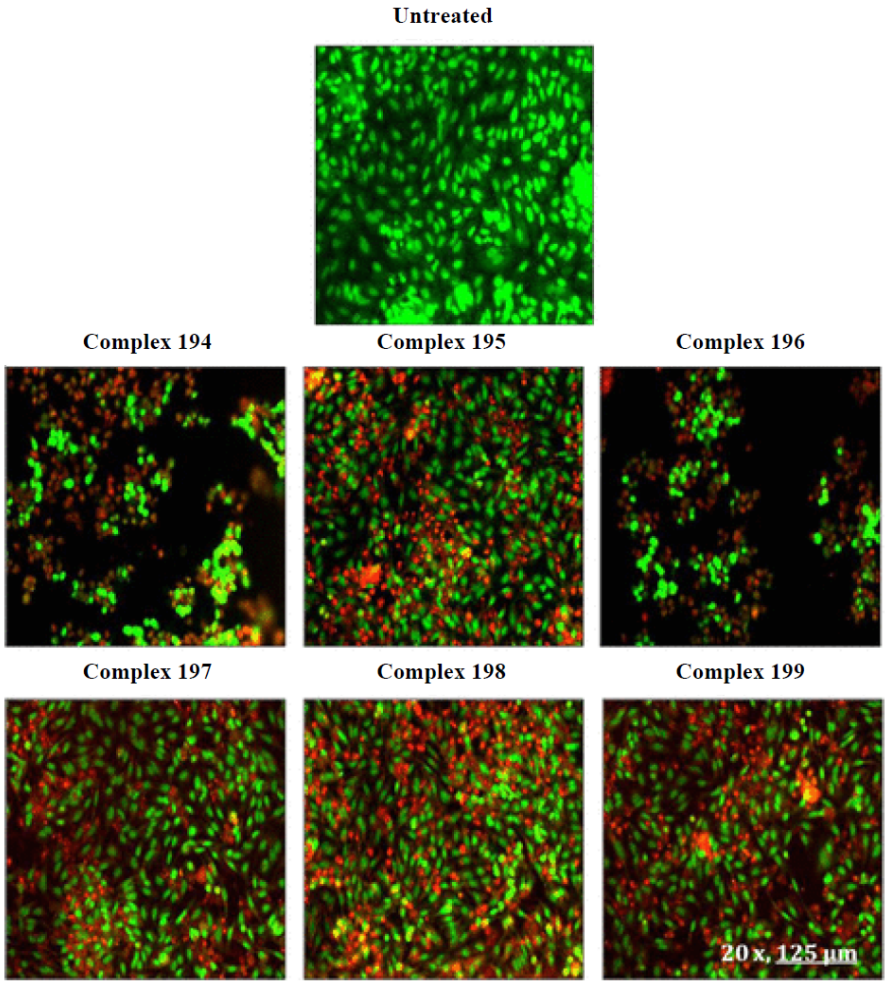

Figure 34. Confocal fluorescence micrographs of A549 cells stained with acridine orange and ethidium bromide after treatment with complexes **194-199** for 48 hours. Reproduced with permission from Ref. [157], Copyright © 2022, American Chemical Society.

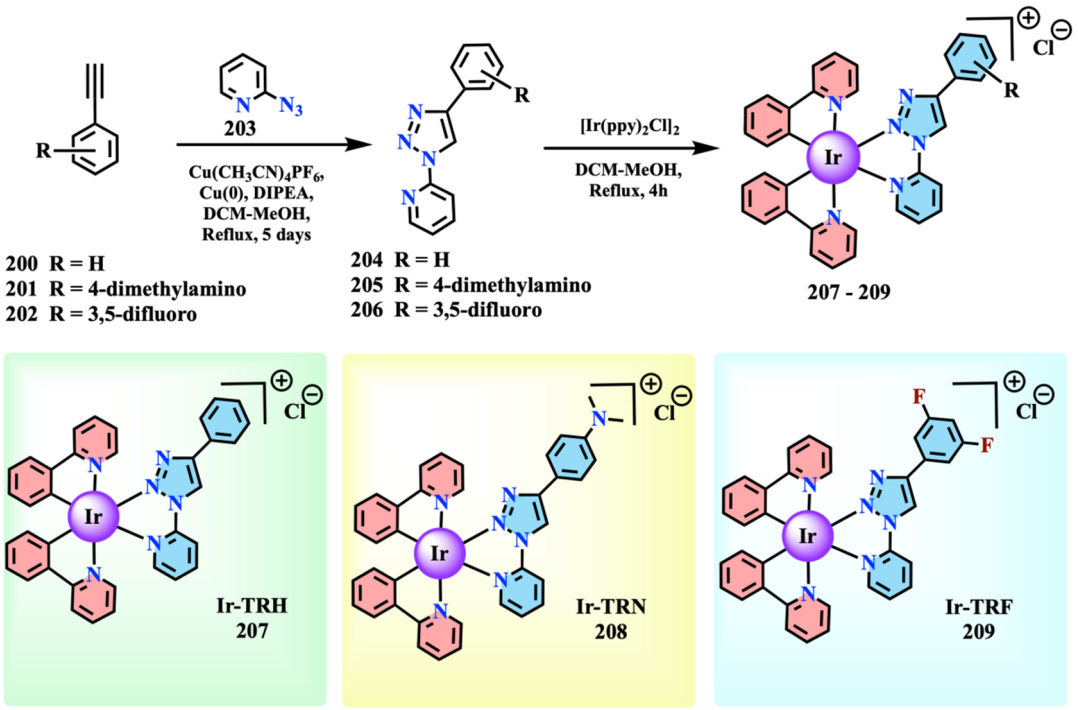

Scheme 27. Design and synthesis of iridium(III) triazole complexes **207-209**.

The triazole complexes were able to target cervical cancer through multiple modes of action. First, the complexes increased ER stress via the UPR pathway, as demonstrated by observed upregulation of the ER chaperone protein Erp29, which triggered apoptosis. Complexes **207**-**209** also inhibited cell proliferation and migration by downregulation of the ERK2/MAPK kinase pathway, which is necessary for downstream expression of genes involved in cell migration as well as transitioning to the S phase of the cell cycle. Additionally, the complexes activated P53, another protein involved in cell cycle regulation, that led to cell cycle arrest before the S phase. Finally, the complexes induced production of ROS, triggering apoptotic cell pathways. A summary of these mechanisms is illustrated in Figure 35. As a result, the complexes resulted in decreased cancer cell growth by cell cycle arrest and induction of apoptosis. When examined against the ME-180 cervical cancer and A549 cancer cell lines, all complexes showed specificity for the cancer cells over non-cancerous human keratinocytes. The most active complex **209** exhibited IC_{50} values of 14.48 μM for ME-180 cells and 17.95 μM for A549 cells, compared to 60 μM for keratinocytes.

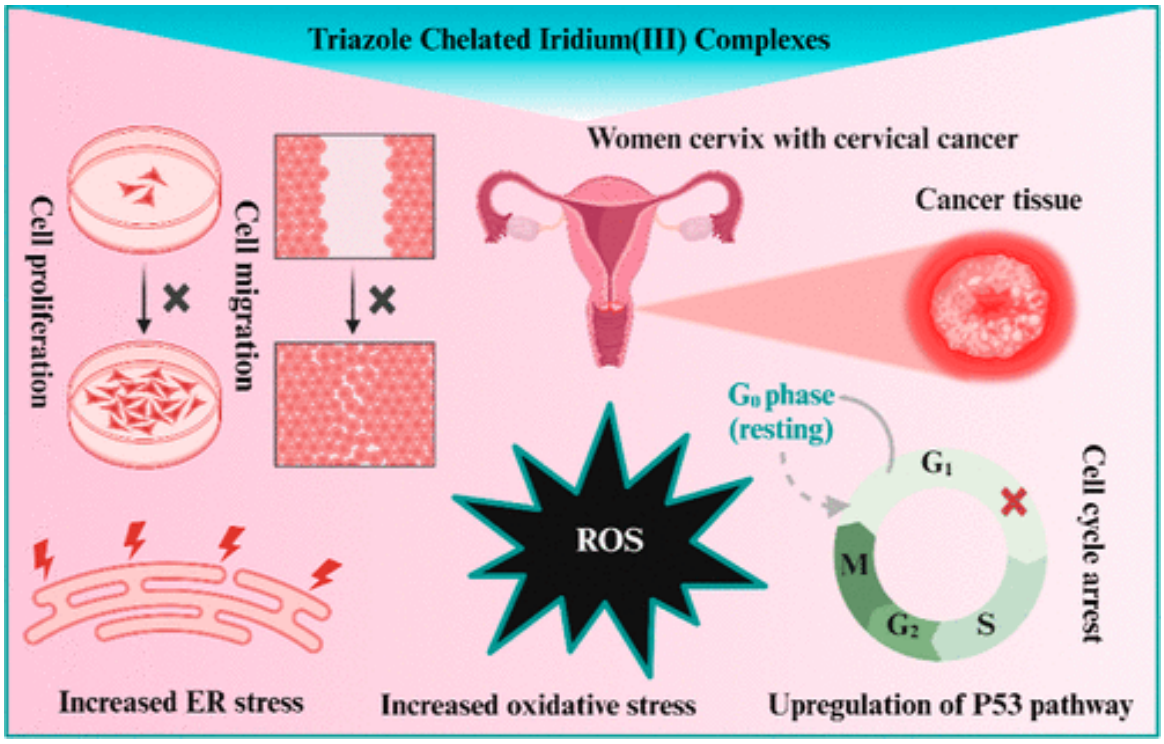

Figure 35. Summary of anticancer mechanisms for triazole-chelated Ir(III) complexes **207**-**209**. Reproduced with permission from Ref. [167], Copyright © 2024, American Chemical Society.

Cyclometallated Ir(III) complexes **210-214** were prepared by Wu et al. (Figure 36) for their ER-targeting properties and ability to induce pyroptosis [168]. Pyroptosis is a necrotic cell death pathway characterized by cell lysis that releases molecules to stimulate the inflammatory response. Therefore, pyroptosis induced by the complexes would result in an immunogenic effect, allowing a response to cancer cells that would normally be ignored by the immune system. Ir(III) complexes **213** and **214** showed enhanced efficacies for all three tested breast cancer cell lines (MDA-MB-231, MCF-7 and 4T1) relative to cisplatin, while maintaining specificity for the cancer cells over the healthy MCF-10A mammary epithelial cells. The inhibitory activity of the complexes was highest against 4T1 cells, with IC_{50} values of 0.25 μM for complex **213** and 0.28 μM for complex **214**, compared to 5.76 μM for cisplatin and lowest against MCF-7 cells, with IC_{50} values of 1.21 μM for complex **213** and 1.22 μM for complex **214**, compared to 5.76 μM for cisplatin. Against the healthy MCF-10A cells, IC_{50} values of 6.54 μM were observed for complex **213** and 6.85 μM for complex **214**, compared to 27.2 μM for cisplatin. Both complexes were also shown to induce pyroptosis due to microscopic observation of cell swelling and membrane rupture, as opposed to the cell shrinking and membrane blebbing associated with apoptotic cell death. Furthermore, several markers of apoptosis, including poly(ADP-ribose) polymerase (PARP), caspase-3 and Bax did not show any upregulated gene expression, while the expression of antiapoptotic protein Bcl-2 was not downregulated. It was therefore concluded that the mode of cell death favoured pyroptosis over apoptosis.

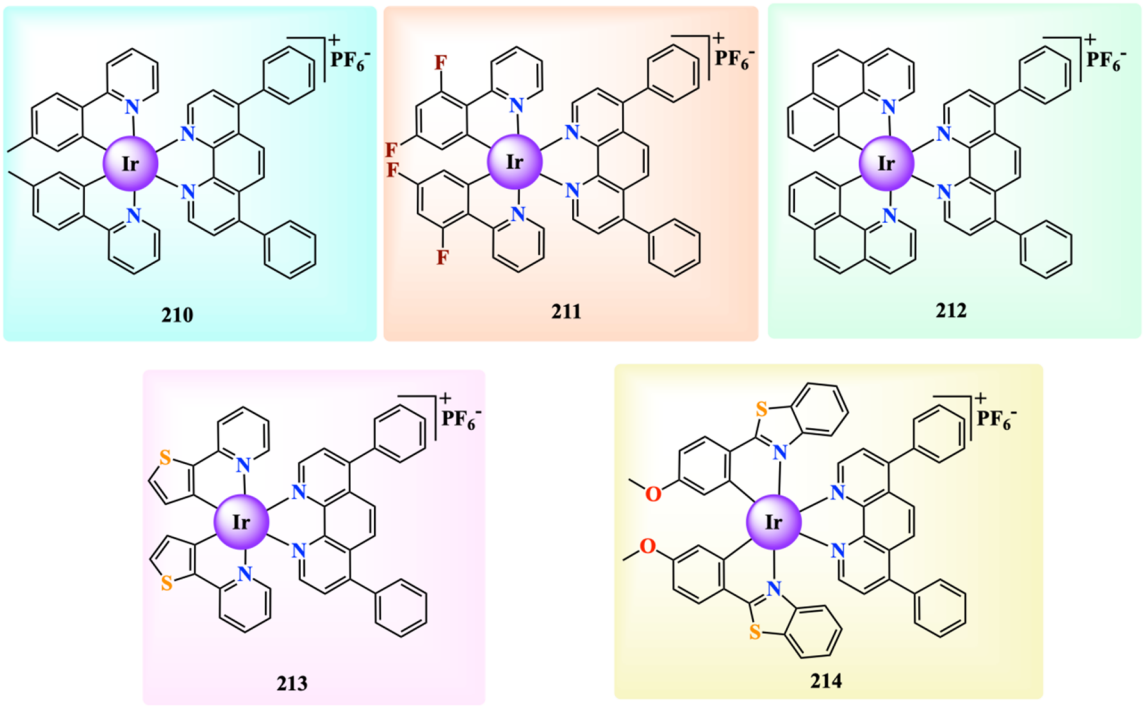

Figure 36. Structures of cyclometallated Ir(III) complexes **210-214**.

An *in vivo* antitumour model is outlined in Figure 37a, in which one or three injections of either complex **213** (Ir4) or complex **214** (Ir5) were given weekly as prophylactic treatments (which the authors referred to as "vaccines") to mice bearing tumours of the 4T1 breast cancer cell line. The greatest reduction in tumour volume (Figure 37b) was shown for the group given three injections of complex **213**, although all treatments caused significant improvement compared to cisplatin (CDDP). Complex **214** did not show any significant difference between the one-injection and three-injection treatment groups. Three injections of complex **213** also resulted in the smallest size or, in some cases, even complete elimination of tumours in the subjects, as shown by the ex vivo tumour photographs in Figure 37c. Furthermore, the health of the mice was not significantly affected by any of the treatments, as shown by the body weights in Figure 37d.

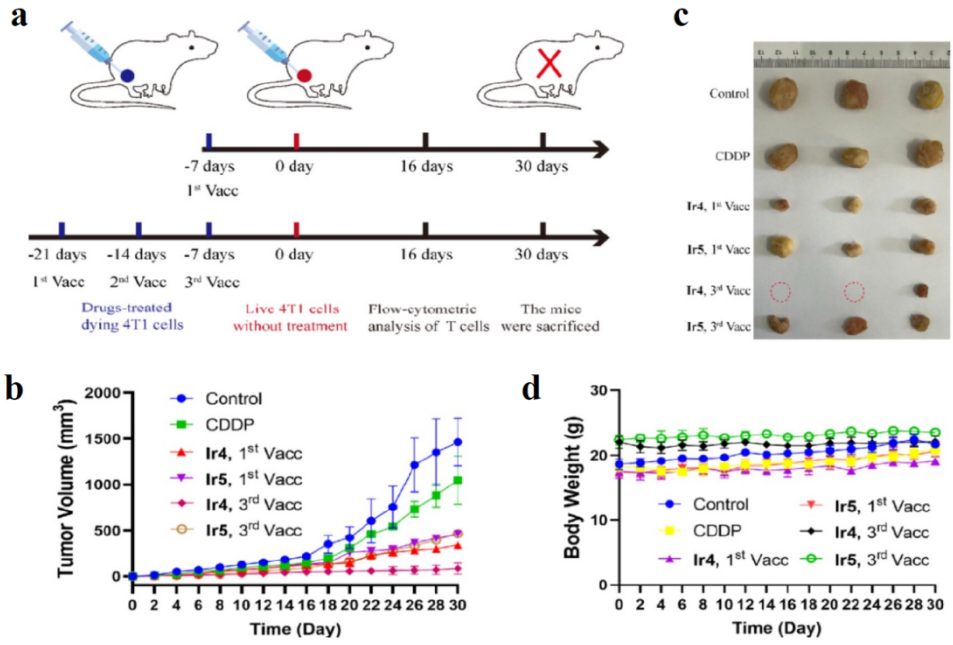

Figure 37. *In vivo* anticancer study for mice bearing 4T1 tumours, showing (**a**) experimental design using one or three weekly injections of complexes **213** (Ir4) or **214** (Ir5) prior to injection of tumour cells, (**b**) inhibition of tumour volume, (**c**) photographs of ex vivo tumours after the end of the experiment and (**d**) body weight of the mice. Adapted with permission from Ref. [168], Copyright © 2025, American Chemical Society.

Jiang et al. designed Ir(III) complexes for induction of other different programmed necrotic pathways of cell death [169]. These pathways include ferroptosis and pyroptosis, as previously described, as well as oncosis, characterized by swelling of the ER or mitochondria, cytoplasm coagulation and chromatin aggregation, and paraptosis, which also involves swelling of ER or mitochondria as well as cytoplasmic vacuolation [170,171]. To do so, the complexes were designed to target several different organelles, with complex **215** (Mito-Ir) for targeting of mitochondria and complex **216** (Lyso-Ir) for targeting of lysosomes (Figure 38).

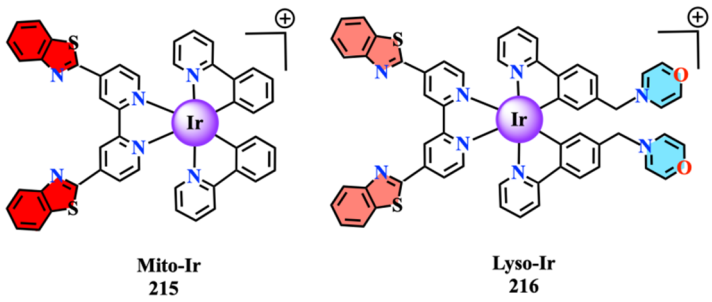

Figure 38. Structures of mitochondria-targeting complex **215** (Mito-Ir) and lysosome-targeting complex **216** (Lyso-Ir).

These complexes were examined for their activity against the MKN-45 gastric cancer cell line in vitro and exhibited specificity for cancer cells, with IC_{50} values for non-cancer cells >100 μM. The mode of cell death for complex **216** involved swelling of lysosomes and increased lysosome membrane permeability, leading to paraptosis, while complex **215** resulted in mitochondrial swelling and cytoplasmic vacuolation that caused oncosis. To overcome poor solubility and improve biocompatibility, nanoparticles of the phospholipid 1,2-distearoyl-sn-glycero-3-phosphoethanolamine-N-PEG_{2000} (DSPE-PEG_{2000}) were used to encapsulate complexes **215** and **216** for *in vivo* experiments. Figure 39a illustrates the experimental design for BALB/c nude mice inoculated with MKN-45 cells and left to grow tumours for seven days, then treated with phosphate buffered saline (PBS) as a negative control, encapsulated nanoparticles of complex **215** or complex **216**, or cisplatin (CDDP) as a reference drug. Encapsulation with DSPE-PEG_{2000} nanoparticles resulted in low toxicity, with neither of the complexes having any impact on the body weight of the mice, compared to the significant decrease in body weight caused by cisplatin (Figure 39b). Further, no observable damage was noted for any of the organs by histopathological examination as well as markers of liver and kidney function. In terms of the antitumour effect, Figure 39c demonstrates that nanoparticles of either complex reduced tumour volume to 412 mm^3 for complex **215** and 446 mm^3 for complex **216**, compared to 1400 mm^3 for the negative control (PBS). Additionally, both complexes were significantly more effective than cisplatin at reducing tumour volume (* $p < 0.05$). Finally, although both complexes were found to enhance the activity of immune dendritic cells and natural killer cells *in vivo*, only complex **215** was able to increase macrophage targeting of the tumour as well as the T cell-mediated immune response.

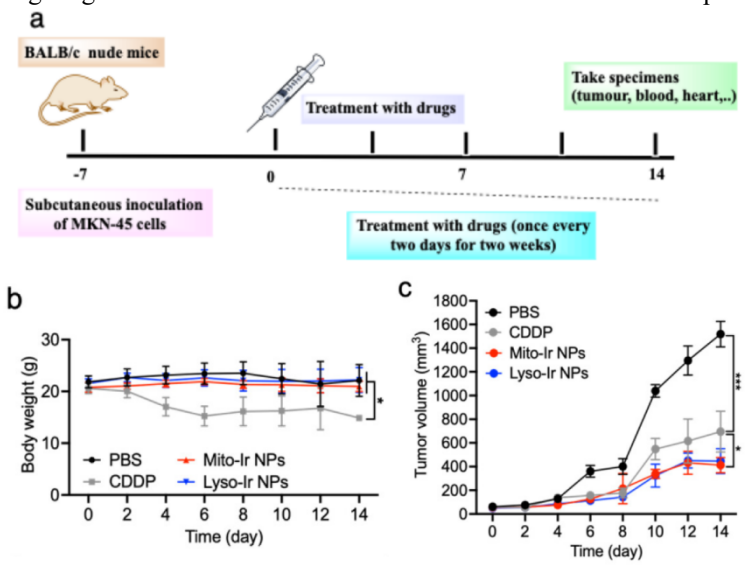

Figure 39. (**a**) Experimental design of mouse model of gastric cancer using BALB/c nude mice inoculated with MKN-45 cells and treated with nanoparticles of complex **215** (Mito-Ir NPs), complex **216** (Lyso-Ir NPs) or cisplatin

(CDDP), as well as the (**b**) body weights of the mice and (**c**) tumour volumes over the course of the study. * $p <$ 0.05, *** $p < 0.001$. Adapted with permission from Ref. [169], Copyright © 2026, American Chemical Society.

3.5. Palladium and Platinum Complexes

As palladium and platinum are in the same group in the periodic table (d8 elements), and platinum complexes have been well researched for their antiproliferative activities, palladium complexes can offer alternatives to platinum complexes such as cisplatin. Organometallic palladium complexes provide improved stability that may allow for their use as anticancer agents. In a critical review by Scattolin et al., several types of organopalladium complexes demonstrated in vitro and ex vivo anticancer efficacy with various modes of action including some not exhibited by platinum-containing complexes [172]. Additionally, some of these complexes were active against cisplatin-resistant cell lines.

To improve the anticancer activity and toxicity of existing square planar Pt(II) complexes, a series of square-planar Pd(II) complexes were prepared by da Silva et al. [173]. First, *p*-phenylenediamine (**218**) was added to *p*-anisaldehyde (**217**) solution to give the organic compound **219**, which was then complexed with $PdCl_2$ to produce complex **220**. Various salts were reacted with **220** to yield complexes **221-225**, as shown in Scheme 28.

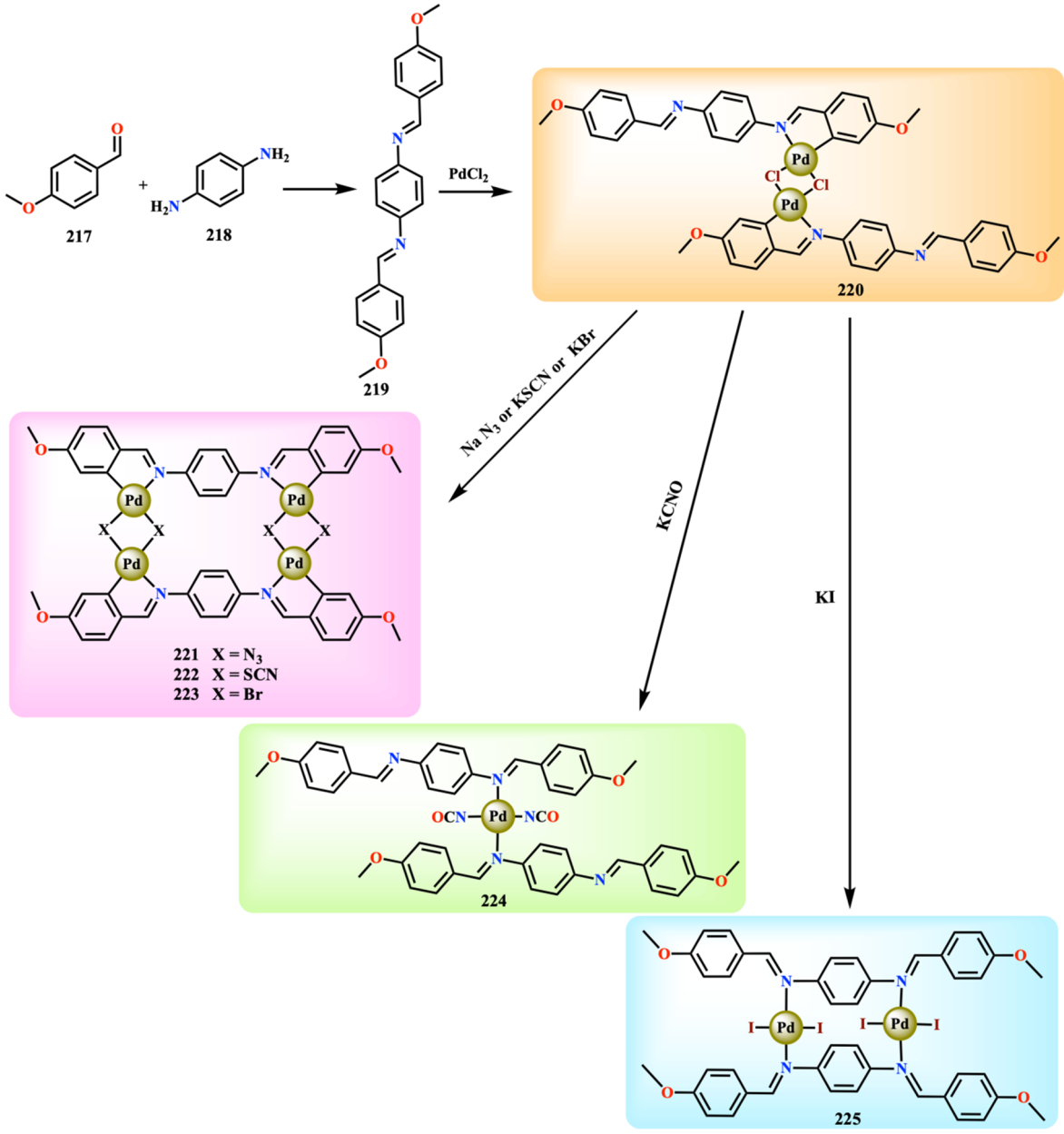

Scheme 28. Preparation of Pd(II) complexes **220-225**.

The antiproliferative activities of the complexes **220-225** and the organic compound **219** were tested against the MCF-7 breast cancer and MDA-MB-435 melanoma cell lines. The greatest inhibition for MCF-7 cells was observed for complex **223** and complex **225**, with IC50 values of 0.0397 μg/mL and 0.0393 μg/mL, respectively, which are significantly lower than 0.066 μg/mL for organic compound **219** and 0.0544 μg/mL for cisplatin (Figure 40). The lowest IC_{50} values of the complexes for MDA-MB-435 cells were 0.0331 μg/mL for complex **220** and 0.0320 μg/mL for complex **225**, significantly lower than the 0.0521 μg/mL for organic compound **219** and 0.0384 μg/mL for cisplatin. The morphological changes in both cell types were examined using H&E staining under an optical microscope. In both cancer cell lines, cisplatin and complexes **220-225** showed cell shrinkage and rounding, in addition to chromatin condensation, while the ligand **219** displayed fewer less notable changes compared to the negative control. In addition, all complexes and cisplatin decreased the average cell length measured for both MCF-7 and MDA-MB-435 due to the shrinking and rounding of the cells, while cells treated with the organic compound **219** were significantly longer, indicating less shrinkage. Similarly, the organic compound **219**, complexes **220-225** and cisplatin all induced significantly high levels of cell death for both cell lines (>70%). These results are consistent with the high degree of DNA fragmentation observed in cells treated with Pd(II) complexes. However, the complexes were also shown to cleave free double stranded DNA without cells, suggesting a second mechanism of DNA damage they may be able to achieve.

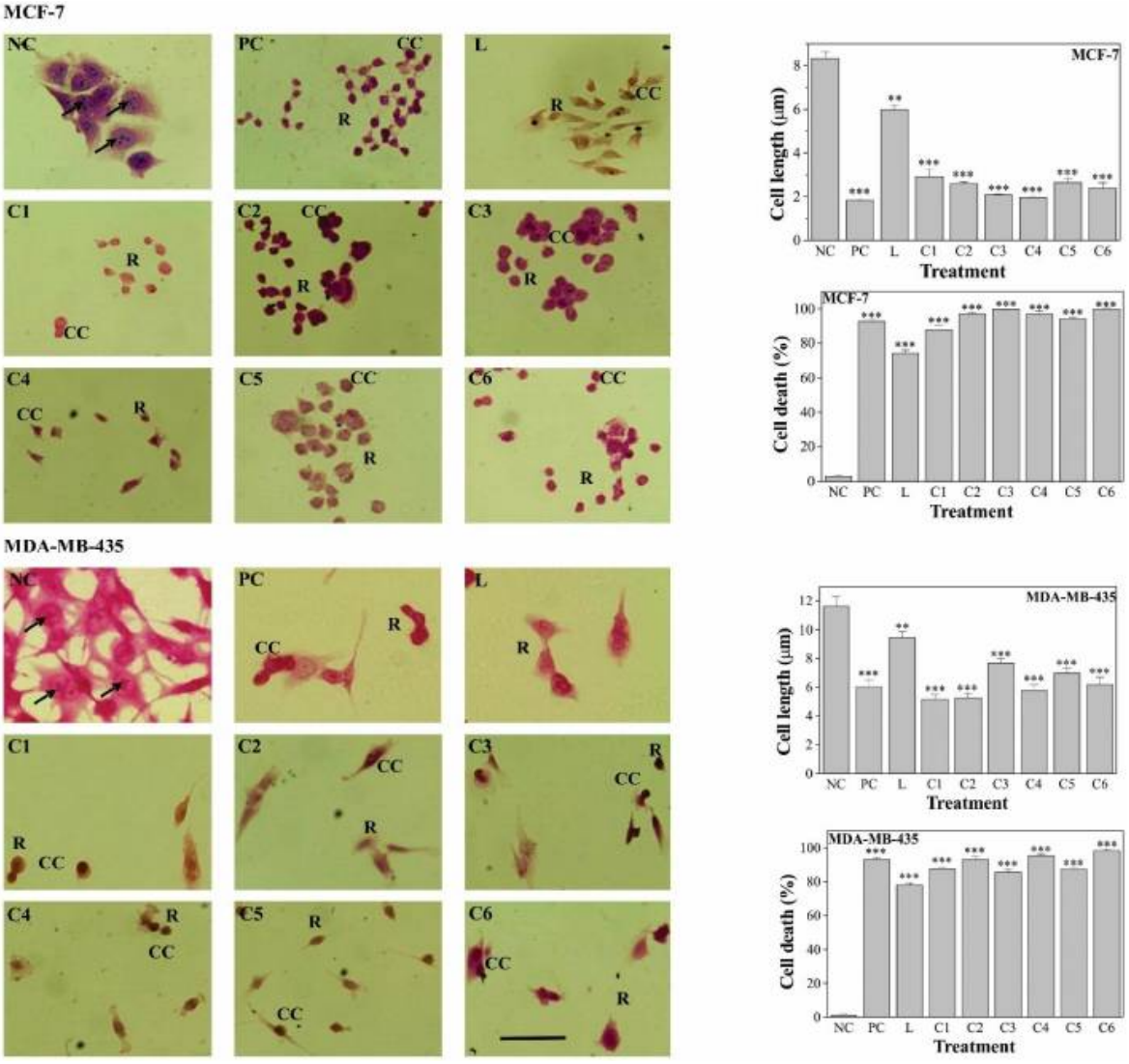

Figure 40. (**Left**) Micrographs showing morphology of MCF-7 breast cancer and MDA-MB-435 melanoma cells treated with compound **219** and complexes **220-225** exhibiting rounding, R, and chromatin condensation, CC. (**Right**) Graphs of cell length and cell death in both cell lines. NC = negative control, PC = cisplatin, L = compound **219**, C1-C6 = Pd(II) complexes **220-225**. ** $p < 0.01$; *** $p < 0.001$. Reproduced with permission from Ref. [173], https://doi.org/10.34172/apb.2023.017 (accessed on 14 May 2026), under the terms of the CC BY 4.0 license, https://creativecommons.org/licenses/by/4.0/.

Lighvan et al. designed a Pd(II) complex with the phosphorous-containing ligand PTA for improved hydrophilicity and enhanced DNA-binding interactions [174]. Reaction of 2-phenylaniline (**226**) with $PdCl_2$ produced the palladacycle **227**, which was then reacted with PTA to yield the PTA-conjugated complex **228** as shown in Scheme 29.

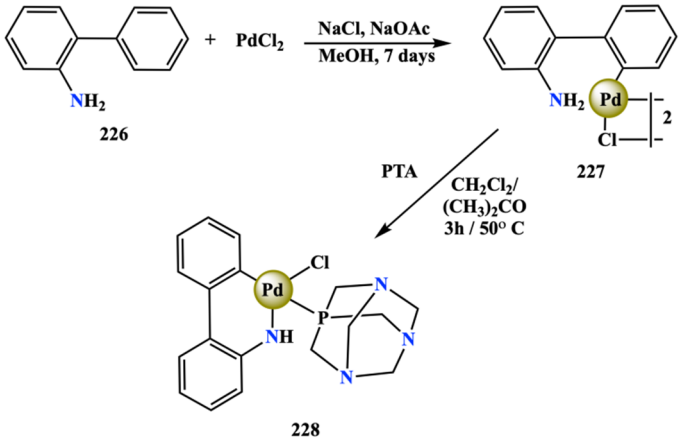

Scheme 29. Design of PTA-containing Pd(II) complex **228**.

Docking simulations of complex **228** showed high binding affinity with DNA as well as bovine serum albumin (BSA). The mechanism of action was therefore suggested to be DNA crosslinking leading to apoptosis, which is common for many Pd(II) and Pt(II) complexes such as cisplatin. Albumin is a serum protein that acts as a carrier for many molecules, including drugs, in the bloodstream, and BSA is commonly used to study drug transport in the body. Drug release profile studies were performed using dialysis bags as semi-permeable membranes. It was demonstrated that the release of complex **228** adsorbed onto BSA nanoparticles was slow and controlled compared to the free complex, which would result in more favourable pharmacokinetic properties for the drug in the body. The antiproliferative activities of complexes **227** and **228** were assayed against MCF-7 breast cancer and Jurkat human leukemic T cell lines (Figure 41a and Figure 41b, respectively). The complexes showed potent inhibition of the Jurkat cells, with IC_{50} values of 76 μM for complex **412** and 51 μM for complex **228**. Both complexes were more cytotoxic against MCF-7 cells, although complex **228** was more toxic than **227**, with IC_{50} values of 49 μM and 35 μM, respectively.

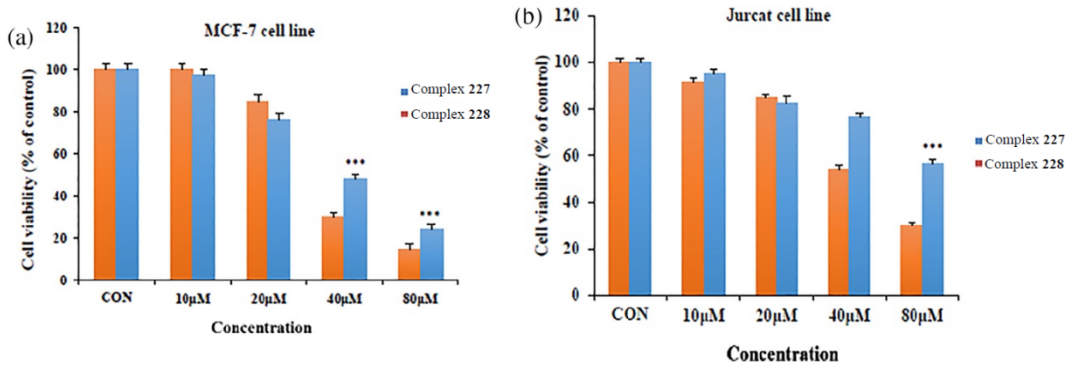

Figure 41. Concentration-dependent cell viability for (**a**) MCF-7 and (**b**) Jurkat cell lines given complex 227 or complex 228 (CON = negative control). Adapted from Ref. [174] with permission from John Wiley & Sons, Copyright © 2020 Wiley-VCH GmbH.

Classical platinum drugs including cisplatin, oxaliplatin and carboplatin have been well studied and used as standard anticancer drugs. While these are coordination complexes, there are fewer organometallic platinum complexes that have been developed and examined for their antiproliferative activities [175–181]. One recent example reported by Su et al. described three Pt(IV) complexes with terthiophene ligands **230-232** as well as complex **229** lacking thiophene [182]. Unlike conventional platin drugs such as cisplatin, the terthiophene-containing complexes **230-232** use Pt(IV) to disrupt zinc homeostasis by changing the expression levels of different zinc regulatory proteins. The complexes upregulated the Zrt- and Irt-like proteins (ZIP) responsible for zinc transport into the cell and downregulated Zn transporters (ZnT) that export zinc from the cell, resulting in a

higher intracellular Zn^{2+} concentration, as well as inhibiting feedback regulation that increased transcription of zinc transport proteins through downregulation of expression of the metal-regulatory transcription factor 1 (MTF-1). Furthermore, the platinum complexes also caused buildup of ROS by inhibiting the expression of metallothioneins (MT) and superoxide dismutase 1 (SOD1). It should be noted that none of these effects were detected for cancer cells treated with either cisplatin or complex **229**, demonstrating the importance of the terthiophene moiety in the anticancer mechanism. These changes to zinc homeostasis led to DNA damage and mitochondrial disruption, causing pyroptosis that not only kills tumour cells but also releases pro-inflammatory cytokines to trigger an immune response, as outlined in Figure 42. This immune response involves both maturation of dendritic cells and T cells infiltrating into tumour tissues, which can occur at the site of the local tumour, as well as distant tumours, due to circulation of the cytokines throughout the body.

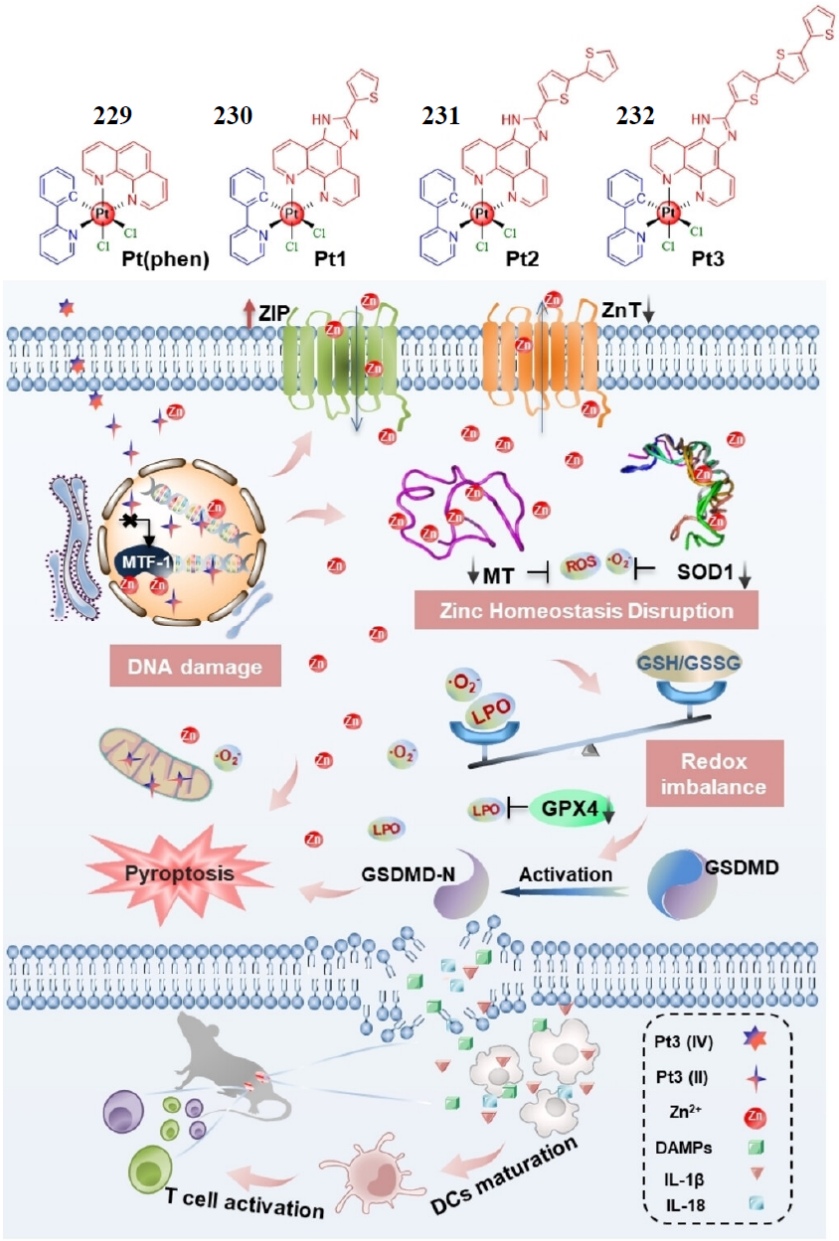

Figure 42. Structures of thiophene-containing Pt(IV) complexes **230-232** and the thiophene-free analogue **229**, as well as their pyroptotic mechanism leading to an antitumour immune response. Reproduced from Ref. [182] with permission from John Wiley & Sons, Copyright © 2023 Wiley-VCH GmbH.

Complexes **230-232** all exhibited greater inhibition against MDA-MB-231 and MCF-7 breast cancer cells in vitro in comparison with cisplatin or the thiophene-free complex **229**. Only complex **230** maintained specificity for cancer cells over healthy MCF-10A breast epithelial cells, although it should be noted that cisplatin was also more toxic against the healthy cells than either cancer cell line. The highest activity against MDA-MB-231 triple

negative breast cancer cells was detected for complex **232**, with an IC_{50} of 0.11 μM, compared to 1.2 μM for its corresponding ligand 2-([2,2':5',2''-terthiophen]-5-yl)-1H-imidazo [4,5-f][1,10]phenanthroline, 16.9 μM for thiophene-free complex **229** or 43.2 μM for cisplatin. Complex **232** was therefore selected for an *in vivo* study in which two tumours per mouse were formed by inoculation with 4T1 breast cancer cells into the flank. The primary tumour on the right side received either no treatment (negative control) or injection with cisplatin, complex **232** or its corresponding organic ligand, while the distant tumour on the left side received no injections, in order to measure the immune anticancer response. The photographs of ex vivo tumours in Figure 43A and mice in Figure 43B showed a visible decrease in primary tumour size for mice treated with cisplatin or ligand, with the largest effect for mice treated with platinum complex **232**, which was confirmed to be statistically significant by the graph of the primary tumour volumes in Figure 43D. These photographs as well as the graph of distant tumour volumes in Figure 43C also indicated that the only significant change in the size of the distant tumours was in the group given complex **232**. Despite the in vitro cytotoxicity of the complex, the overall health of the mice was not affected by any of the treatments, as shown by the lack of significant changes to body weight (Figure 43E). The immunogenic activity of complex **232** was evaluated by flow cytometry using fluorescently labelled antibodies for various cluster of differentiation (CD) proteins that act as markers of specific immune cell lineages. A statistically significant increase was observed for mature $CD80^+CD86^+$ dendritic cells (Figure 43F), $CD3^+CD8^+$ cytotoxic T lymphocytes (Figure 43G and $CD3^+CD4^+$ helper T lymphocytes (Figure 43H) for the mice treated with complex **232** compared to the negative control or the corresponding organic ligand, demonstrating the ability of the complex to stimulate the adaptive immune response.

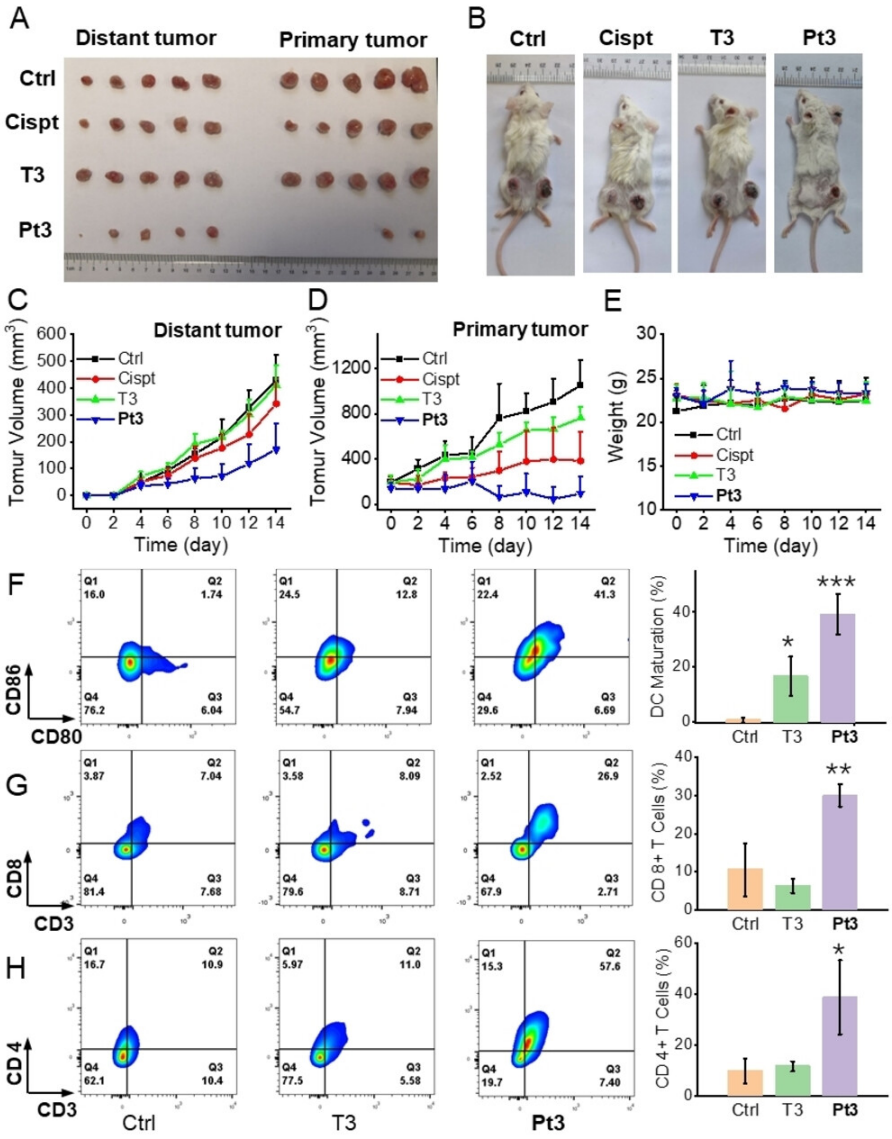

Figure 43. Antitumour activity of complex **232** in mice bearing 4T1 tumours (T3 = 2-([2,2':5',2''-terthiophen]-5-yl)-1H-imidazo [4,5-f][1,10]phenanthroline, Pt3 = complex **232**). Photographs of (**A**) ex vivo tumours and (**B**) mice

on day 14 prior to sacrifice. Volumes of (**C**) distant tumour and (**D**) primary tumour over the experimental period. **(E)** Changes in mouse body weight. Quantitative flow cytometry and graphs of relative percentages of (**F**) $CD80^+CD86^+$ mature dendritic cells, (**G**) $CD3^+CD8^+$ cytotoxic T cells and (**H**) $CD3^+CD4^+$ helper T cells (* $p <$ 0.05, ** $p < 0.01$, *** $p < 0.001$). Reproduced from Ref. [182] with permission from John Wiley & Sons, Copyright © 2023 Wiley-VCH GmbH.

Another example of organometallic platinum complexes was the series of platinum complexes **234-237** designed by Panda et al. to be kinetically inert [183]. A major limitation of platinum complexes is the kinetic lability of the platinum moiety, which leads to systemic toxicity, including nephrotoxicity due to buildup in kidney tissue, and development of drug resistance by cancer cells. Unfortunately, this lability is also necessary for forming covalent bonds with nucleophilic biomolecules that result in the cytotoxicity of the complexes. To form more kinetically inert complexes with different mechanisms of action, the [(7,8-benzoquinoline)Pt(μ-Cl)]$_2$ dimer (**233**) was reacted with $AgNO_3$ and the corresponding substituted phenanthroline ligands to produce the mononuclear cyclometallated Pt(II) complexes **234-237**, as illustrated in Scheme 30.

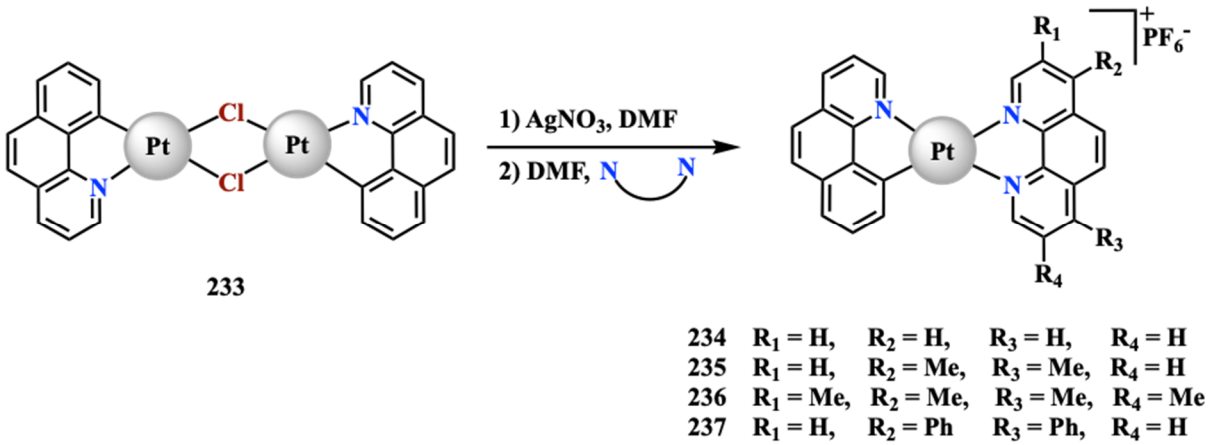

Scheme 30. Design of cyclometallated Pt(II) complexes **234-237**.

The anticancer activity was evaluated by assays of HeLa ovarian cancer cells, and all four complexes were more effective than cisplatin. The most potent activity was exhibited by complex **237** with an IC_{50} of 0.16 μM compared to 2.9 μM by cisplatin against the same cell line. The effect of complex **237** was therefore tested in vitro against cisplatin-susceptible and their A2780 ovarian, A549 lung and DU145 prostate cancer cell lines and their corresponding cisplatin-resistant cell lines, denoted by the addition of "Cis" (e.g., A2780Cis). The IC_{50} values were generally comparable, with values of 0.07 μM for A2780 and 0.08 μM for A2780Cis, 0.51 μM for A549 and 0.48 μM for A549Cis and 0.92 μM for DU145 and 0.76 μM for DU145Cis. It was thus concluded that the activity of complex **237** was unaffected by cisplatin-resistance. Regarding the mechanism, the effect of cisplatin on A2780Cis cells was negatively impacted by addition of GSH, due to redox reaction with labile platinum complexes. On the other hand, complex **237** was unaffected by addition of GSH, demonstrating kinetic inertness. Consequently, the complex **237** remained >90% intact over 24 hours, unlike oxaliplatin, which had a half-life of approximately one hour in human plasma, as shown in Figure 44. *In vivo* studies of cisplatin-susceptible A549 and cisplatin-resistant SKOV3 ovarian cancer tumour xenografts in mice were also performed and showed that complex **237** and cisplatin were effective against both types of tumours, while the SKOV3 cells required a dose of cisplatin containing 2.5 times as much platinum as complex **237** to achieve similar efficacy. The biodistribution of platinum in the A549 model organisms was also examined and was shown to be significantly lower in the liver and kidneys of mice given complex **237** than for mice given cisplatin, which indicates lower Pt accumulation that could cause systemic toxicity. In particular, the level of Pt accumulation in the kidneys of the complex **237**-treated group was one-eighth that of the cisplatin-treated group, which would prevent nephrotoxicity.

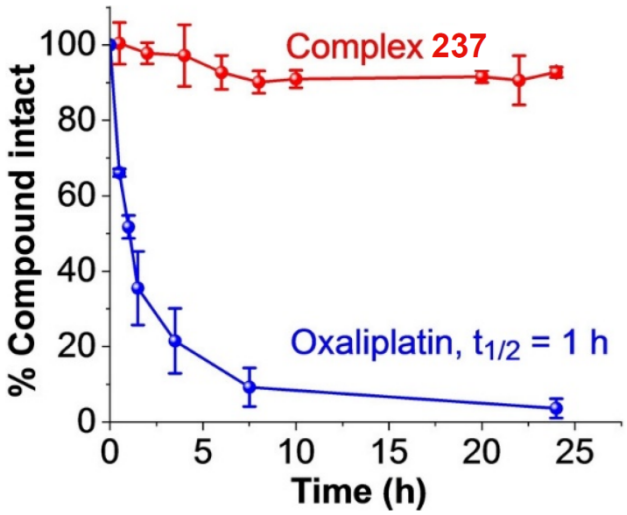

Figure 44. Percentage of intact complex **237** and reference drug oxaliplatin in plasma over a 24-hour period. Reproduced from Ref. [183] with permission from John Wiley & Sons, Copyright © 2023 Wiley-VCH GmbH.

3.6. Copper, Silver and Gold Complexes

Organometallic complexes of group 11 transition metals Cu, Ag and Au with NHCs have been well studied for their anticancer activities. While Au complexes have been the subject of the most study, there are a few examples with Cu and Ag. In a recent example of Cu coordinated to phenanthroline-functionalized NHC ligands, these complexes were found to exhibit antiproliferative activity via induction of oxidative and ER stress [184]. The functionalization of 2-(imidazol-1-yl)-1,10-phenanthroline (**238**) with benzyl, 2,4,6-trimethylbenzyl or cinnamyl groups resulted in the corresponding functionalized organic compounds **239-241**, which were then reacted with Ag_2O and copper to form the Cu(I)-NHC complexes **242-244**, as illustrated in Scheme 31.

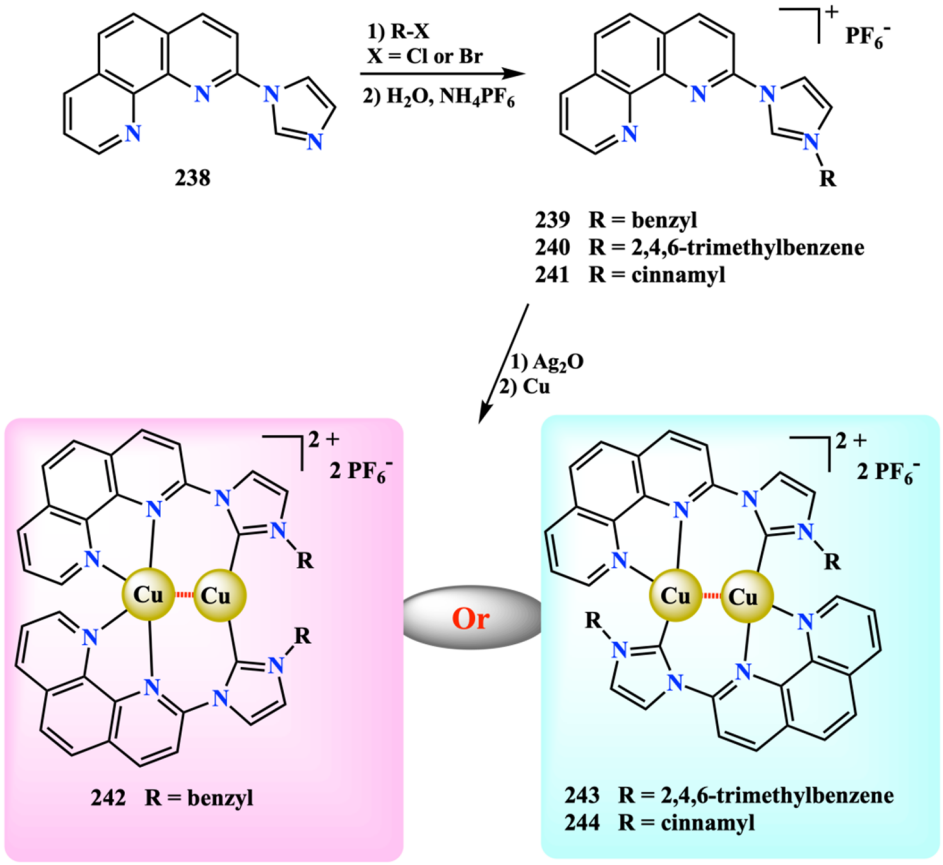

Scheme 31. Design of Cu(I)-NHC complexes **242-244**.

The copper complexes were evaluated for their antiproliferative activity against four colon cancer cell lines: HT-29, HCT-116, LoVo and CT-26. IC_{50} values for all three copper complexes were found to be comparable to cisplatin, with specificity for the colon cancer cells over healthy human umbilical vein endothelial cells (HUVEC). The lowest IC_{50} values were observed for complex **243**, with 6.00 μM against HT-29, 4.36 μM against HCT-116, 5.57 μM against LoVo and 5.67 μM against CT-26, compared to 8.20 μM against HT-29, 6.91 μM against HCT-116, 6.91 μM against LoVo and 7.20 μM against CT-26 for cisplatin. The antiproliferative activity at a concentration of 4 μM of each complex was confirmed by 5-ethynyl 2'-deoxyuridine (EdU) incorporation assay and visualized using confocal microscopy (Figure 45a), where proliferating cells were stained in green and non-dividing cells in blue. The average proliferation rate (Figure 45b) for the negative control HCT-116 cells was 48.0%, which was reduced to 24.5% for cells incubated with complex **242**, 16.1% for complex **243** and 27.8% for complex **244**. The greatest antiproliferative activity was therefore confirmed for complex **243**. The mode of cell death for complex **243** was confirmed to be apoptosis using AO/EB staining of HCT-116 cells, which was a result of ROS generation that triggered ER stress and mitochondrial membrane disruption.

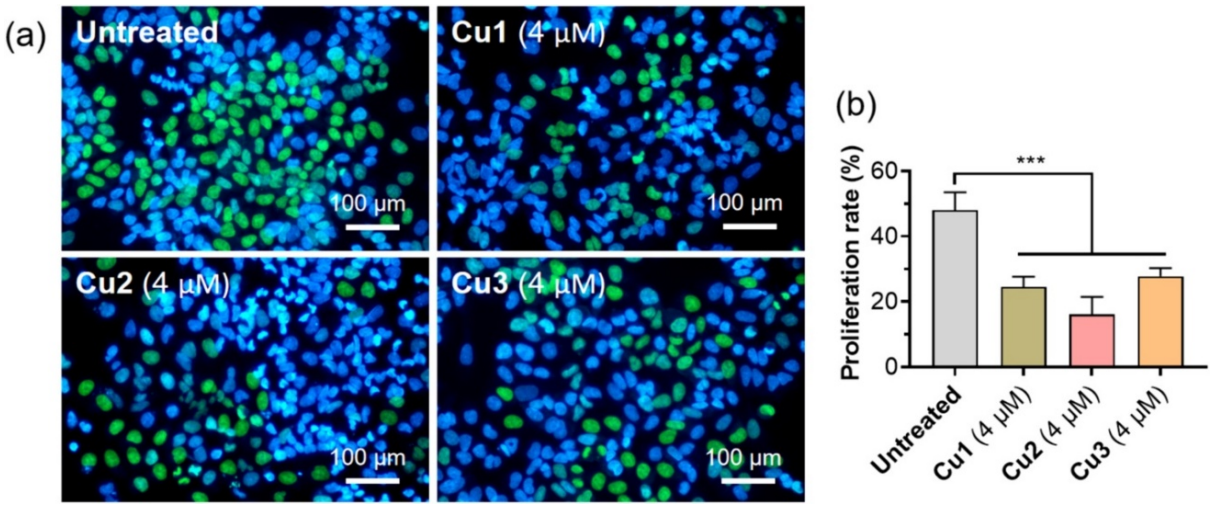

Figure 45. (**a**) Confocal micrographs of HCT-116 cells treated with complexes **242-244** (Cu1 = complex **242**, Cu2 = complex **243**, Cu3 = complex **244**) using the EdU incorporation assay. (**b**) Calculated proliferation ratios for the cells treated with complexes **242-244** (*** $p < 0.001$). Reproduced from Ref. [184] with permission from John Wiley & Sons, Copyright © 2024 Wiley-VCH GmbH.

Mariconda et al. utilized Ag(I)-NHC complexes to design multimodal anticancer agents [185]. Substitution of Ag(I)-iodide NHC complexes **245-248** with acetate yielded the complexes **249-252**, which could form the corresponding *bis*-carbene complexes, as described in Scheme 32. This equilibrium may have enhanced the biological activity of these complexes.

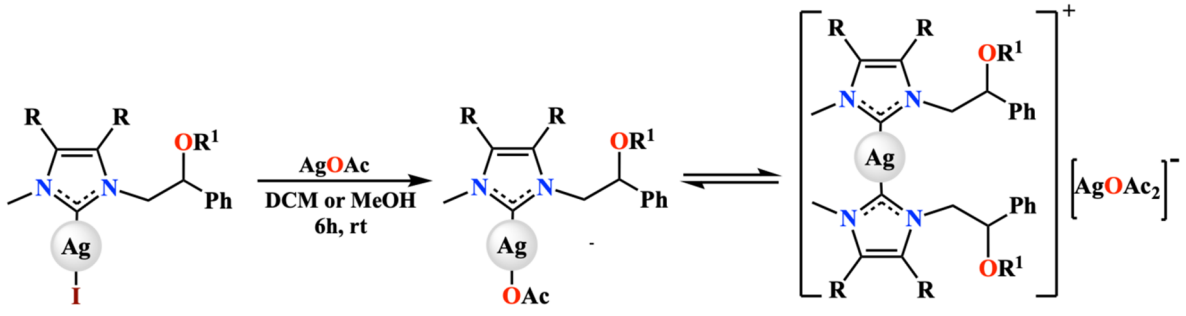

245 R = H R¹ = Na
246 R = H R¹ = CH3
247 R = H R¹ = H
248 R = Cl R¹ = H

249 R = H R¹ = Na
250 R = H R¹ = CH3
251 R = H R¹ = H
252 R = Cl R¹ = H

Scheme 32. Design of Ag(I)-NHC complexes **249-252**.

The in vitro cytotoxicity against MDA-MB-231 and MCF-7 breast cancer cell lines and healthy MCF-10A cells was compared with two reference drugs: cisplatin and the actin assembly inhibitor latrunculin A. Complexes **249-252** were less effective than latrunculin A, but all were more effective than cisplatin against either cancer cell

line, except for complex **251**, which was ineffective against MDA-MB-231 (IC_{50} > 100 μM). It is important to note that none of the complexes showed significant inhibition for the healthy cell lines with IC_{50} values >200 μM, while IC_{50} values of 81.3 μM and 0.045 μM were calculated for cisplatin and latrunculin A, respectively. The complexes all therefore exhibited excellent specificity for the cancer cell lines. Complexes **249** and **252** were selected for further study, as they exhibited the most inhibition against MDA-MB-231 and MCF-7 cell lines, with IC_{50} values of 7.0 μM for complex **249** against MDA-MB-231 cells and 13.2 μM for complex **252** against MCF-7 cells. The antiproliferative activity of these complexes was confirmed to be via apoptotic cell death pathways by detection of DNA fragmentation. An assay of polymerization of the monomer G-actin into filamentous F-actin showed that both complexes as well as latrunculin A and the actin polymerization inhibitor cytochalasin B could inhibit F-actin polymerization. However, latrunculin A and complex **252** could enhance depolymerization of F-actin, while complex **249** only inhibits the formation of new F-actin similar to cytochalasin B. Actin polymerization was observed via immunofluorescence of cancer cells using a primary anti-β-actin antibody which was visualized with a secondary antibody conjugated with the Alexa Fluor® 568 stain, as well as DAPI for nuclei, and observed with confocal microscopy. For MDA-MB-231 cells (Figure 46), the untreated cancer cells showed organized actin networks, while latrunculin A-treated cells became round and brightly stained due to aggregation of unpolymerized actin monomers. For the cells treated with complex **249**, the actin elongated and stretched as a result of aggregation of actin into thick bundles, and the inability of the complex to depolymerize existing F-actin. Conversely, MCF-7 treated with complex **252**, which showed the highest inhibitory activity against this cell line, exhibited similar rounding to latrunculin A, due to its ability to favour F-actin depolymerization. Furthermore, both complexes were found to inhibit topoisomerase enzymes I and II, although topoisomerase I only required a concentration of 1 μM of either complex **249** or **252**, while a 10 μM concentration of either complex was needed for topoisomerase II.

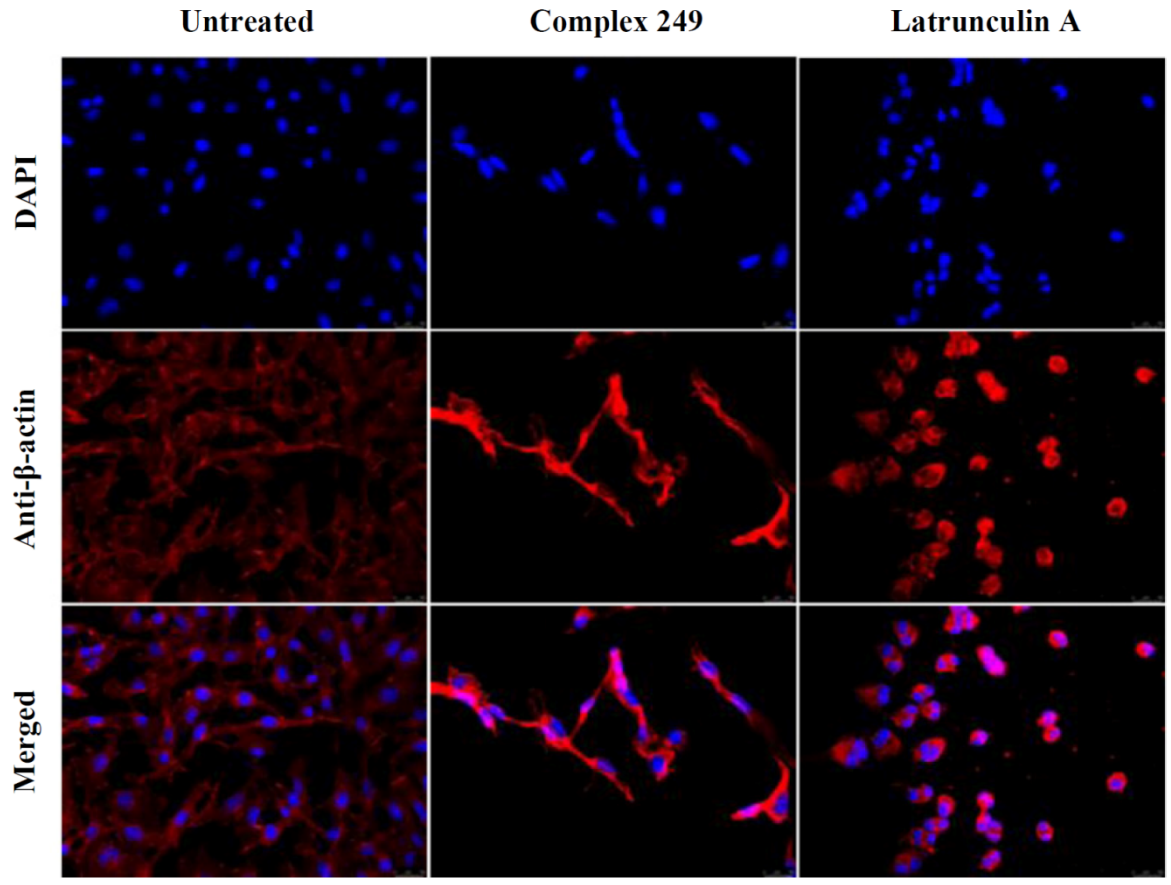

Figure 46. Immunofluorescence of MDA-MB-231 cells stained with DAPI (blue), anti-β-actin antibody (visualized with Alexa Fluor® 568 stain in red) and merged images for untreated cells as well as cells treated with complex **249** or latrunculin A. Reproduced from Ref. [185], https://doi.org/10.1002/cmdc.202200345, under the terms of the CC BY NC ND 4.0 license, http://creativecommons.org/licenses/by-nc-nd/4.0/.

A series of quinoline-functionalized benzimidazole salts was prepared by Zheng et al. to take advantage of the antitumour properties of quinoline compounds for Ag(I)-NHC complexes [186]. The addition of 2-

(chloromethyl)quinoline (**253**) to the benzimidazole derivatives (**254-256**) formed organic ligands with ethyl (**257**), benzyl (**258**), 2-picolyl (**259**) substituents, which were reacted with Ag_2O to give rise to the corresponding Ag(I)-NHC complexes **260-262**, as shown in Scheme 33.

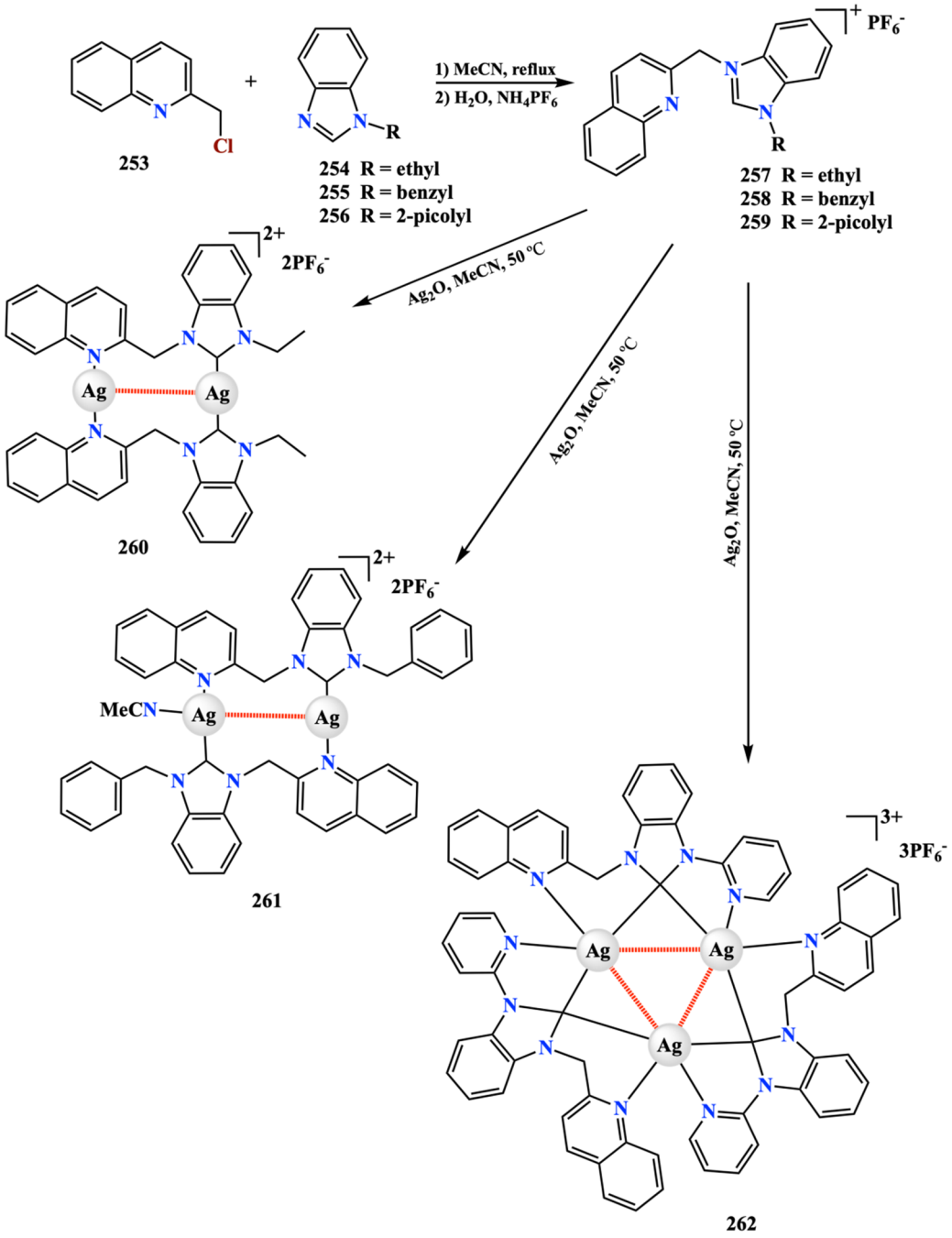

Scheme 33. Preparation of Ag(I)-NHC complexes **260-262**.

All three silver complexes **260-262** were more effective against A2780 cells than cisplatin, although greater cytotoxicity was also observed for healthy HUVEC cells. On the other hand, the complexes were also effective against cisplatin-resistant ES-2 and SKOV3 cells, while cisplatin showed no significant activity (>100 μM). The benzyl-substituted complex **261** showed the lowest IC_{50} values of 1.74 μM for A2780, 4.54 μM for ES-2, and 4.14 μM for SKOV3, as well as 6.42 μM for the non-cancerous HUVEC cells. Cisplatin exhibited an IC_{50} of 24.74 μM for A2780, with no detectable activity against the other three cell lines. It was also demonstrated using a DCFH-DA assay that complex **261** induced ROS production, in addition to depolarization of mitochondrial membrane, which was confirmed by TEM. The loss of cell membrane integrity was evaluated by AO/EB staining of A2780 cells treated with cisplatin or complex **261** (at 2 μM or 4 μM concentrations), as shown in Figure 47. Disruption of cell membrane integrity and cell death was indicated by the presence of orange-stained condensed chromatin for both concentrations of complex **261**. Additionally, the higher concentration of 4 μM resulted in even greater

disruption of the cell membrane. Meanwhile, 4 μM cisplatin showed little effect on the cell membrane. These findings, in addition to the effectiveness of the complexes against cisplatin-resistant cancer cells, indicated that the silver-NHC complexes may be able to target drug-resistant cancers through a potential alternative mechanism to conventional platinum-containing drugs.

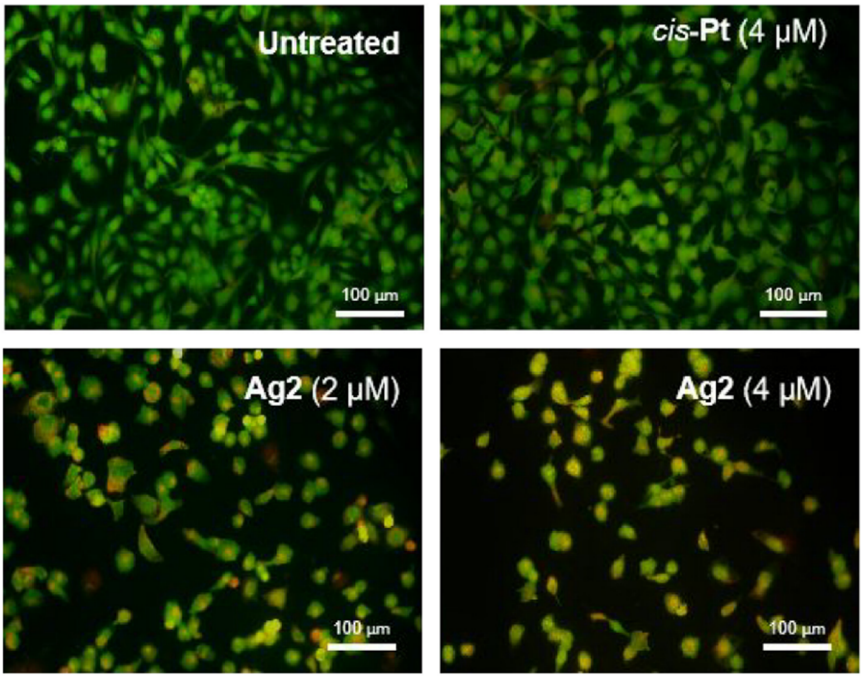

Figure 47. AO/EB staining of A2780 cells treated with 2 μM or 4 μM complex **261** or 4 μM cisplatin, as well as untreated cells (cis-Pt = cisplatin, Ag2 = complex **261**). Reproduced from Ref. [186] with permission from John Wiley & Sons, Copyright © 2021 Wiley-VCH GmbH.

Miglionico et al. prepared NHC complexes **268** and **269** with a Ag(I) moiety and complexes **270** and **271** with a Au(I) moiety for the induction of autophagy as an anticancer mechanism [187]. The compounds 1-(2-hydroxy-2-phenylethyl)-1H-imidazole (**263**) and 1-(2-hydroxy-2-phenylethyl)-1H-4,5-dichloroimidazole (**264**) were each reacted with 1,3-propanesulfone (**265**) to produce cationic complexes **266** and **267**, which were reacted with Ag_2O to give the *bis*-Ag(I)-NHC complexes **268** and **269**, as shown in Scheme 34. Chloro(dimethylsulfide) gold was utilized to substitute gold for the silver moiety, yielding the analogous *bis*-Au(I) complexes **270** and **271**.

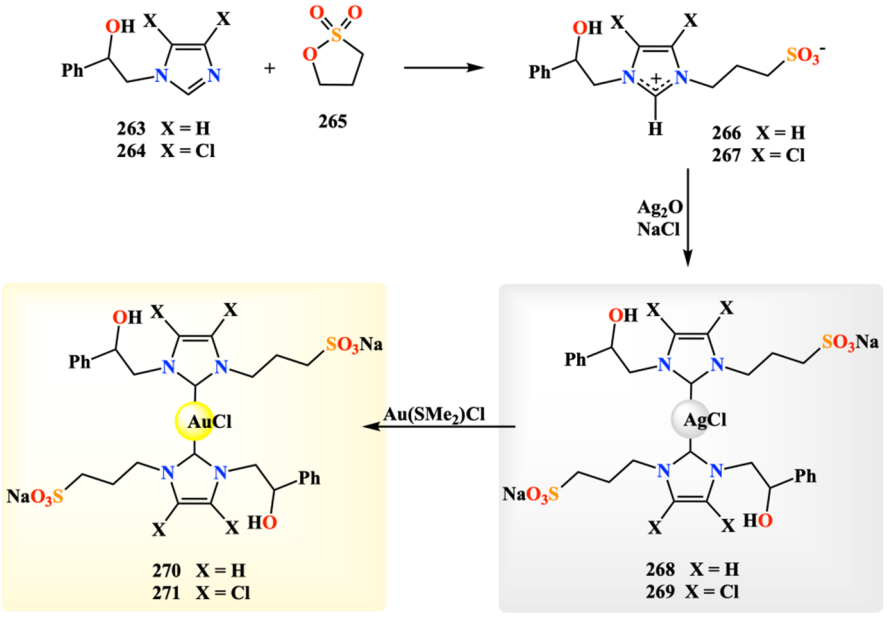

Scheme 34. Design of N-heterocyclic carbene complexes with silver (**268** and **269**) and gold (**270** and **271**).

The highest in vitro antiproliferative activity was found for the chloro-substituted Ag-containing complex **269** and Au-containing complex **271** against the hepatocarcinoma cell lines HepG2 and HuH7. Both complexes showed greater activity against HepG2, with IC_{50} values of **31.51** μM for complex **269** and 43.84 μM for complex **271**, in comparison with 52.14 μM for complex **269** and 63.60 μM for complex **271** against HuH7 cells. The specificity for cancer cells was determined by low cytotoxicity for the healthy liver cell line IHH (IC_{50} of 95.01 μM for complex **269** and >100 μM for complex **271**). ROS production was enhanced compared to the negative control, as shown in Figure 48, which demonstrated a significant increase above 30 μM of Ag complex **269**, as well as 40 μM or 50 μM of Au complex **271**. At concentrations of 40 μM complex **269** and **50** μM complex **269**, comparable ROS levels were measured to those induced by the positive control, 2000 μM (i.e., 2 mM) *tert*-butyl hydroperoxide (TBH). However, the cytotoxic activity of these complexes was determined to occur via an autophagic mechanism rather than an apoptotic one. The observed morphology exhibited a lack of chromatin condensation. Combined with the low levels of caspase-3 activation or cleavage of PARP-1, both of which are indicative of apoptosis, it was concluded that apoptosis was not induced by the complexes. Conversely, upregulation of two proteins that act as markers of autophagy, Beclin-1 and LC3-II, was observed. In addition, lower levels of phosphorylation of mTOR in the AKT/mTOR signaling pathway that suppresses autophagy further supported the presence of autophagy.

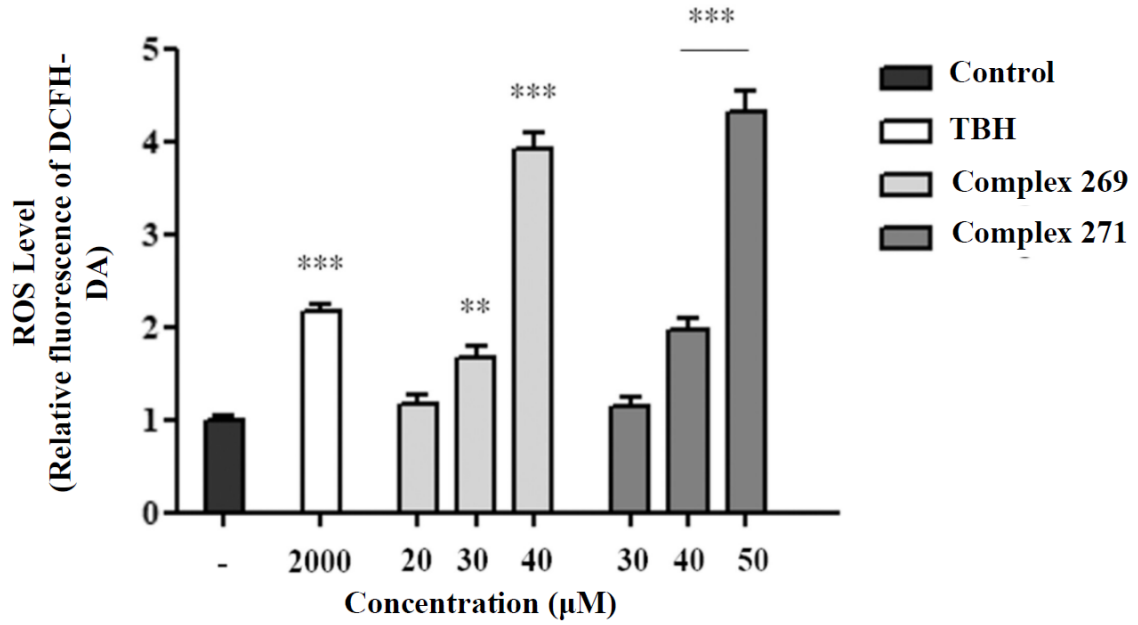

Figure 48. ROS production in HepG2 cells treated with complexes **269** and **271** or positive control TBH (** $p < 0.01$, *** $p < 0.001$). Adapted with permission from Ref. [187], https://doi.org/10.1111/cbdd.70283 (accessed on 22 April 2026), under the terms of the CC BY 4.0 license, https://creativecommons.org/licenses/by/4.0/.

A series of biphenyl-based organogold(III) complexes was prepared with the general structure [(C^C)Au(NHC-pyr)X], containing a bidentate 4,4′-ditertbutylbiphenyl ligand (C^C), a chloride or phenylacetylide group (X), and a pyridyl-substituted NHC (NHC-pyr) as illustrated for the most effective complex **272**, which contained a 4-CF_3-pyridyl ligand, is shown in Figure 49 [188]. Antineoplastic activity was tested against the triple-negative breast cancer cell line MDA-MB-231 in vitro and for an *in vivo* xenograft model, as well as a xenograft model of neuroblastoma using SKN-FI cells *in vivo*. The mechanism of action of complex **272** did not involve cell cycle arrest, but rather induction of apoptosis leading to cytotoxicity. When compared with cisplatin in vitro, complex **272** exhibited four times greater anticancer activity (IC_{50} = 5.4 μM for complex **272** and 20.4 μM for cisplatin), as well as lower cytotoxicity against healthy cell lines (IC_{50} = 14.8 μM for complex **272** and 2.9 μM for cisplatin). *In vivo*, the MDA-MB-231 tumours showed lower growth, as well as higher levels of necrosis, and the activity against the neuroblastoma model was comparable to standard chemotherapy consisting of a combined therapy of the alkylating agent temozolomide and the topoisomerase I inhibitor irinotecan. Additionally, the complex was found to be localized to the cytoplasm but was not eliminated from the cell, either through passive diffusion or by efflux pump proteins. The authors concluded that the organogold complexes, especially complex **272**, were promising antineoplastic agents that could be used as alternative or complementary chemotherapy treatments.

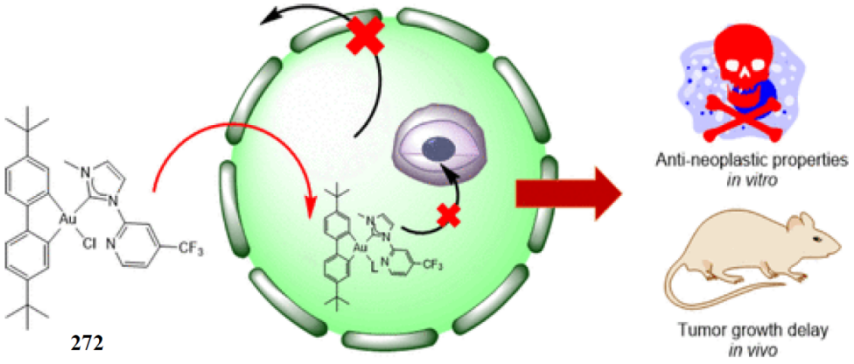

Figure 49. Summary of structure and antineoplastic activity of organogold complex **272**. Adapted with permission from Ref. [188], Copyright © 2025, American Chemical Society.

Lacoma et al. designed a series of hemilabile biphenyl Au(III)-NHC complexes that could dissociate from a fully coordinated neutral form, which could exhibit structural toxicity via stacking with biological molecules, to a cationic form that could instead react directly with other targets, theoretically allowing for multimodal activity [189]. One of the most toxic complexes produced was complex **275**, which was synthesized from the reaction of [(*t*-Bu$_2$biPh)AuCl]$_2$ (**273**) and N-(2-methylpyridiyl)-pyridoimidazolium bromide (**274**), and could be converted into the cationic complex **276**, as illustrated in Scheme 35. The observed IC$_{50}$ values for complex **276** after 72 hours were 1.8 μM against HeLa (ovarian cancer), 1.4 μM against HuH7 (hepatocarcinoma) and 2.0 μM against MDA-MB-231 (breast cancer) cell lines. Unfortunately, comparably effective cytotoxicity (IC$_{50}$ =1.6 μM) was observed against healthy MCF-10A cells, indicating a lack of specificity for cancer cell lines that would need to be improved with further modifications. Interestingly, similar antiproliferative activity was observed for the neutral complex **275**. Additionally, ^{1}H NMR experiments showed that the presence of chloride ions in cell culture media resulted in conversion of cationic complex **276** to the neutral complex **275**. The anticancer effects therefore resulted from the neutral complex **275**, regardless of whether the cells were treated with the neutral complex **275** or the cationic complex **276**.

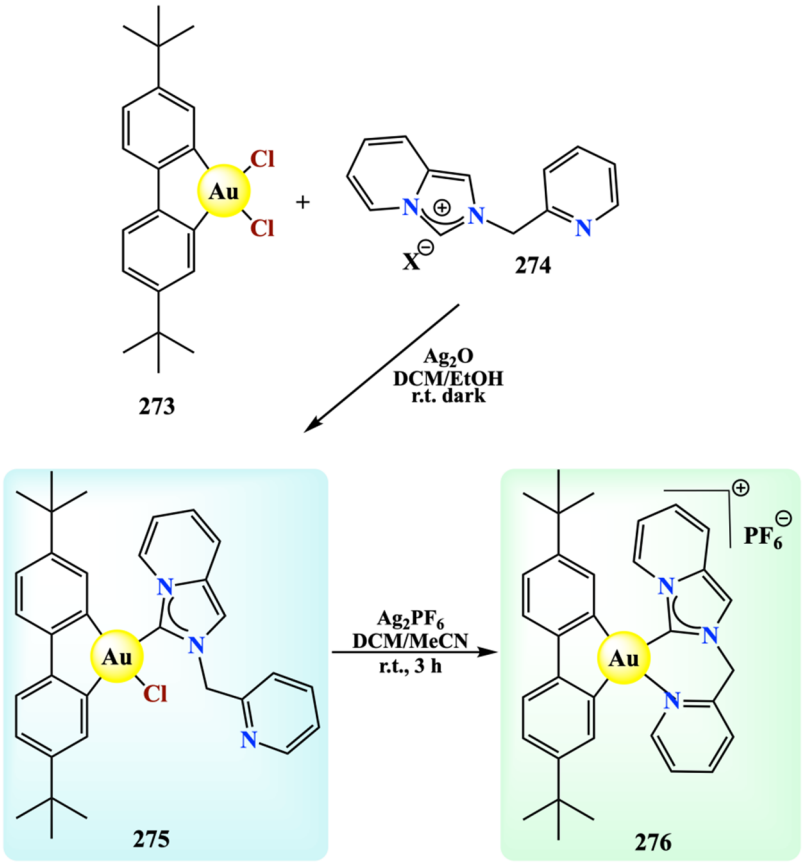

Scheme 35. Preparation of hemilabile Au complex **275** and its cationic analogue **276**.

The morphological changes associated with apoptosis, including membrane blebbing and cell adhesion, as well as activation of the caspase pathway through caspase-3 and caspase-7, were analyzed through fluorescence microscopy using a caspase 3/7 fluorogenic substrate. For HeLa cells incubated with complex **276** at its IC_{50}, the proportion of cells that displayed adhesion over time decreased, while those that exhibited membrane blebbing and caspase pathway activation increased (Figure 50A). These effects were faster than similar cells treated with the mitochondrial uncoupling agent carbonyl cyanide *m*-chlorophenyl hydrazone (CCCP) at its IC_{50} (Figure 50B). An example of the morphological changes in HeLa cells is shown in Figure 50D. Furthermore, depolarization of the mitochondrial membrane was also evaluated, and after 4 hours of incubation with complex **276** or CCCP, comparable depolarization was observed for both groups relative to the negative control. Remarkably, the proportion of non-apoptotic cells over time, shown in Figure 50C, approached ~50% after 48 hours for both treatments, although the decrease occurred with faster kinetics for complex **276**, suggesting an alternative mechanism to that of CCCP.

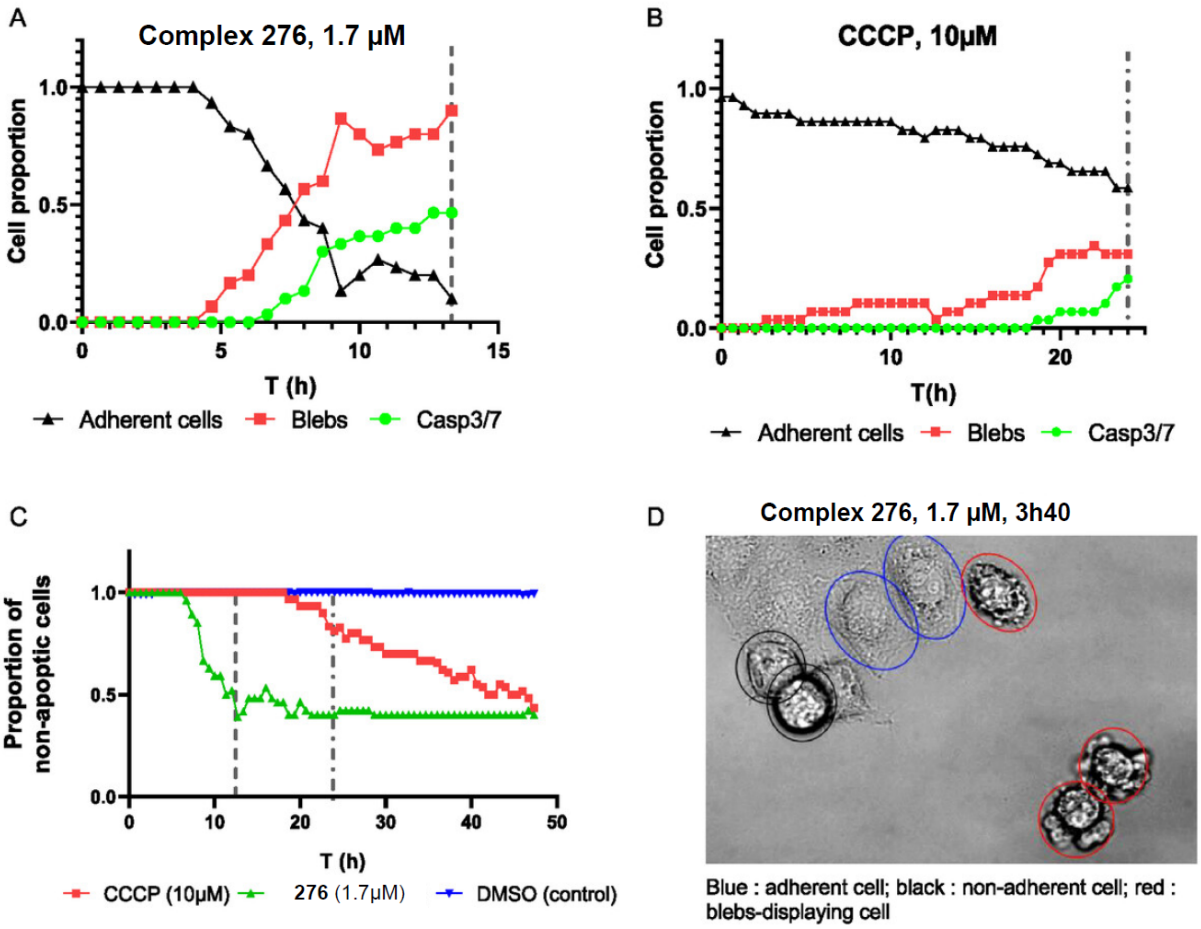

Figure 50. Morphological changes and adhesion of HeLa cells treated with (**A**) complex **276** or (**B**) CCCP. (**C**) Non-apoptotic cell proportion under each treatment (including DMSO as negative control). (**D**) Example of observable changes to morphology and adhesion for HeLa cells treated with complex **276** after 3 hours and 40 minutes of incubation. Adapted with permission from Ref. [189], https://doi.org/10.1002/cmdc.202500302, under the terms of the CC BY 4.0 license, https://creativecommons.org/licenses/by/4.0/.

Another type of organogold complexes containing NHC moieties was proposed by Steinbrueck et al. who designed gold(I)-NHC complexes containing 1,4-dihydroxyanthraquinone (quinizarin) moieties and examined them for their antiproliferative activities [190]. 2-(bromomethyl)-1,4-dimethoxyanthracene-9,10-dione (**277**) was reacted with N-methylimidazole to produce the imidazolium compound **278**, which was further reacted with either 1 eq. $AuCl(Me_2S)$ to yield the neutral gold complexes with methoxy (**279**) or 0.5 eq $AuCl(Me_2S)$ to yield the cationic *bis*-complexes with methoxy (**281**) as shown in Scheme 36. Complexes **279** and **281** were then converted to the corresponding complexes with hydroxyl substituents **280** and **282** via reaction with boron trichloride.

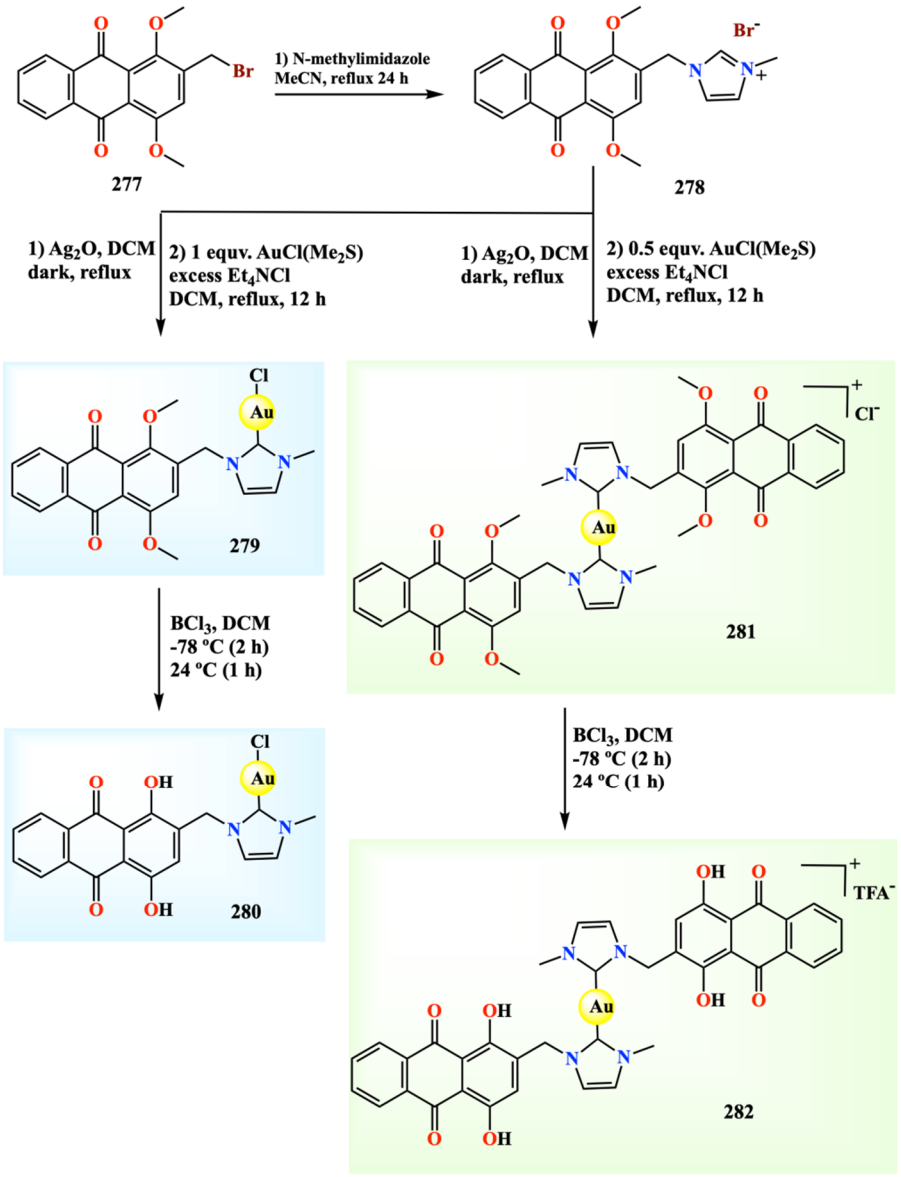

Scheme 36. Preparation of quinizarin-containing Au(I)-NHC complexes **279-282**.

Cytotoxicity against HeLa cells was demonstrated to be greater for the hydroxyl-substituted *mono*-complex **280** (IC_{50} = 5.3 μM) and the *bis*-complex **282** (IC_{50} = 2.4 μM) than the corresponding methoxy-substituted complexes **279** (IC_{50} = 26.4 μM) and **281** (IC_{50} = 23.9 μM), although they were still slightly less effective than the reference compound doxorubicin (IC_{50} = 1.1 μM). Additionally, complex **280** was shown to enhance sensitivity to anthracycline-type topoisomerase inhibitors such as doxorubicin. This effect was believed to be related to mitochondrial metabolism, as complex **282** was not localized to mitochondria, despite the positive charge that generally favours mitochondrial localization. The synergistic effect of sensitization was examined for the Nalm-6 leukemia cell line and the resistant Nalm-6 Daures cell line. As illustrated in Figure 51, doxorubicin increased the apoptotic cell fraction of Nalm-6 cells, unlike complex **280**. However, the synergistic activity of both increased apoptosis, with superior activity compared to either component individually at both 0.02 μM and 0.04 μM concentrations of doxorubicin with 0.5 μM of complex **280**. As expected, Nalm-6 Daures cells are resistant to doxorubicin, so minimal effects were observed for either concentration of doxorubicin alone, while 1.0 μM of complex **280** only achieved 15.3% apoptotic cells. On the other hand, the combinations showed even more significant synergy, 1.0 μM of complex **280** increasing the percentage of apoptotic cells by a further 36.9% in combination with 0.02 μM doxorubicin and 42.5% with 0.04 μM doxorubicin, relative to the additive effect of either component. Complex **280** was therefore concluded to increase sensitivity of the cancer cells to doxorubicin or other anthracycline-type topoisomerase inhibitors, likely due to altering the mitochondrial activity. Not only is this a potential avenue for combination therapy, but it also demonstrates that the cytotoxicity alone may not fully describe the activity of these organogold complexes.

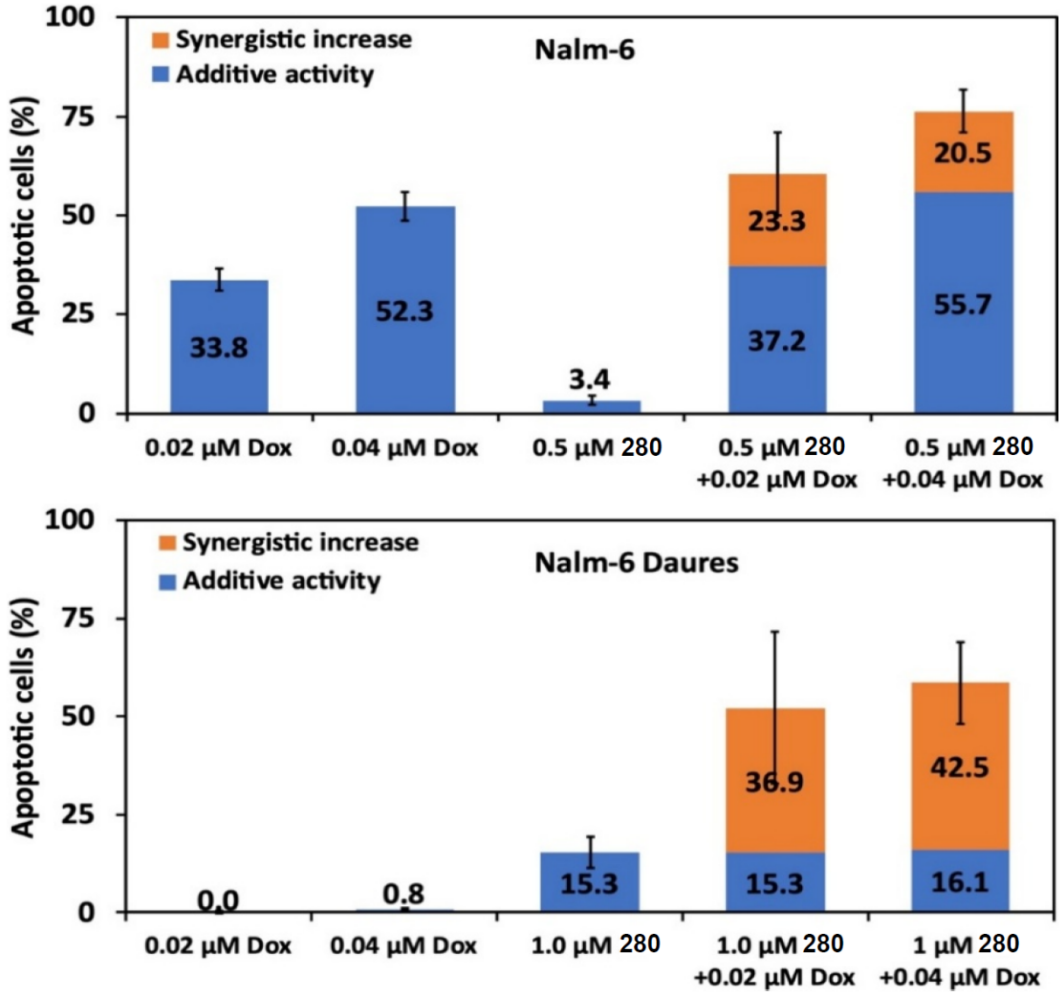

Figure 51. Percentage of apoptotic Nalm-6 and Nalm-6 Daures cells treated with various combinations of doxorubicin (Dox) and complex **280**. Reproduced from Ref. [190], https://doi.org/10.1002/chem.202404147, under the terms of the CC BY NC ND 4.0 license, http://creativecommons.org/licenses/by-nc-nd/4.0/.

Tabrizi et al. prepared several gold(I)-NHC complexes **284-286** with triphenylphosphine and ibuprofen moieties, as shown in Figure 52, as antiproliferative agents [191]. The in vitro antiproliferative activities of these complexes, the analogous organic compound **283** and reference drugs cisplatin and auranofin, an organogold complex drug, were evaluated against the MCF-7, MDA-MB-231 and HT-29 cancer cell lines, as well as healthy MCF-10A breast epithelial cells. Complexes **284** and **285** exhibited cytotoxicity with IC_{50} values in the micromolar range for all three cancer cell lines, comparable with cisplatin and auranofin. Against the MCF-10A cell line, however, complexes **284** and **285** displayed higher selectivity with IC_{50} values of 67.65 µM and 89.25 µM, unlike the IC_{50} values of 35.42 µM for cisplatin or 47.25 µM for auranofin. The mechanism of the anticancer activity involved induction of ROS as well as inhibition of thioredoxin reductases, which are known targets of anticancer organogold complexes, and the glutathione reductase enzyme, which has high structural homology with thioredoxin reductases. The ROS generation induced by complexes **284** and **285** was determined using a DCFH-DA assay in HT-29 cells, with the fluorescence levels normalized to the negative control (treatment with PBS), and both were significantly higher than the negative control or the reference drug antimycin (Figure 52). Complex **285** resulted in the greatest increase in ROS production, with an increase 8.3 times greater than the negative control. Furthermore, complexes **284** and **285** were more effective at inhibiting the cytosolic and mitochondria-localized forms of thioredoxin reductase, TrxR1 and TrxR2, respectively, compared to auranofin. Conversely, auranofin showed greater inhibition against glutathione reductase than either complex **284** or **285**. These findings suggested that the mechanism of action for these complexes involved both induction of oxidative stress with ROS in addition to inhibition of thioredoxin reductase activity.

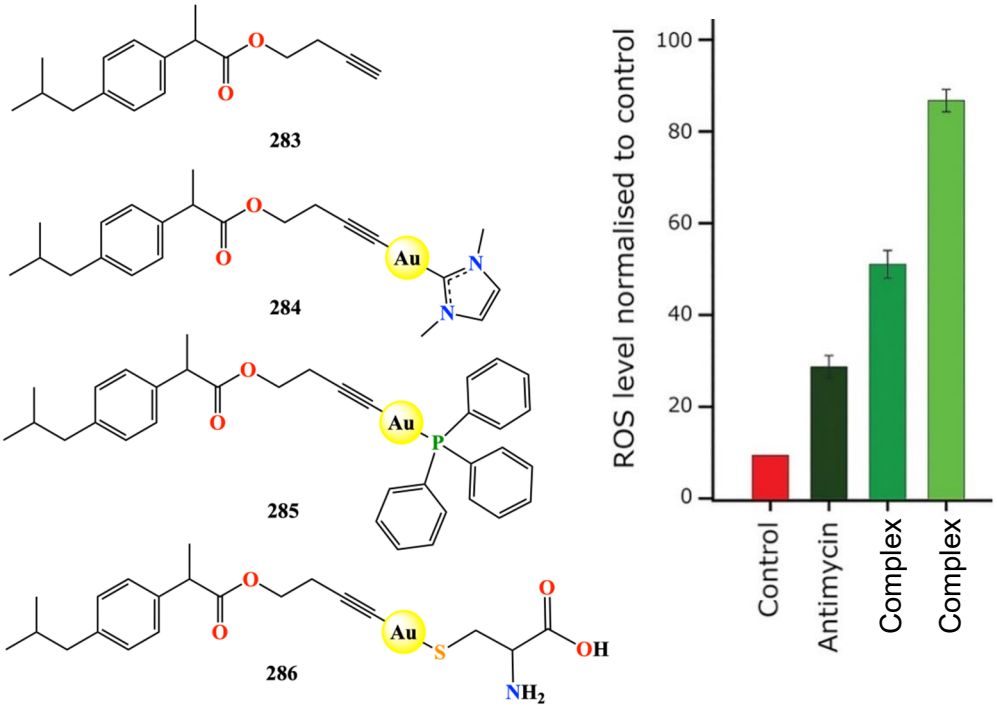

Figure 52. (**Left**) Structures of organic compound **283** and complexes **284-286**. (**Right**) Induction of ROS by complexes **284** and **285**, as well as auranofin, relative to negative control (PBS). Reproduced from Ref. [191] with permission from John Wiley & Sons, Copyright © 2020, Wiley-VCH Verlag GmbH & Co. KgaA, Weinheim.

3.7. Heterometallic Complexes

3.7.1. Iron and Palladium

In addition to single metal centers, the complementary properties and synergistic antiproliferative effects of multiple metals in heterobimetallic structures resulted in better cancer cell selectivity and lower cytotoxicity against healthy human cells [32,192,193]. As an example of a organometallic structure with multiple different metal centers for anticancer activity, Bortolamiol et al. incorporated a ferrocene moiety into the organopalladium complex precursors **287-289** by displacement of the labile 2,2,4-trimethyl-1,2-dihydroquinoline (TMQ) ligand by the ferrocenyl diphosphine ligand (dppf) to form the Fe(II)/Pd(II) complexes **290-292**, as illustrated in Scheme 37 [194].

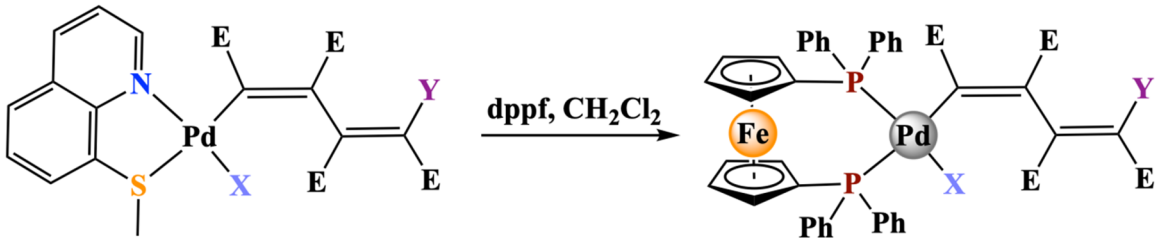

Scheme 37. Preparation of Fe(II)/Pd(II) complexes **290-292**.

The in vitro anticancer activity of the complexes was assayed for the OVSHAO, SKOV-3, OVCAR-5, KURAMOCHI and MDA-MB 231 cancer cell lines, as well as MRC-5 fibroblasts, and compared with cisplatin (Table 3). Complexes **290-292** exhibited specificity for the cancer cell lines, as well as superior biocompatibility with non-cancer MRC-5 cells than cisplatin, with almost negligible cytotoxicity displayed by complex **290**. Cisplatin showed greater inhibition against all cancer cell lines, with the exception of MDA-MB-231, with IC_{50} values of 36.3 μM for cisplatin, 7.1 μM for **290**, 9.3 μM for **291** and 8.1 μM for **292**. The triple negative breast cancer cell line MDA-MB-231 is challenging to treat with existing anticancer agents, which indicates that these complexes, especially complex **290**, may have potential for targeting drug-resistant cancer cell lines.

Table 3. IC_{50} values (in μM) of heterobimetallic Fe(II)/Pd(II) complexes **290-292** and cisplatin against cancer (OVSHAO, SKOV-3, OVCAR-5, KURAMOCHI, MDA-MB 231) and non-cancer (MRC-5) cell lines.

Compound	Cisplatin	290	291	292
OVSHAO	0.6 ± 0.1	1.2 ± 0.1	2.0 ± 0.3	2.9 ± 0.5
SKOV-3	3.1 ± 0.2	31 ± 3	16 ± 3	12 ± 3
OVCAR-5	0.44 ± 0.09	5 ± 1	4.5 ± 0.3	5.3 ± 0.4
KURAMOCHI	1.25 ± 0.08	4.0 ± 0.5	2.1 ± 0.1	2.6 ± 0.2
MDA-MB-231	36.3 ± 0.8	7.1 ± 1.5	9.3 ± 0.4	8 ± 1
MRC-5	1.52 ± 0.08	>100	20 ± 9	31 ± 5

3.7.2. Titanium and Gold

Another example of a heterometallic design was proposed by Contel and coworkers for heterobimetallic titanium–gold complexes to inhibit renal cancer cell proliferation [195]. These complexes took advantage of the individual anticancer activities of titanocene dichloride and gold(I)-triphenylphosphine moieties. The Ti- and Au-containing moieties were connected by a strongly bound carboxylate ligand, in order to prevent release of the gold-TPP moieties after hydrolysis of the Ti-Cp bond at physiological pH. Two of the most effective candidate complexes were complex **293**, containing two Au-TPP-Cl ligands, and complex **294**, where the Au-TPP was connected to the carboxylate ligand via a thiolate group (Figure 53).

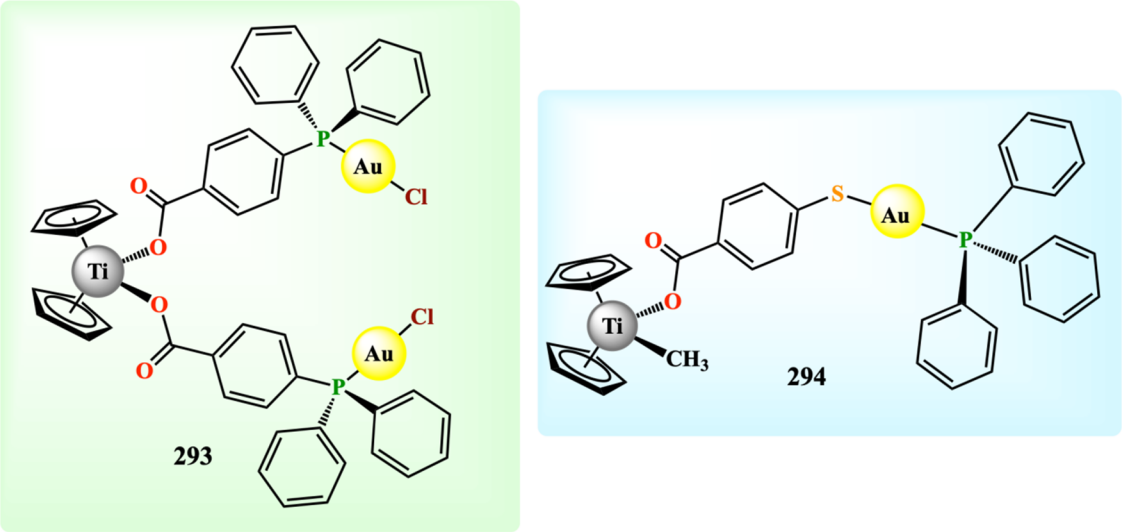

Figure 53. Structures of heterobimetallic titanium-gold complexes **293** and **294**.

Cytotoxicity against Caki-1 renal cancer cells showed that complex **294** had low specificity against cancer as opposed to healthy HEK-293T cells. This specificity was inferior compared to titanocene Y, which only showed activity against the cancer cell line, but superior to cisplatin, which was more toxic to the non-cancer cells than it was to Caki-1. In addition, complex **294** showed the most inhibition against Caki-1 compared to either reference drug, with an IC_{50} of 0.12 μM compared to 29.00 μM for cisplatin or 29.42 μM for titanocene Y (Figure 54). The *in vivo* activity of complexes **293** and **294** in mice bearing Caki-1 tumours was evaluated, and a small but significant decrease was observed in the average tumour volume from the average volume in the control group 397.07 mm^3 to 311.11 mm^3 in the group given complex **293**. Complex **294**, meanwhile, reduced the tumour volume to 41.33 mm^3, indicating its potent antitumour efficacy. Thioredoxin reductase inhibition was also analyzed to demonstrate that the heterobimetallic complexes maintained the anticancer mechanism of gold(I) complexes. The activity of thioredoxin reductases in Caki-1 cells treated with complex **294** showed comparable inhibition to the reference auranofin, while complex **293** was not as effective as auranofin, but still displayed a significant decrease in activity relative to the negative control (DMSO). These findings were consistent with the higher cytotoxicity of complex **294**.

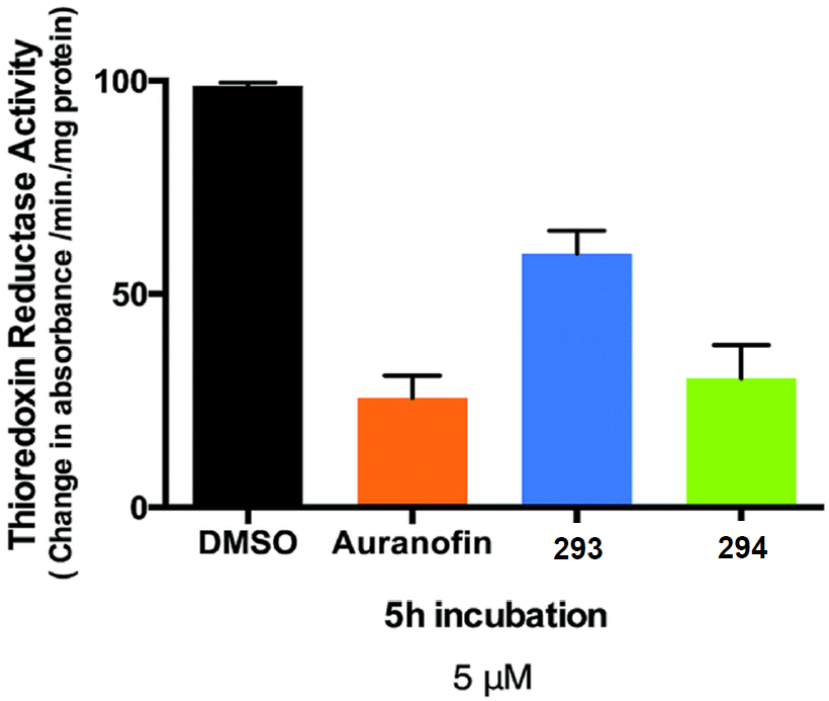

Figure 54. Percentage of inhibition of thioredoxin reductase enzyme activity by complexes **293** and **294**. Adapted from Ref. [195], https://doi.org/10.1039/C5SC01753J, under the terms of the CC BY NC 3.0 license, http://creativecommons.org/licenses/by-nc/3.0/.

3.7.3. Gold and Palladium or Platinum

The research team of Hashmi and Scattolin synthesised a series of heterobimetallic Au/Pd and Au/Pt organometallic complexes and examined their anticancer activities [196]. A one-pot synthetic strategy was reported for the design of Au(I)/Pt(II) complexes **301** and **302** as well as Au(I)/Pd(II) complex **303** [197]. Reaction of the Au(I)-carbene complexes 295-297 with Pt(II) complex **298**, Pt(II) complex **299** or Pd(II) complex **300** yielded the heterobimetallic complexes **301-303**, as illustrated in Scheme 38.

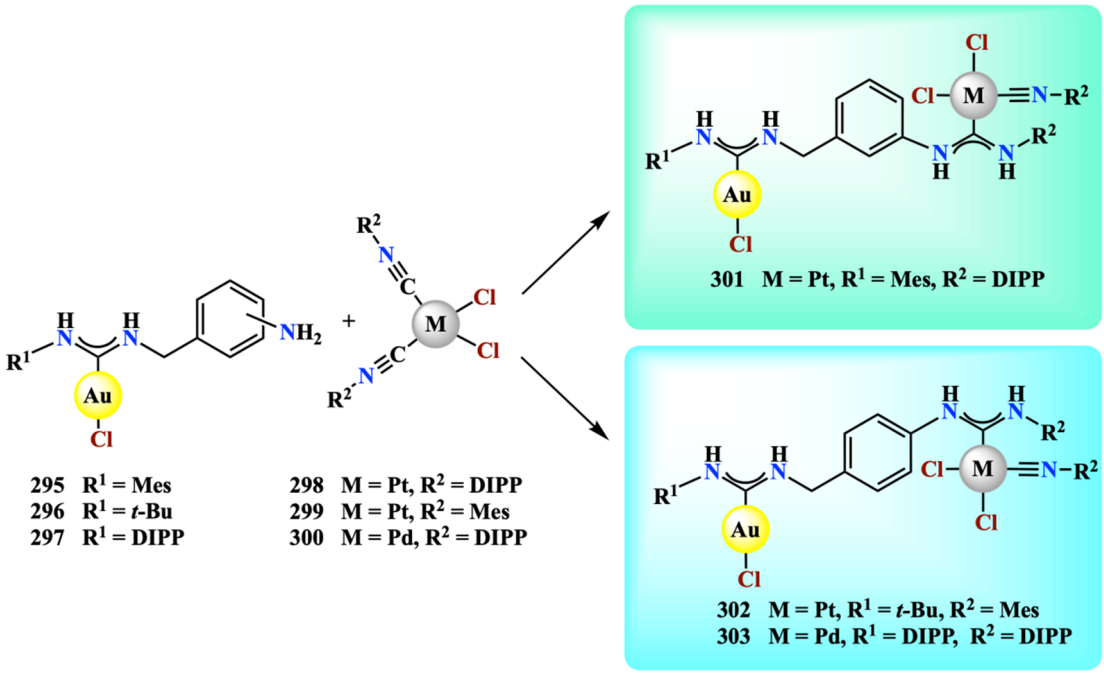

Scheme 38. Synthetic methodology for the production of heterobimetallic Au(I)/Pt(II) complexes **301** and **302** and Au(I)/Pd(II) complex **303**.

Two of the complexes showed specific activity against one specific cancer cell line in vitro with improved activity compared to cisplatin: complex **301** against MDA-MB-231 breast cancer cells with an IC_{50} of 0.05 μM, compared to 15 μM for cisplatin, and complex **302** against A549 lung cancer cells with an IC_{50} of 0.36 μM, compared to 11 μM for cisplatin. IC_{50} values of 0.5 μM for complex **302** and 0.3 μM for complex **303** were observed for the colorectal HCT116 cell line. Unlike cisplatin, however, no activity was observed for any of the complexes against A2780 lung cancer and OVCAR-3 ovarian cancer. On the other hand, cisplatin showed cytotoxicity against healthy MRC-5 fibroblasts (IC_{50} = 2 μM), which none of the heterobimetallic complexes exhibited (IC_{50} >100 μM), demonstrating higher specificity of the heterobimetallic complexes for cancer cells.

Organometallic complexes, polymers and dendrimers have demonstrated their value as antiproliferative agents across a wide range of cancers, including colon, breast, liver, lung and ovarian cancer. These molecules and macromolecules have also shown a wide variety of mechanisms, including interactions with proteins such as thioredoxin reductase, production of ROS and induction of cell death pathways such as autophagy and apoptosis. Interestingly, organometallic structures can utilize metal-specific modes of anticancer activity such as ferroptosis, allowing them to overcome existing drug resistance. However, the specific molecular targets responsible for the antiproliferative activity remain unknown in many cases, which will require further study for deeper understanding and optimization of the molecular mechanisms of action. In addition to non-infectious diseases like cancer, organometallic complexes and macromolecules have also displayed efficacy against infectious disease. To that end, the next section will discuss their application in therapeutic antimicrobial agents.

4. Development of Antimicrobial Pharmaceutical Treatments

Since the discovery of penicillin by Alexander Fleming in 1928, antimicrobial agents have been critical for treatment of infectious diseases as well as wound healing [198]. Unfortunately, the overuse of antimicrobials has resulted in the evolution of AMR, which continues to be a global challenge [199]. Furthermore, the development of AMR for one agent means that any compounds based on the same structure may be more likely to also be resisted [200]. In addition, the appearance of multidrug-resistant (MDR) strains that resist several different classes of antibiotics, such as methicillin-resistant *Staphylococcus aureus* (MRSA), have made treatment more costly and difficult [201]. New antimicrobial agents or approaches with mechanisms designed to overcome AMR are therefore needed including the use of nanomaterials, immunomodulation, or combination therapies [202,203]. Metals such as silver, gold, and platinum have historically been used as treatments against bacterial and fungal infections [204–208]. However, several limitations remain for metal-based antimicrobial agents compared to conventional organic compounds, including lack of specificity for the microbial cells over host cells, metal-resistant mechanisms in the target microbes, and the environmental health impacts of metals, especially heavy metals [209]. The tunable and biocompatible characteristics of organometallic compounds are therefore of great value for improving the activity and safety of metal-based antimicrobial agents. Organometallic polymers and dendrimers may provide an alternative approach by enhancing drug delivery and local concentration of conventional antimicrobial agents, which may also act synergistically with the action of the metal moieties [31,210,211]. This section will examine some examples of antimicrobial organometallic complexes and macromolecules with different metallic moieties.

4.1. Titanium Complexes

In 2025, Casali et al. reviewed the diverse applications of functionalized titanocenes in various fields including medicinal chemistry [212]. One of the earliest examples of organometallic titanium complexes with antimicrobial activity was reported in the 1990s, where titanocene complexes conjugated with phenylalanine and 4-fluorophenylalanine inhibited the growth of Gram-negative *Escherichia coli* [213]. More recently, Srivastava et al. reported the synthesis of titanocene-based complexes and their antimicrobial activities [214]. Reaction of bis(cyclopentadienyl)titanium chloride with 4-amino-5-(nicotinic/picolinic/isonicotinic/indole-3-propyl/indole-3-ethyl)-3-mercapto-1,2,4-triazole allowed for the isolation of five new functionalized titanocenes, [η^5-$C_5H_5)_2$TiClL(1-5)], as illustrated in Scheme 39.

The antibacterial activity was determined by measuring the minimum inhibitory concentration (MIC) values for **309**-**313** and reference drug ciprofloxacin against two Gram-positive bacteria (*S. aureus* and *Bacillus subtilis*) and two Gram-negative strains (*Pseudomonas aeruginosa* and *Salmonella typhi*), as shown in Figure 55. The lowest MICs against these bacteria, as well as three species of fungi (*Aspergillus niger, A. flavus, Colletotrichum falcatum*), were observed for complexes **312** and **313** with indole substituents. The indole rings distributed the positive charge from the metallic moiety over a larger area, as well as increased delocalization of π-bonding, both

of which would enhance lipophilicity. The complexes were also generally more active against the tested Gram-positive strains than the Gram-negative bacteria.

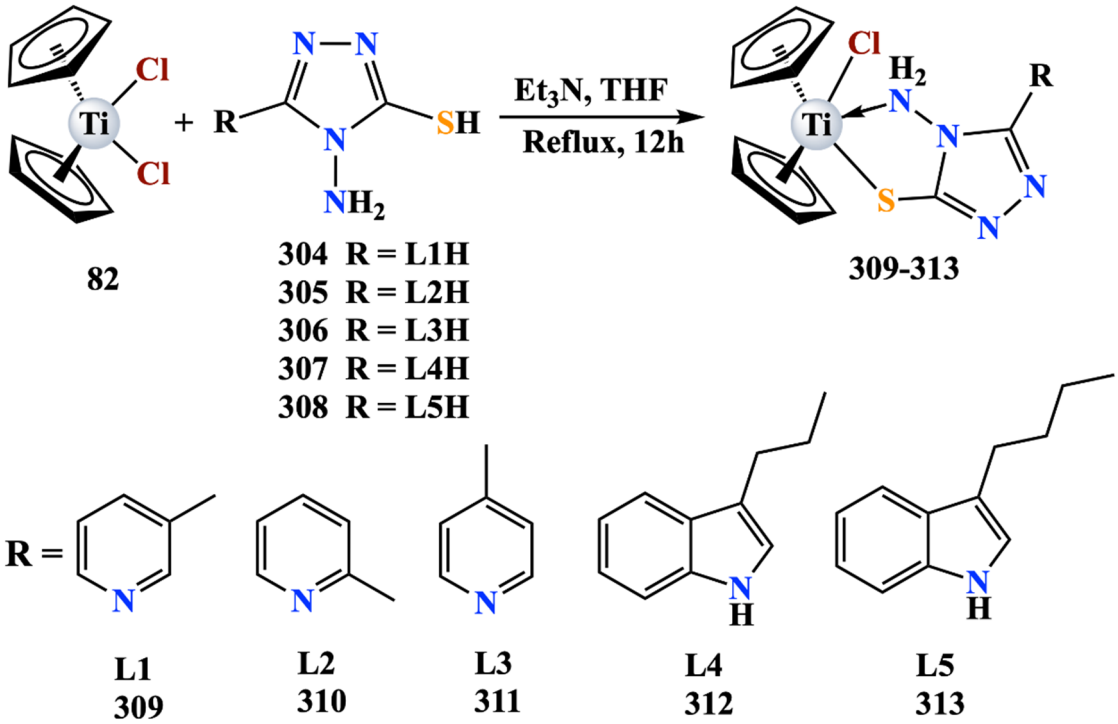

Scheme 39. Synthesis of functionalized titanocene complexes **309-313**.

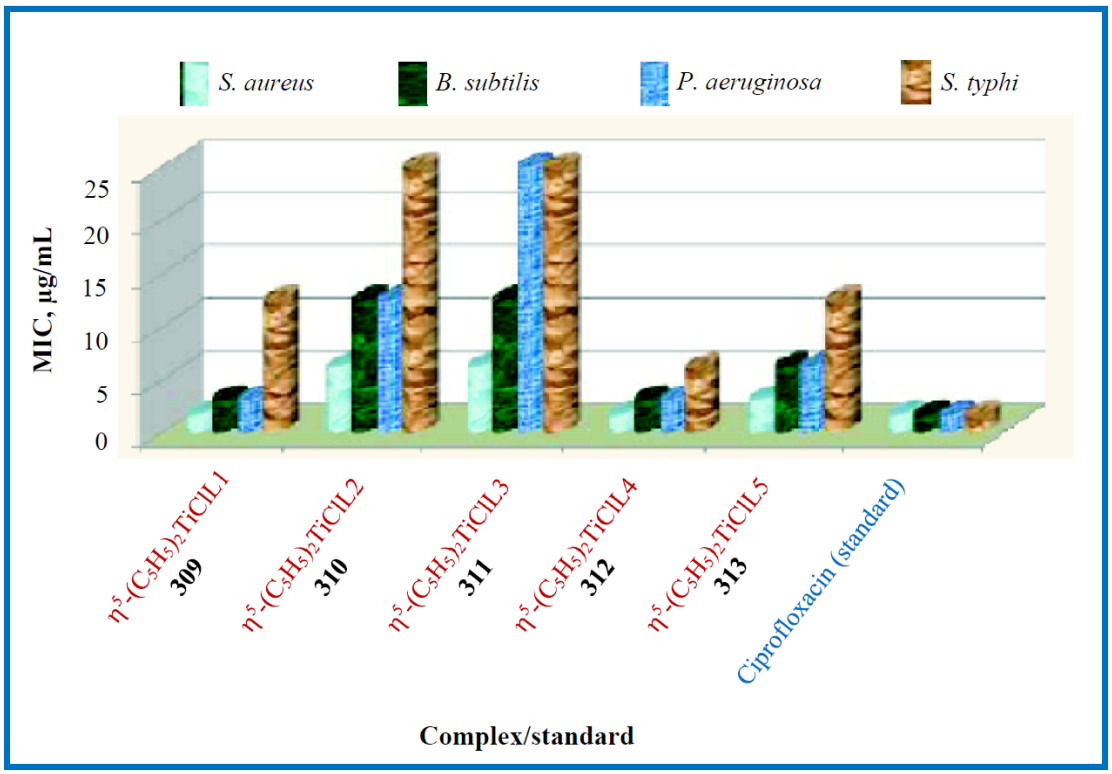

Figure 55. Antibacterial activity for titanocene complexes **309-313** and ciprofloxacin against two Gram-positive (*S. aureus* and *B. subtilis*) and two Gram-negative strains (*P. aeruginosa* and *S. typhi)*. Reproduced from Ref. [214], https://doi.org/10.5281/zenodo.5656098, under the terms of the CC BY 4.0 license, https://creativecommons.org/licenses/by/4.0/.

4.2. Manganese Complexes

Manganese (I) tricarbonyl complexes have been demonstrated to exhibit antimicrobial activity that could be modified by various N^N ligands and axial ligands [215]. As an example, Friães et al. prepared Mn(I) complexes **316**, **319**, and **320** containing three carbonyl ligands, the antimicrobial agent clotrimazole and different N^N ligands [216]. As outlined in Scheme 40, $MnBr(CO)_5$ **(92)** was reacted with one of the triazole ligands **L1**, **L2** or **L3** to yield complexes **315**, **317** or **318**, followed by substitution of the bromo ligand with clotrimazole to produce complexes **316**, **319** or **320**, respectively.

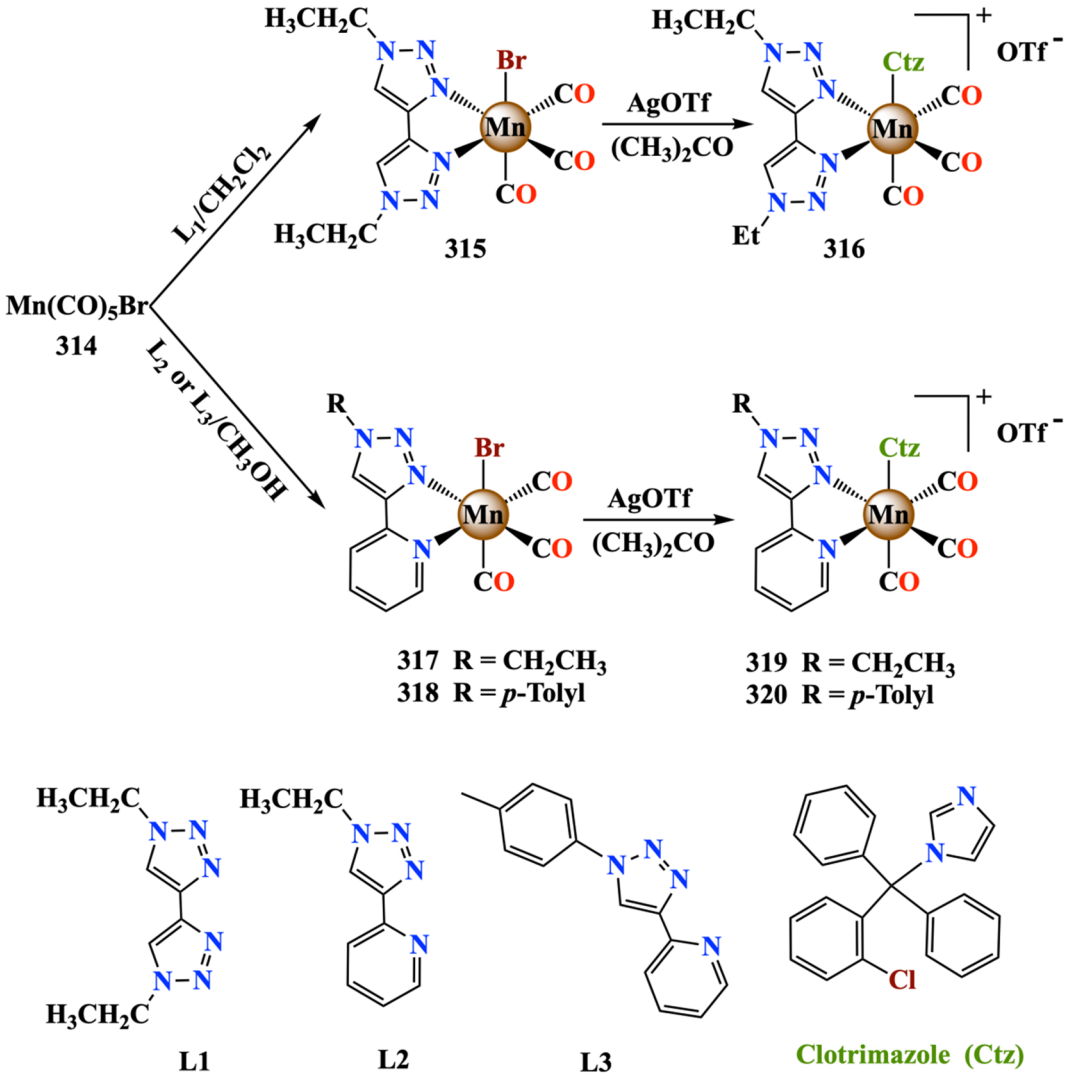

Scheme 40. Preparation of tricarbonyl Mn(I) complexes **316**, **319**, and **320**.

The complexes were evaluated for their antibacterial activity and showed the most activity against *S. aureus* and *Acinetobacter baumannii*, followed by *P. aeruginosa*, *Salmonella* Typhimurium, and finally *Klebsiella pneumoniae*. The MIC values calculated for the three strains that showed the highest activity for *S. aureus* and *A. baumannii* were 1.89 μM for complex **316**, 1.93 μM for complex **319** and 1.79 μM for complex **320**, while MICs for *E. coli* were 15.15 μM for complex **316**, 15.48 μM for complex **319** and 7.19 μM for complex **320**. The example growth curves for bacteria treated with complex **316** in Figure 56 demonstrate the effectiveness of the complex at the MIC and minimum bactericidal concentration (MBC). On the other hand, analysis of the cytotoxicity against the human THP-1 monocyte cell line showed that **316** and **319** exhibited good biocompatibilities, while the strongest antimicrobial complex **320** was highly toxic. Although all three complexes displayed less activity than the reference antibiotic tetracycline, they were more active than thioridazine, a phenothiazine compound known to exhibit antimicrobial activity.

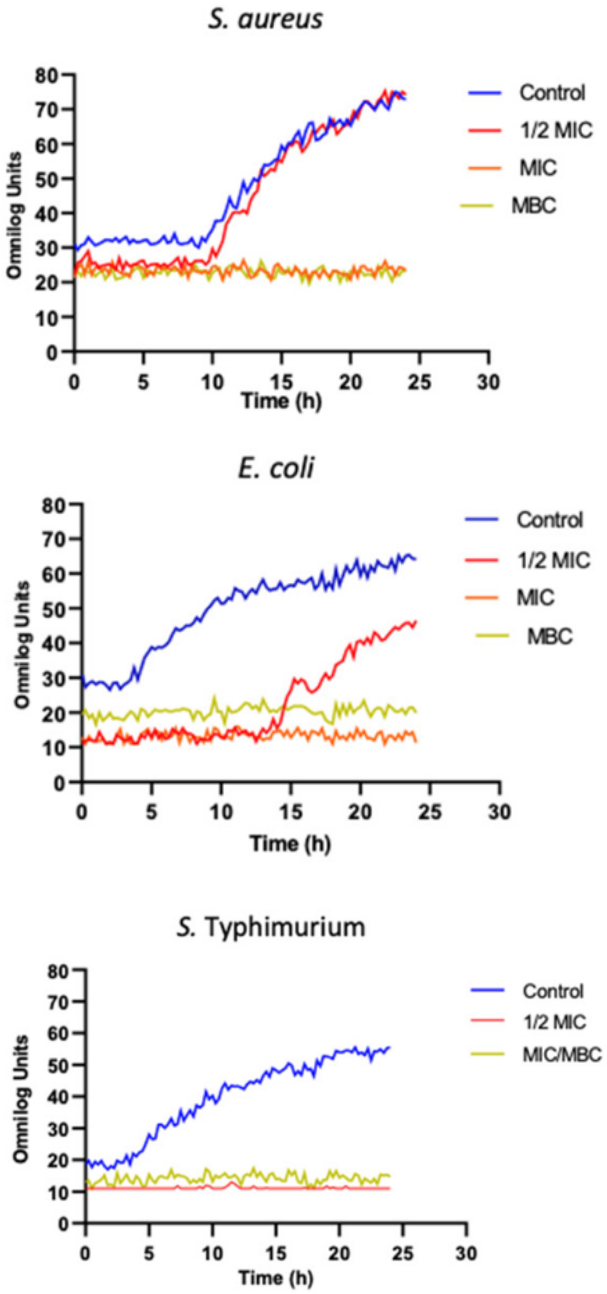

Figure 56. Growth curves for *S. aureus*, *E. coli*, and *S.* Typhimurium incubated with complex **316**. 0–500 OmniLog Units represent relative absorbance from 0–100%. Reproduced from Ref. [216], https://doi.org/10.3390/molecules28217453, under the terms of the CC BY 4.0 license, https://creativecommons.org/licenses/by/4.0/.

4.3. Iron and Ruthenium Complexes and Macromolecules

Iron-containing ferrocene complexes conjugated to different compounds have been investigated to their antimicrobial activities [217,218]. Hybridization with existing drugs has been employed to use the lipophilic nature of ferrocene to increase cellular uptake [219,220], while Kovačević et al. used ferrocene to induce turns for peptides that mimic conformations found in natural peptides [221]. One example of ferrocene-containing compounds examined for their antimicrobial activity was a series of 5-aryl-6-ferrocenoyltetrahydropyrazolo [1,2-*a*]pyrazol-1(5*H*)-one complexes were prepared in both their *trans*- (complexes **351-364**) and *cis*-isomer forms (**365-378**)[222]. The general synthetic methodology was to react 3-pyrazolidinone (**321**) with the aromatic aldehydes **322-335** to produce the *N*,*N*′-cyclic azomethine imines **336-349**, followed by reaction with acryloylferrocene (**350**), which yielded complexes **351-378**, as described in Scheme 41. The highest antifungal activity for these complexes against *C. albicans* and *A. brasiliensis* was determined for *trans*-isomeric complexes **351**, **352** and **353** with methylphenyl substituents, complex *trans*-isomeric complex **356** with a methoxyphenyl substituent, and *cis*- isomeric complex **368** with 4-methylphenyl substituent, with MIC values ranging between

≤0.02 mM and 2.34 mM. However, these complexes were still less effective in comparison with the two reference antifungals nystatin and ketoconazole, which exhibited MIC values between <0.3 μM and 75.3 μM. Nevertheless, the addition of ferrocene improved the antifungal activity of the resulting tetrahydropyrazolopyrazolone complexes, indicating its potential use for further drug discovery experiments.

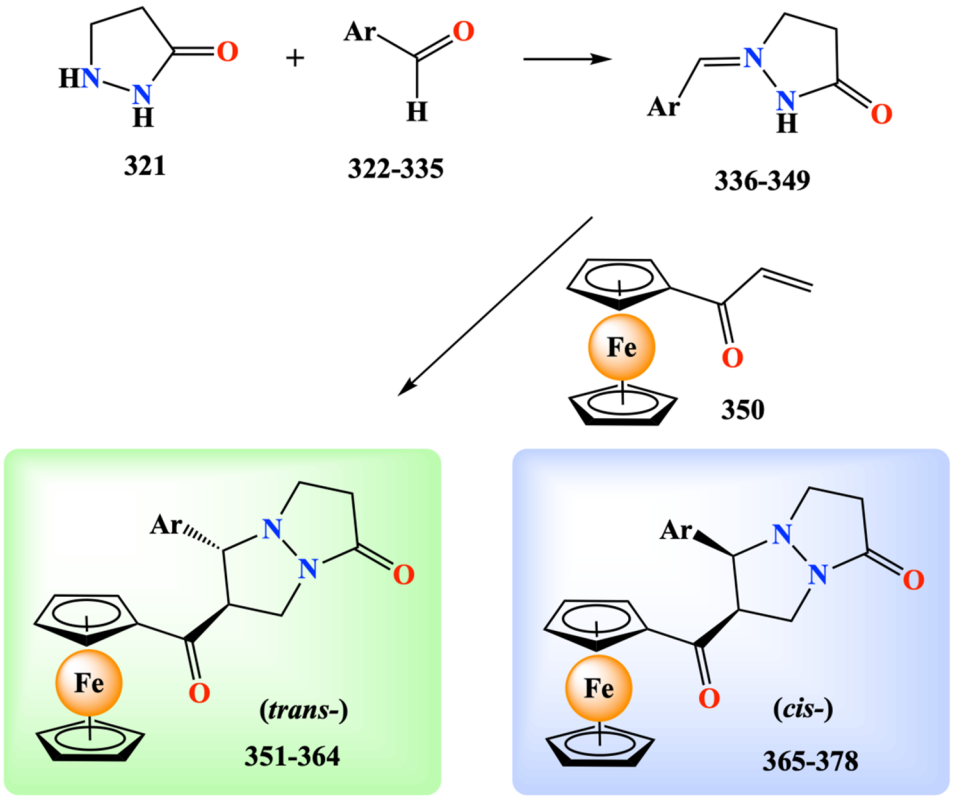

No.	Ar	No.	Ar	No.	Ar
322, 336, 351, 365	Ph	327, 341, 356, 370	2-MeOPh	332, 346, 361, 375	4-ClPh
323, 337, 352, 366	2-MePh	328, 342, 357, 371	3-MeOPh	333, 347, 362, 376	4-NO_2Ph
324, 338, 353, 367	3-MePh	329, 343, 358, 372	4-MeOPh	334, 348, 363, 377	1-NaPh
325, 339, 354, 368	4-MePh	330, 344, 359, 373	2-ClPh	335, 349, 364, 378	2-NaPh
326, 340, 355, 369	2,4,6-Me_3Ph	331, 345, 360, 374	3-ClPh		

Scheme 41. Synthesis of complexes **351-378**, with the aromatic group of each compound defined in the included table.

To improve the antimicrobial activity of bisphosphonate drugs, Anusionwu et al. designed a number of ferrocene-bisphosphonate hybrid complexes, of which the most active were found to be complexes **379** and **380** (Scheme 42) [220]. Both complexes were shown in vitro to be active against a range of Gram-positive and Gram-negative bacteria. In particular, two Gram-negative bacterial strains showed high inhibitory activity, namely *Proteus mirabilis* and *Klebsiella aerogenes*, with MIC values of ≤3 μM and 7 μM for complex **379** and MIC values of ≤ 3 μM and ≤ 3 μM for complex **380**, respectively. This was comparable to the reference antibiotic fosfomycin (MIC ≤ 14 μM for either *P. mirabilis* or *K. aerogenes)*. In terms of their antifungal activities, both complexes inhibited *Aspergillus ochraceus*, *Penicillium citrinum* and *C. albicans*, with MIC values of 107 μM, 214 μM and 214 μM for complex **379** and MIC values of 209 μM, 417 μM and 417 μM for complex **380**, respectively. Although the reference antifungal nystatin was less effect against *A. ochraceus* and *P. citrinum* (MIC = 540 μM for either strain), it should be noted that it was more effective against *C. albicans* (MIC = 17 μM). Molecular docking results showed both complexes were found to bind strongly to the active site of the urease enzyme of *K. aerogenes* (PDB ID: 1FWE) as well as a bacterial adhesion protein in *P. mirabilis* (PDB ID: 6Y4F), both of which are necessary virulence factors for these bacteria. The calculated binding energies for 1FWE were −5.821 Kcal/mol for complex **379** and −5.271 Kcal/mol for complex **380**, compared to −6.727 Kcal/mol for fosfomycin, while the binding energies for 6Y4F were −4.645 Kcal/mol for complex **379** and −3.973 Kcal/mol for complex **380**, compared to −3.141 Kcal/mol for fosfomycin.

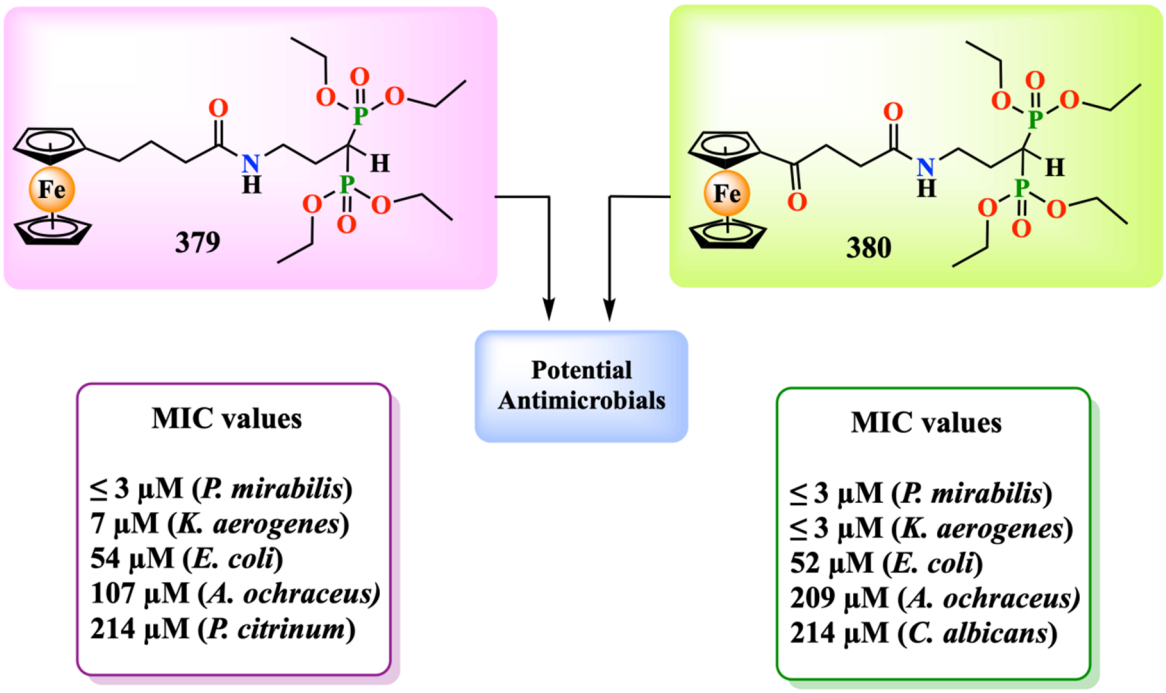

Scheme 42. Structure and MIC values against several microbial species for potential antimicrobial complexes **379** and **380**.

Abd-El-Aziz and coworkers designed a number of dendrimeric materials with pendent cyclopentadienyliron cations that possess various biomedical activities. A series of dendrimers **381-386** were prepared, as shown in Scheme 43 [223]. These dendrimers were found to be effective antibacterial agents against Gram-positive MRSA, vancomycin-resistant *Enterococcus faecium* (VRE), and *Staphylococcus warneri*. The dendrimers with PF_6^- counter ions were more active than those with BF_4^- counterions, with the most active being the methyl-substituted complex **382**, which had IC_{50} values of 1.8 µM for MRSA, 2.2 µM for VRE, and 2.5 µM for *S. warneri*. By contrast, dendrimer **382** only exhibited an IC_{50} of 20 µM for the human cell line HTB-26.

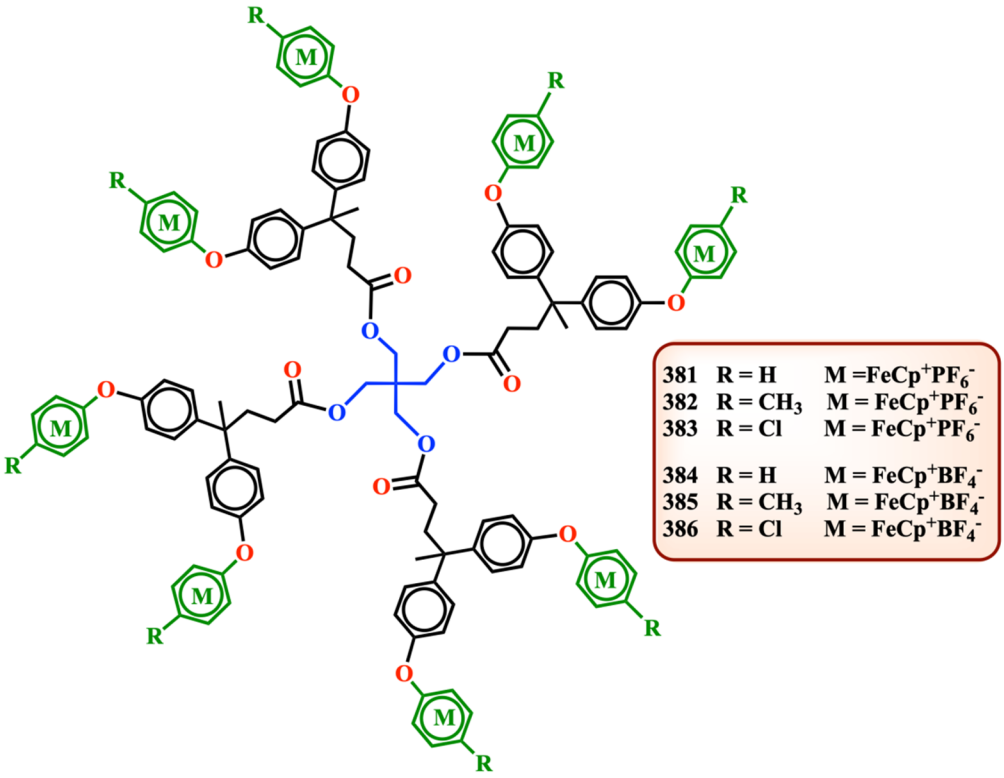

Scheme 43. Structures of ferrocene-containing dendrimers **381-386**.

Antibacterial activity through induction of ROS was confirmed using a DCFH-DA assay, in which dendrimers **382** and **383** resulted in ROS levels comparable to the reference antibiotic vancomycin. Additionally, the survival of human BJ fibroblast cells after 24 hours of exposure to 128 μg/mL dendrimer **382** showed that this dendrimer had low cytotoxicity and was therefore highly biocompatible. On the other hand, cell membrane shrinkage and damage were observed in MRSA cells treated with the same dendrimer (Figure 57b) in comparison to healthy bacterial cells (Figure 57a), demonstrating the membrane damage as a result of the induced oxidative stress.

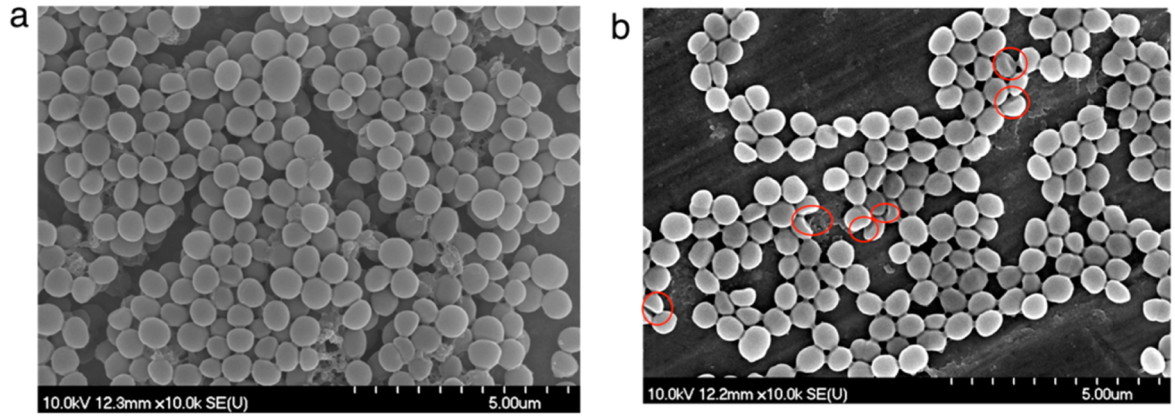

Figure 57. SEM images of MRSA cells (**a**) without and (**b**) with addition of 1.8 μM dendrimer **382**. Adapted with permission from ref. [223]. Copyright © 2015, American Chemical Society.

Polymeric materials with ferrocene offer different advantages to complexes. For example, Jańczewski and coworkers used reductive amination to add ferrocene to linear polyethyleneimine (PEI) with varying molecular weights and levels of ferrocene content [224]. The ferrocene-grafted polymers exhibited slight reductions to the antimicrobial effects against Gram-positive *S. aureus*, Gram-negative *E. coli* and fungus *C. albicans,* the activity became tunable. Oxidative conditions resulted in ferrocenium cations that were expected to be more toxic to the bacteria, but instead decreased the inhibition against *E. coli*, which was believed to be due to enhanced iron transport by the polymer.

A second example of a polymer containing ferrocene moieties was used by Mu et al. to prepare composite hydrogels with antimicrobial activity via ring-opening metathesis polymerization (ROMP) utilizing the third-generation Grubbs catalyst [225]. The AgNPs were surrounded by a terpolymer with ferrocene moieties, which forms a composite with gelatin hydrogels. The authors investigated the effect of cationic ferrocenium in comparison with neutral ferrocene by preparing four different hydrogel-silver nanoparticles: AgNPs-1 **(389)**, AgNPs-2 **(390)**, AgNPs-3 **(391)** and AgNPs-4 (**388**) (Figure 58). The copolymer **387** was blended with gelatin and silver nitrate with or without the reducing agent $NaBH_4$ to form nanoparticles **388** and **389**, respectively, or first used to produce the copolymer-gelatin hydrogel, then soaked in silver nitrate to form nanoparticle **390**, which was then followed by in situ reduction to yield nanoparticle **391**. Antimicrobial activity was evaluated for nanoparticles **389-391** by measuring the zone of inhibition in disc diffusion assays, where no inhibition was observed for copolymer-gelatin hydrogels without silver. The ferrocene-containing nanoparticle **391** was significantly less active, with inhibition zone diameters of 6.4 mm for *E. coli* and 5.9 mm for *S. aureus* compared to either ferrocenium-containing nanoparticles **389** or **390**, with diameters of 11.0 mm and 10.7 mm for *E. coli* and 8.7 mm and 10.7 mm for *S. aureus.*

In addition to its previously described release of antiproliferative drug paclitaxel, the antibiofilm coating of the ferrocene-containing film composed of the negatively charged copolymer **163** and the positively charged copolymer **164** by Woo et al. will be described in this section [145]. The addition of two bilayers decreased both cell adhesion of both Gram-positive *S. aureus* and Gram-negative *E. coli* cell adhesion to <20% compared to the uncoated glass substrate. The inhibition of bacterial cell adhesion was a consequence of increased hydrophilicity and low surface energy of the polymer layers. In addition, the DMAEMA moiety is known to be bactericidal, and if a positively charged layer is placed on surface, the number of dead bacteria increased.

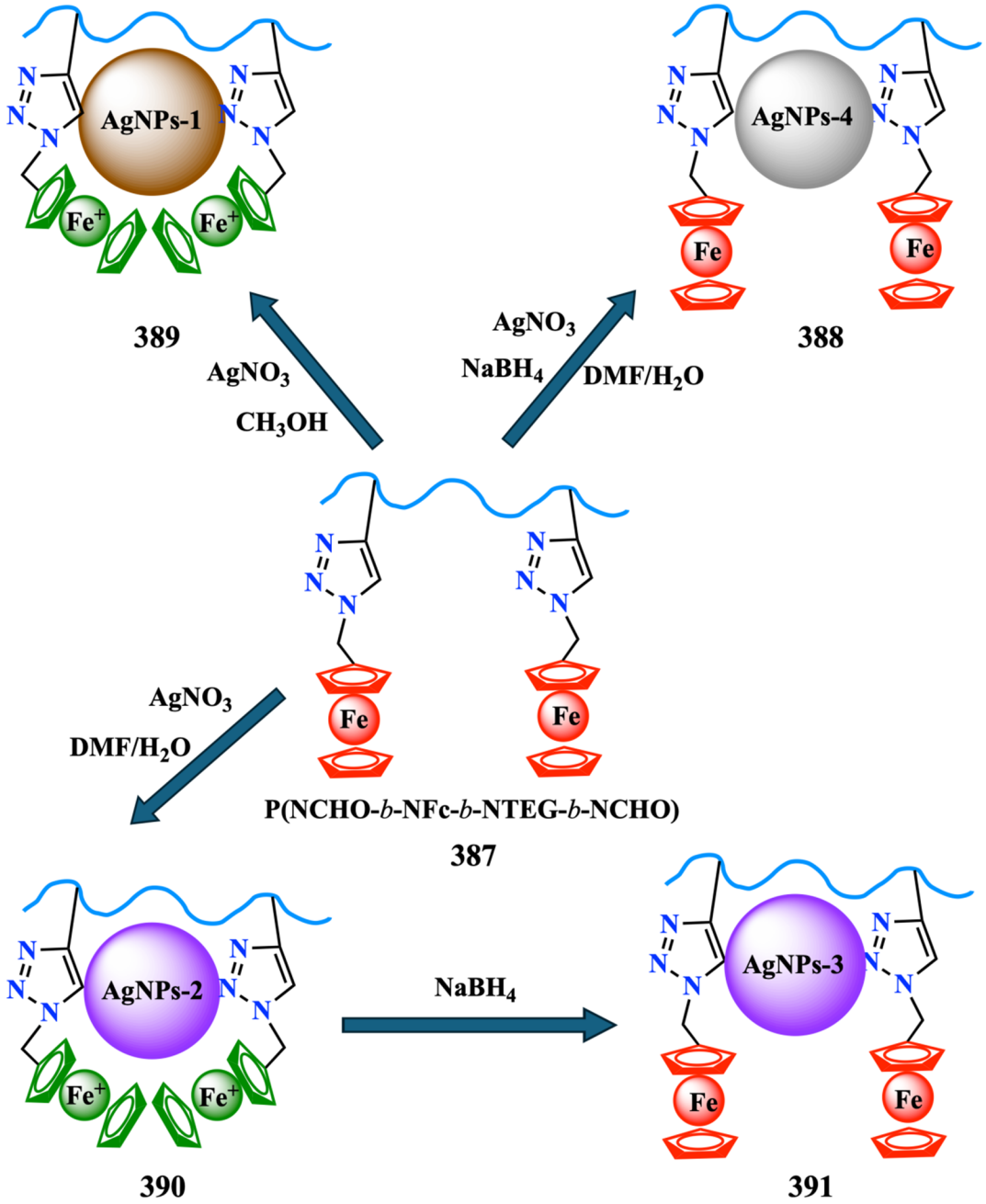

Figure 58. Preparation of four ferrocene-containing hydrogel silver nanoparticles **388-391**.

Bhunya et al. synthesized a series of four ruthenium(II) complexes with thiazolidine-based ligands **395**, **398**, **401** and **404** which feature a distinctive donor environment with contribution from one nitrogen (N) and one sulfur (S) per complex, as shown in Scheme 44 [226]. All four complexes started from 2-aminoethane-1-thiol hydrochloride (**392**), which was reacted with 2-methyl-2-(pyridin-2-yl)thiazolidine (**393**), 2-(pyridin-2-yl)thiazolidine (**396**), 2-methyl-2-(5-methylpyridin-2-yl)thiazolidine (**399**) and 2-(isoquinolin-3-yl)-2-methylthiazolidine (**402**) to yield the corresponding ligands **394**, **397**, **400** and **403**, which then formed the Ru(II) complexes **395**, **398**, **401** and **404** by reaction with [Ru(*p*-cymene)Cl_2]$_2$. These complexes were evaluated for their antibacterial activity against highly resistant clinical pathogens, specifically the Gram-positive MRSA and Gram-negative *K. pneumoniae*. The complexes were found to bind to DNA via a partial groove binding mode, as evidenced by spectroscopic studies using calf thymus DNA, as well as a minor increase in DNA melting temperature. Scanning electron microscopy (SEM) analysis confirmed that the active complexes disrupt bacterial adhesion. For both bacterial strains *K. pneumoniae*, the complexes caused cells to disperse, indicating disruption of cell-cell adhesion and biofilm, as a result of reduced production of extracellular polymeric substances (EPS). The higher activity of complexes **395** and **398**, as opposed to the inactive complexes **401** and **404**, was attributed to their smaller HOMO-LUMO energy gap, suggesting higher chemical reactivity that facilitates interaction with bacterial targets.

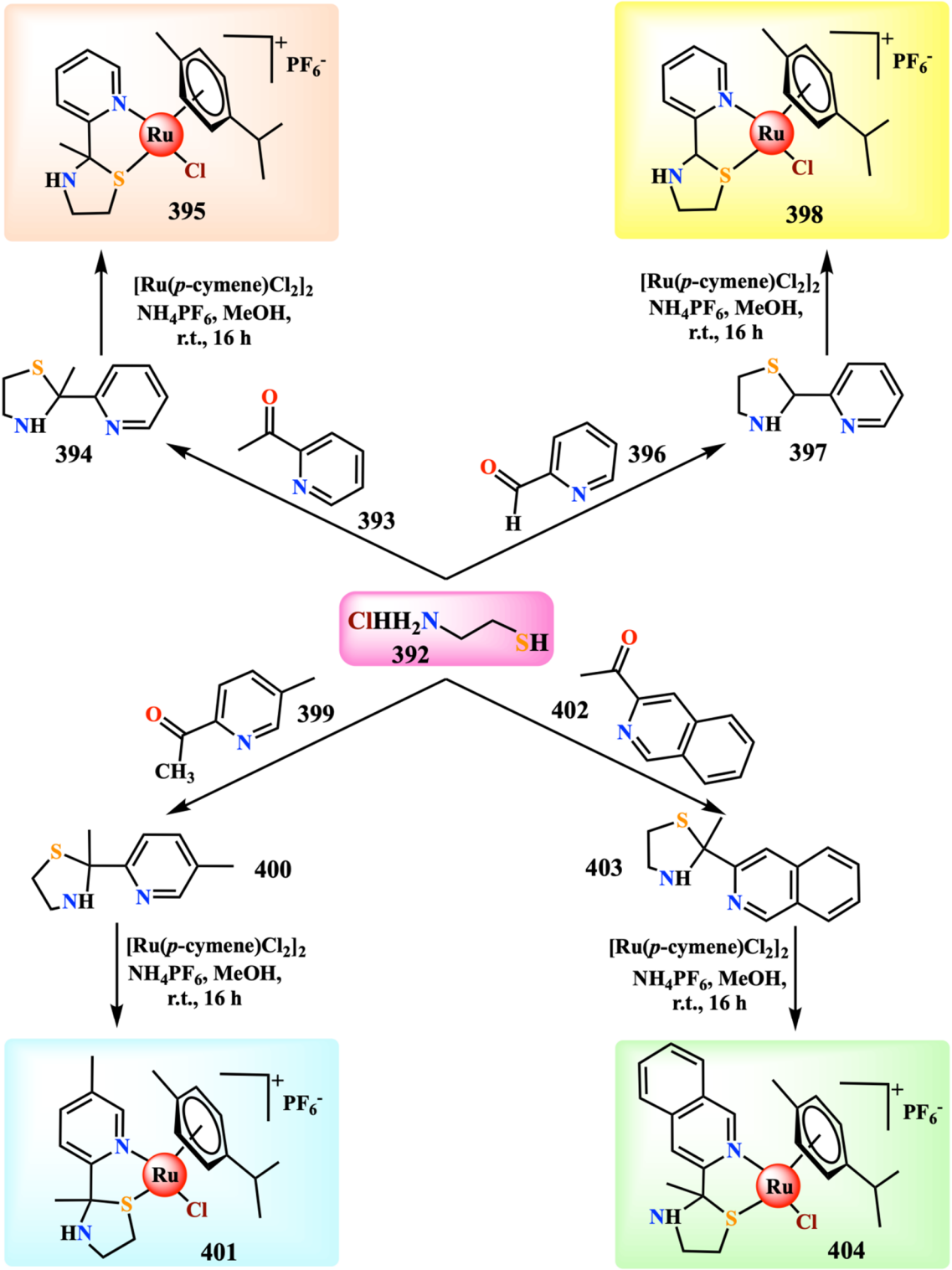

Scheme 44. Synthesis of ruthenium(II) complexes with thiazolidine-based ligands **395**, **398**, **401** and **404**.

4.4. Cobalt and Rhodium Complexes and Macromolecules

The Tang research group has designed a number of cobaltocenium complexes, polymers and copolymers and evaluated their activities. For example, a cobaltocenium complex with norbornene was prepared as a monomer for polymerization [227]. The resulting polymer was added to double network hydrogels with polyacrylamide and poly(3-acrylamidophenylboronic acid) (PPB) with and without conjugation to penicillin-G by immersion in aqueous solution [228]. Growth inhibition assays for Gram-positive *S. aureus* as well as Gram-negative *E. coli* and *P. aeruginosa* showed low activity for the network of polyacrylamide and the cobaltocenium-containing copolymer alone against Gram-negative, but higher activity for *S. aureus* (up to 70% inhibition), which was increased with addition of penicillin-G. In comparison, the network with 3-acrylamidophenylboronic acid (APBA)

and the cobaltocenium copolymer was more active against all bacteria as a consequence of the boronic acid moiety, and conjugation with penicillin-G resulted in this network displaying the highest activity against all tested strains. This class of cobaltocenium-containing polymers has been shown to block access to penicillin from bacterial β-lactamase enzymes that could degrade it by hydrolysis [229]. Another cobaltocenium-containing copolymer was prepared using PPB and conjugated with penicillin, but using polycaprolactone (PCL) for its biodegradability [230]. The resulting copolymer inhibited bacterial growth for Gram-negative *E. coli, P. vulgaris, P. aeruginosa* and *K. pneumoniae*, all of which showed increases in activity due to conjugation of antibiotic and the presence of boronic acid moiety. Furthermore, the biodegradability of the polymer with PPB and cobaltocenium was measured under physiological conditions (pH 7.4), acidic pH representing bacterial infection (pH 5.5) and addition of a bacterial lipase enzyme. Both addition of acid and lipase resulted in high levels of degradation (70% for acid and 83% for lipase) after a three-day period.

This research group also prepared a cobaltocenium-containing polymer in combination with three different antibiotics to target drug-resistant strains of Gram-negative bacteria and their biofilms [231]. Addition of cobaltocenium carboxylic acid to 2-aminoethyl methacrylate hydrochloride gave rise to the 2-cobaltocenium amidoethyl methacrylate complex with hexafluorophosphate as a counterion (**405**), which was then polymerized by reacting it with 2-cyano-2-propyl benzodithioate (**406**) in the presence of AIBN, as illustrated in Scheme 45. The resulting cationic polymer with hexafluorophosphate (**407**) then underwent ion exchange with chloride to give polymer **408**, which was then mixed with one of three antibiotics: ceftazidime (**409**), rifampicin (**410**) and minocycline (**411**), to generate the corresponding polymer-antibiotic combinations **412-414**.

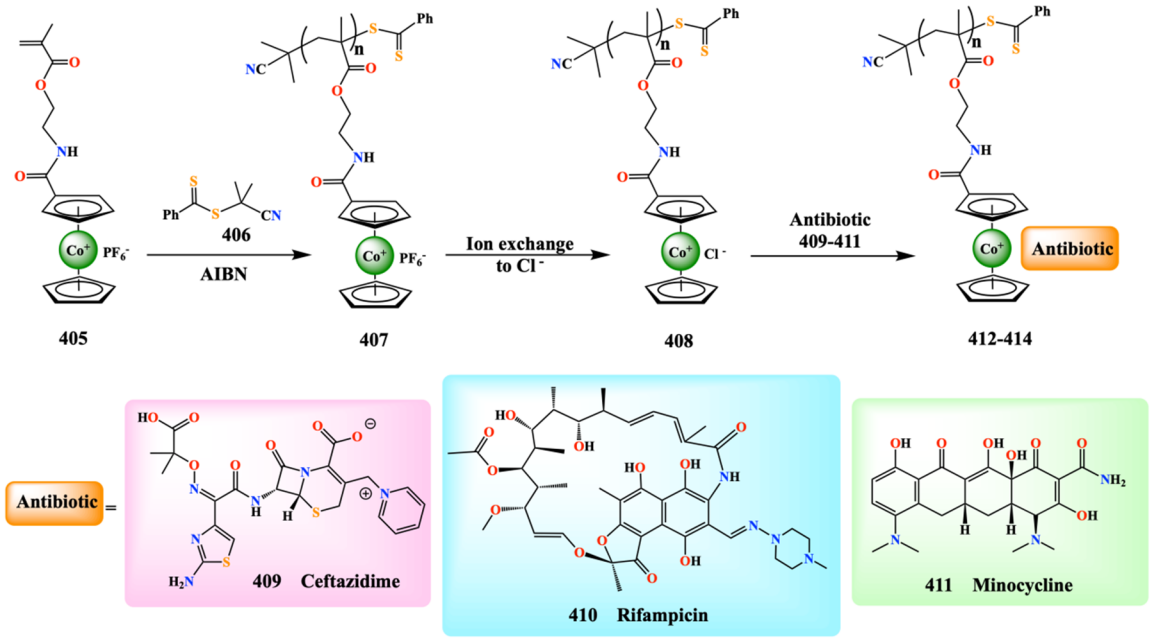

Scheme 45. Preparation of combinations **412-414** from cobaltocenium polymer (**408**) and one of three antibiotics (**409-411**).

There were several mechanisms by which the polymer-antibiotic combinations **412-414** enhanced the activity of different antibiotics, as illustrated in Figure 59. The combination with ceftazidime (**412**) inhibited β-lactamases that could hydrolyze it and other β-lactam antibiotics, while the polymer with rifampicin (**413**) permeabilized the outer membrane allowing the antibiotic access through it. Finally, for the combination with minocycline (**414**), the polymer caused depolarization of the membrane, which removes the electrical potential across the membrane required for efflux pump proteins to remove it from the cell. An important target for these polymers is preventing the formation of bacterial biofilms that are more difficult to treat than planktonic bacteria, as the lower layers of the biofilm are dormant and only become active if the top layers die. This is consistent with the polymer itself exhibiting low antibacterial activity against Gram-negative bacterial biofilms of *E. coli* (30% reduction in biomass) or *P. aeruginosa* (36% reduction), with the addition of antibiotics resulting in significant reductions in biomass. For example, free ceftazidime displayed minimal impacts on the biomass of *E. coli*, while the same concentration in combination with the polymer caused a decrease in biomass to 80%. At the same concentration, free rifampicin achieved a reduction in biomass of *P. aeruginosa* to 54% and the combination with the polymer resulted in an 88% reduction in biomass. The lower activity of ceftazidime may be due to its negatively charged carboxylate

group. However, interaction with cationic cobaltocenium allows the antibiotic to more easily interact with the negatively charged phospholipid membrane. Furthermore, since the ceftazidime only electrostatically interacted with the cobaltocenium, this does not remove the positive charge to interact with negatively charged components of the cell wall, such as lipopolysaccharide (LPS).

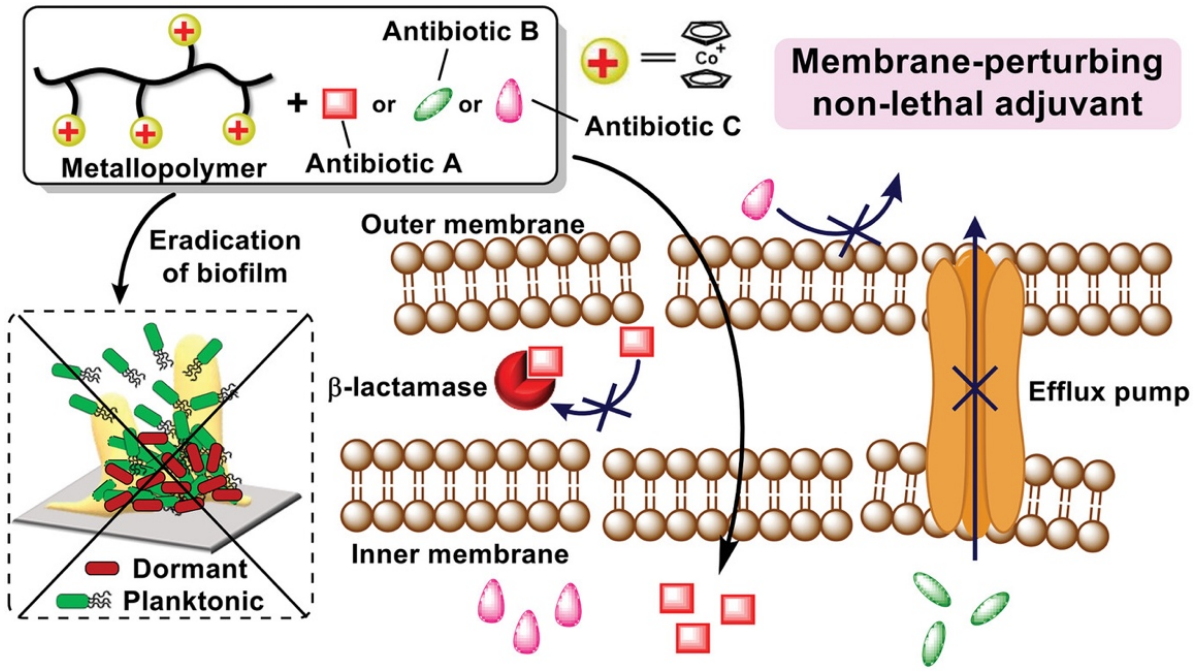

Figure 59. Inhibition of antibiotic resistance mechanisms in Gram-negative bacteria by cobaltocenium for eradication of biofilm. Reproduced from Ref. [231], https://doi.org/10.1002/adhm.202301764, under the terms of the CC BY NC 4.0 license, http://creativecommons.org/licenses/by-nc/4.0/.

Recently, this research group prepared two cobaltocenium and ammonium-containing methacrylate copolymers, namely copolymers **417** and **419**, to target multidrug-resistant Gram-negative bacteria [232]. Synthesis of these copolymers began with poly(aminoethyl methacrylate) (PAEMA, **415**), which was reacted with dimethyl substituted cobaltocenium carboxylic acid (**416**) to yield PAEMA-dmCC (**417**) and cobaltocenium carboxylic acid (**418**) to yield PAEMA-CC (**419**) (Scheme 46). Copolymers **417** and **419** were tested for their antibacterial activity against strains of *E. coli* and *K. pneumoniae* with the New Delhi metallo-β-lactamase (NDM-1) enzyme. The addition of cobaltocenium improved the activity in comparison with poly(aminoethyl methacrylate) containing only ammonium groups. Despite both side chains having the same charge, cobaltocenium distributed the single positive charge over a larger surface area, resulting in greater lipophilicity, allowing them to more easily cross cellular membranes for uptake.

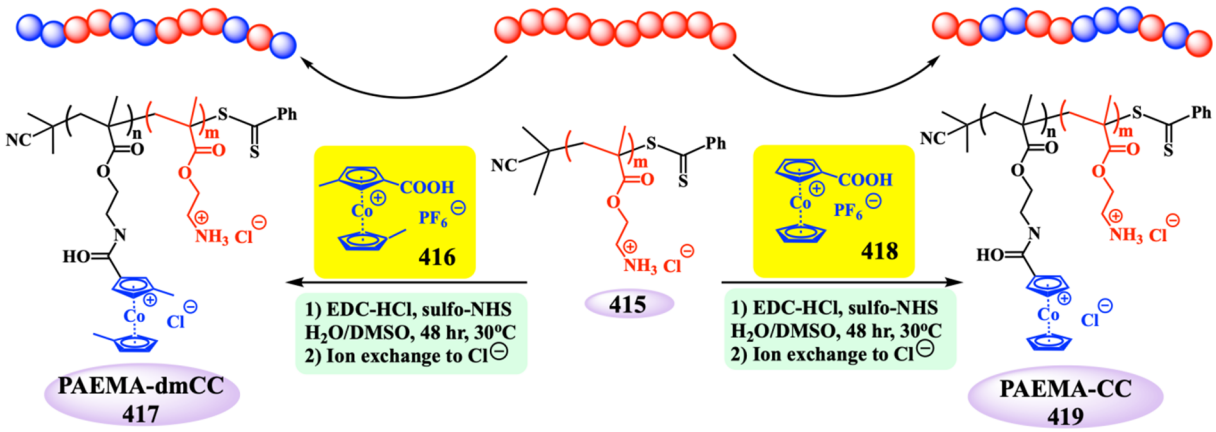

Scheme 46. Synthetic methodology for copolymers PAEMA-dmCC (**417**) and PAEMA-CC (**419**).

These copolymers were shown to permeabilize the Gram-negative outer membrane resulting in their antibacterial efficacy. The three most active compositions of these copolymers were copolymer **419** containing 81% cobaltocenium side chains (P4), copolymer **417** with 58% dimethylcobaltocenium side chains (P6), and copolymer **417** with 69% dimethylcobaltocenium side chains (**P7**). As can be seen from Figure 60A for planktonic *E. coli* cells and Figure 60B for planktonic *K. pneumoniae* cells, after 8 hours, all three preparations eliminated the bacteria at even the lower concentration of 16 μg/mL. As well as antibacterial activity, membrane disruption enhanced the biofilm activity, as shown by the effectiveness of the copolymers against the inactive stationary cells found in biofilms of *E. coli* (Figure 60C) and *K. pneumoniae* (Figure 60D). After 12 hours, both bacterial strains showed complete elimination, which could not be achieved by either of the reference antibiotics (aztreonam or imipenem). In terms of haemotoxicity, mouse red blood cells (RBCs) were used as a model system and all preparations of PAEMA-dmCC (**417**) exhibited minimal haemotoxicity (<10%), while PAEMA-CC (**419**) showed similar haemotoxicity to PAEMA (**415**), which was still low (~20%). In addition to its activity, copolymer **417** also demonstrated low development of AMR. After 14 passages of the *K. pneumoniae* strain incubated with copolymer **417** and the reference drug polymyxin B, only a two-fold increase in the MIC of the copolymer was observed, compared to a 256-fold increase of polymyxin B.

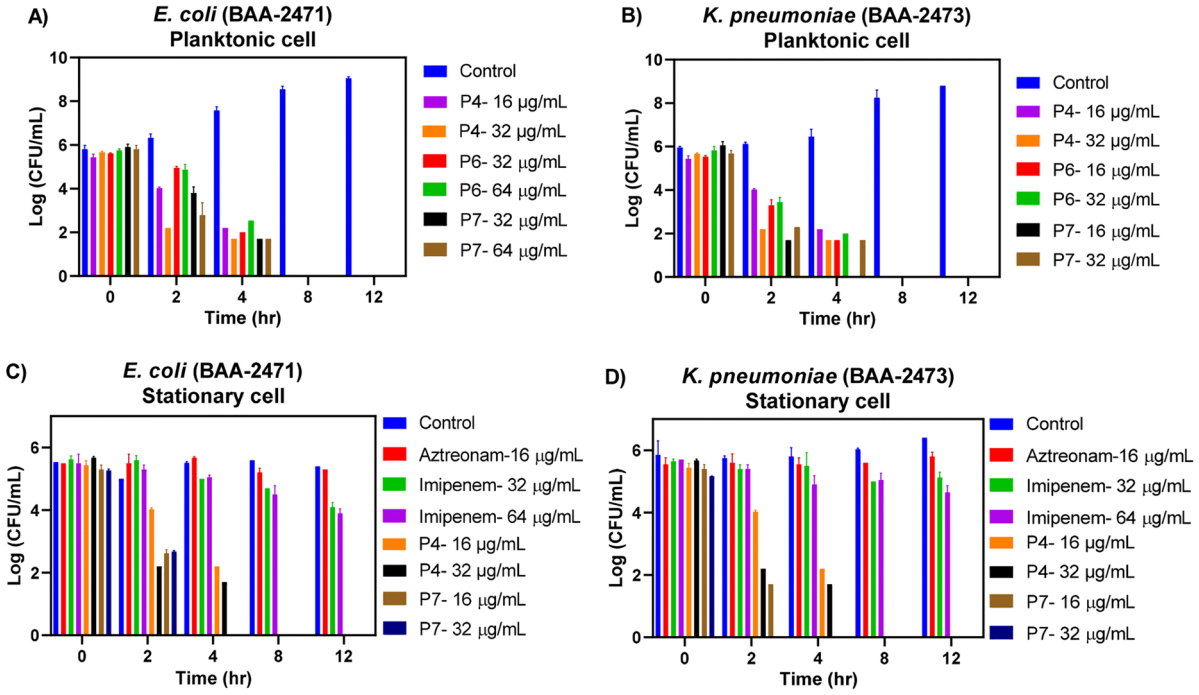

Figure 60. Antimicrobial activity of copolymer **417** (P6 and P7) and copolymer **419** (P4) against planktonic (**A**) *E. coli* and (**B**) *K. pneumoniae*, as well as stationary (**C**) *E. coli* and (**D**) *K. pneumoniae*. Adapted from Ref. [232], https://doi.org/10.1039/D5BM00497G, under the terms of the CC BY NC 3.0 license, http://creativecommons.org/licenses/by-nc/3.0/.

In order to combat multidrug-resistant (MDR) bacteria, specifically *Klebsiella pneumoniae*, fluoroazolium salts and their complexes with Rh^{+} have been synthesized, eight of which (**420-427**) are illustrated in Figure 61 [233]. The antimicrobial activities of these compounds and complexes were then tested using three clinical isolates of MDR *K. pneumoniae* as well as several reference strains. While the organic salts showed low to no activity against all tested strains, the highest activities against the reference ATCC strains were observed for complexes **420**, **421** and **427** with MIC values ranging between 3.9–250 μg/mL, while MIC values ranging between 62.5–250 μg/mL were observed for complexes **420**, **422**, **424** and **427** against MDR strains. Computational absorption, distribution, metabolism, excretion, and toxicity (ADMET) analysis was performed. Only complexes **421**, **422** and **425** were predicted to not be orally bioavailable, but all the complexes could cross the blood-brain barrier. In addition, all the metal complexes were non-carcinogenic as well as possessing low acute oral toxicity. All complexes except **423**, **425** and **427** were calculated to have intestinal absorption properties similar to cisplatin, and Caco-2 cells (used as a model of intestinal cell permeability) were only impermeable for complexes **425-427**. Despite this, when the ADMET properties were assessed in combination with the antimicrobial properties, **420** and **427** emerged as the most promising candidates for future drug design.

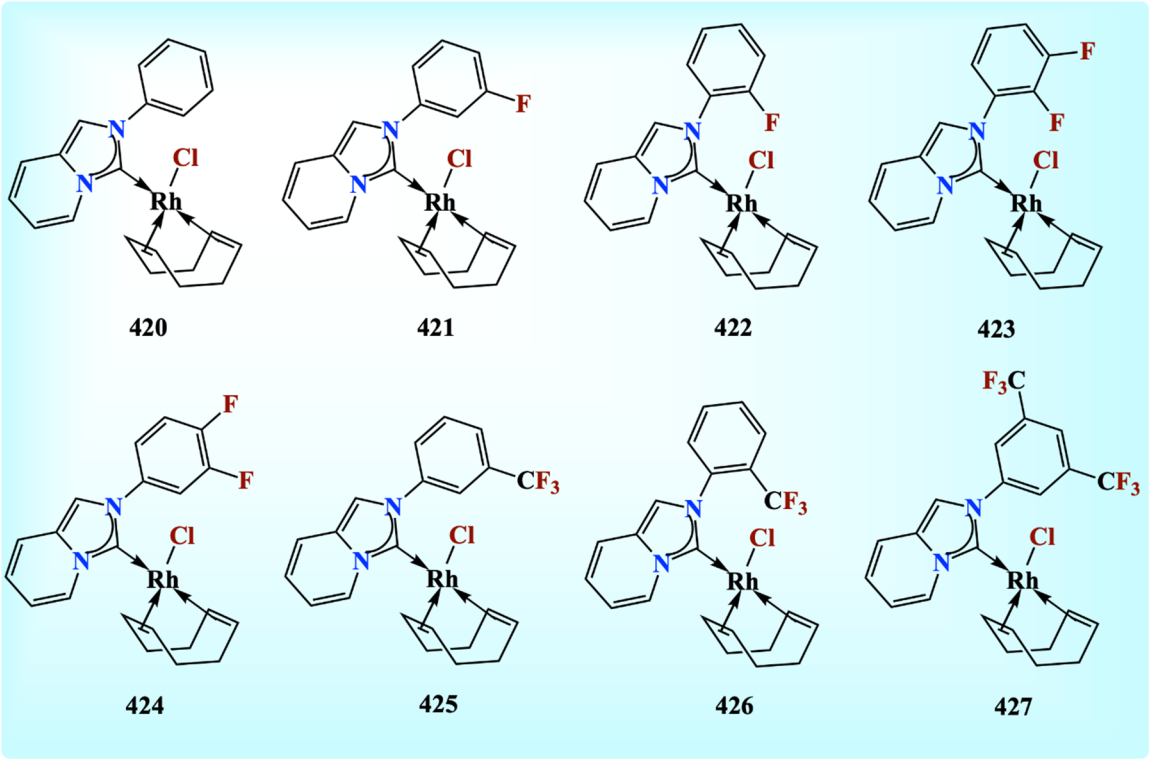

Figure 61. Structures of complexes **420**-**427**.

4.5. Silver and Gold Complexes and Macromolecules

There are several examples of organometallic silver and gold complexes that have shown to be effective antimicrobial agents. One class of complexes that has been reported for their antimicrobial activities is the group of silver and gold N-heterocyclic carbene complexes [234,235]. Two early reports in the beginning of the 21st century by Youngs and coworkers described the design of two water-soluble complexes: silver(I)−2,6-bis(ethanolimidazolemethyl)pyridine hydroxide (**428**) and silver(I)−2,6-bis(propanolimidazolemethyl)pyridine hydroxide (**429**), as well as the silver(I)-imidazole cyclophane *gem*-diol complex (**430**) (Figure 62), and demonstrated their effectiveness when compared with silver nitrate [236,237]. Another study published around the same time by Özdemir et al. reported the preparation of gold(I) imidazolidin-2-ylidene complexes and their antimicrobial efficacies [238].

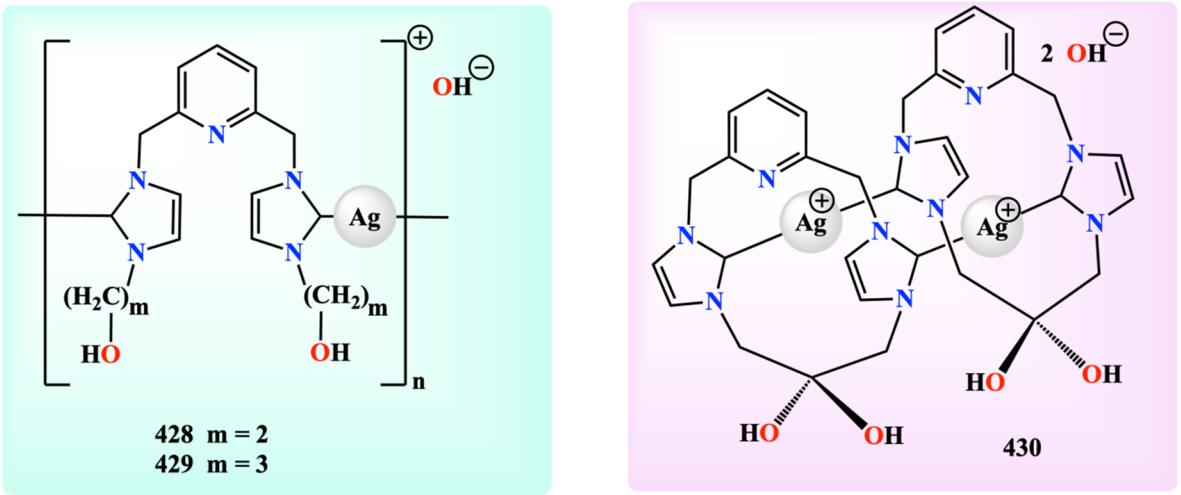

Figure 62. Structures of complexes **428**-**430**.

Following these studies, there have been many studies using various N-heterocyclic carbene (NHC) ligands complexed with silver and gold. For example, Prencipe et al. prepared silver-NHC complexes containing either acridine or pyrazole moieties, as well as one bis-carbene Ag(I) complex [239]. The *bis*-carbene Ag(I) complex

was shown to be more active than the mono-carbene complexes or organic ligands against Gram-positive *E. coli* and *P. aeruginosa* and Gram-negative *B. subtilis* and *S. aureus.* Another work that examined silver-NHC complexes focused on the development of Ag(I)-benzimidazolium complexes and their organic salts [240]. In addition to the broad-spectrum activity against both Gram-positive and Gram-negative bacteria (*S. aureus* and *E. coli*, respectively), molecular docking studies demonstrated high binding affinity to DNA, stronger than ethidium bromide or cisplatin, indicating it may be involved in the antibacterial mechanism. In terms of gold-NHC complexes, a hybrid of the conventional antibiotic metronidazole with an Au(I)-benzimidazolium complex was designed by Büssing et al. to take advantage of multiple antimicrobial mechanisms to overcome AMR [241]. The Au(I)-NHC complex was demonstrated to be effective against strains of the Gram-positive bacterium *Clostridioides difficile* that were either sensitive to or resistant to metronidazole. Mármol et al. designed Au(I)-NHC complexes with alkynyl moieties to increase the lipophilicity of the complexes, thereby increasing their uptake [242]. Inhibition of the enzyme thioredoxin reductase was observed in Gram-positive bacteria *E. faecalis, Listeria monocytogenes, Staphylococcus epidermidis*, and *S. aureus,* which is known to be active for Au(I)-NHC complexes. As expected, this effect was only detected in Gram-positive bacteria, not Gram-negative bacteria *E. coli, P. aeruginosa, Salmonella enterica* or the human Caco-2 cell line. However, antimicrobial activity was observed against *E. coli,* as well as inhibition of the enzyme dihydrofolate reductase, suggesting that it played a role in the alternative Gram-negative bactericidal mechanism.

In this section, we will highlight some specific examples to demonstrate the antibacterial and antifungal activities of this class of complexes. Mather et al. prepared silver complexes **432-439** and gold complexes **440-447** with various 1,2,4-triazolylidene and imidazolylidene-based N-heterocyclic carbene ligands based on the general azolylidene ligand structure **431** (Scheme 47) [243]. The gold(I) complexes with phenyl substituents (**440-443**) demonstrated the highest inhibitory activity against Gram positive bacteria *E. faecium* and *S. aureus*. In addition, gold complexes **442** and **443** with 1,2,4-triazolylidene ligands were superior to complexes **440** and **441**, with the most effective gold complex **442** having an MIC of 4–8 μg/mL against *E. faecium* and 2 μg/mL against *S. aureus.* The silver(I) complexes **438** and **439** exhibited broader activity by also targeting Gram-negative *A. baumannii*, with MIC values of 2–4 μg/mL and 2 μg/mL, respectively. The most promising silver(I) complex **437** and gold(I) complex **442** were evaluated against multidrug-resistant *A. baumannii* and *E. faecium* strains. As anticipated, the gold complex **442** was more active against *E. faecium* and the silver complex **437** was more active against *A. baumannii*. Furthermore, both complexes showed comparable MICs for the corresponding resistant and susceptible strains, demonstrating that the antibiotic resistance did not affect their activity. Additionally, AMR did not develop for either complex but did develop in both bacteria for the existing antibiotic ciprofloxacin.

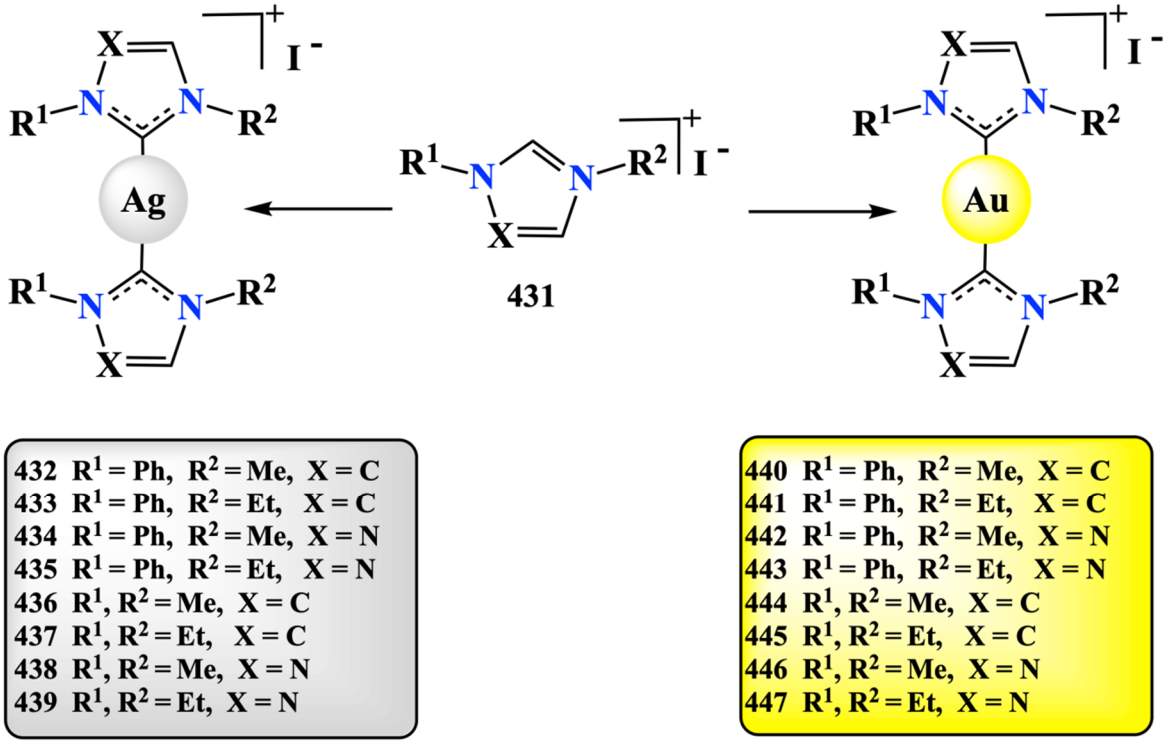

Scheme 47. Preparation of silver(I) complexes **432-439** and gold(I) complexes **440-447**.

The research group of de la Mata outlined the preparation of carbosilane dendrimers with cationic heterocyclic carbene groups **448-452** and their silver(I)-complexed analogues **453-457**, as displayed in Scheme 48 [244,245]. Both sets of dendrimers were analyzed for their antibacterial activities against Gram-positive *S. aureus* and *B. subtilis* and Gram-negative *E. coli*. The greatest inhibitory activity for the cationic dendrimers was the first-generation dendrimer **451** with mesityl substituents on the imidazolium ring with MICs of 0.5 μg/mL for *S. aureus,* 0.5 μg/mL for *B. subtilis* and 1 μg/mL for *E. coli*. Similarly, the corresponding Ag(I) first-generation dendrimer **456** also exhibited the highest inhibition in its class with MICs of 1μg/mL for *S. aureus,* 1 μg/mL for *B. subtilis* and 2 μg/mL for *E. coli*. The addition of Ag did not tend to result in an increase in activity, except for the first-generation dendrimer **453** with methyl substituents, which showed a dramatic improvement over cationic dendrimer **448** without Ag, particularly for *E. coli*, with MIC values of 4 μg/mL for dendrimer **453** and 32 μg/mL for dendrimer **448**. A lower MIC for $AgNO_3$ was also observed compared to any of the silver-containing dendrimers, suggesting that the Ag^+ ions were more active for antimicrobial activity than the silver complexes. The authors also concluded that there was a necessary balance between lipophilicity and hydrophilicity to optimize the antimicrobial activity. The Ag(I)-containing dendrimers were demonstrated to cause stress on the cell envelope of *B. subtilis*, but not depolarize the cell membrane, whereas the cationic dendrimers could depolarize the cell membrane but not perturb the cell envelope. This finding suggested that the Ag(I)-containing dendrimers exhibited a different mechanism of inhibition for bacterial growth compared to the analogous cationic organic dendrimers.

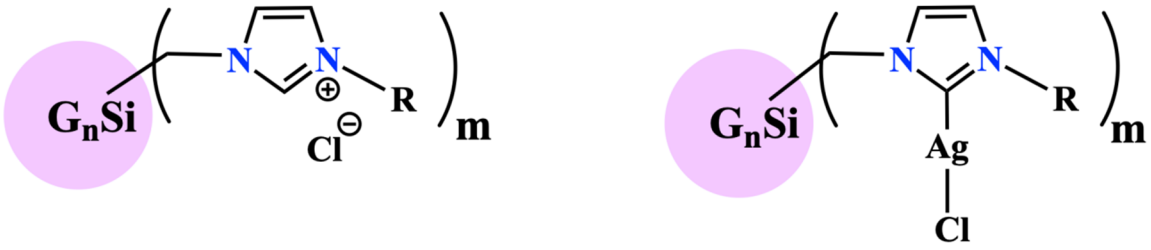

448 n = 1 m = 4 R = Me
449 n = 2 m = 8 R = Me
450 n = 3 m = 16 R = Me

451 n = 1 m = 4 R = Mes
452 n = 2 m = 8 R = Mes

453 n = 1 m = 4 R = Me
454 n = 2 m = 8 R = Me
455 n = 3 m = 16 R = Me

456 n = 1 m = 4 R = Mes
457 n = 2 m = 8 R = Mes

Scheme 48. Carbosilane dendrimers **448-452** and their Ag(I)-containing analogues **453-457**.

Lach et al. successfully fabricated carbosilane silver metallodendrimers **458** and **459** (Figure 63) and investigated their co-administration with the CHAP domain of endolysin, an enzyme that can hydrolyze peptidoglycan, derived from the bacteriophage phi 812 [246]. The authors targeted Gram-negative bacteria using *P. aeruginosa* as a model species. Three modes of action were employed to overcome different resistance mechanisms of Gram-negative bacteria. The dendrimers can interact with anionic LPS in the outer membrane to disrupt it, induce ROS generation and inhibit enzymes involved in bacterial respiration. The endolysin, on the other hand, hydrolyzes the middle peptidoglycan layer of the cell wall and results in cell lysis, as shown in Figure 64. The disruption of the outer membrane by the AgNPs allows the endolysin easier access to the peptidoglycan, improving the overall antibacterial activity. This multimodal approach overcomes the resistance of Gram-negative bacteria to the silver nanoparticles, allowing for synergistic antibacterial activity.

Inhibition of Gram-negative *P. aeruginosa* when treated with endolysin, silver dendrimers and the endolysin-silver dendrimer is shown in Figure 65A, with the most significant inhibition achieved by dendrimer **458** with 2 μg/mL endolysin. However, inhibition of bacterial growth was only observed at the higher concentration, as it was not effective for 1 μg/mL endolysin. Figure 65B showed degradation of peptidoglycan was still increased by endolysin at 1 μg/mL with either dendrimer **458** or dendrimer **459**, relative to the dendrimers without addition of endolysin, but this effect was not sufficient on its own to inhibit growth. The antibacterial activity of treatment with dendrimer **458** and endolysin was examined using SEM (Figure 65C), which showed the formation of pores in the bacteria, as well as TEM (Figure 65D), which demonstrated lower bacterial adhesion. LIVE/DEAD staining of *P. aeruginosa* bacteria treated with dendrimer **458** (Figure 65E) showed mostly live bacteria stained in green. Bacteria

treated with dendrimer **458** and endolysin complex (Figure 65F), on the other hand, mostly showed dead cells stained in red, showing that endolysin was necessary for this combination to have its synergistic antimicrobial effects.

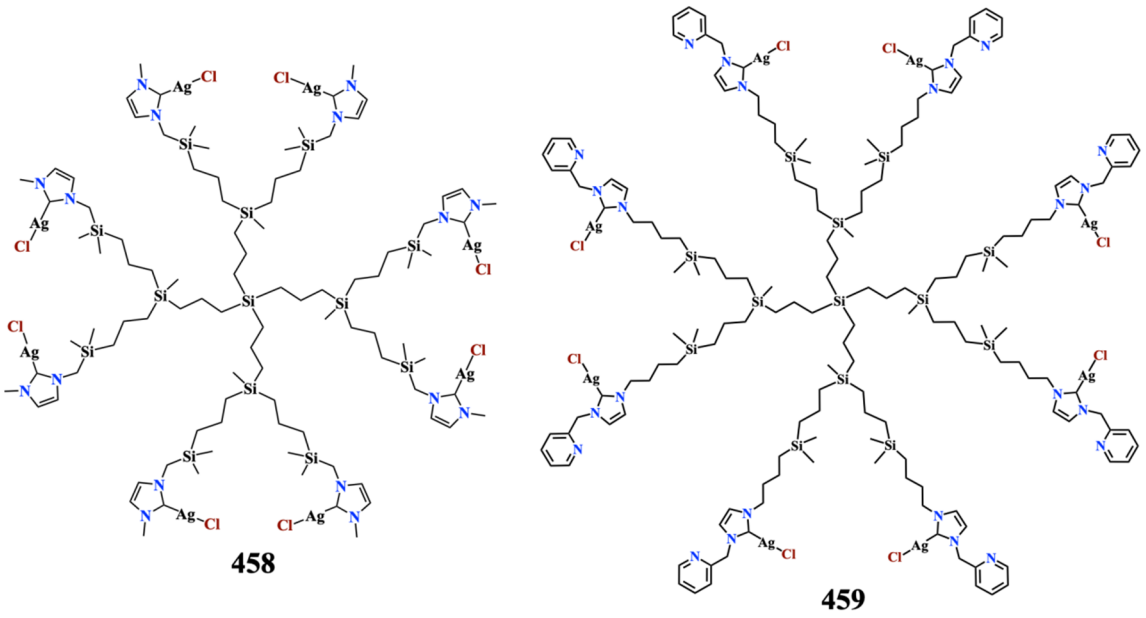

Figure 63. Structures of dendrimers **458** and **459**.

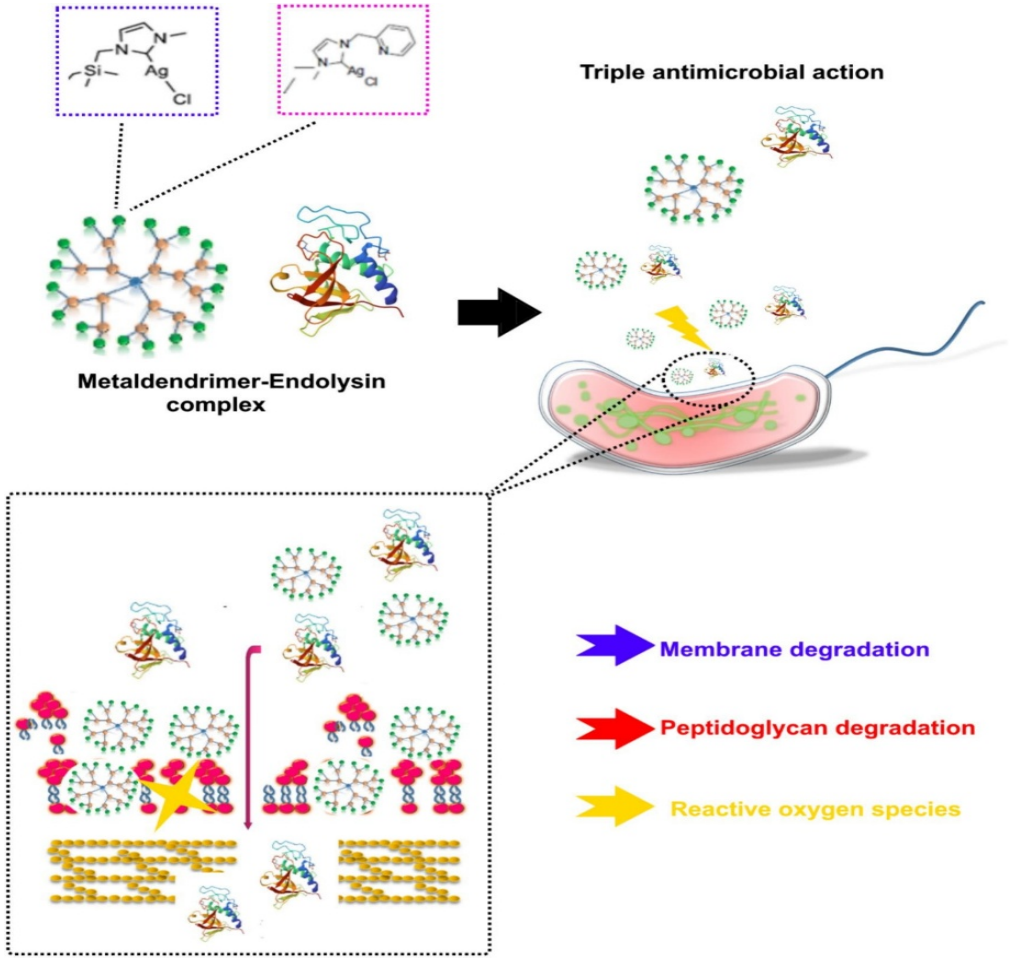

Figure 64. Multimodal mechanism of the combination of metallodendrimer and endolysin against Gram-negative bacteria. Reproduced from Ref. [246], https://doi.org/10.1016/j.ijbiomac.2024.134634, under the terms of the CC BY 4.0 license, https://creativecommons.org/licenses/by/4.0/.

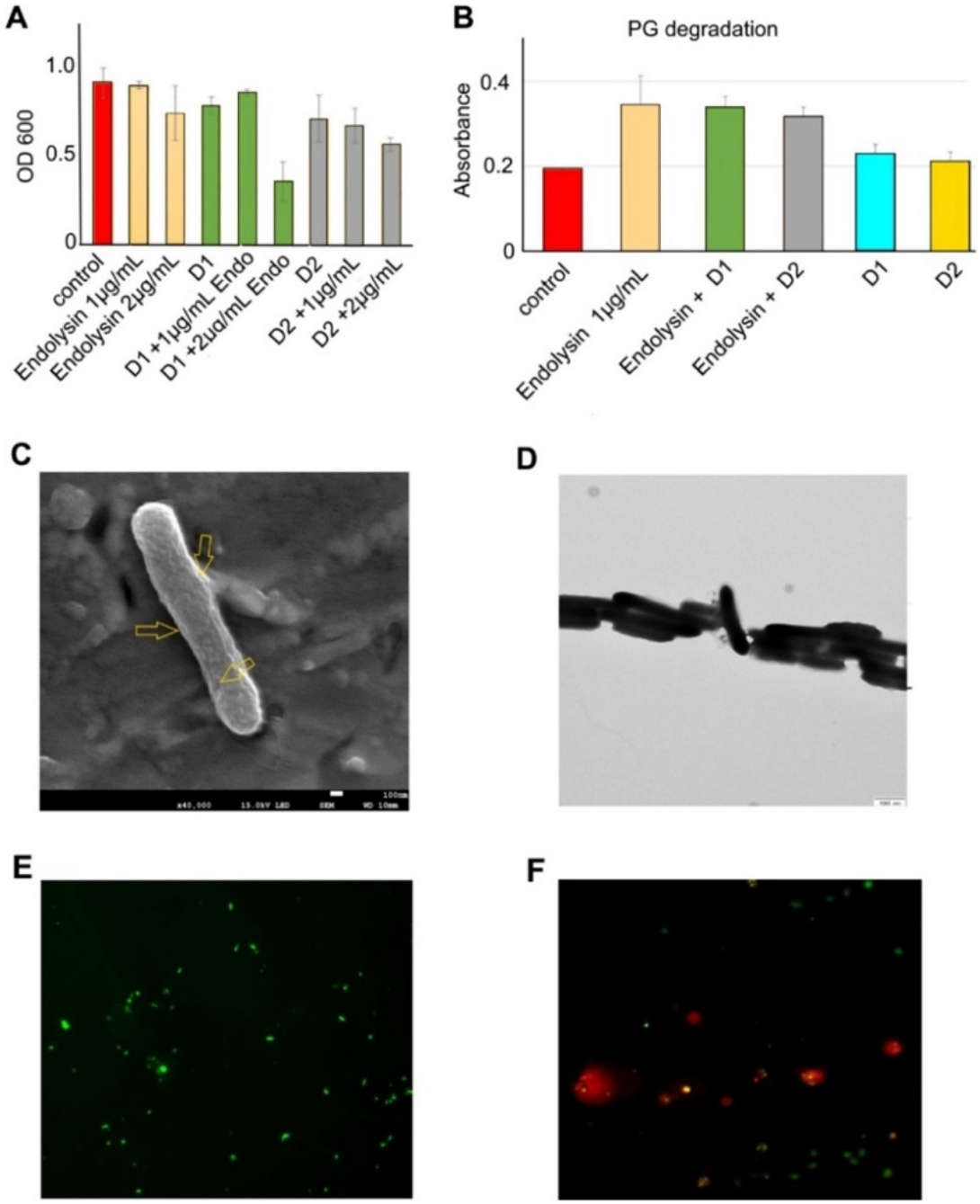

Figure 65. (**A**) Growth inhibition for *P. aeruginosa* treated with two concentrations of endolysin, dendrimer **458** (D1), dendrimer **459** (D2) and various combinations of the dendrimers and endolysin. (**B**) Effect of dendrimers and endolysin on peptidoglycan degradation. (**C**) SEM and (**D**) TEM micrographs of *P. aeruginosa* cells treated with dendrimer **458**. (**E**) LIVE/DEAD staining for *P. aeruginosa* cells treated with dendrimer **458** or (**F**) with dendrimer **458** and endolysin. Reproduced from Ref. [246], https://doi.org/10.1016/j.ijbiomac.2024.134634 (accessed on 5 May 2026), under the terms of the CC BY 4.0 license, https://creativecommons.org/licenses/by/4.0/.

The cyclometallated Au(III) C^N complexes **460-466** (Figure 66) were prepared by Chakraborty et al. [247]. The most active complexes **460** and **463** exhibited strong antibacterial activity against several strains of Gram-positive bacteria, including multidrug-resistant strains such as MRSA, decreasing viable cell count within 1.5 hours at an MIC of 12.5 µM for complex **460** and 6.25 µM for complex **463**. These values were only slightly higher than the MIC of 3.12 µM for the reference drug kanamycin.

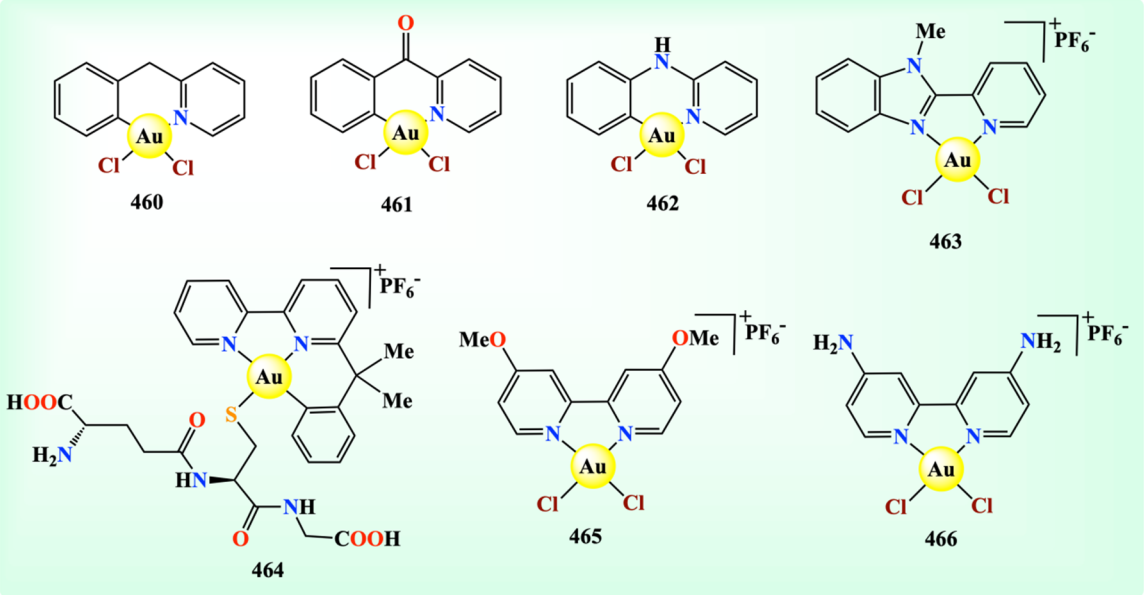

Figure 66. Structures of cyclometallated gold complexes **460-466**.

The mechanism of action for these complexes differs from other common antimicrobial mechanisms such as induction of oxidative stress or disruption of the cell membrane, instead reducing levels of NADH and ATP needed for cellular respiration, resulting in a cell stress response. Figure 67 shows different mechanistic studies using gold-containing complex **460** as a representative example. The growth curves of *B. subtilis* treated with various concentrations of the complex in Figure 67A show a dramatic change at concentrations above half MIC, indicating the inhibitory effect of the complex. Two fluorescence assays were performed, a resazurin microtiter assay (REMA) for NADH (Figure 67B) and an ATP luciferase assay for ATP (Figure 67C). The level of NADH was reduced even further by the gold complex relative to the reference drug vancomycin. ATP was initially reduced only by 50% after five minutes, but after 30 minutes, it was lowered to the same level achieved for cells treated with the positive control carbonyl cyanide *m*-chlorophenyl hydrazine (CCCP), suggesting that this was a downstream effect instead of a direct inhibition of ATP synthesis. On the other hand, depolarisation of the cell membrane was determined by the membrane potential assay with $DiSC_3$ (3,3'-dipropylthiadicarbocyanine iodide), a fluorescent compound that inserts into cell membranes, quenching its fluorescence unless the membrane is depolarized to release it. As shown in Figure 67D, complex **460** at MIC did not show an immediate or large release of the fluorescent $DiSC_3$ from the cell membrane as observed for the reference drug nisin at 30 minutes, indicating that membrane depolarization was not involved in the antibacterial mechanism. The observed fluorescence was concluded to be likely a consequence of release from cells killed by the bactericidal complex. It was also observed that the toxicity of the complex resulted in upregulation of genes related to metal transport and homeostasis. Additionally, the incidence of mutations causing resistance to complex **460** was determined to be $< 10^{-7}$, which is below the 10^{-6} threshold for a potential new drug candidate. Further, no significant toxicity was observed in an ex vivo experiment of mouse liver and kidney tissues exposed to the complex at the MIC after 24 hours. On the other hand, the liver tissue still showed no damage after 48 hours, while the kidney tissue only showed 60% viability. Overall, these results showed strong antibacterial activity for Gram-positive bacteria, low toxicity for healthy cells, and a multimodal mechanism that differs from other metal-based complexes.

Ratia et al. prepared the cyclometallated gold(III) complexes **467**, **468**, and **469** (Figure 68), where **469** was formed from the reaction of complex **468** with D-penicillamine [248]. Of these, complex **468** showed potent antibacterial activity against both Gram-positive and Gram-negative organisms. For Gram-positive strains, such as non-resistant *S. aureus*, MRSA, and *S. epidermis*, MIC values of 4–8 mg/L were achieved, while for Gram-negative stains such as *P. aeruginosa* and *A. baumannii*, MIC values ranged between 16–32 mg/L. The mechanism of action for the complexes was shown to be membrane permeabilization by binding to membrane proteins, which was validated by TEM. The cytotoxicity was examined against two liver cells: healthy THLE-2 and HepG2 tumour cells as human cell line models and the IC_{50} values were 15 mg/L THLE-2 cells and 9 mg/L for HepG2. The authors suggested the cytotoxicity against HepG2 cells was likely a consequence of the anticancer activity which has been observed for gold(III) complexes. Additionally, no acute toxicity was observed *in vivo* for CD1 mice given 1 mg/kg of the complex for 14 days. Both biofilm and planktonic Gram-negative bacteria were less susceptible to complex **468**, which is common for organogold complexes and is believed to be due to the role of

the outer membrane. This was confirmed by the synergistic bactericidal activity of the organogold complex with colistin, which could disrupt the outer membrane. The combination of colistin and complex **468** drastically reduced the MIC of colistin against colistin-resistant *A. baumannii* from 32 mg/L to 1 mg/L. Finally, no development of antimicrobial resistance for complex **468** was observed even after 30 days of serial passages for the bacterial cells.

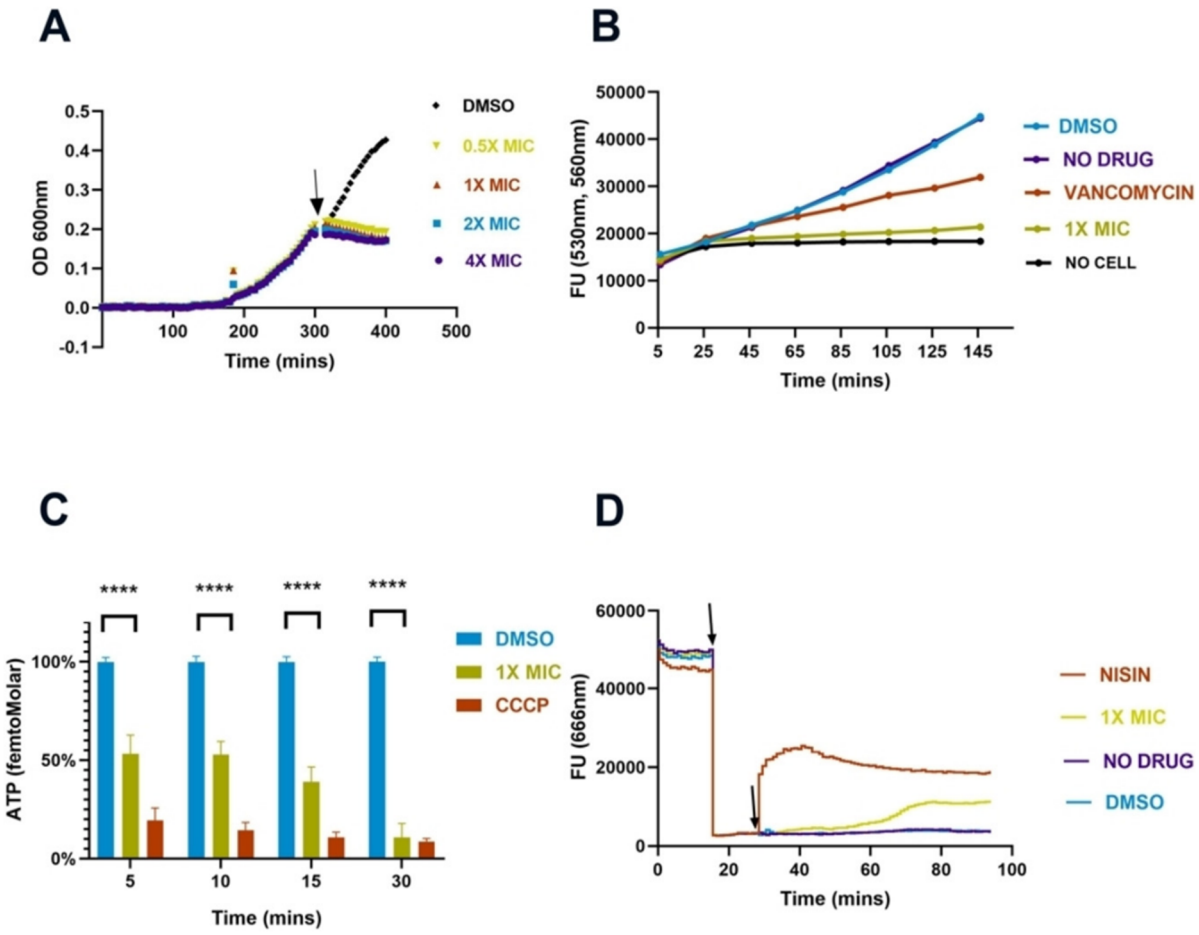

Figure 67. Different concentrations of complex **460** and their effects on (**A**) *B. subtilis* growth and inhibition (measured by optical density at 600 nm), (**B**) NADH production measured by REMA (**** $p < 0.0001$), (**C**) ATP production measured by ATP luciferase and (**D**) membrane depolarization measured by a $DiSC_3$ assay. FU = fluorescence units. Reproduced from Ref. [247], https://doi.org/10.1002/cmdc.202100342, under the terms of the CC BY 4.0 license, https://creativecommons.org/licenses/by/4.0/.

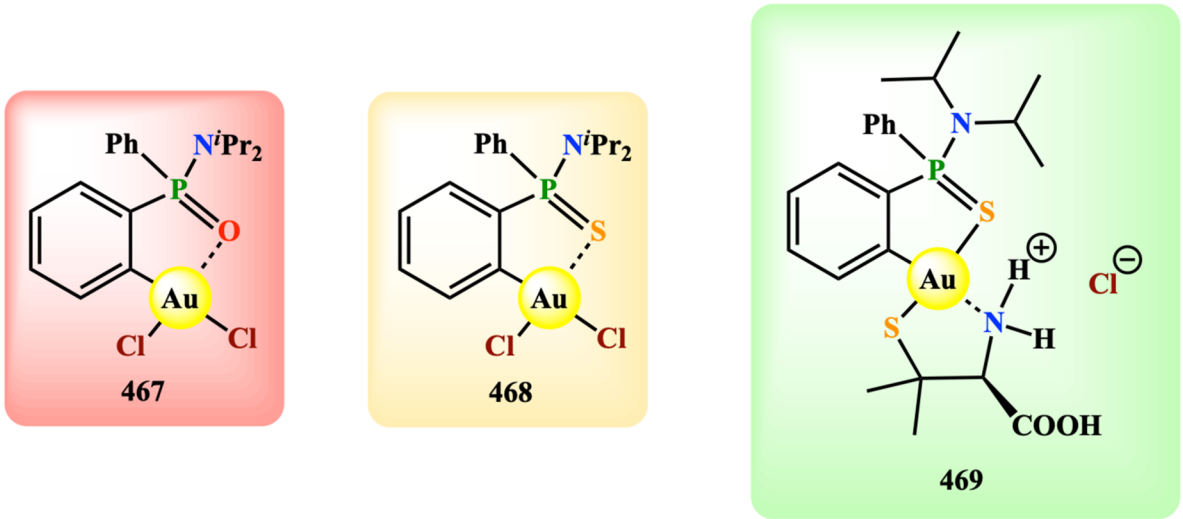

Figure 68. Organogold complexes **467-469**.

The same research group expanded this class of organogold complexes to develop eight complexes containing dithiocarbamate ligands to target clinical strains of MDR veterinary pathogens, as shown in Figure 69 [249]. The cationic complexes **471-477** were derived from the neutral gold complex **470** and were tested against Gram-positive *Staphylococcus* spp. and *Streptococcus uberis*, and Gram-negative *Salmonella* spp., *E. coli*, and *P. aeruginosa*. Complexes **471** and **476** were the most effective against the Gram-positive strains, showing MIC values ranging between 0.03–1 mg/L for complex **471** and 0.06–0.5 mg/L for complex **476**, which were lower than reference antimicrobial vancomycin (MIC = 0.125–64 mg/L). The complexes generally showed selectivity for Gram-positive over Gram-negative strains. On the other hand, the largest complex **476** still exhibited activity against Gram-negative strains with MIC values between 4–8 mg/L, as well as achieving inhibition of Gram-negative biofilms. The combination of complex **476** and colistin caused a three-fold reduction for a colistin-resistant *E. coli* strain compared to the individual MIC values of either compound.

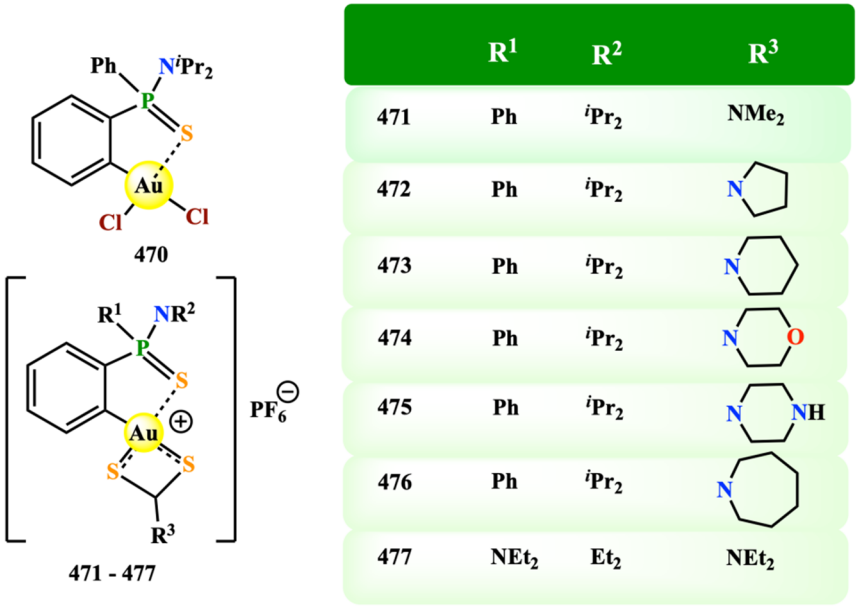

	R1	R2	R3
471	Ph	^{i}Pr$_2$	NMe$_2$
472	Ph	^{i}Pr$_2$	
473	Ph	^{i}Pr$_2$	
474	Ph	^{i}Pr$_2$	
475	Ph	^{i}Pr$_2$	
476	Ph	^{i}Pr$_2$	
477	NEt$_2$	Et$_2$	NEt$_2$

Figure 69. Structures of organogold complexes **470-477** containing dithiocarbamate ligands.

The mechanism of action of these complexes was proposed to be dependent on the type of bacteria. For Gram-negative bacteria, the bulkier complexes were able to intercalate into the lipid bilayer of the outer membrane, resulting in disruption and permeabilization, as illustrated in Figure 70. This effect was synergistic with addition of colistin, which has a similar mechanism, thereby allowing the organogold complexes to more easily access the membrane. For Gram-positive bacteria, the less sterically hindered complexes were able to enter the cell and interact directly with intracellular targets.

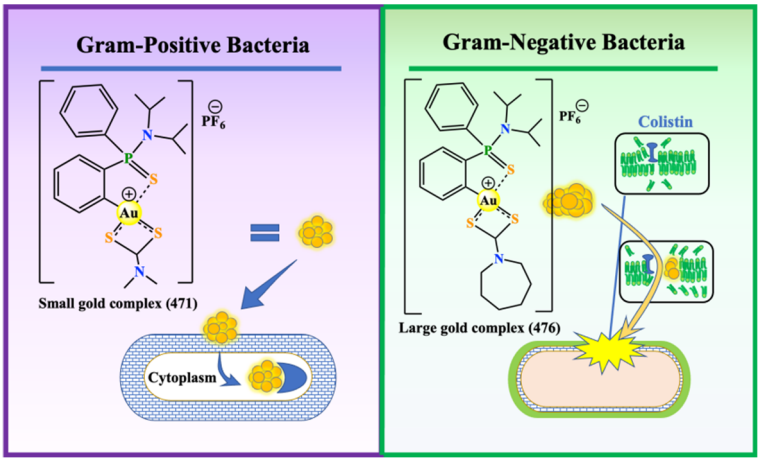

Figure 70. Differences in antibacterial mechanism for smaller organogold complexes (such as complex **471**) in Gram-positive bacteria compared with the mechanism for larger complexes (such as complex **476**) and colistin in Gram-negative bacteria.

4.6. Heterometallic Complexes

4.6.1. Manganese, Iron and Cobalt, Nickel or Copper

The use of macromolecular structures such as dendrimers and polymers in the design of antimicrobial agents has a number of advantages over simple complexes. Compared to individual complexes, a single macromolecule with multiple active moieties can increase the local concentration of the antimicrobial. This also improves binding affinity toward microbial surfaces, reduces the likelihood of drug resistance development, and enhances stability and biocompatibility relative to small-molecule agents. Furthermore, such macromolecular systems allow for controlled release and targeted delivery, thereby improving therapeutic efficacy while minimizing potential side effects. An example of one-dimensional heterotrimetallic coordination polymers with the following metal-metal cores $\{Cu_2Fe\}_n$ (**480**), $\{Cu_2Mn_4Fe\}_n$ (**481**), $\{Co_2Mn_4Fe\}_n$ (**482**), and $\{Ni_2Mn_4Fe\}_n$ (**483**) were reported by Uvarova et al. [250] The synthesis of these polymers involved the reaction of transition metal carboxylates possessing 'paddle-wheel' structures with a (bis)diethoxyphosphoryl ferrocene ligand to self-assemble into staircase-shaped 1D chains, as shown in Scheme 49.

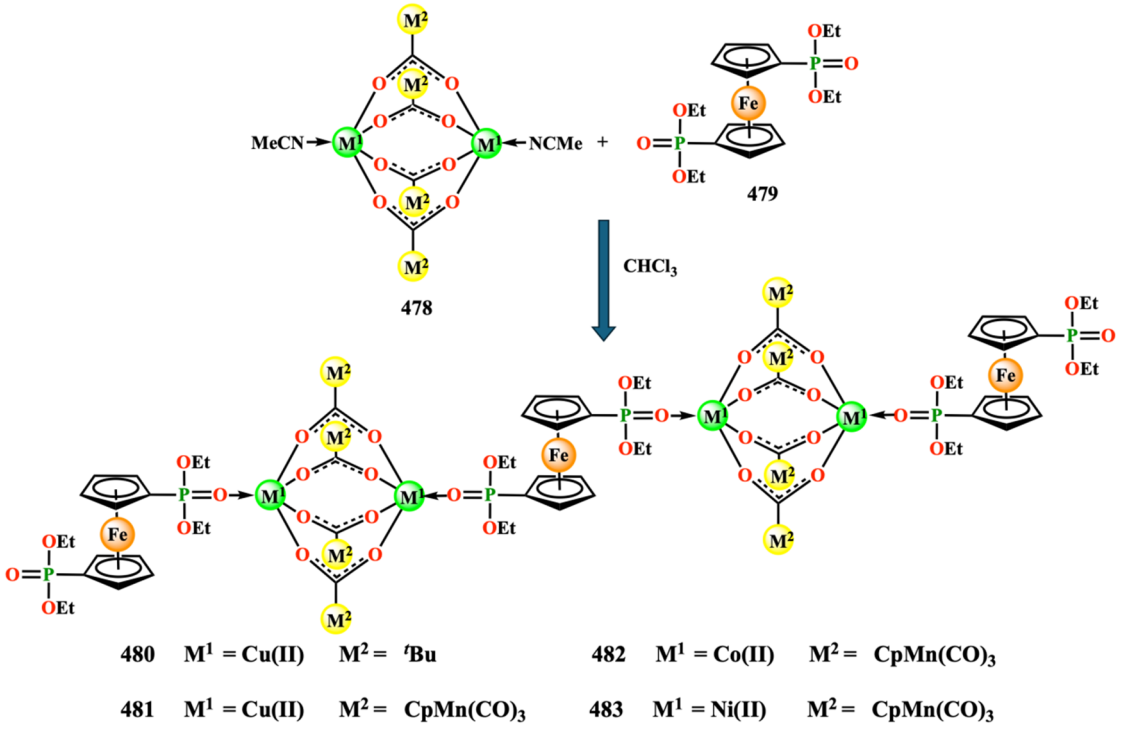

Scheme 49. Design of one-dimensional heterotrimetallic coordination polymers **478**-**483**.

To determine the in vitro activity against tuberculosis, *Mycobacterium smegmatis* was used as a model organism for the primary cause of tuberculosis, *Mycobacterium tuberculosis*. *M. smegmatis* is a fast-growing, non-pathogenic mycobacterium commonly used in the primary screening of anti-tuberculosis agents. Compounds **480** and **481** showed significant inhibitory activity, with MIC values of 6.25 nmol/disk for compound **480** and 100 nmol/disk for compound **481**, compared to 5 nmol/disk for the reference drug rifampicin. The MIC for compound **480** is higher than either component used to prepare it: copper pivalate (MIC = 1000 nmol/disk) or (bis)diethoxyphosphoryl ferrocene (MIC = 250 nmol/disk). The authors therefore concluded that the coordination polymer yielded a potent synergistic effect for the antibacterial activity. It should be noted, however, that this has not been compared with co-administration of the two components to determine whether this synergistic effect is specific to the polymer. Furthermore, the polymer has not been assessed for cytotoxicity against mammalian cells, so this could be offset by a decrease in toxicity, but further research would be required to validate this.

4.6.2. Manganese and Ruthenium

The Ru(II)-*p*-cymene moiety was also employed for its antimicrobial activity by Wojtala et al., who reacted ruthenium complexes conjugated with the fluoroquinolone antibiotics ciprofloxacin **(484)** or norfloxacin **(486)** with $MnCl_2.4H_2O$ to give the corresponding heterobimetallic complexes **485** or **487** as illustrated in Scheme 50 [251]. Broad spectrum antibacterial activity was observed for mononuclear Ru(II) complexes **484** and **486**, giving

them the ability to target Gram-negative *E. coli* and *Yersinia enterocolitica* as well as gram-positive *E. faecalis, B. subtilis,* and *M. luteus*, unlike the fluoroquinolone alone or phosphino-fluoroquinolone conjugates. On the other hand, introduction of the Ru(II)-*p*-cymene complex decreased the antimicrobial activity. The antimicrobial activity was not improved by addition of Mn(II) in the heterobimetallic complexes **485** and **487**. As an example, while the MICs of ciprofloxacin and its phophino-conjugate for *K. pneumoniae* were both 0.0040 μg/mL, the Ru(II) complex with ciprofloxacin **484** had an MIC of 0.0625 μg/mL, while an MIC of 0.2500 μg/mL was detected for the ciprofloxacin-containing Ru(II)-Mn(III) complex **485**. Complex **487** with norfloxacin even became ineffective against *M. luteus* in comparison with the mononuclear Ru(II) complex **486** with norfloxacin (MIC = 4.0 μg/mL). The observed increase in MIC values was concluded to be a consequence of the Mn(II) moiety imposing steric constraints or resulting in less favourable electrostatic and hydrogen bonding interactions of the fluoroquinolone moieties with the bacterial targets.

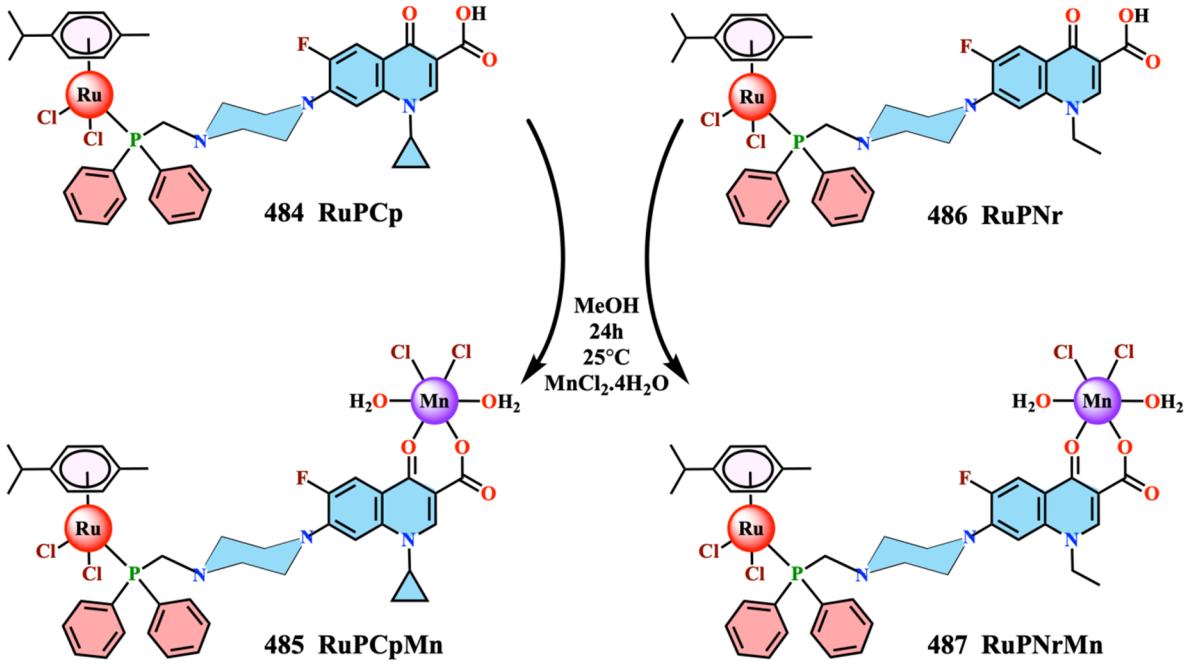

Scheme 50. Heterobimetallic Ru(II)-Mn(II) complexes with conjugated ciprofloxacin (**485**) and norfloxacin (**487**).

4.6.3. Gold and Silver or Mercury

To investigate the impact of multiple metallic moieties, four heterobimetallic Au(I)–Ag(I) and Au(I)-Hg(I) complexes with various methyl or ethyl substituted *bis*-NHC ligands **495-498** were prepared by Li et al. [252]. The organic compound *bis*(imidazol-1-yl)methane (**488**) gave rise to the cationic methyl or ethyl-substituted ligands **489** and **490**, which were then metallated to form mononuclear Au complexes **491** and **492**. These complexes then were modified with an N-ethyl substituent to yield mononuclear complexes **493** and **494**, to which Ag or Hg were added to produce the heterobimetallic complexes **495-498**, as shown in Scheme 51. The heterobimetallic Au(I)-Ag(I) complexes **495** and **496** were evaluated for their antibacterial efficacy and both displayed equivalent broad-spectrum activity against Gram-positive and Gram-negative bacteria. For the Gram-positive bacteria, both complexes exhibited MICs of 8–16 μg/mL for *E. faecium* and 16–32 μg/mL for *S. aureus*, while the MIC values for Gram-negative bacteria were 4–8 μg/mL for *A. baumannii* and 16 μg/mL *E. coli*. By contrast, the homobimetallic Au (I) complex with ethyl substituents (analogous to complexes **496** and **498**) and its corresponding organic ligand exhibited no significant antimicrobial efficacy, while the homobimetallic Ag(I) complex with ethyl substituents showed similar activity to the heterobimetallic complexes with MIC values of 16 for *E. faecium,* 32 μg/mL *for S. aureus*, 8 μg/mL for *A. baumannii* and 16–32 μg/mL for *E. coli.* These findings indicate the critical role the Ag(I) moiety played in the antimicrobial activity.

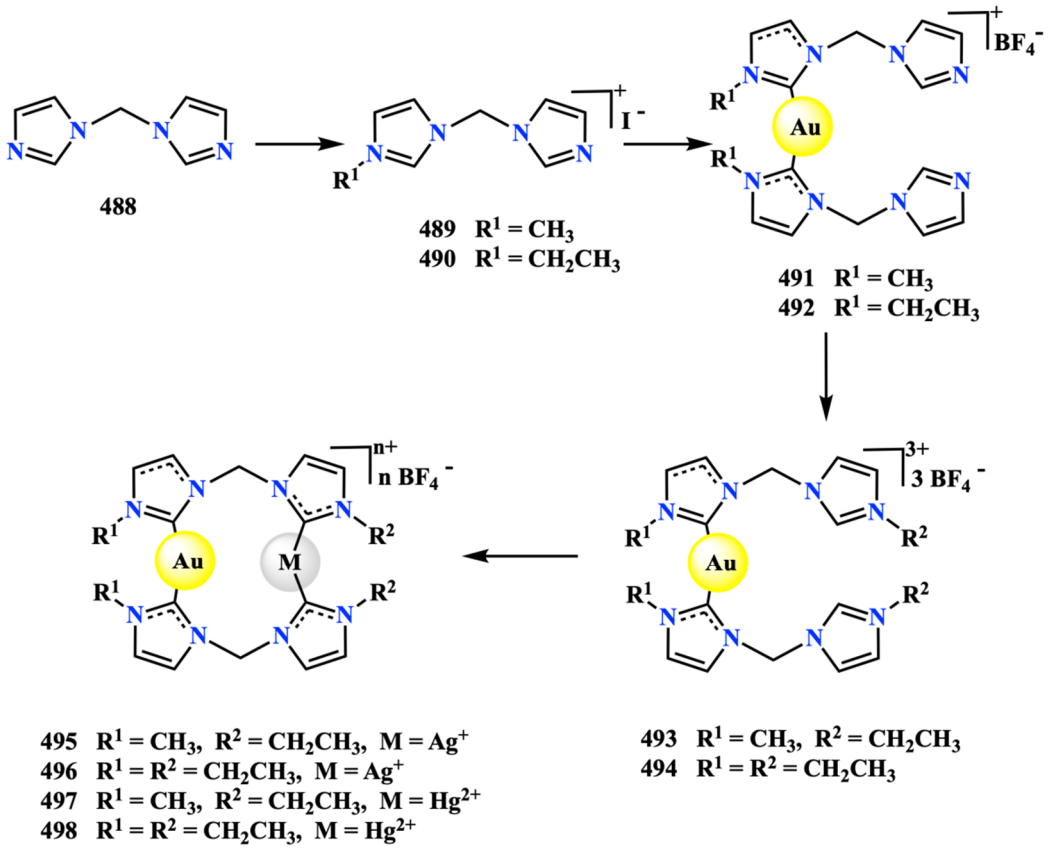

Scheme 51. Synthesis of heterobimetallic Au(I)–Ag(I) and Au(I)-Hg(I) complexes **495-498** with various *bis*-NHC ligands.

Antimicrobial organometallic materials have proven to be effective against various bacterial and fungal species. The combination of an antimicrobial organic compound with a metal moiety has been shown to bypass drug resistance, as well as potentially enhancing the activity of the drug. The ability of organometallic molecules and macromolecules to inhibit development of drug resistance is typically a consequence of multimodal activity, due to a combination of the individual activities of the organic ligands and the metal moiety. As a result, AMR is less likely to be evolved in response to multiple mechanisms simultaneously. Conversely, the metal moieties may cause a decrease in cell uptake and transport across biological membranes, which may reduce the overall antimicrobial efficacy. Furthermore, the metal moieties themselves may be toxic, especially if the free metals are released by metabolic processes. On the other hand, the tunability of organometallic structures may afford new methods to overcome these limitations.

5. Pharmaceuticals with Other Therapeutic Activities

While organometallic complexes with antimicrobial and antiproliferative activities have been extensively covered in this review and in the literature, there are much fewer examples for organometallic complexes with other therapeutic activities, including antiparasitic, antiviral, anti-inflammatory and anti-neurodegenerative. To ensure that this review encompasses these activities, several recent examples of each class will be briefly highlighted.

5.1. Antiparasitic

Parasitic organisms, including mosquitos, flies, ticks, and pathogenic protozoa, have a major impact on human and animal health around the world [253,254]. In particular, parasites are responsible for diseases of global importance such as malaria (*Plasmodium* spp.), leishmaniasis (*Leishmania* spp.), sleeping sickness (*Trypanosoma cruzi*) and toxoplasmosis (*Toxoplasma gondii*) [255]. Although immune responses have evolved to target parasites, parasitic organisms have also developed means of modifying the metabolism of host immune cells to establish long-term infection [256]. New antiparasitic drugs are therefore required to control the spread of parasitic diseases [257]. Metal-containing drugs have demonstrated potential for treatment of parasites, including overcoming resistance to conventional antiparasitic agents as well as the ability to specifically target intracellular parasites [258,259]. The

specific and tunable toxicity of organometallic complexes has primarily been examined for their antimicrobial or anticancer activities; however, certain organometallic structures have also exhibited antiparasitic activities.

Heterobimetallic complexes containing both ferrocene and Au(I)-NHC moieties (Scheme 52) were prepared by Al Nasr et al. for their antiparasitic activity [260]. These complexes were composed of Au(I)-NHC complexes conjugated with ferrocene to enhance their activity against parasitic protozoa. The neutral complexes **499-501** contained a gold moiety with a chloro ligand, while cationic complexes **504-506** possessed a phosphino ligand. In addition, several *bis*-complexes containing Au-NHC moieties were also prepared, where complexes **502** and **503** were connected through the ferrocene and complex **507** was connected through the gold centre. The antiparasitic activity of these complexes was then evaluated against two parasites, *Toxoplasma gondii* and *Leishmania major*, using Vero cells as a mammalian cell model. The selectivity index (SI) was calculated by dividing the cytotoxic concentration for host cells over the effective concentration to inhibit parasite growth. All complexes were found to be toxic against both *L. major* promastigotes (the extracellular form of *L. major* cells that infect mammalian hosts) and *T. gondii* tachyzoites (*T. gondii* cells that act as intracellular parasites). Complexes **500** and **501** containing chloro groups showed higher antiparasitic activity (IC_{50} values of 0.040 μM for complex **500** and 0.022 μM for complex **501**) compared to the corresponding phosphino-substituted complexes **505** and **506** (IC_{50} values of 0.098 μM for complex **505** and 2.52 μM for complex **506)**. The toxicity against *L. major* amastigotes, the intracellular parasitic *form that* infect mammalian host cells, was also examined using mouse macrophages infected with *L. major* amastigotes. The ferrocene-bridged bis-Au(I) complexes **502** and **503** were highly effective against *L. major* amastigotes, with IC_{50} values <0.12 μM and <0.10 μM, respectively, as well as displaying the highest selectivity for the amastigotes over macrophages (SI > 10.4 and SI = 6.8, respectively).

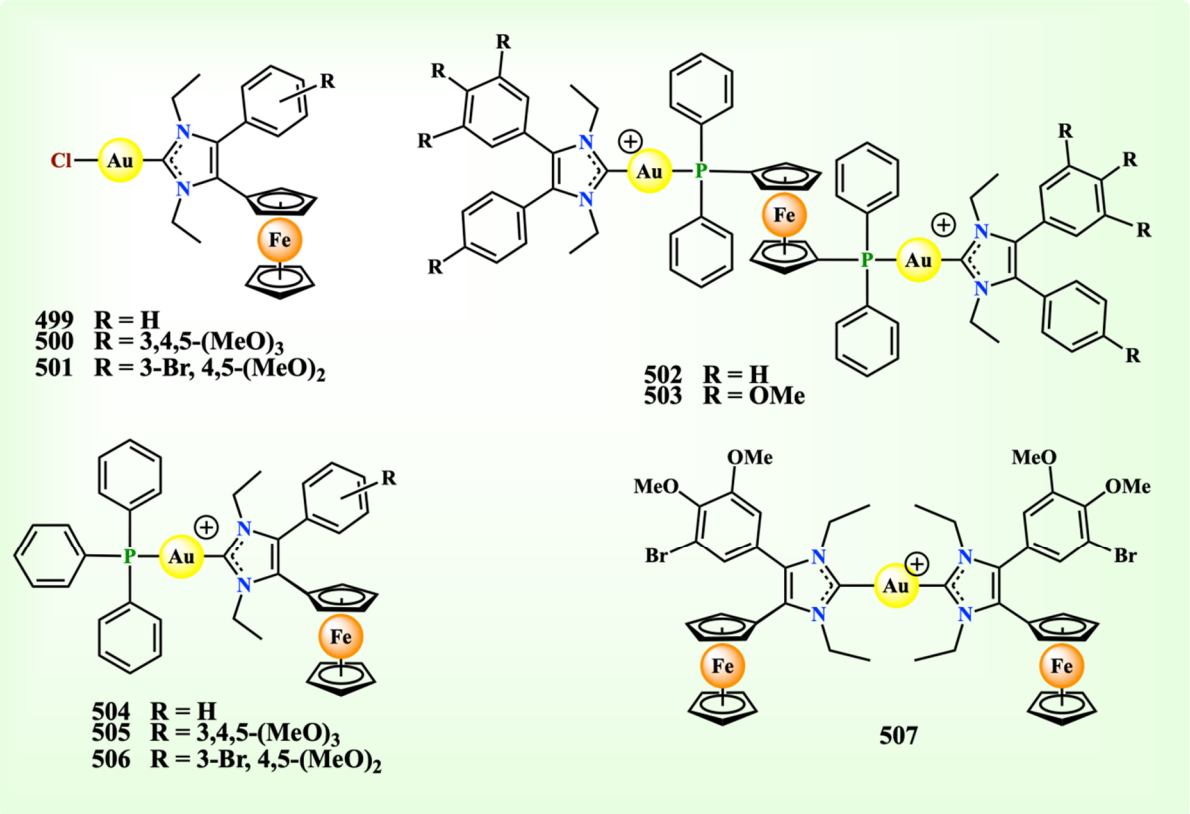

Scheme 52. Heterobimetallic complexes **499-507** containing both ferrocene and Au(I)-NHC moieties.

The group of Toro and coworkers examined the antiparasitic activity of organometallic complexes containing iron or rhenium moieties against two species of trypanosomes, namely *Trypanosoma cruzi*, which causes Chagas disease, and *T. brucei*, which is responsible for African trypanosomiasis (also known as sleeping sickness) [261]. The ferrocenyl complex [Fe(η^5-C_5H_5){(η^5-C_5H_4)-C(O)-NH-NH_2}] (**508**) was reacted with 2-formyl-5-nitrofuran (**509**) or 2-acetyl-5-nitrofuran (**510**) to yield iron-containing complexes **511** and **512**, as described in Scheme 53. Similarly, the tricarbonyl rhenium-containing complex [Re{(η^5-C_5H_4)-C(O)-NH-NH_2}$(CO)_3$] (**513**) underwent similar reactions to yield the formyl-substituted complex **514** and the acetyl-substituted complex **515**. The inhibitory activity against *T. cruzi* epimastigotes, an extracellular cell form that can multiply in the insect vector, and *T. brucei* trypomastigotes, an extracellular form that is transmitted between the animal vector and human host

(or vice versa), was observed, and the L6 rat skeletal muscle cell line was used as a model of mammalian host cells. The IC_{50} values were calculated and compared to the reference antiparasitic nifurtimox. It was observed that the Re-containing complexes were more active than the ferrocenyl complexes against either species, with the most active complex being the acetyl-substituted Re-containing complex **515**. Both Re-containing complexes **514** and **515** were more effective against *T. cruzi* epimastigotes (IC_{50} = 3.54 μM and 2.76 μM, respectively) than nifurtimox (IC_{50} = 4.22 μM). For the *T. brucei* trypomastigotes, Re-containing complexes **514** and **515** as well as the formyl-substituted Fe-containing complex **511** all exhibited lower toxicity with IC_{50} values of 0.78 μM, 0.28 μM and 2.42 μM, respectively, relative to nifurtimox (3.56 μM). The selectivity for parasites over mammalian cells was improved for the formyl-substituted complexes **511** and **514** against *T. brucei* trypomastigotes, with SI values of 26.8 and 31.2, respectively. On the other hand, none of the complexes exhibited higher SI values than nifurtimox compared to *T. cruzi*. The mechanism of these complexes, specifically the acetyl-containing complexes **512** and **515**, was shown to be more effective against parasites expressing high levels of the type I nitroreductase enzyme TbNTR1. This suggested that the mechanism involved opening of the furan ring to form nitrile groups, which are believed to be responsible for the antiparasitic mechanisms of drugs such as nifurtimox.

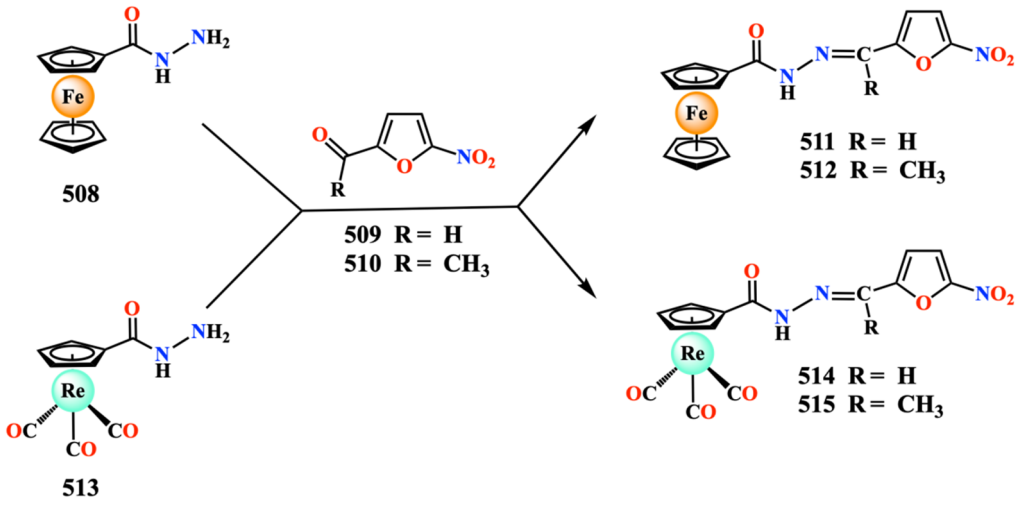

Scheme 53. Preparation of Fe-containing complexes **511** and **512** and Re-containing complexes **514** and **515** with nitrofuran moieties.

The Toro group has also examined other antiparasitic iron- or rhenium-containing complexes with nitrofuran, nitrothiophene or nitrobenzene groups [262,263]. For example, complexes containing iron or rhenium were prepared where the metal moiety was connected to the nitrile end of an N-acylhydrazone, which was functionalized with either a nitrofuran or a nitrothiophene moiety [262]. Ferrocene carboxaldehyde (**137**) and the tricarbonyl half-sandwich rhenium complex **109** were reacted with 5-nitro-2-furancarbohydrazide (**516**) or 5-nitro-2-thiophenecarbohydrazide (**517**) to yield the nitrofuran-functionalized complexes **518** and **519**, as well as nitrothiophene-functionalized complexes **520** and **521**, as illustrated in Scheme 54. The highest selectivity was observed by Fe-containing complex **520** with a nitrothiophene moiety, which exhibited with no measurable activity against L_6 cells (IC_{50} > 200 μM), but was also the least active against either *Trypanosoma* species (46.6 μM for *T. cruzi* epimastigotes and 9.86 μM for *T. brucei* trypomastigotes). Conversely, the most effective complex **521** was only superior to nifurtimox against *T. brucei* (IC_{50} = 2.25 μM for complex **521** and 3.56 μM for nifurtimox), but displayed a lower SI of 1.84 for L_6 over *T. cruzi* cells and 7.45 for L_6/*T. brucei* for complex **521**, compared to SI values of 21 for L_6/*T. brucei* and 24.9 for L_6/*T. brucei* for nifurtimox. These findings indicated that these complexes were generally less effective than the analogous complexes **511**, **512**, **514** and **515**, which highlighted the importance of the position of the N-acylhydrazone between the nitro group and the metal moiety. Also, compared with the Re-containing complex **519** with a nitrofuran group, complex **521** with a nitrothiophene resulted in a decrease in negative charge on the heterocyclic moiety, which was shown to result in an increase in both activity and selectivity against *Trypanosoma* species.

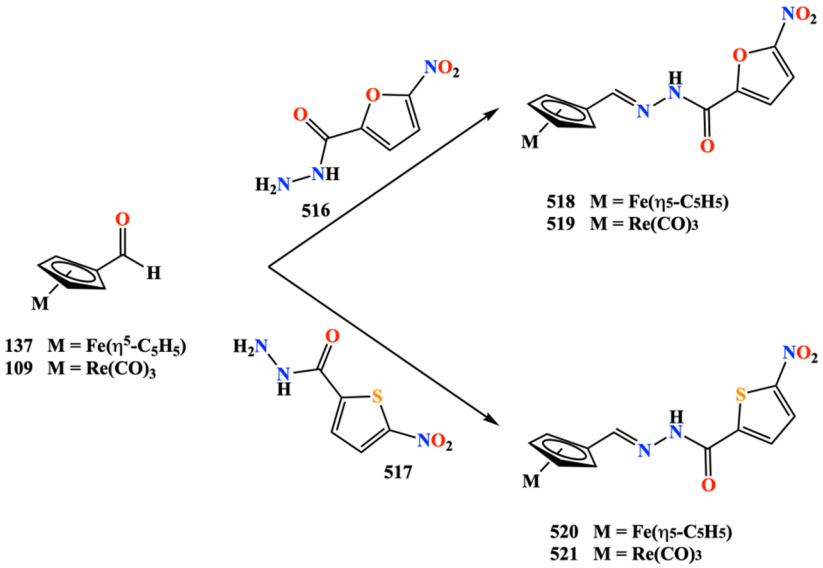

Scheme 54. Design of iron- and rhenium-containing complexes with nitrofuran moieties (**518** and **519**) and nitrothiophene moieties (**520** and **521**).

Four derivatives of artesunate, a semisynthetic compound derived from the antimalarial agent artemisinin isolated from *Artemisia annua* (wormwood), were prepared with ferrocenyl moieties by Munnik et al. [264]. As shown in Scheme 55, artesunate (**522**) was reacted with *N*-(hydroxyethyl)ferrocenamide (**523**) to yield complex **524**, ferrocene methanol (**525**) to yield complex **526**, *N*-(2-aminoethyl)ferrocenamide (**527**) to yield complex **528** or ferrocene methylamine (**529**) to yield complex **530**.

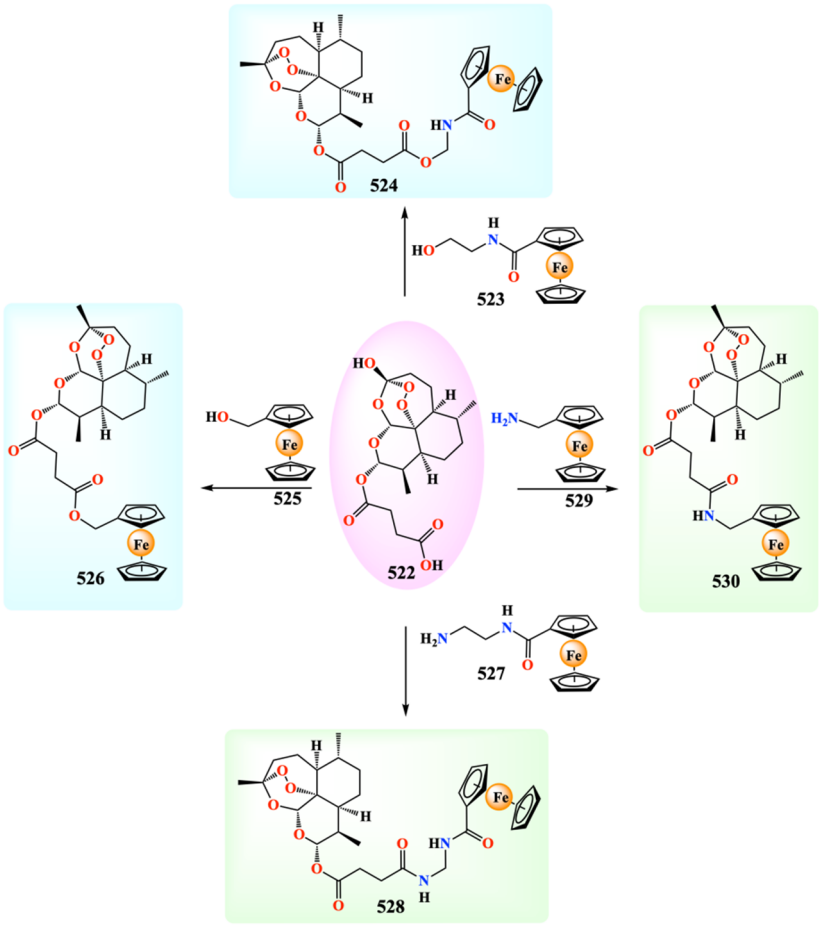

Scheme 55. Ferrocene-containing complexes **524**, **526**, **528** and **530** derived from artesunate (**522**).

In vitro cytotoxicity studies showed that the lowest IC_{50} value against *T. gondii* was exhibited for complex **526** (280 nM), while the highest IC_{50} was observed for complex **528** (1200 nM), and complexes **524** and **530** were in the middle with IC_{50} values of 680 nM and 600 nM, respectively. Unfortunately, complexes **526** and **530** were hydrolyzed rapidly in solution, with half-lives of 3 minutes and 9 minutes, respectively. It should be noted, however, that these two complexes were the most effective of the four ferrocenyl-artesunate derivatives, which suggests the hydrolysis products were responsible for the antiparasitic activity. None of the complexes were as effective as artesunate, with an IC_{50} of 200 nM. Since both ferrocene and artesunate are known to be capable of generating ROS, the ROS production was measured for complexes **524**, **528** and **530** by comparison of growth with and without addition of the ROS scavenger N-acetyl cysteine (NAC). All tested complexes as well as artesunate displayed lower inhibition upon addition of NAC, as shown in Figure 71, indicating an ROS-dependent mechanism of action. Additionally, the inhibition of *Plasmodium falciparum* strain NF54 by complexes **524**, **526**, **528** and **530** were also investigated, with the most active complexes **526** and **530** showing the lowest IC_{50} values 19 μM for complex **526** and 12 μM for complex **530**. Complexes **524** and **528** had significantly lower activity, with IC_{50} values 3 400 nM and 4 900 nM). As with T. *gondii*, however, all ferrocenyl complexes were less effective than artesunate (IC_{50} = 3 nM). Despite the lower effectiveness of the complexes against either parasite species, all four complexes exhibited low cytotoxicity, with no observed toxicity against the human prostate (PNT1A) cell line. Only complexes **526** and **530** exhibited low toxicity towards HEK293 cells, with IC_{50} values of 53 000 nM and 34 000 nM, still resulting in excellent selectivity for both *T. gondii* and *P. falciparum.*

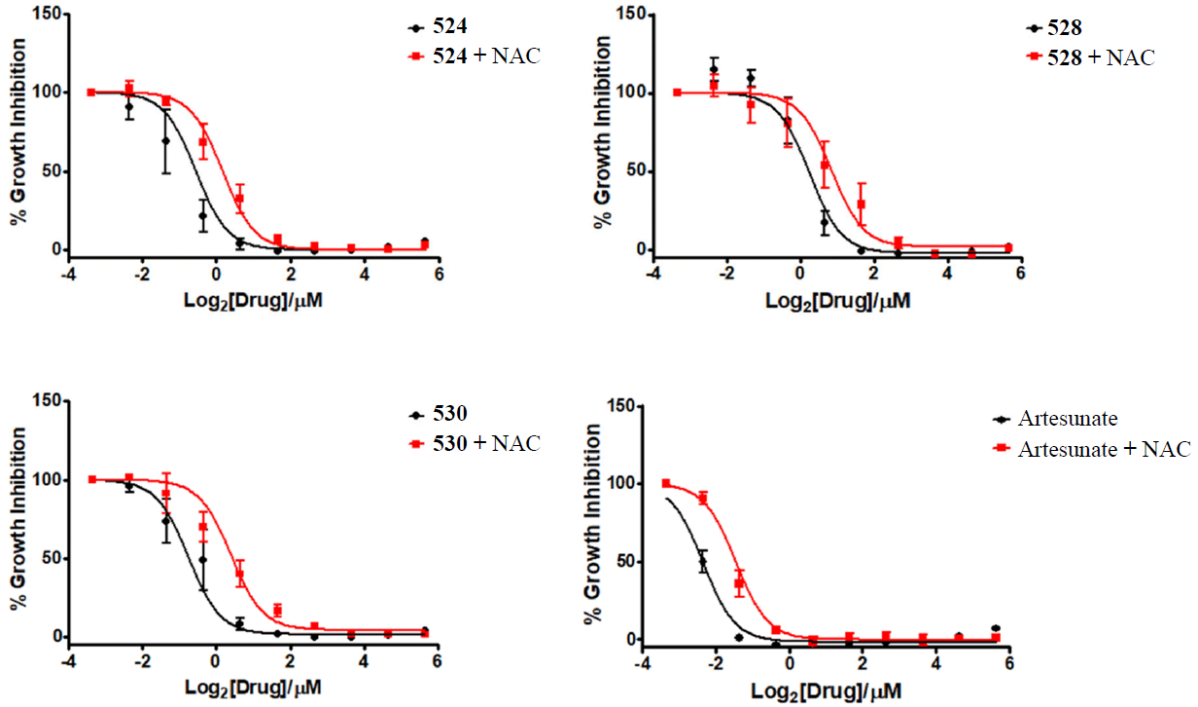

Figure 71. Inhibition of growth due to ROS generation in *T. gondii* cells treated with complexes **524**, **528**, **530** or artesunate (**522**), with or without addition of 5 mM N-acetylcysteine (NAC). Reproduced with permission from Ref. [264], https://doi.org/10.1039/D3DT02254D, under the terms of the CC BY 3.0 license, https://creativecommons.org/licenses/by/3.0/.

Betts et al. used another commercial antiparasitic drug, decoquinate, as a scaffold for organometallic derivatives with activity against *T. gondii* [265]. These compounds consisted of decoquinate with various substitution patterns, including N-linked ferrocenylmethyl (**531**), ruthenocenylmethyl (**532**), benzyl (**533**), (2-ferrocenylvinyl)methyl (**534**), (2-ruthenocenylvinyl)methyl (**535**) and (2-phenylvinyl)methyl (**536**) groups, as well as the O-linked (2-phenylvinyl)methyl derivative (**537**), as shown in Scheme 56.

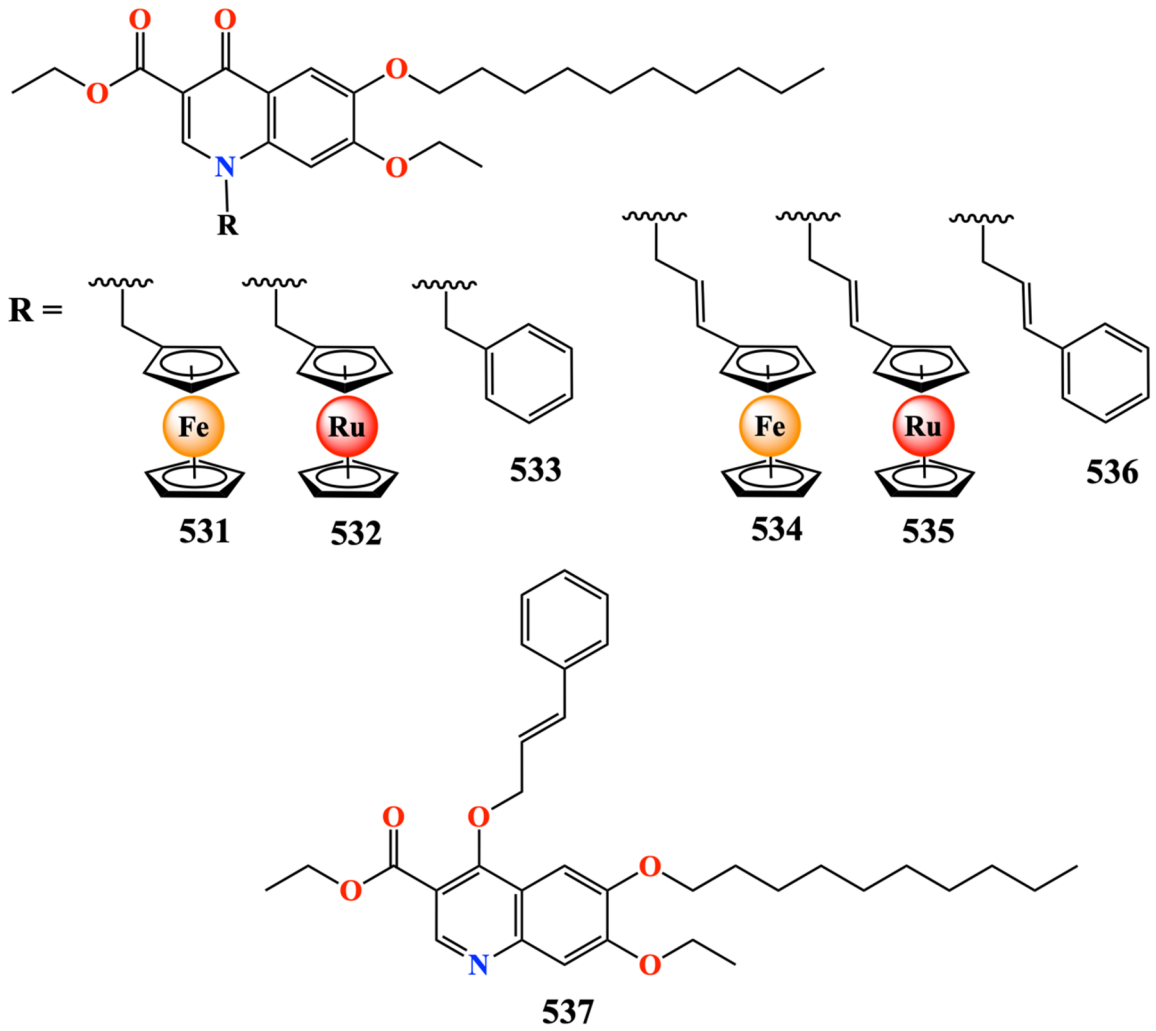

Scheme 56. Substituted compounds and complexes **531-537** based on decoquinate.

Transgenic *T. gondii* tachyzoites with constitutive expression of the β-galactosidase enzyme from *E. coli* were used to measure proliferation via a fluorescent chlorophenol red-β-d-galactopyranoside assay. The IC_{50} values for Fe-containing complex **531**, benzyl-containing compound **533** or Ru-containing complex **535** could not be calculated, as the inhibitory effect did not plateau at the maximum concentration of 2.5 μM. The greatest inhibition against *T. gondii* was observed for both of the (2-phenylvinyl)methyl containing derivatives **536** and **537**, both of which had IC_{50} values of 0.6 μM, followed by the Ru-containing complex **532** (IC_{50} = 0.7 μM), and the Fe-containing complex **534** (IC_{50} = 1.4 μM). Also, none of the derivative compounds were observed to have any effect on viability of human foreskin fibroblast (HFF) cells at concentrations up to 2.5 μM. However, the starting material decoquinate was still more effective than any of the derivatives, as it showed an IC_{50} of 0.0024 μM.

The ferrocenyl-quinoline hybrids **538-541** (Figure 72) were designed to improve the biological activity of quinoline compounds against *L. major* with a goal of overcoming resistance or reducing host toxicity [266]. Figure 73 shows the concentration-dependent effect of each hybrid on the viability of *L. major* promastigotes, as well as the reference drug amphotericin B. The amino-linked complex **539** was the only complex to exhibit higher activity than amphotericin B, with IC_{50} values of 1.16 μM and 2.10 μM, respectively. The IC_{50} values of remaining complexes were higher than amphotericin B, with 69.49 μM for the imine-linked complex **538**, 8.83 μM for the imidazole-linked complex **540** and 86.27 μM for the ethenyl)phenyl-linked complex **541**. However, higher cytotoxicity was observed against macrophages, yielding lower SI values (≤2.11) for all four complexes, while toxicity against amphotericin B was outside of the tested range, yielding a high SI value (>25). Complexes **539** and **540** were therefore identified as potential scaffolds for further antileishmanial drug design.

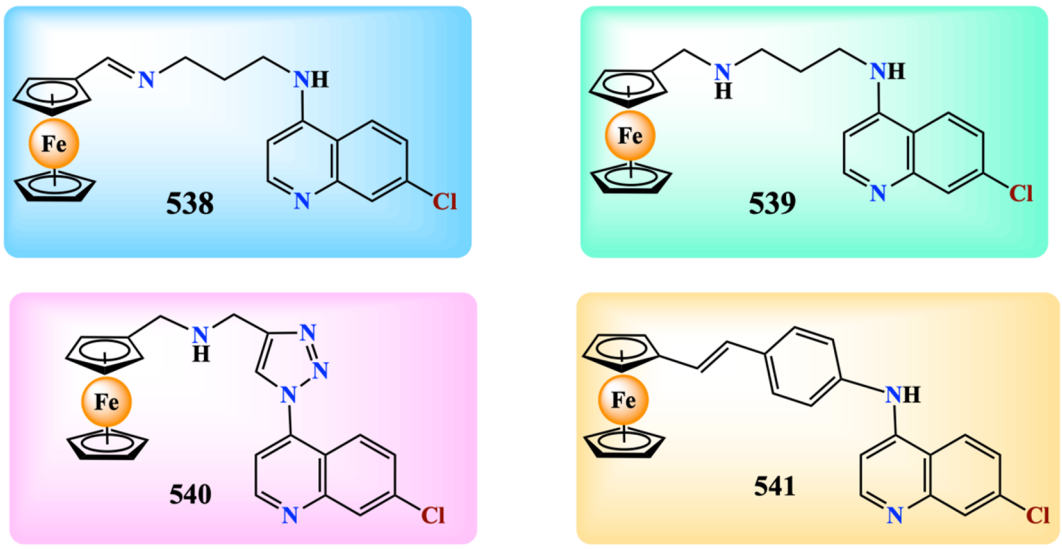

Figure 72. Structures of hybrid ferrocenyl-quinoline complexes **538-541**.

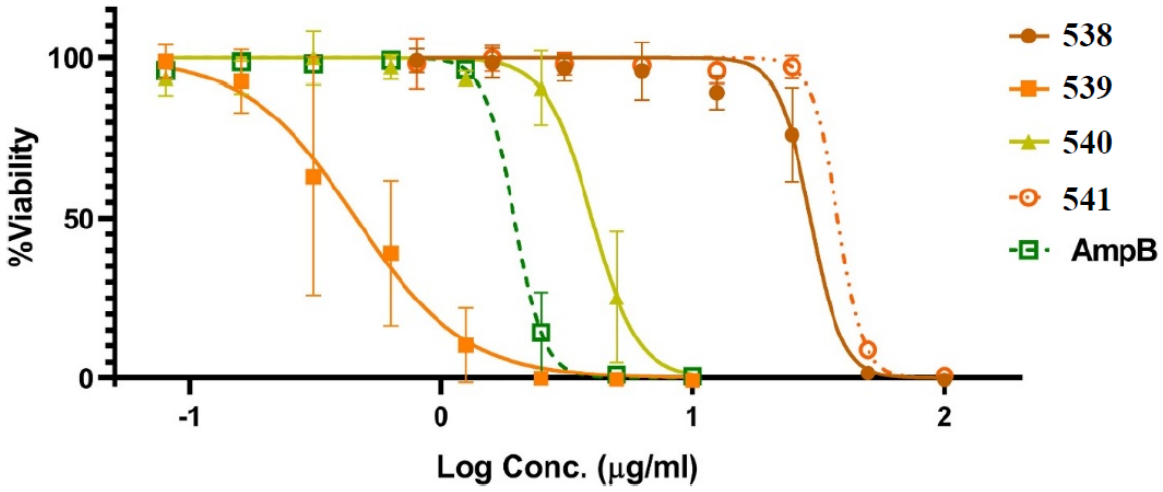

Figure 73. Concentration-dependent viability of *L. major* promastigotes treated with complexes **538-541** or amphotericin B. Reproduced with permission from Ref. [266], https://doi.org/10.1016/j.jorganchem.2025.123935, under the terms of the CC BY 4.0 license, https://creativecommons.org/licenses/by/4.0/.

The group of Furrer, Păunescu and Hemphill have designed ruthenium(II)-arene complexes and analyzed their antiparasitic activities in vitro and *in vivo* [267–273]. To illustrate the importance of this class of ruthenium complexes, we will highlight a few examples against *Toxoplasma gondii* and *Trypanosoma brucei* [274–276]. For example, dinuclear *p*-cymene-ruthenium complexes with bridging thiol units were used to target the mitochondria of the intracellular parasite *Neospora caninum*, the causative organism for neosporosis in dogs [274]. The best candidates identified by the authors included complexes where one of the bridging thiols was functionalized with a phenyl group (**542**), a *t*-butylphenyl group (**543**) or a phenol group (**544**), as illustrated in Figure 74.

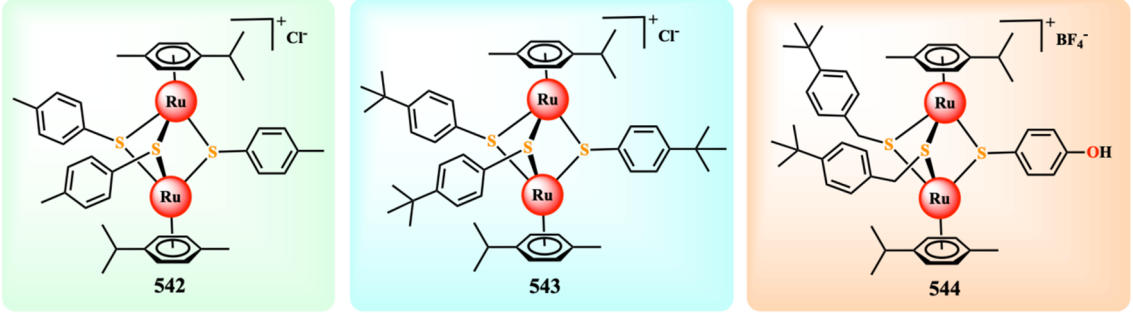

Figure 74. Ru-bridged complexes **542-544**.

The antiparasitic activity of *N. caninum* infecting HFF cells (as a host model) was examined, and low IC_{50} values were observed for all three of the most effective candidates: 15 nM for complex **542**, 5 nM for complex **543** and 1 nM for complex **544**. Additionally, the viability of HFF cells was unaffected by all three complexes, even above a concentration of 5 μM (5 000 nM). The effects on *N. caninum* cells within the HFF host cells were investigated using transmission electron microscopy (TEM). While all three candidates showed similar effects, TEM micrographs of infected HFF cells treated with complex **544** are shown as a representative example. After 6 hours, the intracellular vacuoles of HFF cells containing *N. caninum* cells exhibited lighter coloured mitochondria due to decreased electron density (Figure 75A), although the mitochondria of the host cells were unaffected. This effect was not observed for other organelles including the secretory organelles rhoptries, dense granules and micronemes, however, indicating low impact on other cellular functions. However, after a total of 24 hours, shown in Figure 75B, the mitochondria were no longer observable and the *N. caninum* cells instead displayed large empty vacuoles as well as vacuoles filled with tight stacks of membranes, which are characteristic of autophagosomes involved in autophagic cell death. By the 72-hour time point, the vacuoles were observed to contain disrupted or lysed parasite cells, with heavy organelle damage, as can be seen in Figure 75C,D, while the host cell mitochondria remained unaffected by the treatment with complex **544**. However, *in vivo* experiments with complexes **542-544** in a mouse model of neosporosis showed no significant decreases in parasite load or spread to the central nervous system, indicating that the limitation of these complexes was related to pharmacokinetic properties, specifically low bioavailability.

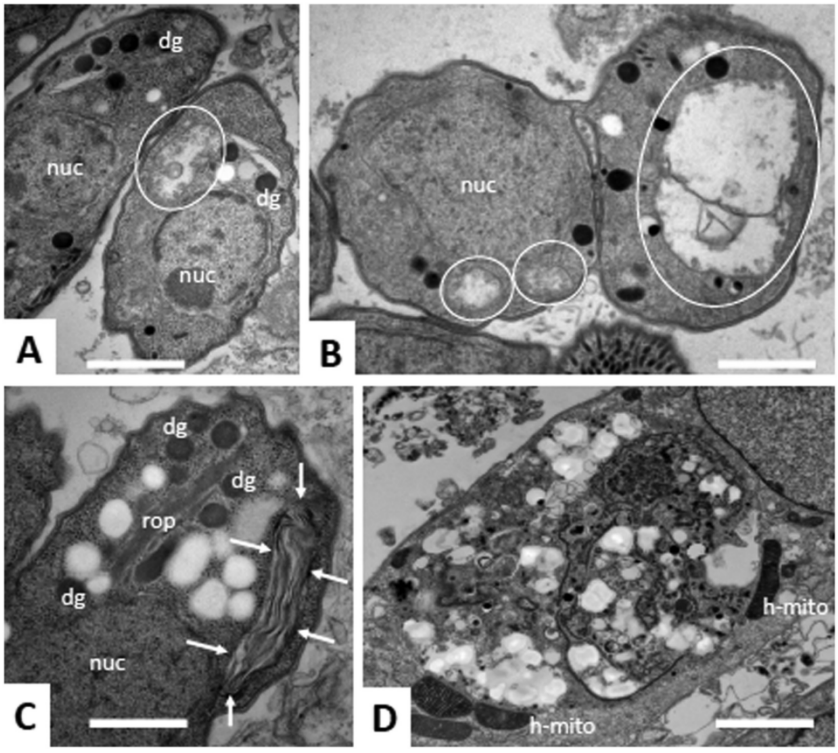

Figure 75. TEM micrographs of HFF cells infected with *N. caninum* and incubated with complex **544** for (**A**) 6, (**B**) 24 and (**C**,**D**) 72 hours (scale bars = 1 μm). The circles identify mitochondria or their residues while the arrows represent stacks of membranes. Labelled *N. caninum* structures: dg = dense granules, rop = rhoptries, nuc = nucleus, while h-mito = mitochondria from host HFF cells. Reproduced from Ref. [274], https://doi.org/10.1039/c8mt00307f (accessed on 18 May 2026), under the terms of the CC BY NC 3.0 license, http://creativecommons.org/licenses/by-nc/3.0/.

To increase the bioavailability of these trithiolatodiruthenium complexes, similar structures functionalized with nucleotides were examined for use against *T. gondii* and *T. brucei*, with the thiol group being attached to phenyl ligand that was connected to adenine via an ester (**545**) or to thioxanthine (**546**), as shown in Figure 76 [275]. Both adenine and thioxanthine are purine nucleotides, which were used to take advantage of the purine transport mechanisms of parasite cells. These organometallic complexes were compared to 9–(2–hydroxyethyl)–adenine (**547**) as a comparison with an organic purine-containing compound.

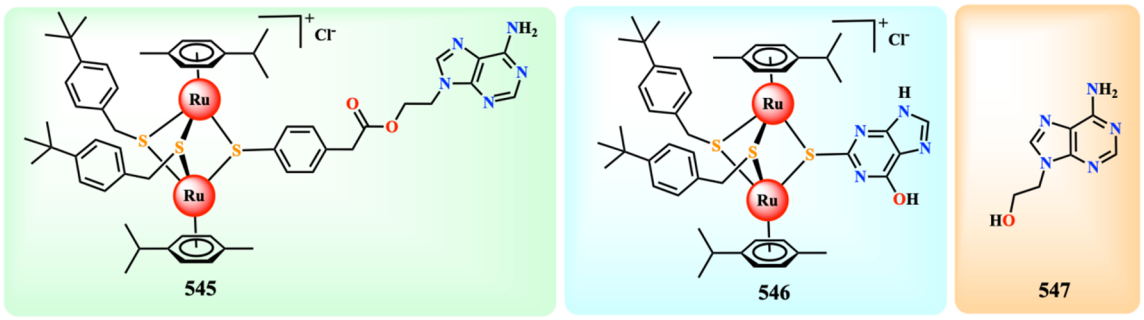

Figure 76. Structures of complexes **545** and **546** as well as 9–(2–hydroxyethyl)–adenine (**547**).

Only complex **545** showed inhibitory activity against either *T. gondii* (IC_{50} = 59 nM) or *T. brucei* (IC_{50} = 29 nM), suggesting the enhanced activity of the ruthenium-containing moiety as well as the necessity of the alkyl spacer. The influence of the spacer for protein binding interactions was also shown by a binding assay for a variety of proteins through differential affinity chromatography, which showed that complex **545** bound specifically to 128 proteins from *T. gondii* and 46 proteins from *T. brucei* that complex **546** and 9–(2–hydroxyethyl)–adenine (**547**) could not. TEM of *T. gondii* tachyzoites cultured in HFF cells and incubated with 500 nM of complex **545** was used to observe the effect on the morphology of the parasite cells. The untreated *T. gondii* tachyzoites, shown in Figure 77A with increased magnification in Figure 77B, exhibited functional mitochondria as well as other characteristic organelles, including secretory organelles (rhoptries, dense granules and micronemes), in addition to the apical complex and the conoid. After six hours (Figure 77C), the organized structure of the mitochondrial membrane was no longer observed, while the secretory organelles appeared unaffected. Further TEM studies at 12- and 24-hours post-treatment indicated that the changes to the mitochondria as well as the lack of impacts on other organelles, with the exception of a few lipid droplets. Importantly, no structural changes were observed for *T. gondii*-infected HFF cells treated with either complex **546** or 9–(2–hydroxyethyl)–adenine (**547**), which validated the observed growth inhibition results.

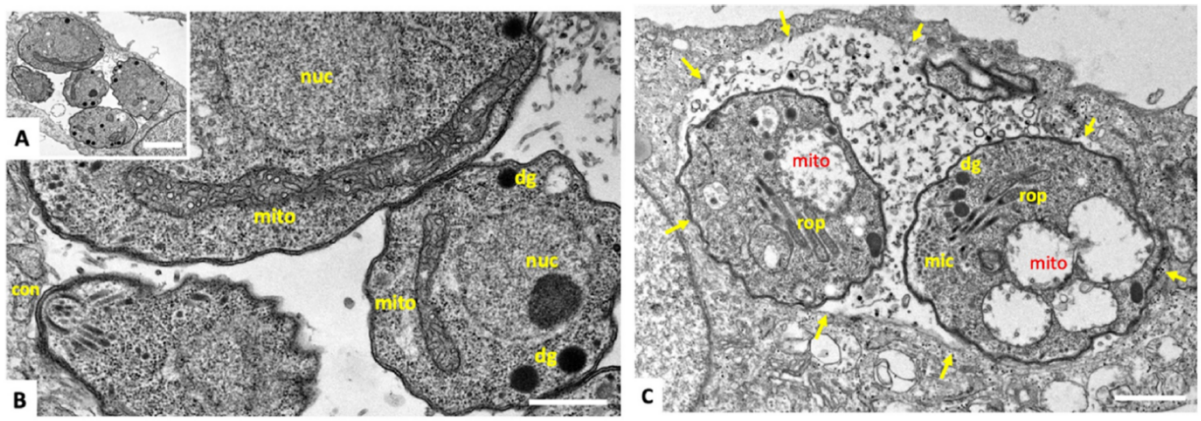

Figure 77. TEM micrographs of *T. gondii*-infected HFF cells after (**A**,**B**) no treatment or after (**C**) six hours of treatment with complex **545**. Legend: nuc = nucleus, mito = mitochondrion, rop = rhoptries, dg = dense granules, mic = micronemes, con = conoid. Scale bars = 1.0 µm for (**A**) and = 0.3 µm for (**B**,**C**). Reproduced with permission from Ref. [275], https://doi.org/10.3390/ijms221910787, under the terms of the CC BY 4.0 license, https://creativecommons.org/licenses/by/4.0/.

The bridged ruthenium-arene complex scaffold was also used as a basis for a conjugate with the antiparasitic drug sulfadoxine, which was then evaluated for its antiparasitic activity against *T. gondii* both in vitro and *in vivo* [276]. The sulfadoxine conjugate complex (**550**) was compared to its individual starting materials sulfadoxine (**548**) and the trithiolatodiruthenium complex with a carboxylic acid (**549**), all of which are shown in Figure 78.

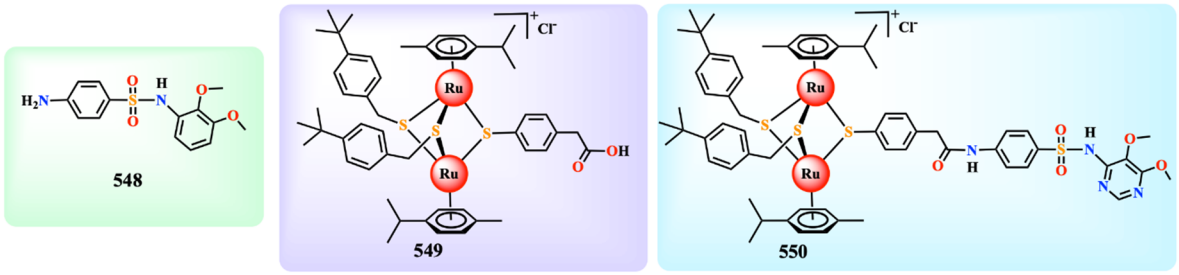

Figure 78. Structures of sulfadoxine (**548**) and complexes **549** and **550**.

Growth inhibition of *T. gondii* tachyzoites infecting HFF cells was evaluated for sulfadoxine-conjugated complex **550** and compared with sulfadoxine, complex **549** and an equimolar combination of complex **549** and sulfadoxine. Sulfadoxine exhibited no inhibitory effect on tachyzoite proliferation up to the maximum tested concentration of 5 μM. Complex **549**, meanwhile, started decreasing proliferation at 1.25 μM and achieved complete inhibition at 5 μM. The combination of complex **549** and sulfadoxine did not improve this activity, while the conjugate **550** began reducing proliferation at a concentration of 0.1 μM, with complete inhibition at 1 μM. The IC_{50} values for complex **550** against *T. gondii* infection in HFF cells were calculated for addition of the complex along with the tachyzoites as well as treatment with the complex three hours post-infection and were found to be 112 nM and 145 nM, respectively, indicating a similar level of activity. However, the inhibition of *T. gondii* proliferation was not cytotoxic for the tachyzoites, only cytostatic, as after six days of treatment with complex **550**, the tachyzoites re-emerged after an additional four days without treatment. In terms of host toxicity, complex **550** was more toxic at 1 μM, resulting in 71% surviving HFF cells compared to the lack of cytotoxicity for complex **549** at the same concentration. On the other hand, at a 10 μM concentration, complex **549** completely inhibited HFF viability, while complex **550** still showed a survival rate of 31%. An *in vivo* mouse model of *T. gondii* was also treated with the sulfadoxine-conjugated complex **550**. The parasite load from mouse tissue cells was determined by qPCR, and the *T. gondii*-specific DNA sequences were then quantified using a standard curve of serial dilutions of *T. gondii* DNA to calculate the numbers of tachyzoites per 20 ng of host DNA. Minimal impact on the parasite load was detected in the central nervous system of mice treated with sulfadoxine-conjugated complex **550** (Ru-SDX), as shown for the DNA collected from brain cells in Figure 79A. On the other hand, a notable decrease in parasite load was detected in DNA from eye cells (p = 0.008) and heart cells (p = 0.020), as shown in Figure 79B and Figure 79C, respectively.

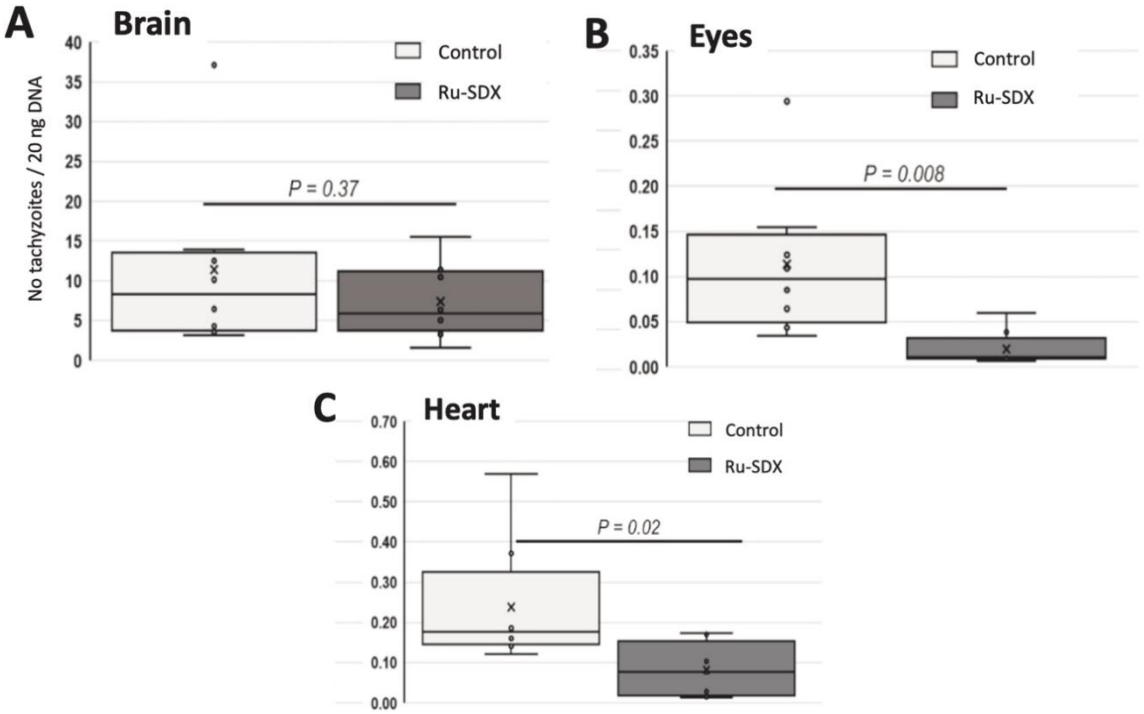

Figure 79. Parasite load in tachyzoites per 20 ng DNA from (**A**) brain, (**B**) eye and (**C**) heart cells in an *in vivo* mouse model of *T. gondii* infection treated with complex **550** (Ru-SDX). Adapted with permission from Ref. [276],

https://doi.org/10.1016/j.ijpddr.2024.100544, under the terms of the CC BY 4.0 license, https://creativecommons.org/licenses/by/4.0/.

Lin et al. reported the synthesis of fluconazole derivatives with cobaltocenium, ferrocene, and ruthenocene substituents [277]. Reaction of 1-azido-2-(2,4-difluorophenyl)-3-(1*H*-1,2,4-triazol-1-yl)propan-2-ol (**551**) with ethyenylmetallocenes (**552-555**) in the presence of copper sulfate and sodium ascorbate in THF/H_2O to yield metallocene complexes **556-559** (Scheme 57). The authors also reacted 1-amino-2-(2,4-difluorophenyl)-3-(1*H*-1,2,4-triazol-1-yl)propan-2-ol (**560**) with the metallocene acyl chlorides (**561-564**) in the presence of triethylamine with THF or DCM to produce the cobaltocenium complexes **565** and **566**, the ferrocene complex **567** or the ruthenocene complex **568**, as described in Scheme 58.

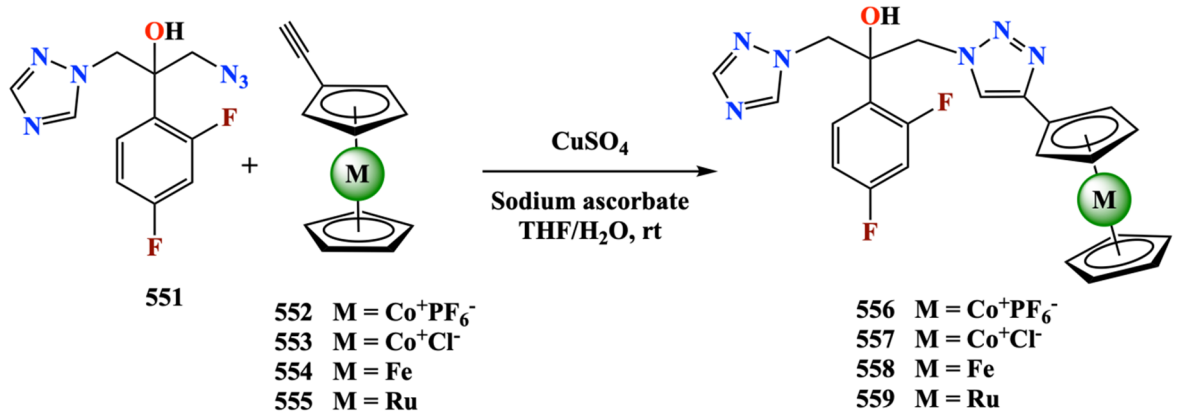

Scheme 57. Synthesis of the 1,2,3-triazole-containing complexes **556-559**.

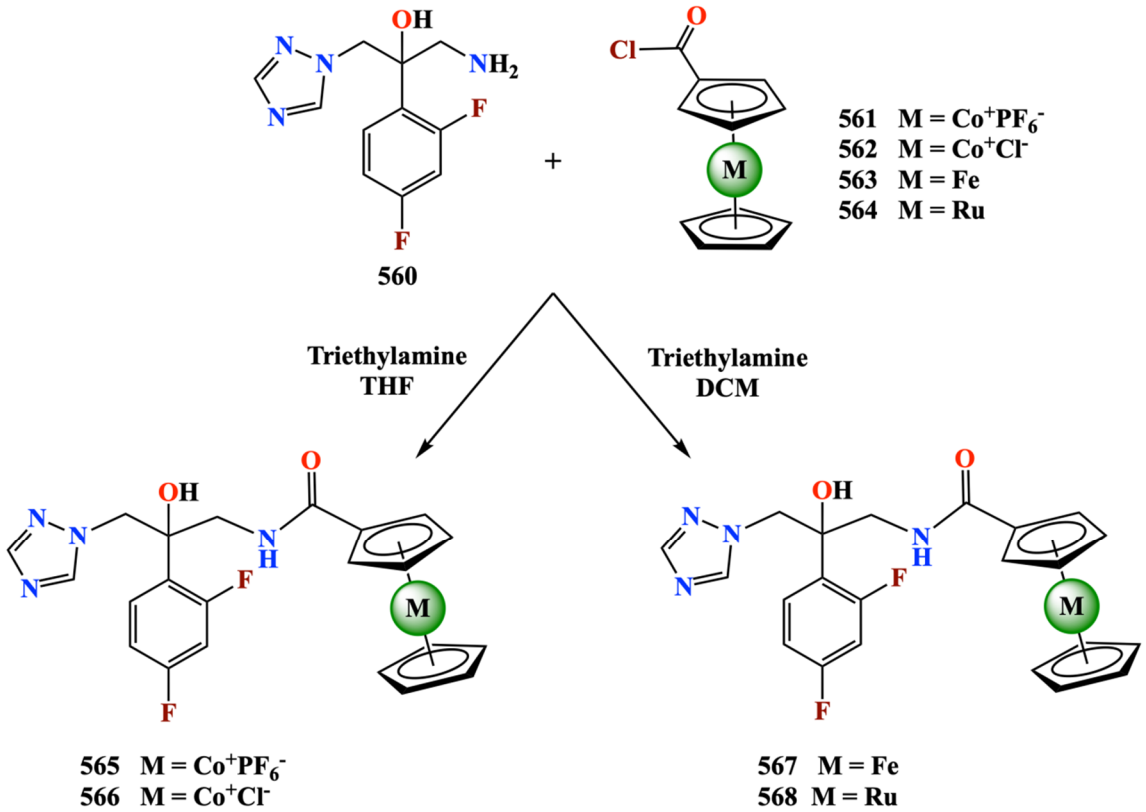

Scheme 58. Preparation of the amide-containing complexes **565-568**.

Low cytotoxicity was observed for complexes **556-559** and **565-568** against a healthy mammalian cell line (Vero), with IC_{50} values ≥ 68.50 μM. In contrast, the complexes were more toxic to a range of clinically isolated *Candida* strains, although the amide-containing complexes **565-568** were generally more effective than 1,2,3-triazole-containing complexes **556-559**. Additionally, the complexes were also effective against the parasitic protozoan *T. cruzi*, with IC_{50} values much lower than for the control cell line. The greatest activity was achieved for

the 1,2,3-triazole-containing complexes **557** and **558**, with IC_{50} values of 4.9 μM and 2.5 μM, respectively, as well as showing high selectivity index values (SI = IC_{50} VERO cells/IC_{50} *T. cruzi* cells) of 22.5 and 27.7, respectively.

The crystal structure of the sterol 14α-demethylase enzyme CYP51 from *T. cruzi* complexed with fluconazole (PDB ID: 2WX2, Figure 80a) was used for molecular docking with complexes **556-559** and **565-568**. All tested compounds exhibited negative interaction energies, representing favorable binding. A majority of docking poses for fluconazole were oriented toward the heme group, while alternative orientations were less frequent and associated with weaker binding. The binding site for fluconazole was localized to the region surrounded by the haem group and amino acid residues Y103, F110, Y116, and M360 (Figure 80b). Complexes **556-559** exhibited superior docking scores and therefore stronger interactions compared to fluconazole, with the strongest impact on binding from contact with residue M360, indicating its potential role in enzyme inhibition. Furthermore, complexes **565-568** demonstrated weaker interactions as well as less contact with residue M360. While the differences in binding energies were relatively minor due to lower sensitivity for modelling the organometallic complexes, stable enzyme-ligand conformations were able to be observed. These initial results represent potential templates for further optimization.

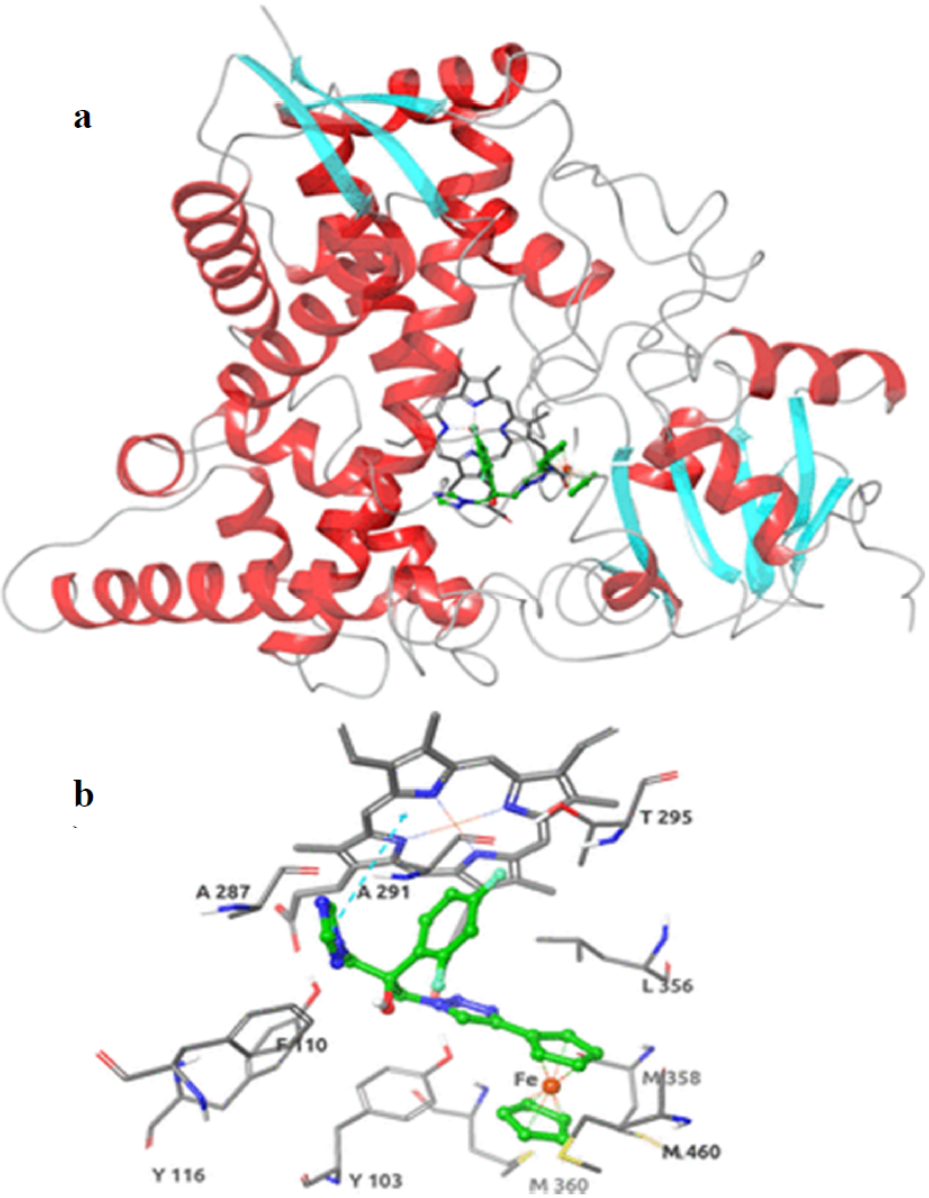

Figure 80. (**a**) Structure of *T. cruzi* sterol 14α-demethylase CYP51 bound to fluconazole (PDB ID: 2WX2) and (**b**) example conformation of complex **567** docked in the fluconazole binding site, showing heme group and key amino acid residues (Y103, F110, Y116, A287, A291, T295, L356, M358, M360, and M460) that contribute to binding. Reproduced with permission from Ref. [277], Copyright © 2024 American Chemical Society.

Yagmurlu et al. examined a series of functionalized NHC-Cu complexes for their antiparasitic activities [278]. Five complexes **569-573** (Figure 81) were prepared according to previously reported strategy and their efficacy against *L. major* promastigotes and amastigotes, as well as *T. gondii* tachyzoites, was examined, and compared to their cytotoxicity against mouse macrophages (for *L. major*) and Vero cells (for *T. gondii*). All complexes exhibited high activity against the promastigotes, with IC_{50} values <0.08 μM, except for complex **570**, which showed a relatively high IC_{50} of 1.3 μM. Complex **573** exhibited the greatest antiparasitic activity with IC_{50} values of 0.027 μM against promastigotes and 0.39 μM against amastigotes, respectively, as well as high selectivity, with SI values of 157.40 for promastigotes and 10.90 for amastigotes. Conversely, for *T. gondii* tachyzoites, complex **571** was the most effective and its IC_{50} was calculated to be 0.14 μM. Similar to complex **573**, however, complex **571** also showed the highest selectivity in addition to the highest inhibitory activity, with an associated SI of 20.00.

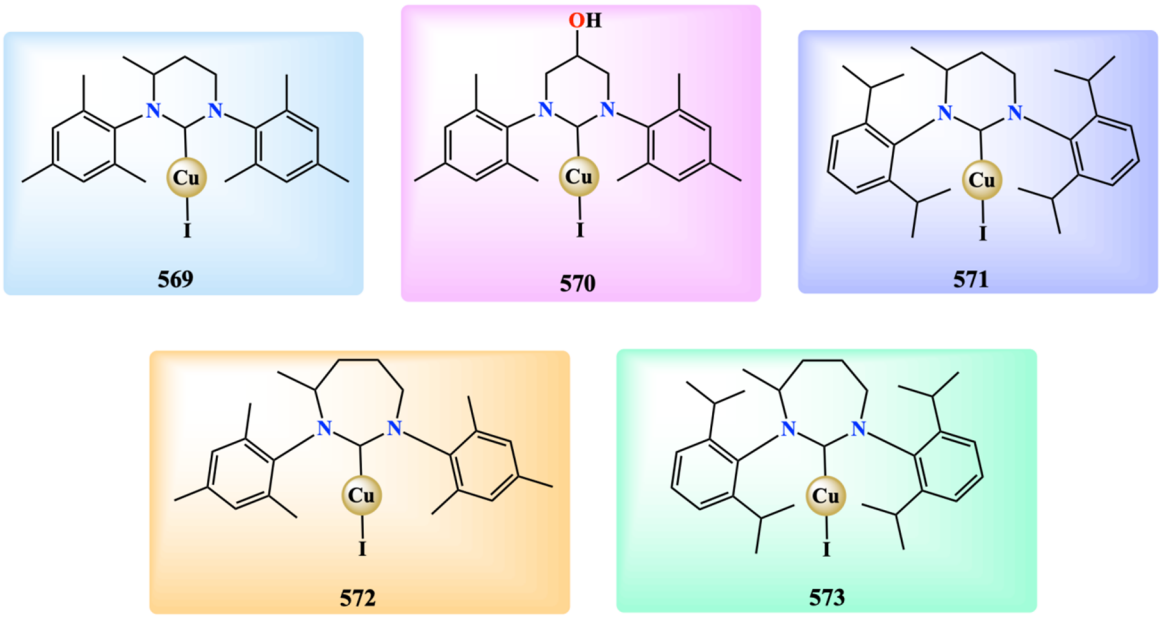

Figure 81. Structures of Cu(I)-NHC complexes **569-573**.

Pérez-Ramos et al. prepared organometallic Au(III) cyclometallated complexes **577-590**, as shown in Scheme 59, as candidates for antitrypanosomal activity against *T. cruzi* [279]. *N*,*N*-diisopropyl-*P*,*P*-diphenylphosphinothioic amide (**574**) reacted with *n*-BuLi/TMEDA (N,N,N',N'-tetramethylethylenediamine) followed by electrophilic quenching with Me_2SnCl_2 to yield *o*-trimethylstannylated phosphinothioic amide **575** [280]. Upon reaction with $K[AuCl_4]$, the cycloaurated phosphinothioic amide complex (**576**) was formed. Further reaction with this complex allowed for the generation of a series of gold complexes, including gold(III) azol(in)ium dithiocarboxylate complexes **577-579** and gold(III)-dithiocarbamate hexafluoro-phosphate complexes **580-586** as well as the gold(III)-dithiocarbamate tetrafluoroborate and hexafluoroantimoniate complexes **587** and **588**. The gold(III) azol(in)ium-2-(methoxy)methane-dithiolate complexes **589** and **590** were also prepared. In addition to the antiparasitic activity, this class of complexes has previously demonstrated antimicrobial activity, suggesting that it may be an effective drug design scaffold [248]. Complexes **577-590** all showed more improved toxicity against *T. cruzi* trypomastigotes than the reference drugs benznidazole and nifurtimox for two *T. cruzi* strains, namely NINOA and INC-5 strains. Furthermore, the selectivity against the trypomastigotes was also enhanced for either strain relative to the J774.2 mouse macrophage cell line, with complexes **581** and **590** even achieving SI values >200. The five complexes that showed the highest SI values, **581**, **583**, **587**, **589** and **590**, were then analyzed for their inhibitory activity against *T. cruzi* amastigotes of the NINOA strain. Only complex **589** was more cytotoxic to the J774.2 macrophages than the amastigotes, while the other four complexes all showed IC_{50} >193 μM for the macrophages. Of the remaining four complexes, complexes **581** and **587** were inactive against the amastigotes (IC_{50} >200 μM) in the tested concentration range, while **583** and **590** exhibited IC_{50} values of 94.8 μM and 57.4 μM, respectively. Complex **590** was determined to be the best candidate, as it not only showed superior inhibitory activity compared to benznidazole and nifurtimox (IC_{50} = 71.2 μM and 76.3 μM, respectively), it also exhibited higher selectivity, with a calculated SI >3.48, compared to 1.88 for benznidazole and 2.15 for nifurtimox.

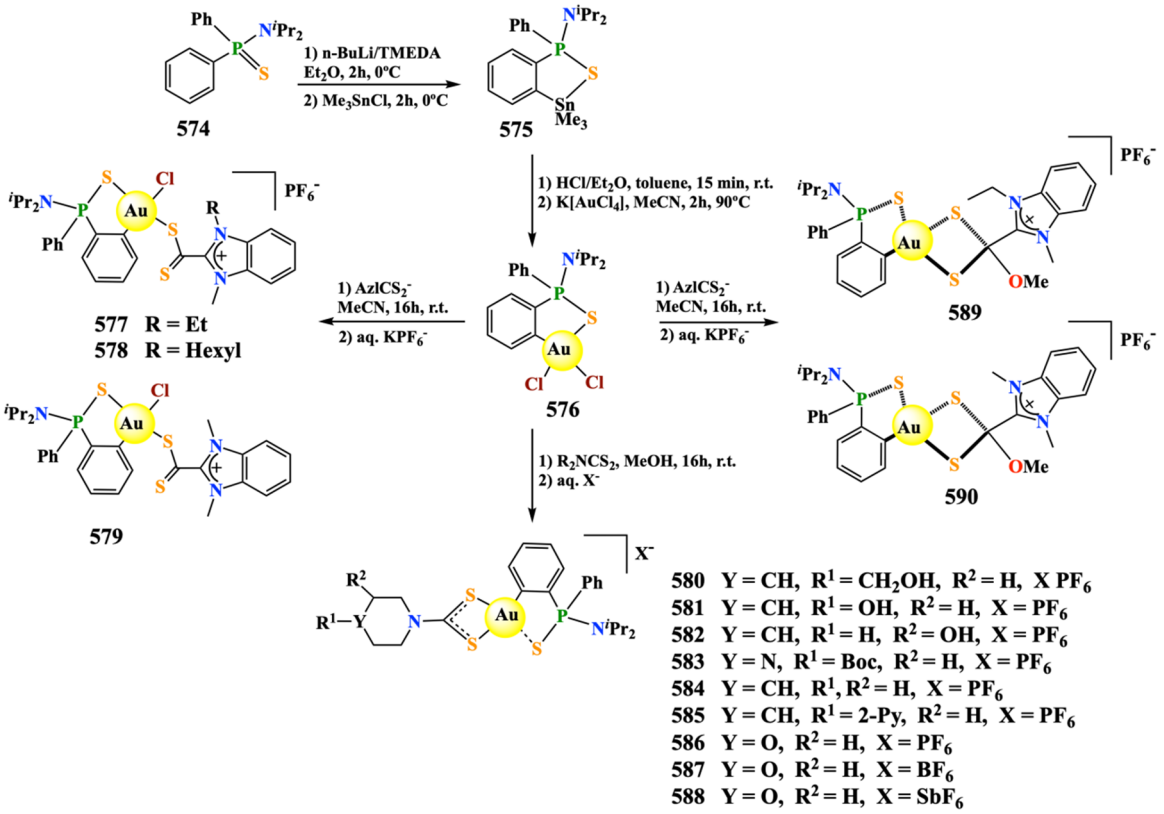

Scheme 59. Preparation of cyclometallated organogold complexes **577-590**.

In order to target a wide range of parasites, including protozoans and helminths (parasitic worms), Feng et al. prepared an organogold compound containing the glucopyranose sugar found in the structure of the drug auranofin [281]. First, octa-1,7-diyne (**591)** and 2-bromopyridine (**592)** were reacted to give rise to the diyne compound **593**, which was cyclized using the zirconocene complex [$ZrCp_2Cl_2$], forming the bis(2-pyridyl)phosphole compound **594**. AuCl(tetrahydrothiophene) (**595**) was then reacted with compound **594** to form the (1-phenyl-2,5-di(2-pyridyl)phosphole)AuCl complex (**596**), which was then modified with the addition of 1-thio-β-D-glucopyranose to form complex **597**, as shown in Scheme 60. The gold complex could inhibit glutathione and thioredoxin reductase enzymes, as well as binding to DNA, resulting in its antiparasitic activity, while the addition of the glucopyranose group allowed for enhanced solubility and bioavailability.

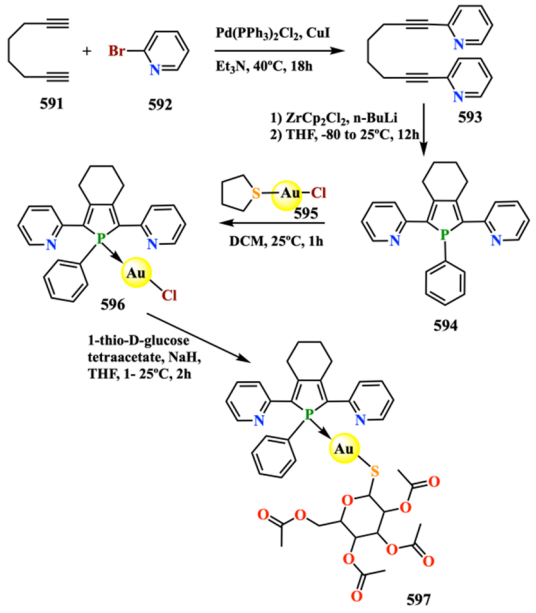

Scheme 60. Design of glucopyranose-modified organogold complex **597**.

Complex **597** was effective against a range of parasites including *Schistosoma mansoni, Brugia pahangi, Loa loa, Onchocerca ochengi, T. brucei, T. cruzi, Leishmania infantum, Leishmania donovani, Theileria annulata, and Acanthamoeba castellanii*. As a representative example, *T. annulata* is a parasite that can infect B lymphocytes and results in lymphoproliferative disease that resembles cancer. The proliferation of uninfected bovine lymphosarcoma cells (BL3) and BL3 cells infected with *T. annulata* (TBL3) infected cells was examined with and without incubation of complex **597** at a concentration of 0.25 μM (Figure 82A) or 0.50 μM (Figure 82B) over a 96-hour period. The BL3 cells incubated with complex **597** demonstrated lower cell numbers than the untreated BL3 cells, and a similar trend was observed for treatment of infected TBL3 cells with the complex. However, while the BL3 cells displayed inhibited proliferation, only the TBL3 cells treated with either concentration of the gold complex exhibited any decrease in growth. This indicated that the complex was specifically cytotoxic against the TBL3 cells compared to the uninfected cell line. The most notable inhibitory effects of complex **597** were demonstrated against *L. donovani* amastigotes as well as two helminth species: *S. mansoni*, which can cause schistosomiasis (bilharziasis) and *B. pahangi*, which can cause lymphatic filariasis (elephantiasis). Complex **597** did show comparable levels of cytotoxicity against host cells as auranofin in the micromolar range, necessitating further engineering to reduce its harmful effects. The authors did note, however, that auranofin itself is approved for clinical use despite the potential toxicity, indicating that the new complex **597** may still be used as an antiparasitic therapeutic agent.

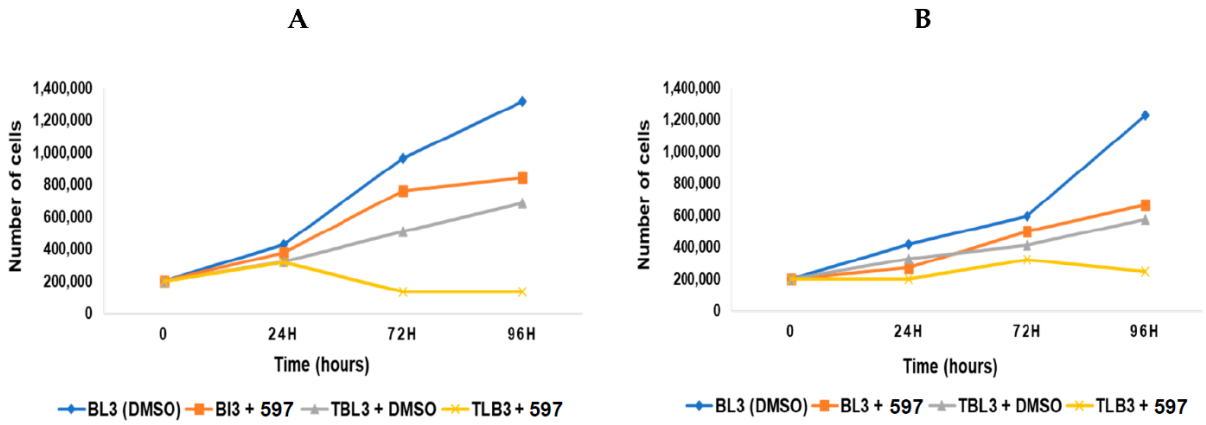

Figure 82. Proliferation of bovine lymphosarcoma cells infected with *T. annulata* and treated with (**A**) 0.25 μM or (**B**) 0.50 μM of complex **597** for 96 hours. Reproduced with permission from Ref. [281], https://doi.org/10.3390/molecules25215075, under the terms of the CC BY 4.0 license, https://creativecommons.org/licenses/by/4.0/.

Khanye et al. designed poly(propylene imine) (PPI) dendrimers with peripheral ferrocenyl groups for inhibitory activity against *Plasmodium falciparum*, the parasite responsible for the most pathogenic form of malaria [282]. The 1st generation PPI dendrimers **602** and **603** were prepared through the reactions of ferrocenecarboxaldehyde (**137**) or acetylferrocene (**148**) with methyl hydrazinecarbodithioate (**598**) to yield the ferrocenylthioesters **599** and **600**, followed by reaction with the poly(propylene imine) dendrimer **601**, as illustrated in Scheme 61. The inhibition of the chloroquine-resistant W2 strain of *P. falciparum* was evaluated for the dendrimers **602** and **603** in vitro, and compared with complexes **599** and **600**, as well as two common antimalarial agents: chloroquine and artemisinin. Both ferrocene complexes **599** and **600** were ineffective, as was the organic PPI dendrimer **601** alone, while dendrimers **602** and **603** exhibited moderate inhibition, with IC_{50} values of 6.59 μM and 1.79 μM, respectively. Although these are still significantly higher than the 0.0082 μM for artemisinin or even the 0.049 μM for the resisted chloroquine, the improvement over the complexes and organic dendrimer was concluded to demonstrate the antimalarial potential of ferrocenyl-modified dendrimers.

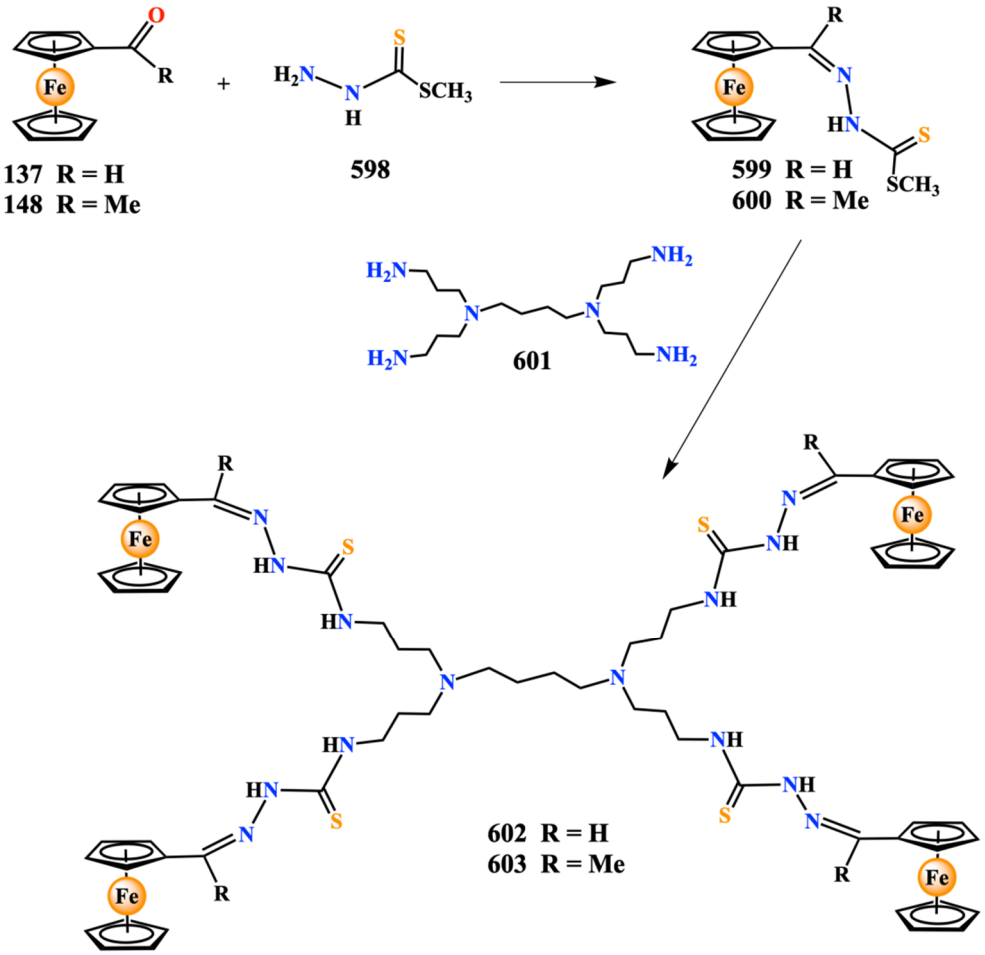

Scheme 61. Design of poly(propylene imine) dendrimers with ferrocenylthiosemicarbazone moieties (**602** and **603**).

5.2. Antiviral

Antiviral agents are needed for treatment of viral infections including HIV, hepatitis and influenza. The mechanisms of antiviral drugs can interfere with different stages of the viral replication cycle, including replication of the viral genome, inhibition of viral entry into host cells, and immunomodulation [283]. The development of viral resistance to existing antiviral agents has led to a need for new drugs and combination therapies [284]. While there have been many coordination complexes tested for their antiviral activities, there are limited examples of organometallic complexes that have been investigated [285,286]. These organometallic complexes include a number of transition metals like titanium, molybdenum, rhenium, iron, ruthenium, rhodium, copper, silver and gold [287–295]. One example of an organometallic complex with antiviral activity was the tricarbonylrhenium(I) complex **604** containing a pyrithione ligand [291]. Pyrithione is a natural organic compound that forms complexes with metals such as zinc and copper, which display antimicrobial activity against a wide range of organisms. The antiviral activity of complex **604** was evaluated for inhibiting replication of the herpes simplex virus 2 (HSV-2) within Vero cells. The level of viral DNA replication in the cells was determined using qPCR for specific viral DNA sequences and calculating the threshold cycle (Ct) value as a relative measure of initial DNA concentration. As shown in Figure 83, complex **604** inhibited replication of viral DNA sequences above a concentration of 0.391 μM, with Ct values between −17.7 to −14.1, while the reference tricarbonyl complex with bipyridine *fac*-[$Re(CO)_3$(bpy)Cl] exhibited little inhibition of viral replication.

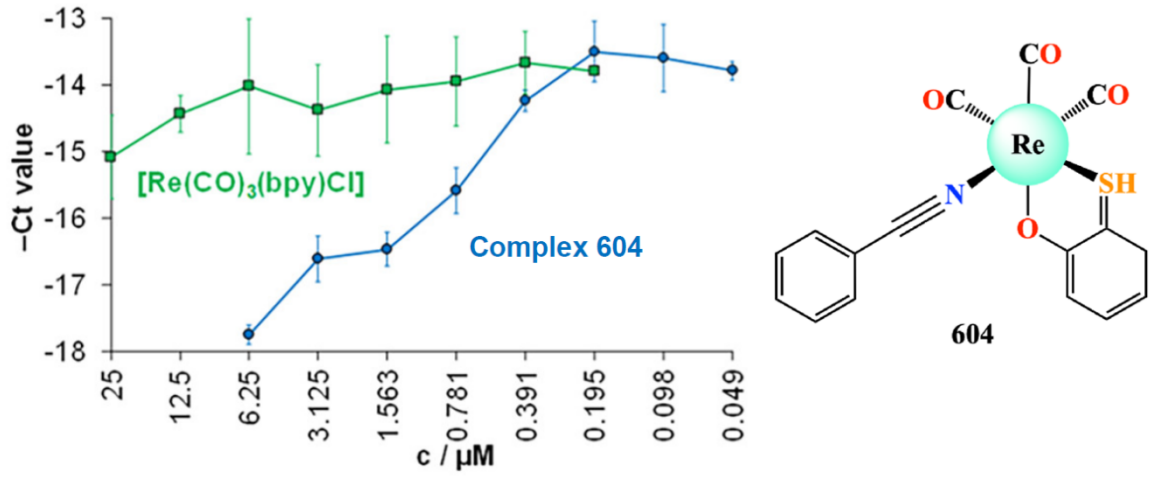

Figure 83. Structure of tricarbonylrhenium(I) complex **604** as well as its inhibitory effect on viral replication measured with qPCR and compared with the *fac*-[Re(CO)$_3$(bpy)Cl]. Adapted with permission from Ref. [291], https://doi.org/10.1021/acsomega.5c06647, under the terms of the CC BY 4.0 license, https://creativecommons.org/licenses/by/4.0/.

The research team of Kowalski has prepared many ferrocene-containing complexes and examined their biological studies [292,296,297]. In 2026, they designed a series of ferrocenyl–containing dinucleosides and examined them for their antiviral activity, as shown in Schemes 62 and 63 [293]. In this study, copper(I)–catalyzed azide–alkyne cycloaddition reaction of a 1,1'–dimethyloxypropargyl ferrocene (**605**) with 5′–azido–2′,3′–*O*–isopropylidene adenosine (**606**), 3′–azido–3′–deoxythymidine (**608**) and 9–(2–azidoethyl)–adenine (**610**) was utilized to prepare the desired complexes **607**, **609** and **611** (Scheme 62). However, reaction of an equimolar ration of complex **605** with 3′–azido–3′–deoxythymidine (**608**) allowed for the formation of the intermediate complex **612**, as shown in Scheme 63. This complex was then reacted with complexes **606** and **610** to yield complexes **613** and **614**, respectively.

The coronavirus HCoV–OC43 was used as a model of SARS-CoV-2 to measure the antiviral activity of the Fe-containing complexes **605**, **607**, **609** and **611-614**, as well as the reference antiviral Remdesivir, using the RD rhabdomyosarcoma cell line as a host. The resulting IC_{50} values for inhibition of HCoV–OC43 replication and CC_{50} values for cytotoxicity against RD cells are tabulated in Table 4. Only complexes **607**, **611** and **612** showed any inhibitory activity against the virus, with IC_{50} values of 211 µM, 250 µM and 254 µM. While none of the complexes examined showed notable activity compared to remdesivir, it should also be noted that none of the Re(I) complexes exhibited cytotoxicity to the RD cells (IC_{50} >10 µM).

Table 4. Antiviral activity against HCoV–OC43 and cytotoxicity against Vero cells for complexes **605**, **607**, **609** and **611-614**, as well as antiviral drug Remdesivir.

Compound	Antiviral Activity IC_{50} [µM]	Cytotoxicity CC_{50} [µM]
605	**>500**	**>500**
607	**211 ± 68**	**>500**
609	**>500**	**>500**
611	**250 ± 12**	**>500**
612	**254 ± 36**	**>500**
613	**>500**	**>500**
614	**>500**	**>500**
Remdesivir	**0.09 ± 0.02**	**>10**

In 2013, Santoro et al., prepared a series of organometallic copper(I)-N-heterocyclic carbene complexes with the formula [Cu(NHC)] [298]. The synthesis was accomplished according to the following scheme (Scheme 64). Two methods were used to give rise to the salts **616-618** composed of an imidazolium cation and a $[CuXCl]^-$ anion, either reaction of the substituted imidazolium chloride **615** with the appropriate copper halide salt or reaction of compounds **615**, **619** and **620**, containing chloride, bromide, or iodide anions, with copper chloride. Complexes **621-623**, with the general structure Cu(IPr)X, where X is a chloro (**621**), bromo (**622**), or iodo group (**623**), were then prepared by reaction of the salts **616-618** with potassium carbonate. The activity of complexes **621-623**

against Chikungunya virus (CHIKV) replication, as well as their cytotoxicity against the host Vero cells, was examined by Fontes and coworkers [294]. The SI was calculated by dividing the cytotoxic concentration for host cells by the effective concentration to inhibit viral replication. The bromo-containing complex **622** showed the highest SI of 4.83, demonstrating its selectivity for viral inhibition and indicating this complex may be promising for development of antiviral agents targeting CHIKV.

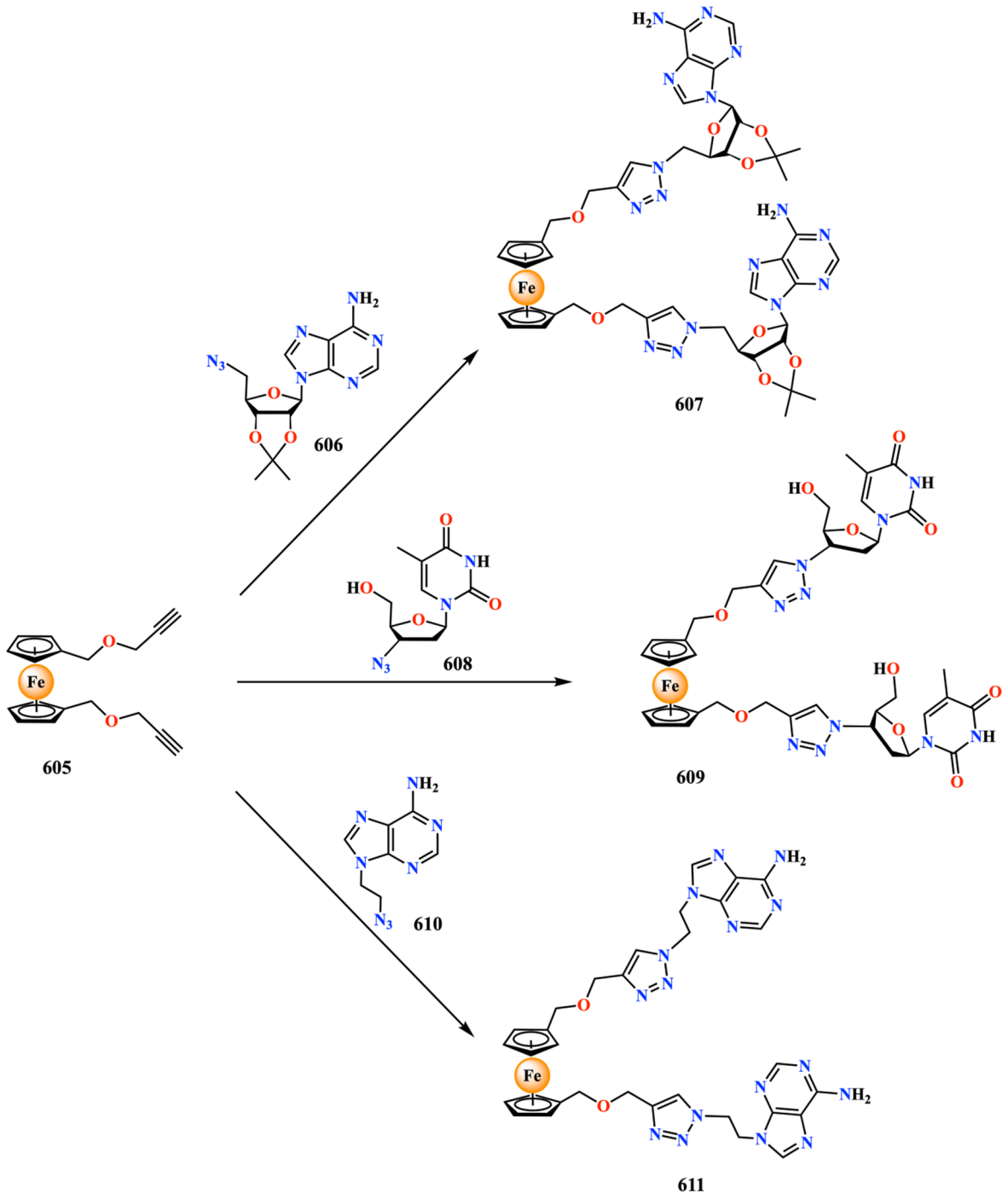

Scheme 62. Preparation of ferrocene-containing complexes **607**, **609** and **611**.

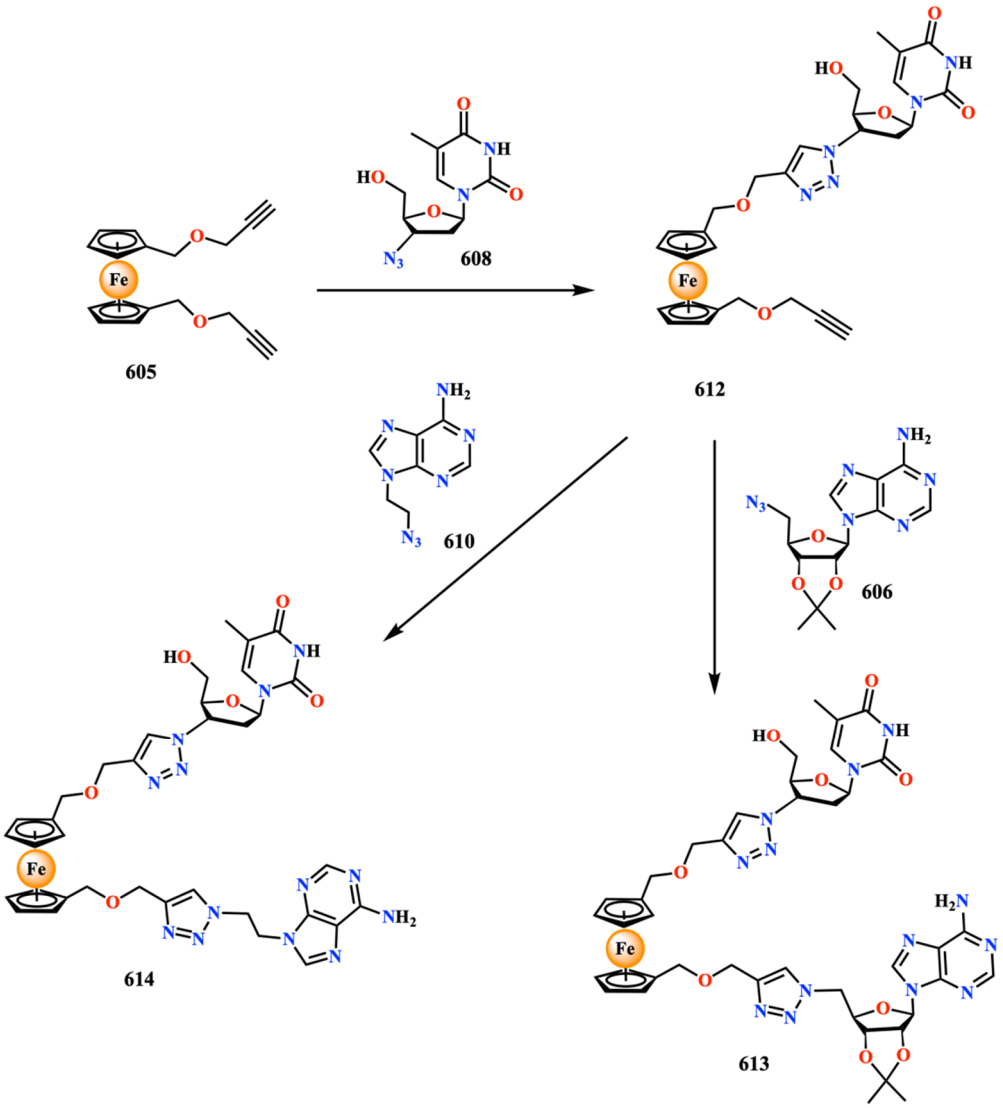

Scheme 63. Preparation of ferrocene-containing complexes **612**, **613** and **614**.

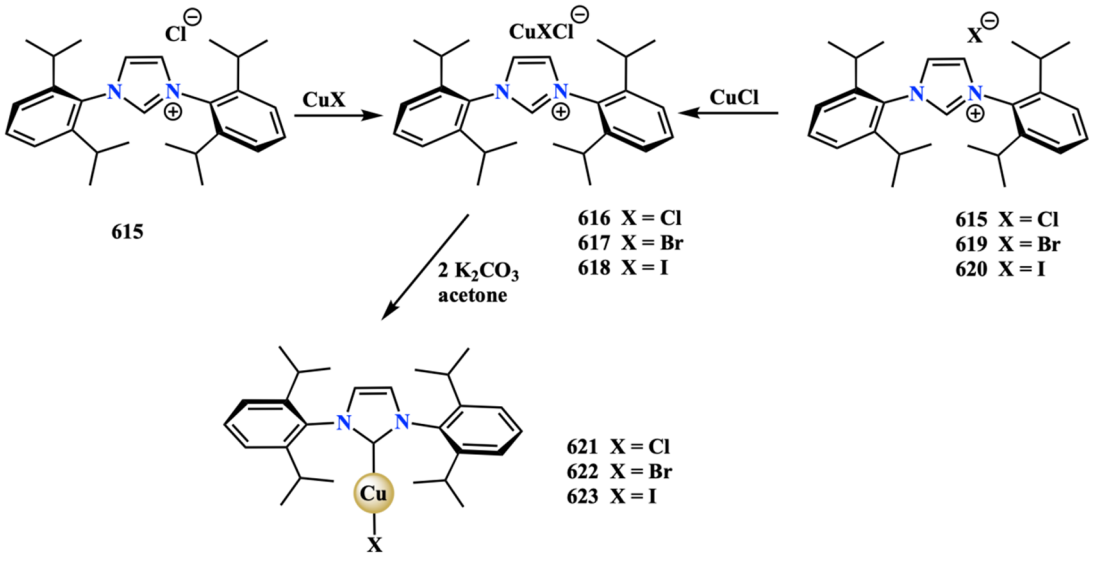

Scheme 64. Synthetic organometallic copper(I)-N-heterocyclic carbene complexes **621-623**.

Most recently, the same group examined not only the Cu(IPr)Cl but also Cu(IMes)Cl and $Cu(IMes)_2BF_4$ for their ability to inhibit SARS-CoV-2 [299]. The Cu(IPr)Cl complex (**621**) inhibited the entry stage of viral replication by 48% and the post-entry stages by 95%. However, the mesityl-containing complexes were able to inhibit viral replication at any stage. Incubation of the host cells with Cu(IMes)Cl and $Cu(IMes)_2BF_4$ prior to infection resulted in 99% and 87.7% inhibition, respectively, while treatment during the entry stage caused inhibition of 99.6% and 74%, respectively and during the post-entry stages caused inhibition of 99.6% and 87.6%, respectively. Additionally, the $Cu(IMes)_2BF_4$ was also demonstrated to prevent the spread of the virus to uninfected cells. Also, Cu(IMes)Cl was found to bind strongly to the papain-like protease (PL^{pro}), which is involved in the assembly and processing of the replicase polyprotein complex during viral replication for coronaviruses.

Gil-Moles et al. conducted a study of SARS-CoV-2 using organogold complexes **624-628** (Figure 84) to investigate protein interactions with two targets for antiviral efficacy against coronaviruses, namely inhibition of PL^{pro} and inhibition of the binding interactions between the viral Spike protein and the host receptor angiotensin-converting enzyme 2 (ACE2) [300].

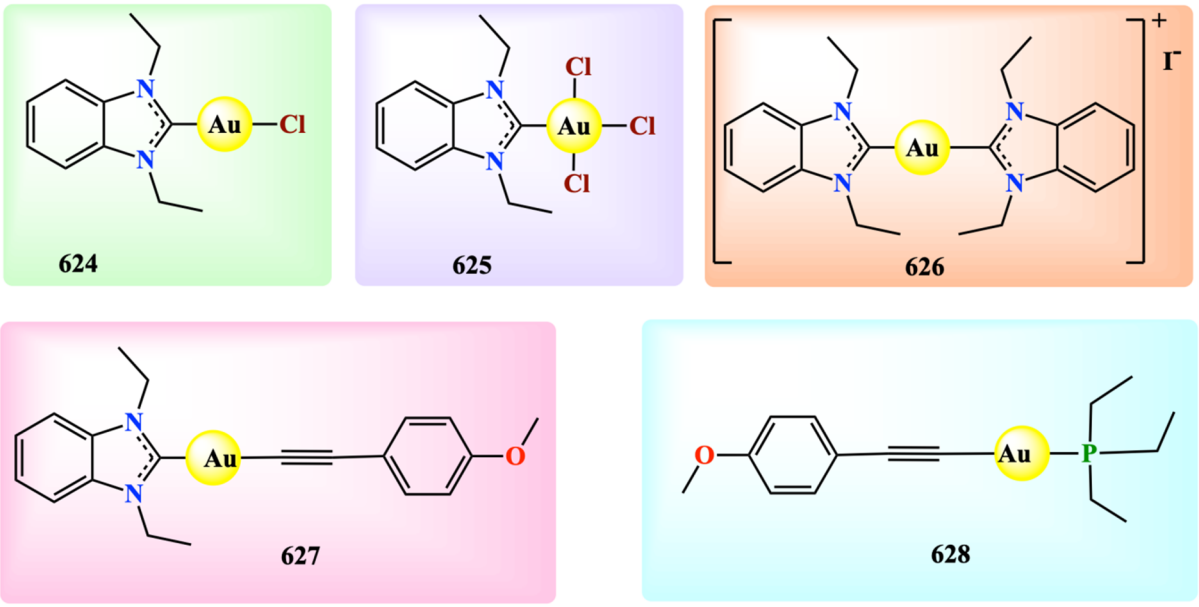

Figure 84. Organogold complexes **624-628**.

The antiviral mechanisms were targeted towards two key points in the viral replication cycle for SARS-CoV-2 illustrated in Figure 85. First, the Spike protein acts as a ligand for the ACE2 receptor on the surface of human cells, which is involved in entry of the viral particles into the cells. After entry, uncoating of the viral capsid occurs, releasing the viral genomic RNA that uses the machinery of host cell to synthesize a polypeptide known as replicase. As previously described, PL^{pro} is critical for processing of the replicase polypeptide. This polypeptide can then replicate the viral genome as well as performing transcription of viral genes for translation into proteins, eventually resulting in complete virus particles that can be released from the cell. Comparable inhibition of Spike-ACE2 binding to the reference organogold complex auranofin was observed, with IC_{50} values between 16.2–25.0 μM compared to 22.2 μM for auranofin. The inhibition of enzyme activity for PL^{pro} from SARS-CoV-1 resulted in lower IC_{50} values for all complexes relative to auranofin (25.5 μM) but complexes **624**, **625** and **628** exhibited the lowest IC_{50} values of 6.3 μM, 5.5 μM and 6.7 μM, respectively. Against PL^{pro} from SARS-CoV-2, however, auranofin exhibited slightly higher inhibitory activity (IC_{50} = 0.75 μM) than complexes **624**, **625** and **628** (IC_{50} = 1.04 μM, 1.44 μM and 0.96 μM), while complexes **626** and **627** were unable to reach 50% inhibition within the tested concentrations.

The same group then studied a wide range of metallodrugs in addition to organogold complexes for their effects on Spike/ACE2 interactions and protease PL^{pro} inhibition, with a number of metal-containing structures provided by collaboration with various research groups in order to combat the COVID-19 pandemic [295]. In addition to protein interaction, they also studied the in vitro antiviral activity of these compounds using Caco-2 cells infected with SARS-CoV-2. The most effective candidates for inhibiting both proteins were primarily organometallic complexes, including titanocene dichloride (**82**), the organosilver complex **629** and organogold complexes **630-633** (Figure 86).

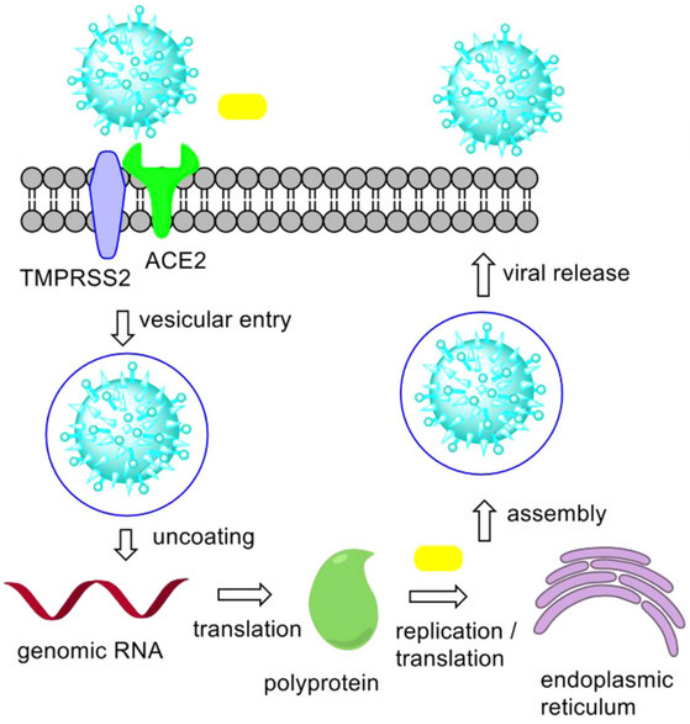

Figure 85. Viral replication cycle for SARS-CoV-2, showing cell receptors transmembrane protease serine 2 (TMPRSS2) and angiotensin-converting enzyme 2 (ACE2). Adapted with permission from Ref. [300], https://doi.org/10.1002/chem.202004112, under the terms of the CC BY 4.0 license, https://creativecommons.org/licenses/by/4.0/.

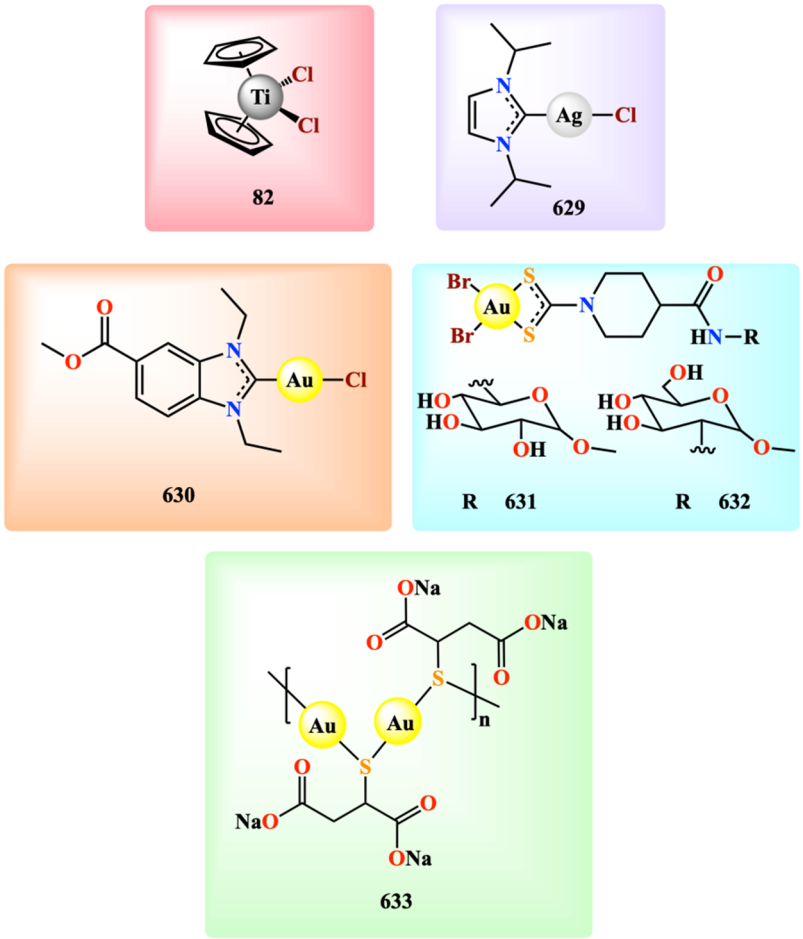

Figure 86. Titanocene (**82**), organosilver complex **629** and organogold complexes **630-633**.

Immunohistochemistry using antibodies targeting the viral S protein was employed to measure the inhibition of viral replication in Caco-2 cells infected with SARS-CoV-2 treated with complexes **82** and **629-633**. The resulting graphs of viral inhibition for a range of concentrations of these complexes and the reference drug remdesivir are shown in Figure 87. Complex **633** was not effective even at the maximum concentration of 500 μM, while for titanocene dichloride (**82**) and organogold complexes **631** and **632**, a significant increase in inhibition of viral replication was only observed at 500 μM, showing low antiviral activity. For complex **629**, significant viral inhibition (>60%) was observed above 12.5 μM, but the cytotoxicity of the complex against Caco-2 cells was also observed above a 50 μM concentration, explaining the high antiviral activity by killing host cells. On the other hand, cytotoxicity was not observed at the 12.5 μM concentration, suggesting that there was still some antiviral activity without killing host cells. The Au-containing complex **630** exhibited ~100% viral inhibition at 25 μM but did not display any significant cytotoxicity until a concentration of 100 μM, demonstrating that its activity was independent of host cell death. It was noted, however, that none of the candidate complexes were as effective as the reference antiviral remdesivir, which approached complete inhibition at 2.5 μM, indicating that further optimization would be required from these initial screening results.

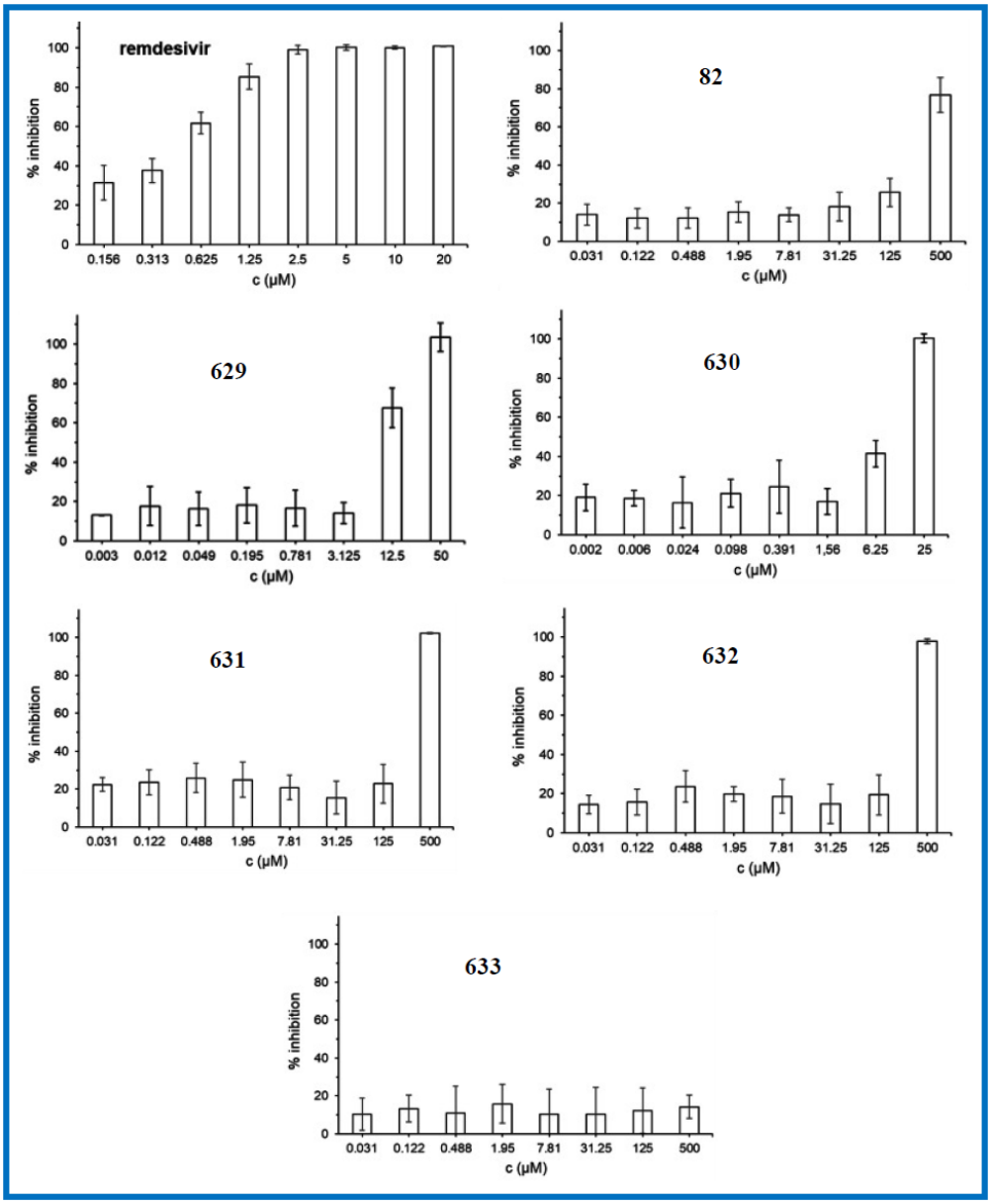

Figure 87. Concentration-dependent inhibition of SARS-CoV-2 replication in Caco-2 cells by remdesivir, titanocene dichloride (**82**), the organosilver complex **629** and organogold complexes **630-633**. Adapted with permission from Ref. [295], https://doi.org/10.1002/chem.202103258, under the terms of the CC BY 4.0 license, https://creativecommons.org/licenses/by/4.0/.

5.3. Anti-Inflammatory

Inflammation is an immune response caused by an injury to a tissue to clear damaged tissue, pathogens or toxins as well as recruiting immune cells. The inflammatory response results in swelling and heat due to dilation and increased permeability of blood vessels, and is controlled by a network of inflammatory mediators known as cytokines, which can be pro- or anti-inflammatory [301]. However, while inflammation is a natural part of the immune response and can assist in healing, chronic inflammation can be harmful and plays a role in a range of diseases [302]. As a result, anti-inflammatory drugs have been developed to reduce harmful levels of inflammation. A few examples of organometallic complexes that exhibit anti-inflammatory activity will be described in this section.

Zhang et al. prepared a series of electron-deficient half-sandwich metal complexes, including half-sandwich complexes of carborane with osmium (**634**), ruthenium (**635**) and iridium (**636**) as well as benzene-dithiolato complexes with osmium (**637**), ruthenium (**638**) and iridium (**639**) (Figure 88) [303]. The 16-electron complexes could directly bind to the inflammatory mediator nitric oxide (NO) to form stable 18-electron adducts with NO, lowering the NO concentration in the cell and thereby inhibiting the inflammatory response. Critically, this anti-inflammatory mechanism differs from conventional anti-inflammatory agents that display harmful side effects.

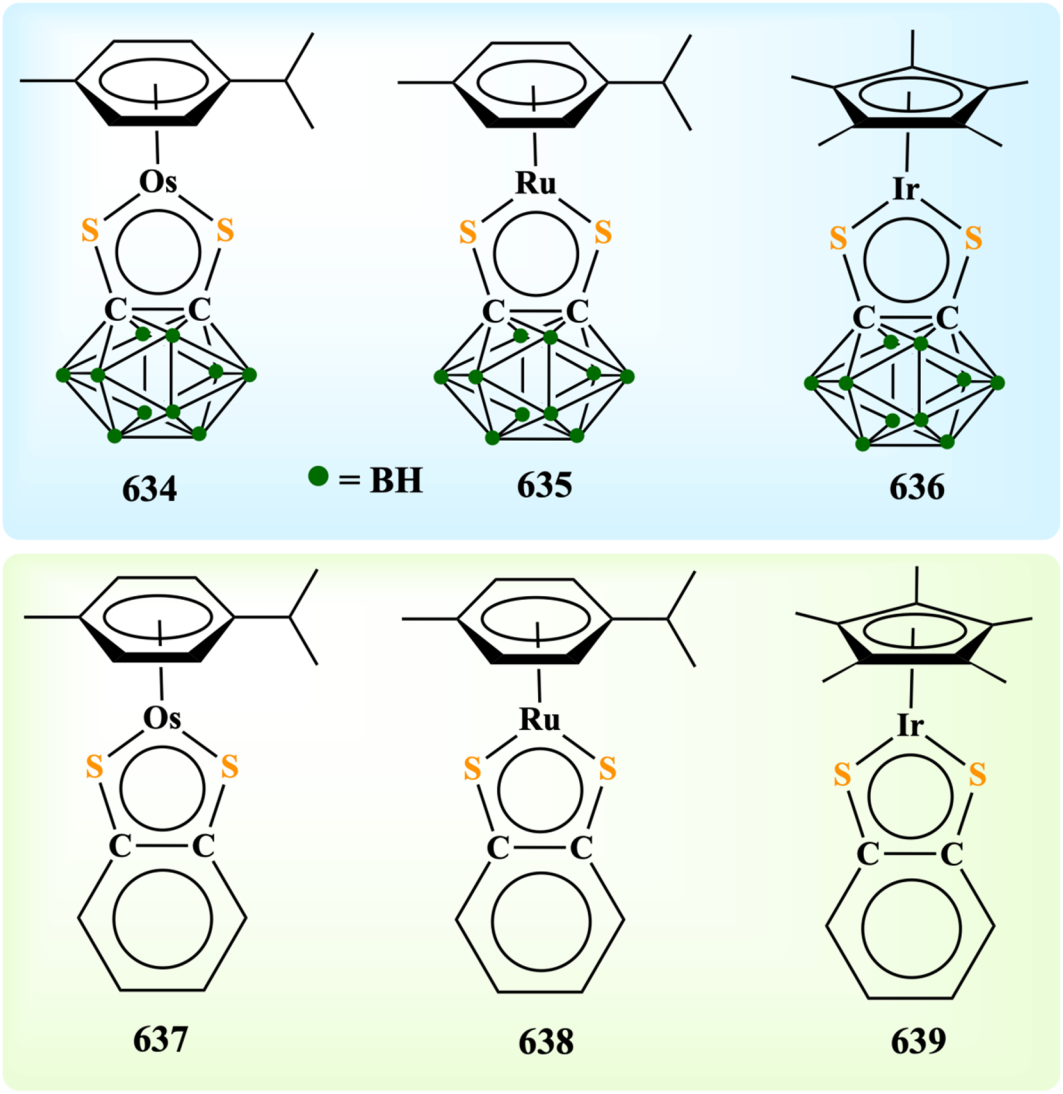

Figure 88. Half-sandwich complexes **634-639**.

The induction of inflammation modelled using bacterial lipopolysaccharide (LPS), a bacterial endotoxin found in the cell wall of Gram-negative bacteria that triggers a strong inflammatory response. The LPS-induced production of NO was measured for RAW 264.7 mouse macrophage cells incubated with various concentrations of complexes **634-639**, as shown in Figure 89. All complexes displayed concentration-dependent inhibition of NO production below a concentration of 50 μM, apart from the osmium-containing complex **634** with a carborane moiety, which significantly increased NO production at concentrations of 50 μM and 100 μM. An advantage of

the iridium-containing complexes **636** and **639** was their kinetic inertness, preventing side interactions with other biomolecules such as glutathione, resulting in lower cytotoxicity while maintaining the anti-inflammatory efficacy. Similar results were obtained for MRC-5 fibroblasts treated with the complexes **634-639**. Complex **634** exhibited increased NO for concentrations above 50 μM, while the remaining complexes all inhibited NO production at all concentrations examine, except for complex **635**, which increased NO at a 100 μM concentration.

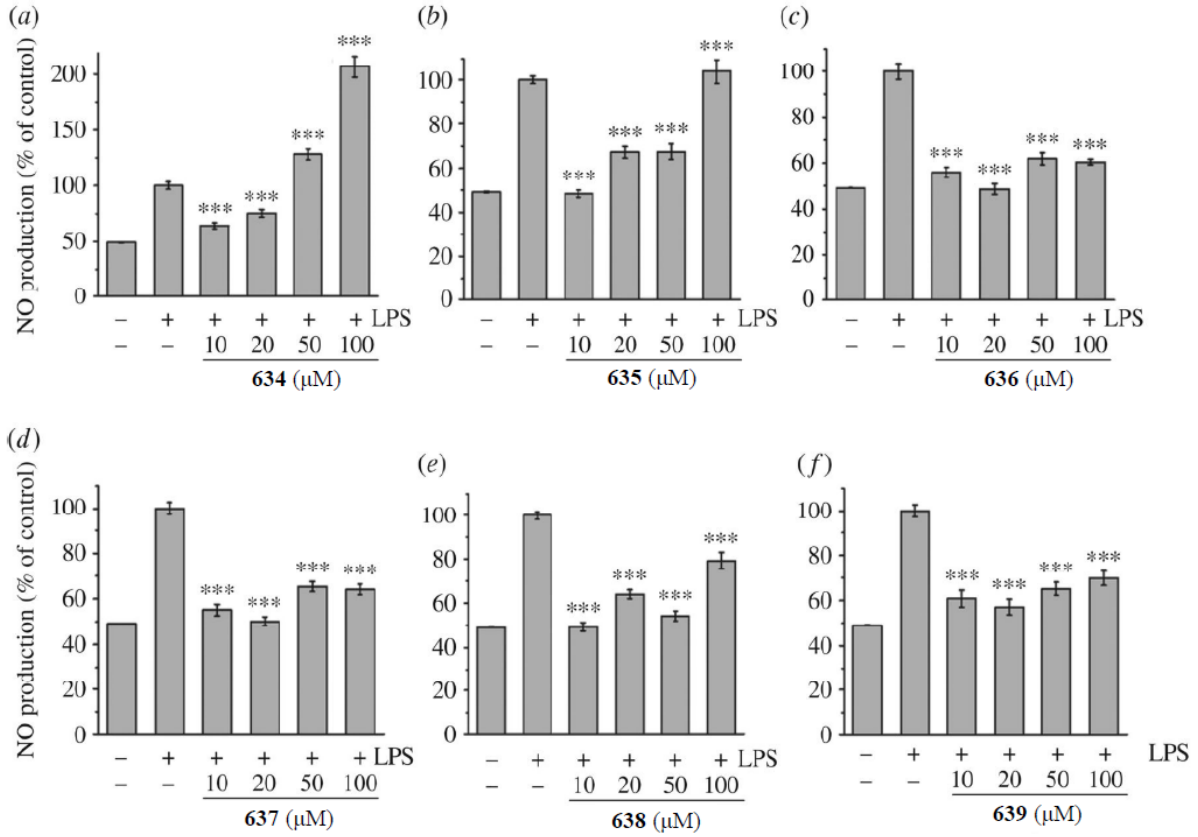

Figure 89. Inhibition of NO production in LPS-stimulated RAW 264.7 macrophages by complexes (**a**) **634**, (**b**) **635**, (**c**) **636**, (**d**) **637**, (**e**) **638** and (**f**) **639**. *** $p < 0.001$. Reproduced with permission from Ref. [303], https://doi.org/10.1098/rsos.170786 (accessed 6 May 2026), under the terms of the CC BY 4.0 license, https://creativecommons.org/licenses/by/4.0/.

The ruthenium-arene complexes **640-642**, as shown in Figure 90, were prepared by Jayakumar et al. and shown to inhibit the LPS-induced inflammatory response in the liver by examination of both liver cells and macrophages [304]. The most active anti-inflammatory and hepatoprotective effects were displayed by complex **642**. An *in vivo* mouse model with LPS-induced inflammation in the liver was employed to evaluate the prevention of damage to the liver cells by measuring serum concentrations of alanine transaminase (ALT) and aspartate transaminase (AST), two enzymes upregulated in liver cells in response to injury. Compared to the positive LPS control, complex **642** resulted in a significant decrease in levels of both ALT (~45 units/L compared to ~70 units/L) and AST (~175 units/L compared to ~325 units/L), in addition to visible reduction in signs of hepatic tissue injury, including wide sinusoids between cells and disruption of the endothelial tissue of the central vein. Additionally, complex **642** was found to downregulate expression of the pro-inflammatory cytokines TNF-α and IL-1β and the inflammatory nitric oxide synthase enzyme (iNOS), which also decreased production of NO. The mechanism of action for complex **642** was determined to involve disruption of JNK/NK-κB pathway involved in a number of cellular processes, including the inflammatory response. Complex **642** was found to inhibit phosphorylation of JNK, as well as preventing the degradation of IκB-α and nuclear translocation of the p65 component of NF-κB caused by LPS. An important finding was that the inhibition of JNK phosphorylation was specific to JNK, but not other mitogen-activated protein kinases (MAPKs) such as ERK and p38 MAPK.

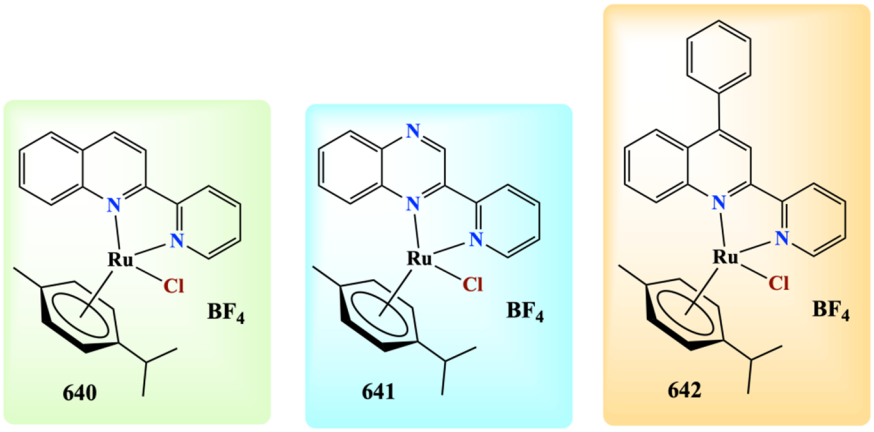

Figure 90. Structures of ruthenium-arene complexes **640-642**.

Trommenschlager et al. modified Au(I)-NHC complexes with coumarin-conjugated compounds **643-645**, containing coumarin moieties to increase their anti-inflammatory activity and caffeine-based moieties for decreased toxicity, yielding the gold-containing complexes **646-650** (Figure 91) [305]. The gold-containing complexes (at a concentration of 1 μg/mL) were used to measure the effect on IL1-β production in peripheral blood mononuclear cells (PBMCs) taken from human blood given by healthy donors. The strongest inhibitory effects were observed for **646** and **650**, with decreases of 98% and 47%, respectively. Complexes **647** and **648** induced only minimal inhibition, with decreases of 20% for complex **647** and 5% for complex **648**. For complex **649**, the treated cells instead had a pro-inflammatory response, with an increase of 53% in production of IL1-β. The decrease in inhibitory activity was correlated with direct substitution of the methyl group on the imidazole ring, such as for complexes **647** and **649** compared to their methyl-functionalized analogues **646** and **649**. On the other hand, complex **650** contained a coumarin moiety, but the coumarin was separated from the imidazole ring by a carbon atom, which resulted in the second highest inhibition of IL1-β production. This suggests that the steric hindrance of the coumarin located adjacent to the imidazole was responsible for the anti-inflammatory effect, possibly due to interference with protein binding.

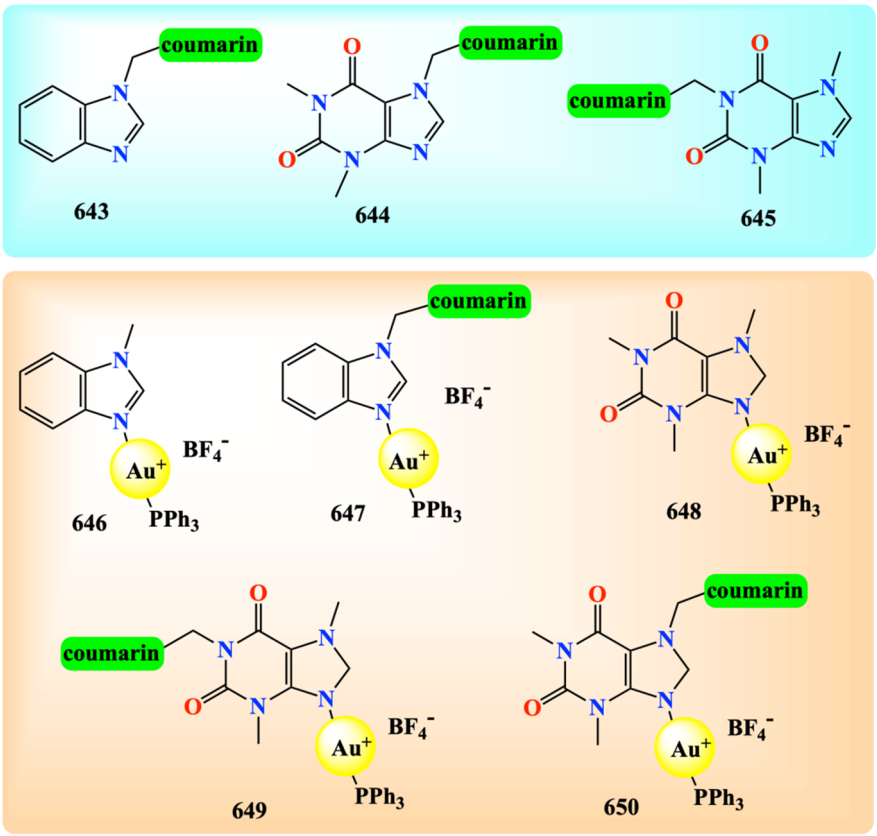

Figure 91. Coumarin-containing compounds **643-645** and complexes **646-650**.

Two of the most recognized and utilized non-steroidal anti-inflammatory drugs are aspirin and ibuprofen [306]. The anti-inflammatory effect of aspirin is primarily caused by the inhibition of cyclooxygenase (COX) enzymes, resulting in decreased levels of prostaglandin E2 (PGE2). One of the major side effects of aspirin is damage as well as hemorrhaging of the gastric mucosa. The Abd-El-Aziz research group designed organoiron dendrimers decorated with aspirin and ibuprofen at the periphery and examined their potential uses as anti-inflammatory agents [307,308], as shown in Figure 92.

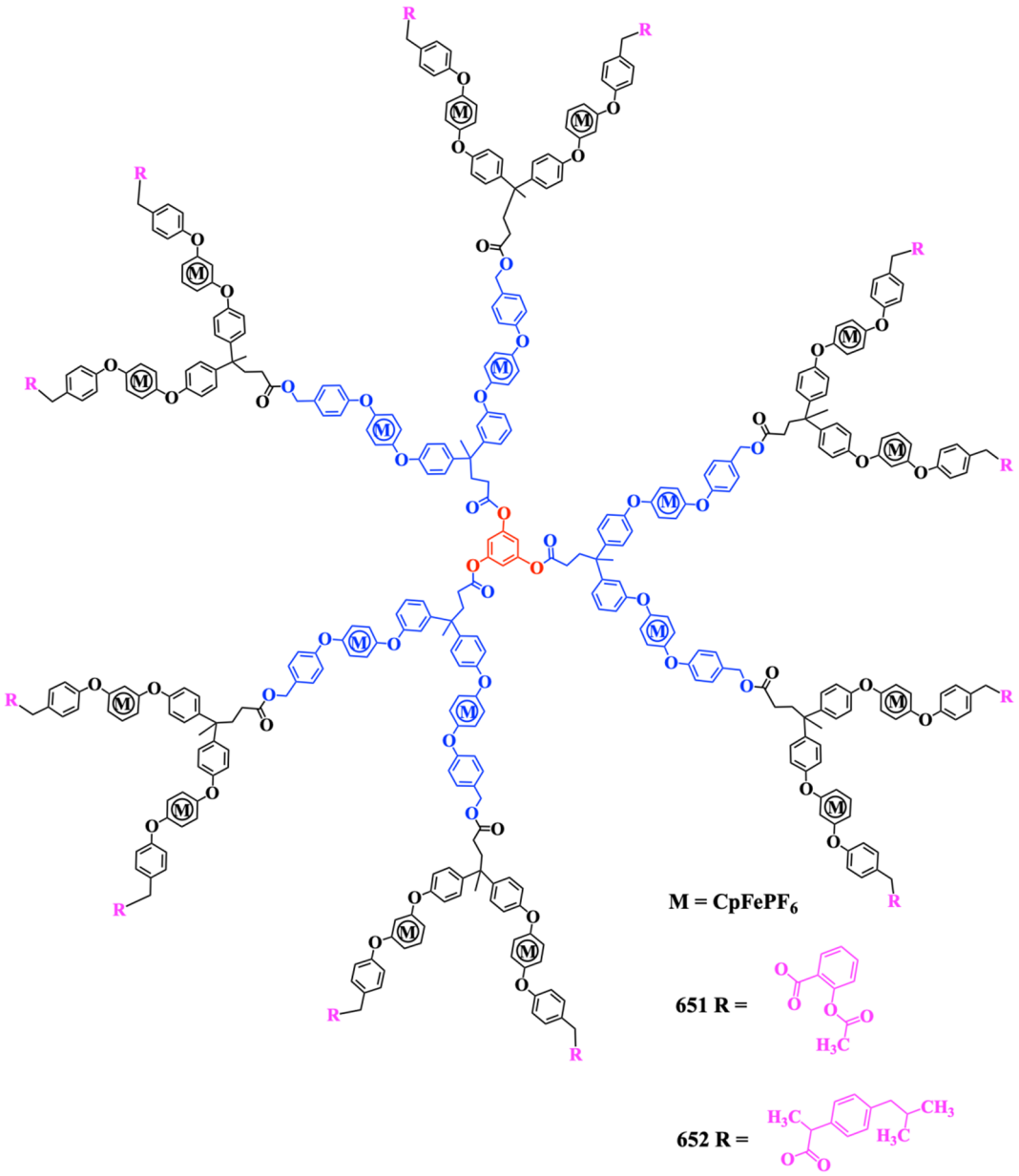

Figure 92. Structure of second-generation organometallic dendrimers decorated with aspirin (**651**) or ibuprofen moieties (**652**).

The organometallic dendrimers could prevent the gastric toxicity of free aspirin or ibuprofen, while maintaining the anti-inflammatory effects. Dendrimers **651** and **652** are two examples representing the second generation of the four generations of organoiron dendrimers that were prepared and examined in this study, where dendrimer **651** contains aspirin moieties and dendrimer **652** contains ibuprofen moieties. A rat paw edema (swelling) assay of inflammation induced using carrageenan demonstrated that the second-generation aspirin-decorated dendrimer **651** caused the largest decrease in inflammation compared to the first-, third- or fourth-generation dendrimers, as seen in Figure 93, with comparable activity to free aspirin. Additionally, histopathological staining and microscopy of gastric mucosal tissue showed that the free aspirin caused significant damage, while the dendrimers exhibited a trend of lower tissue damage with an increase in generation. Although almost no damage was observed for the fourth-generation dendrimer, the greatest balance between reduced gastric

toxicity and high anti-inflammatory efficacy was achieved for the second-generation dendrimer **651**. The first-generation dendrimer resulted in a smaller number of drug groups and effective surface area, while the large third- and fourth-generation dendrimers exhibited steric hindrance, inhibiting the ability of the dendrimers to be transported across cell membranes.

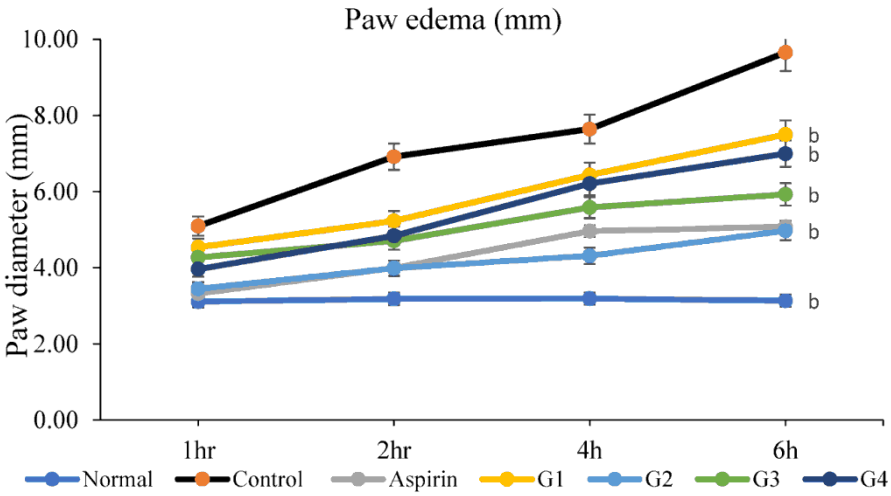

Figure 93. Rat paw edema assay for aspirin and first- (G1), second- (G2, **651**), third- and fourth-generation aspirin-decorated dendrimers compared to normal tissue and inflamed control (injection of carrageenan). Reproduced from Ref. [307], https://doi.org/10.3390/biom11111568, under the terms of the CC BY 4.0 license, https://creativecommons.org/licenses/by/4.0/.

The first-generation aspirin-decorated dendrimer resulted in a smaller number of drug groups and effective surface area, while the large third- and fourth-generation dendrimers exhibited steric hindrance, inhibiting the ability of the dendrimers to be transported across cell membranes. Similar effects were therefore also observed for ibuprofen-decorated dendrimers, where the second-generation dendrimer **652** exhibited the largest decrease of inflammation in a rat paw edema assay using formalin to induce inflammation [308]. A 37% reduction in inflammation compared to the formalin control, while ibuprofen alone only caused a 24% reduction. Micrographs of the H&E-stained tissues are shown in Figure 94. Compared to the untreated rat paw skin (Figure 94a), the injection of formalin (Figure 94b) demonstrated infiltration of white blood cells as well as edema and congestion of capillaries, all signs of an inflammatory response. The treatment with ibuprofen resulted in a moderate inflammatory response, with a visible decrease in immune cell infiltration and edema, in addition to increased dilation of the capillaries, as shown in Figure 94c. Complex **652**, by contrast, showed an even more mild inflammatory reaction, with minimal white blood cell infiltration and edema with only mild congestion of capillaries, as illustrated in Figure 94d.

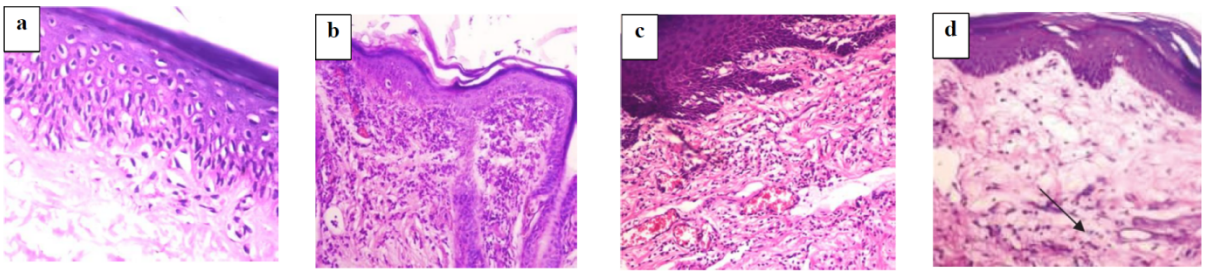

Figure 94. Rat paw skin photomicrographs for (**a**) untreated rats, or rats injected subcutaneously with (**b**) formalin, (**c**) formalin and ibuprofen or (**d**) formalin and ibuprofen-decorated dendrimer **652**. Adapted from Ref. [308] with permission from John Wiley & Sons, Copyright © 2020 Wiley-VCH GmbH.

Hybrids of Au(I)-NHC complexes with carbazoles were designed to combine the anti-inflammatory activity of both moieties [309]. The resulting hybrid complexes **653-660** (Figure 95) were also compared with the gold-carbazole complex **661** alone. The anti-inflammatory activity was determined using a colourimetric NO assay based on the Griess reaction to measure the concentration of nitrite produced from NO. The inhibition of NO

production was therefore examined for LPS-stimulated RAW 264.7 macrophages after 24 hours of incubation. Two concentrations, 5 μM and 10 μM, were tested for each compound as well as the control NSAID indomethacin. All complexes reduced NO production, except for complex **657**, which exhibited no effect at either concentration. The levels of inhibition for complexes **653-656**, **658** and **661** were less than or equivalent to indomethacin, which showed 8% and 23% inhibition for 5 μM and 10 μM concentrations, respectively. By comparison, complex **660** caused inhibition of NO synthesis by 8% at 5 μM and 57% at 10 μM, while complex **659** yielded inhibition values of 19% at 5 μM and 38% for 10 μM. As a result, complexes **659** and **660** were found to exhibit significantly enhanced inhibition of NO production compared to the reference indomethacin. This effect on NO production was not a consequence of cytotoxicity, as none of the gold complexes or indomethacin exhibited any toxic effects at either tested concentration.

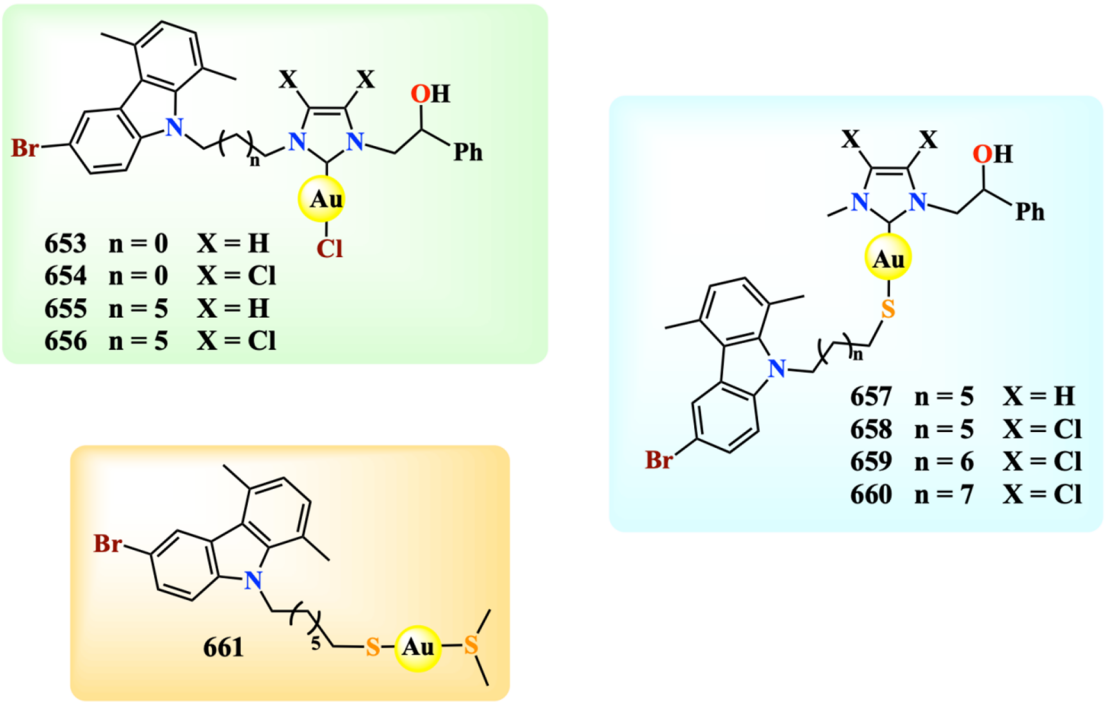

Figure 95. Carbazole-conjugated Au(I)-NHC complexes **653-660** and gold-carbazole complex **661**.

5.4. Anti-Neurodegenerative

Neurodegenerative diseases, diseases which cause the death of neurons and neural tissue, are a group of diseases that are becoming increasingly common for a number of aging populations [310]. The most prevalent neurodegenerative disease globally is Alzheimer's disease, which is difficult to treat due to the inability of many drugs to cross the blood-brain barrier and the harmful side effects of existing therapies [311]. Although research is still ongoing into the pathology of Alzheimer's disease, two key features of neurodegeneration based on proteins have been identified: amyloid-β (sometimes referred to as β-amyloid) and neurofibrillary tangles (NFT). Additionally, inflammation and oxidative stress are factors that can influence the onset of Alzheimer's disease symptoms and interact with other mechanisms. While Alzheimer's disease has been linked to neurotoxicity due to disruption in metal homeostasis, metal-containing complexes, including organometallic complexes, have also shown great promise for treatment via reduction of oxidative stress and preventing the aggregation of amyloid-β [312]. This section will therefore examine several examples of organometallic complexes investigated for treatment of Alzheimer's disease.

A series of half-sandwich cyclopentadienyl-tricarbonyl complexes containing ^{99m}Tc and Re moieties were prepared for use in diagnostic and therapeutic agents in Alzheimer's disease [313]. Ferrocene carboxaldehyde (**137**) was reacted with 2-aminobenzenethiol (**662**) or benzene-1,2-diamine (**663**) to produce the ferrocenyl derivatives of benzothiazole (**664**), benzimidazole (**665**) and *N*-methylbenzimidazole (**666**). The iron centers were then substituted for Re or ^{99m}Tc to yield the corresponding tricarbonyl complexes **667-669** (Re) and **670-672** (^{99m}Tc), as shown in Scheme 65.

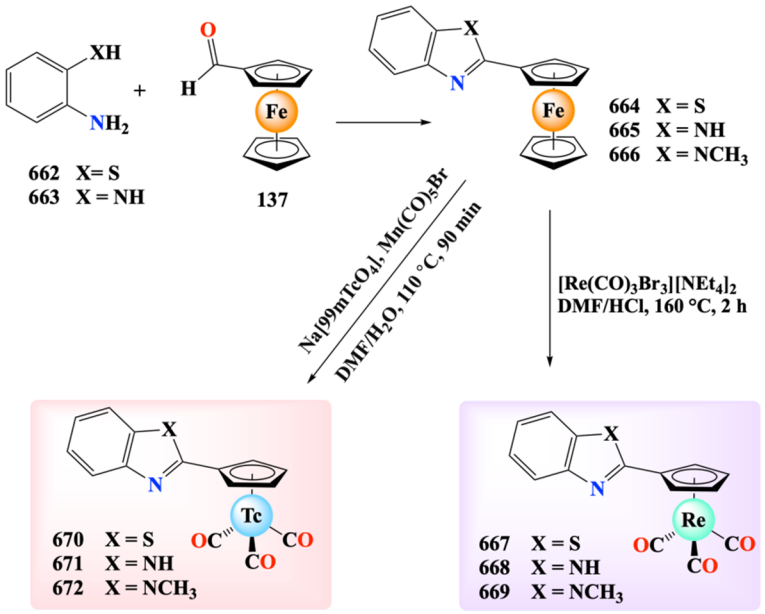

Scheme 65. Synthetic preparation of tricarbonylrhenium complexes **667-669** and tricarbonyltechnetium complexes **670-672.**

In terms of therapeutic activity, the Re-containing complexes **667-669** were shown to competitively bind to plaques and fibrils of amyloid-β, as well as inhibiting the formation of amyloid-β fibrils in solution. All three complexes were also capable of significantly recovering the cell viability of hippocampal neurons reduced by addition of 1 μM of amyloid-β 42 (Aβ42), which resulted in 50% of cells being viable. When a 2 μM concentration of complex **667** was added to the cells, 72% cell viability was observed, while the same concentration of complexes **668** and **669** led to 79% and 81% survival, respectively. Additionally, minimal cytotoxicity was observed for the complexes without addition of Aβ42. Due to the effect of oxidative stress on the pathology of Alzheimer's disease, the effect of complexes **667-669** on ROS levels were measured using a DCFH-DA assay. The addition of 2 μM of the complexes to the cells treated with 1 μM Aβ42 resulted in a decrease in ROS levels (relative to the 1 μM Aβ42 control) of 55.2% for complex **667**, 63.2% for complex **668**, and 68.1% for complex **669**, as illustrated in Figure 96. In the absence of Aβ42, comparable ROS levels to the untreated cells were observed, confirming the antioxidant activity of these complexes in response to Aβ42.

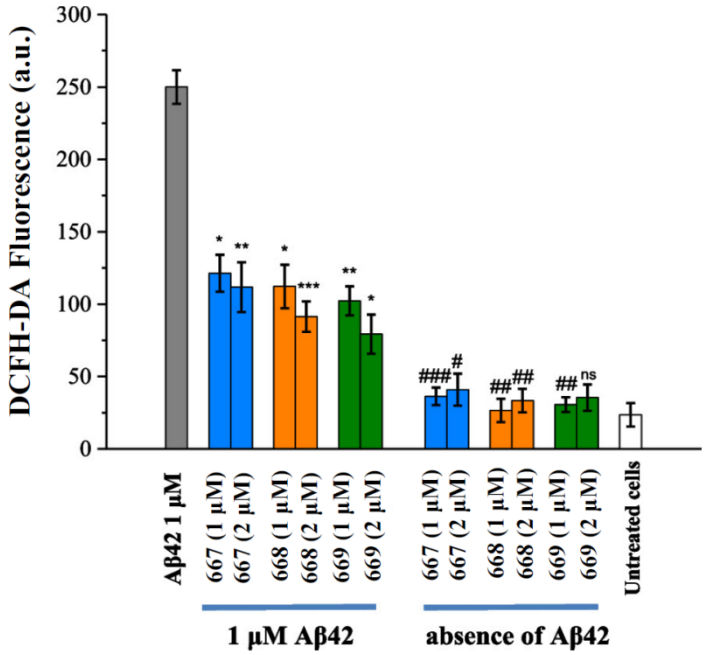

Figure 96. DCFH-DA assay for induction of ROS by complexes **667-669** with or without addition of Aβ42. * $p \leq 0.05$, ** $p \leq 0.01$, *** $p \leq 0.001$ and not significant (ns) > 0.05 compared with treatment using 1 μM Aβ42; $^{\#}p < 0.01$,

$^{\#\#}p < 0.01$ and $^{\#\#\#}p < 0.001$ compared with untreated controls. Reproduced with permission from Ref. [313], Copyright © 2019, American Chemical Society.

Hacker et al. designed Ru(II)-arene complexes with azole ligands for their use as anti-amyloid-β agents [314]. These half-sandwich ruthenium complexes (Figure 97) were comprised of a Ru(II) centre with a η^6-*p*-cymene ligand, two chloro ligands, and an azole ligand, namely 2-aminooxazole (**673**), 2-aminothiazole (**674**), 2-aminobenzimidazole (**675**), 2-aminobenzoxazole (**676**) or 2-aminobenzothiazole (**677**). The effect of complexes **673-677** on cytotoxicity of glial cells induced by Aβ42 showed that all five complexes increased the glial cell viability. Furthermore, the complexes were able to inhibit formation of amyloid-β fibrils and aggregation. The binding of the complexes to human serum albumin (HSA) also demonstrated low binding affinities, which is encouraging for their ability to avoid binding to HSA that could prevent transport across the blood-brain barrier. Overall, the complex **676** containing a 2-aminobenzoxazole ligand exhibited the lowest aggregation and fibril formation, highest reduction in cytotoxicity and weakest binding to HSA, while the other four complexes showed more comparable results to each other.

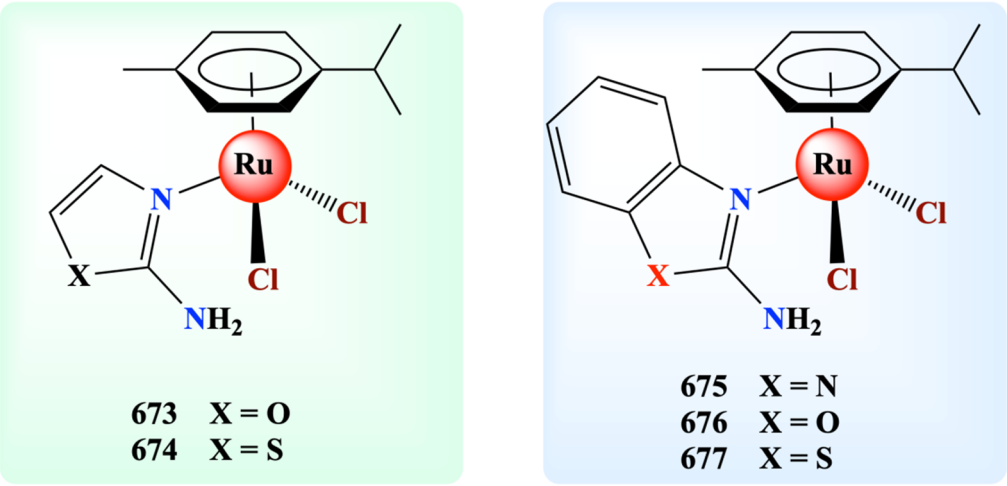

Figure 97. Structures of azole-containing Ru(II)-arene complexes **673-677**.

In addition to the previously described biomedical activities of metal-NHC complexes, their tunable activity can also be employed for design of therapeutic drugs in the treatment of Alzheimer's disease. For example, Ceramella et al. prepared a series of Ag(I)- and Au(I)-NHC complexes (**678-685**, Figure 98) containing proline moieties with a N-protected *t*-butyloxycarbonyl (Boc) group for their neuroprotective effects [315].

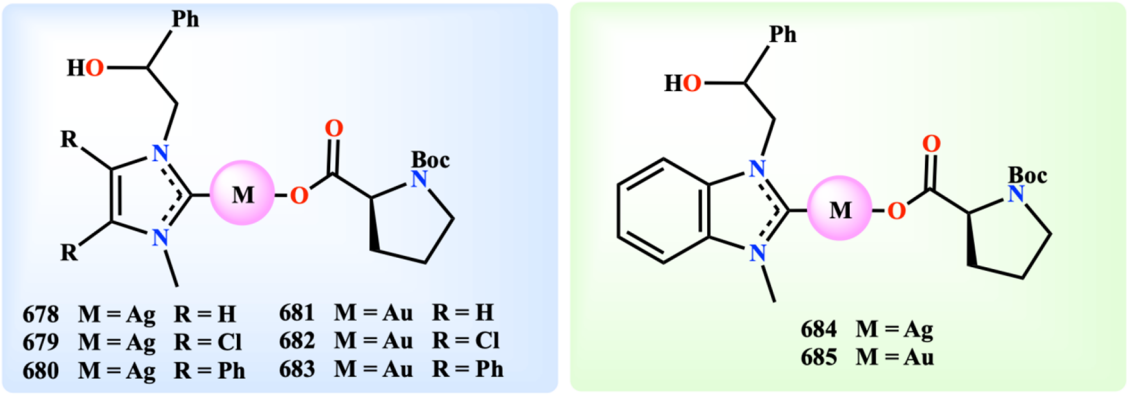

Figure 98. Ag(I)- and Au(I)-NHC complexes **678-685**.

The inhibition of several proteins involved in Alzheimer's disease was analyzed for complexes **678-685**. The inhibition of acetylcholinesterase (AChE) was lower for all tested complexes than the reference drug donepezil, with no detectable activity from silver complexes **678-680**. However, in later stages of Alzheimer's disease, AChE levels decrease, which is a known limitation of conventional therapies such as donepezil. Interestingly, the presence of the benzene ring fused to the carbene moiety of complex **685** allows targeting of the related protein

butyrylcholinesterase (BChE), which can increase during the progression of Alzheimer's disease. IC_{50} values of 0.45 μM for complex **685** and 2.13 μM for donepezil were calculated, indicating a five-fold greater inhibition for the Au(I)-NHC complex **685**. While monoamine oxidase (MAO) inhibition is not a common focus of research for Alzheimer's disease, the oxidative stress associated with high MAO activity may cause neuronal damage. The authors therefore examined the inhibition by the complexes for two human MAO isoforms: *h*MAO-1 and *h*MAO-2, and compared their activity with the reference inhibitors clorgyline for *h*MAO-A and R-(-)-deprenyl for *h*MAO-B. Gold complexes **681-683** and **685** tended to show superior activity compared to their silver analogues **678-680** and **684**. Docking studies suggested that the greater electronegativity in the Au-containing complexes led to improved binding interactions. None of the complexes were as effective as the reference *h*MAO-A or -B, with the strongest inhibition of being observed for complex **685**, with an IC_{50} of 7.13×10^{-2} for *h*MAO-A, compared to 2.00×10^{-3} for clorgyline. Due to the effect of inflammation on the pathology of Alzheimer's disease, the inhibition of NO production by iNOS was also examined. Although only the gold-containing complex **683** showed 52% inhibition in mouse RAW 264.7 macrophages relative to untreated LPS-induced cells, the corresponding silver complex **680** also exhibited a low level of inhibition (8%). Critically, however, both complexes displayed low cytotoxicity, showing that the lower levels of NO were not a consequence of cell death. The complexes were further examined for their antioxidant activity by reduction in ROS levels in 3T3 mouse fibroblasts using a DCFH-DA assay compared to oxidative stress induced by addition of menadione (Men), with NAC as a reference antioxidant. All complexes were tested at a concentration of 10 μM, except for complex **683**, which was used at a 1 μM concentration. As can be observed by the results in Figure 99, Au-containing complexes **683** and **685** demonstrated the highest antioxidant activities, where complex **683** reduced ROS levels to 70% of the positive control and complex **685** to 60% of the positive control.

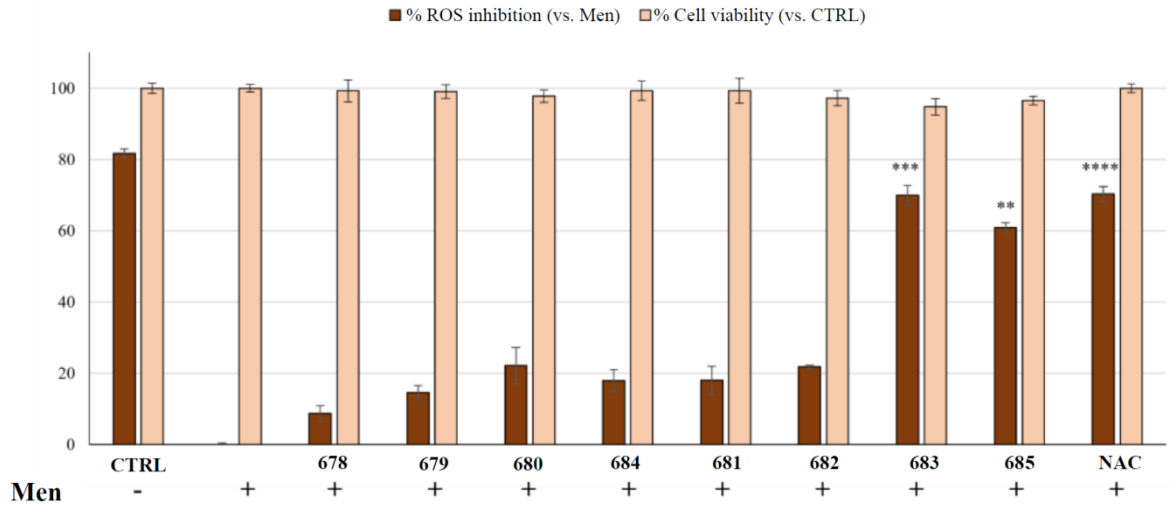

Figure 99. Induction of ROS and cell viability for 3T3 mouse fibroblasts by complexes **678-685** and NAC, compared to menadione (Men) and untreated cells (CTRL), respectively (** $p < 0.01$, *** $p < 0.001$, **** $p < 0.0001$). Reproduced with permission from Ref. [315], https://doi.org/10.3390/ijms26136116 (accessed on 27 May 2026), under the terms of the CC BY 4.0 license, https://creativecommons.org/licenses/by/4.0/.

6. Conclusions and Future Directions

Organometallic complexes have attracted tremendous interest in biomedicine in light of their exceptional stability and diverse characteristics. From complexes to macromolecules containing organometallic moieties, either in the backbone or pendent to the backbone of polymers and dendrimers, these classes of materials have been shown to have numerous uses in the biomedical field. The properties of transition metals and their ligands offer opportunities for their use as promising candidates in biological studies. While some metals can present concerns due to their toxicity, organometallic complexes and macromolecules have demonstrated mechanisms to reduce the toxicity and increase the bioavailability of this class of materials compared with the parent metal(s), by improving transport into cells or solubility in aqueous solutions. There is a rich library of organometallic complexes and macromolecules for combating infectious diseases caused by bacteria, fungi, parasites and viruses as well as their use for treatment of cancers, inflammation and neurodegenerative diseases.

The past five years have shown many complexes with intriguing biological activities that cannot be all fully discussed in this review article, but selective examples have been given to demonstrate the diverse nature of the

metallic moieties as well as the organic ligands. This review highlighted the importance of organometallic complexes not only as potential therapeutic agents but also for their use in bioimaging. Photothermal and photodynamic therapy using organometallic moieties has attracted the attention of many research groups to develop highly selective complexes that can inhibit the proliferation of cancer cells. The design of complexes with moieties for both diagnostic bioimaging and phototherapy also illustrates the potential use of organometallics in the developing area of theranostics. The rich chemistry and the various oxidation states that the metallic moieties possess has allowed for the development of new therapeutic agents that could overcome mechanisms of drug resistance. Organometallic complexes have demonstrated the ability to regulate drug release, as well as to improve cellular uptake and pharmacokinetics, and organometallic macromolecules may further enhance this activity due to increasing local concentration of the active groups.

Research in the field of organometallic molecules and macromolecules has focused on the development of new materials with potential uses in the treatment of various infectious and non-infectious diseases, however, the majority of the biological studies have been devoted to in vitro experiments and there are a limited number of in silico predictive models or *in vivo* studies using animal models. Further, these studies do not necessarily fully explore the pharmacokinetic properties of these molecules, including absorption, distribution and whole-body toxicity. For example, while low cytotoxicity against healthy host cells may demonstrate the utility of a given molecule, the higher load in organs such as the kidneys and liver during excretion may result in higher concentrations with toxic effects. Therefore, additional experimental and computational studies of the pharmacokinetic characteristics of many of these molecules are still needed before they can be considered for clinical trials. While organometallic systems therefore have great potential, a number of challenges remain, including a need for high selectivity in a physiological environment, stability *in vivo* and ensuring that any degradation products are not significantly toxic to humans or the ecosystem, development of new resistance mechanisms, optimizing pharmacokinetics and overcoming the blood-brain barrier for agents with effects in the central nervous system (such as therapies for Alzheimer's disease). The future of organometallic agents in biomedicine lies in the versatility of the organic ligands and the metal moieties to overcome these challenges. This versatility also allows for the design of multifunctional structures, which could have multiple mechanisms of action for a single drug by combining multiple active moieties, could provide a theranostic system that could serve for both diagnosis and treatment, or could be used in a drug delivery system with inherent biological activity, such as antifouling. It is therefore anticipated that new organometallic complexes and macromolecules will continue to be developed to expand the range of potential biomedical materials with tailored activities as well as examinations of their behaviour in clinical trials.

Author Contributions

A.A.-E.-A.: Conceptualisation, methodology, data curation, formal analysis, writing—original draft, writing—reviewing and editing; Z.L.: methodology, data curation, formal analysis, writing—original draft; A.M.Y.: methodology, formal analysis, writing—original draft; N.M.: methodology, writing—reviewing and editing, supervision, resources, project administration; A.S.A.-E-A.; conceptualisation, methodology, formal analysis, writing—original draft, writing—reviewing and editing, supervision, resources. All authors have read and agreed to the published version of the manuscript.

Funding

This work was supported by the WZSB Plan for Long-term Senior Expert Project of Shandong Province, Fundamental Research Funds for the Central Universities (30720205GH1002), and Research Operating Funds of Heilongjiang Provincial Research Institutes (CZBZ202403004).

Data Availability Statement

Accessibility of data in this review is accessible by the authors upon reasonable request

Acknowledgments

The support of Harbin Engineering University and the WZSB Plan for Long-term Senior Expert Project of Shandong Province is gratefully acknowledged.

Conflicts of Interest

The authors declare no conflict of interest.

Use of AI and AI-Assisted Technologies

No AI tools were utilized for this paper.

References

1. Ishii, Y. Organometallic Complexes. In *Coordination Chemistry: Molecular Science of Organic–Inorganic Complexes*; Tanase, T., Ishii, Y., Eds.; Royal Society of Chemistry: Cambridge, UK, 2024; Volume 3, pp. 187–217.
2. Markandeya, G.B.; Budagumpi, S. Organometallic Compounds: The Fundamental Aspects. In *Organometallic Compounds*; John Wiley & Sons, Inc.: Hoboken, NJ, USA, 2023; pp. 1–23.
3. Kumar, A.; Avula, B.; Yadav, S.; Singh, Y.; Eraganaboyina, S.; Zyryanov, G.V.; Nemallapudi, B.R.; Singh, A.K.; Bhimireddi, R. Synthesis, Properties, Environmental Stability and Practical Application of Organometallic Compounds: A Comprehensive Review. *Inorg. Chem. Commun.* **2023**, *158*, 111567. https://doi.org/10.1016/j.inoche.2023.111567.
4. Gao, Y.; Zhang, Z.; Yi, Z.; Zhang, C.; Xu, W. Visualizing the Hierarchical Evolution of Aryl–Metal Bonding in Organometallic Nanostructures on Ag(111). *J. Phys. Chem. Lett.* **2023**, *14*, 10819–10824. https://doi.org/10.1021/acs.jpclett.3c02950.
5. Ye, B.-C.; Li, W.-H.; Zhang, X.; Chen, J.; Gao, Y.; Wang, D.; Pan, H. Advancing Heterogeneous Organic Synthesis with Coordination Chemistry-Empowered Single-Atom Catalysts. *Adv. Mater.* **2024**, *36*, 2402747. https://doi.org/10.1002/adma.202402747.
6. Beig, N.; Goyal, V.; Bansal, R.K. Application of N-Heterocyclic Carbene–Cu(I) Complexes as Catalysts in Organic Synthesis: A Review. *Beilstein J. Org. Chem.* **2023**, *19*, 1408–1442. https://doi.org/10.3762/bjoc.19.102.
7. Jayaraj, A.; Raveedran, A.V.; Latha, A.T.; Priyadarshini, D.; Swamy, P.C.A. Coordination Versatility of NHC-Metal Topologies in Asymmetric Catalysis: Synthetic Insights and Recent Trends. *Coord. Chem. Rev.* **2023**, *478*, 214922. https://doi.org/10.1016/j.ccr.2022.214922.
8. Crisenza, G.E.M.; Faraone, A.; Gandolfo, E.; Mazzarella, D.; Melchiorre, P. Catalytic Asymmetric C–C Cross-Couplings Enabled by Photoexcitation. *Nat. Chem.* **2021**, *13*, 575–580. https://doi.org/10.1038/s41557-021-00683-5.
9. Zhao, Y.; Yu, X.; Bao, T.; Guo, Y.; Su, Y.; Zhao, J. Two-Dimensional Fullerene-Based Ferroelectric Materials: Assembly and Effects on Charge Carrier Lifetime. *Nano Lett.* **2024**, *24*, 13534–13541. https://doi.org/10.1021/acs.nanolett.4c02986.
10. Zhang, J.; Wang, J.; Wei, C.; Wang, Y.; Xie, G.; Li, Y.; Li, M. Rapidly Sequence-Controlled Electrosynthesis of Organometallic Polymers. *Nat. Commun.* **2020**, *11*, 2530. https://doi.org/10.1038/s41467-020-16255-z.
11. Zhong, J.-J.; Zhan, S.-Z.; Li, Y.; Guo, Y.-S.; Ng, S.W.; Deng, Y.-F.; Li, D. A 1D Mixed-Valence Cuprofullerene Pyrazolate Polymer as a Semiconductor Material. *Inorg. Chem.* **2022**, *61*, 10624–10628. https://doi.org/10.1021/acs.inorgchem.2c01478.
12. Banasz, R.; Wałęsa-Chorab, M. Polymeric Complexes of Transition Metal Ions as Electrochromic Materials: Synthesis and Properties. *Coord. Chem. Rev.* **2019**, *389*, 1–18. https://doi.org/10.1016/j.ccr.2019.03.009.
13. Abd-El-Aziz, A.S. Organometallic Polymers of the Transition Metals. *Macromol. Rapid Commun.* **2002**, *23*, 995–1031. https://doi.org/10.1002/marc.200290003.
14. Wang, T.; Zhang, H.; Jin, L.; Tao, P.; Cheng, Y.; Wong, W.-Y. Deep Red to Near-Infrared Thermally Activated Delayed Fluorescence Conjugated Polymers toward Highly Efficient Solution-Processible Deep Red and near-Infrared Organic Light-Emitting Diodes. *FlexMat* **2026**, *1*, n/a. https://doi.org/10.1002/flm2.70096.
15. Melendo, I.; Weatherill, L.A.; Martín, A.; Pander, P.; Dias, F.B.; Fuertes, S.; Sicilia, V. Double Decker NHC-Cyclometallated Pt Complexes for Highly-Efficient Vacuum-Deposited Green OLEDs and NIR Emission. *Mater. Chem. Front.* **2026**, *10*, 1633–1643. https://doi.org/10.1039/d6qm00041j.
16. Tao, P.; Jin, J.; Zheng, X.; Pu, Y.-J.; Wong, W.-Y. Engineering Emissive Excited States in Organic Electroluminescent Materials. *Matter* **2025**, *8*, 102142. https://doi.org/10.1016/j.matt.2025.102142.
17. Tselekidou, D.; Papadopoulos, K.; Zachariadis, A.; Kyriazopoulos, V.; Kassavetis, S.; Laskarakis, A.; Gioti, M. Solution-Processable Red Phosphorescent OLEDs Based on Ir(Dmpq)2(Acac) Doped in Small Molecules as Emitting Layer. *Mater. Sci. Semicond. Process.* **2023**, *163*, 107546. https://doi.org/10.1016/j.mssp.2023.107546.
18. Aziz, K.; Ahmed, K.; Anwar, R.; Qader, A.F.; Abdulkareem, E. Organometallic Complexes and Reaction Methods for Synthesis: A Review. *Rev. Inorg. Chem.* **2024**, *44*, 685–698. https://doi.org/10.1515/revic-2024-0037.
19. Govindaraju, S.; Ramaraj, S.G.; Servesh, A.; Rajprasad, J.; Kumar, N.; Sadaiyandi, V.; Tabassum, S. $Mn_2(CO)_{10}$ Catalyzed Visible-Light-Promoted Synthesis of 1H-Pyrazole-4-Carboxamides; A Sustainable Multi-Component Statergy with Antibacterial and Cytotoxic Evaluations. *J. Organomet. Chem.* **2024**, *1022*, 123384. https://doi.org/10.1016/j.jorganchem.2024.123384.
20. Wang, T.; Astruc, D. Electron-Reservoir Applications of Ferrocenes and Other Late Transition-Metal Sandwich Complexes: Flow Batteries, Sensing, Catalysis, and Biomedicine. *Coord. Chem. Rev.* **2025**, *524*, 216300. https://doi.org/10.1016/j.ccr.2024.216300.
21. Steinlandt, P.S.; Zhang, L.; Meggers, E. Metal Stereogenicity in Asymmetric Transition Metal Catalysis. *Chem. Rev.* **2023**, *123*, 4764–4794. https://doi.org/10.1021/acs.chemrev.2c00724.

22. Astruc, D. *Organometallic Chemistry and Catalysis*, 1st ed.; Springer: Berlin/Heidelberg, Germany, 2007.
23. Li, X.; He, M.; Liu, R.; Guo, S.; Liu, Y. Rational Design of Chloride-Based Ionic Iridium(III) Complex to Construct Phosphorescent Nanoparticles for Cancer Cell Imaging. *J. Organomet. Chem.* **2025**, *1025*, 123485. https://doi.org/10.1016/j.jorganchem.2024.123485.
24. Jiang, J.; Xu, Z.; Li, T.; Lv, Z. Visible to Near-Infrared Light Activated Photoacids: Molecular Architecture for Chemical and Biological Applications. *J. Organomet. Chem.* **2025**, *1027*, 123525. https://doi.org/10.1016/j.jorganchem.2025.123525.
25. Yao, S.; Zhang, Y.; Liu, X.; Dong, X.; Zhang, Z.; Lü, X.; Fu, G. Deep-Red or near-Infrared-Emitting Iridium (III) Complex as Efficient Phosphorescent Dye for Live Cell Imaging through Staining in Cytoplasm. *J. Organomet. Chem.* **2025**, *1024*, 123443. https://doi.org/10.1016/j.jorganchem.2024.123443.
26. Gorshkov, N.I.; Murko, A.Y.; Zolotova, Y.I.; Nazarova, O.V.; Krasikov, V.D.; Shatik, S.V.; Panarin, E.F. Introduction of $Re(CO)_3^+$/$^{99m}Tc(CO)_3^+$ Organometallic Species into Vinylpyrrolidone-Allyliminodiacetate Copolymers. *Polym. (Basel)* **2021**, *13*, 1832. https://doi.org/10.3390/polym13111832.
27. Schibli, R.; Schubiger, A.P. Current Use and Future Potential of Organometallic Radiopharmaceuticals. *Eur. J. Nucl. Med. Mol. Imaging* **2002**, *29*, 1529–1542. https://doi.org/10.1007/s00259-002-0900-8.
28. Guillen, C.; Monroy-Cruz, L.J.; Campo, K.A.-D.; Zimic, M.; Salas, P. Half-Sandwich Ruthenium (II) Complexes with N,O-Quinoxaline Ligand: Synthesis, in Silico Affinity and Mycobacterium Tuberculosis Susceptibility. *J. Inorg. Biochem.* **2026**, *275*, 113094. https://doi.org/10.1016/j.jinorgbio.2025.113094.
29. Abdolmaleki, S.; Aliabadi, A.; Khaksar, S. Bridging the Gap between Theory and Treatment: Transition Metal Complexes as Successful Candidates in Medicine. *Coord. Chem. Rev.* **2025**, *531*, 216477. https://doi.org/10.1016/j.ccr.2025.216477.
30. Astruc, D. From Sandwich Complexes to Dendrimers: Journey toward Applications to Sensing, Molecular Electronics, Materials Science, and Biomedicine. *Chem. Commun.* **2023**, *59*, 7321–7345. https://doi.org/10.1039/D3CC01175E.
31. Abd-El-Aziz, A.; Fouda, M.M.G.; Sharaby, C.M.; Xiao, O.; Zhang, X.; Alzahrany, Y.A.; Ahmed, S.A.; Ma, N.; Abd-El-Aziz, A.S. Recent Developments in Antimicrobial and Antiviral Agents Based on Natural/Synthetic Polymers and Dendrimers: Design and Therapeutic Applications. *Macromol. Chem. Phys.* **2024**, *225*, 2400123. https://doi.org/10.1002/macp.202400123.
32. López-Hernández, J.E.; Contel, M. Promising Heterometallic Compounds as Anticancer Agents: Recent Studies in Vivo. *Curr. Org. Chem. Biol.* **2023**, *72*, 102250. https://doi.org/10.1016/j.cbpa.2022.102250.
33. Abd-El-Aziz, A.S.; Youssef, A.M.; Abd-El-Aziz, A. *Transition Metal-Containing Dendrimers in Biomedicine: Current Trends*; Royal Society of Chemistry: Cambridge, UK, 2023.
34. Peng, K.; Zheng, Y.; Xia, W.; Mao, Z.-W. Organometallic Anti-Tumor Agents: Targeting from Biomolecules to Dynamic Bioprocesses. *Chem. Soc. Rev.* **2023**, *52*, 2790–2832. https://doi.org/10.1039/D2CS00757F.
35. Naoom, N.; Yousif, E.; Zainulabdeen, K.; Salman, I.; Amalia, H.; M Yusop, R.; Redwan, A.; Bufaroosha, M. Synthesis and Applications of Organotin (IV) Compounds: Mini Review. *J. Sustain. Mater. Process. Manag.* **2023**, *3*, 1–8.
36. Abd-El-Aziz, A.S.; Abdelghani, A.A.; Mishra, A.K. Optical and Biological Properties of Metal-Containing Macromolecules. *J. Inorg. Organomet. Polym. Mater.* **2020**, *30*, 3–41. https://doi.org/10.1007/s10904-019-01293-y.
37. Nitin, V.; Anand, T.; Singh, C.K.; Sodhi, K.K. Role of Organometallic Complexes in Targeted Therapies of Different Diseases: Infectious Diseases, Cancer and Neurodegenerative Diseases. *J. Organomet. Chem.* **2024**, *1022*, 123389. https://doi.org/10.1016/j.jorganchem.2024.123389.
38. Jacobs, F.J.F.; Helliwell, J.R.; Brink, A.; Baker, E.N. Time-Series Analysis of Rhenium(I) Organometallic Covalent Binding to a Model Protein for Drug Development. *IUCrJ* **2024**, *11*, 359–373. https://doi.org/10.1107/S2052252524002598.
39. Herrick, R.S.; Ziegler, C.J.; Leeper, T.C. Structure and Function in Organometallic protein Complexes. *J. Organomet. Chem.* **2014**, *751*, 90–110. https://doi.org/10.1016/j.jorganchem.2013.07.004.
40. Ortega-Carrasco, E.; Lledós, A.; Maréchal, J.-D. Assessing Protein–Ligand Docking for the Binding of Organometallic Compounds to Proteins. *J. Comput. Chem.* **2014**, *35*, 192–198. https://doi.org/10.1002/jcc.23472.
41. Zhang, L.; Song, J.; Zhou, J.-M.; Zhou, Y.-L.; Zhang, W. Structural Evolution and Antibacterial Activity of Nickel (II) Coordination Compounds Engineered with Pyrazine Derivatives. *Appl. Organomet. Chem.* **2026**, *40*, e70567. https://doi.org/10.1002/aoc.70567.
42. Graur, I.; Graur, V.; Melnic, E.; Lozan-Tirsu, C.; Balan, G.; Tsapkov, V.; Gulea, A. From Design to Bioactivity: 2-Benzoylpyridine 4-(Bicyclo [2.2.1]Hept-2-Yl)Thiosemicarbazone and Its 3d Metal Coordination Compounds. *ChemistryOpen* **2026**, *15*, e202500590. https://doi.org/10.1002/open.202500590.
43. Bezerra, A.C.; Baptista, L.E.; Couto, M.N.; Kanashiro, M.M. Preclinical Trials of Cancer Stem Cells Targeted by Metal-Based Coordination Complexes: A Systematic Review. *Pharmaceutics* **2025**, *17*, 931. https://doi.org/10.3390/pharmaceutics17070931.
44. Ornelas, C.; Astruc, D. Ferrocene-Based Drugs, Delivery Nanomaterials and Fenton Mechanism: State of the Art, Recent Developments and Prospects. *Pharmaceutics* **2023**, *15*, 2044. https://doi.org/10.3390/pharmaceutics15082044.

45. Silva, M.J.S.A.; Gois, P.M.P.; Gasser, G. Unveiling the Potential of Transition Metal Complexes for Medicine: Translational in Situ Activation of Metal-Based Drugs from Bench to in Vivo Applications. *ChemBioChem* **2021**, *22*, 1740–1742. https://doi.org/10.1002/cbic.202100015.
46. Pellei, M.; Del Bello, F.; Porchia, M.; Santini, C. Zinc Coordination Complexes as Anticancer Agents. *Coord. Chem. Rev.* **2021**, *445*, 214088. https://doi.org/10.1016/j.ccr.2021.214088.
47. Pobłocki, K.; Drzeżdżon, J.; Kostrzewa, T.; Jacewicz, D. Coordination Complexes as a New Generation Photosensitizer for Photodynamic Anticancer Therapy. *Int. J. Mol. Sci.* **2021**, *22*, 8052. https://doi.org/10.3390/ijms22158052.
48. Wang, Y.; Astruc, D.; Abd-El-Aziz, A.S. Metallopolymers for Advanced Sustainable Applications. *Chem. Soc. Rev.* **2019**, *48*, 558–636. https://doi.org/10.1039/C7CS00656J.
49. Lam, Y.-Y.; Lee, N.-S.; Lee, S.-F.; Chung, C.Y.-S. Organometallic D6, D8 and D10 Metal Complexes for Biosensing and Imaging, Cancer Therapy and Theranosis. *J. Organomet. Chem.* **2024**, *1005*, 122982. https://doi.org/10.1016/j.jorganchem.2023.122982.
50. Alberto, R. Role of Pure Technetium Chemistry: Are There Still Links to Applications in Imaging? *Inorg. Chem.* **2023**, *62*, 20539–20548. https://doi.org/10.1021/acs.inorgchem.3c01620.
51. Morais, G.R.; Paulo, A.; Santos, I. Organometallic Complexes for SPECT Imaging and/or Radionuclide Therapy. *Organometallics* **2012**, *31*, 5693–5714. https://doi.org/10.1021/om300501d.
52. Huang, Q.; Chen, Y.; Wang, S.; Liu, K.; Zhao, X.-Z.; Mao, X.; Tang, B.Z.; Rao, L. Intelligent Theranostic Systems Enabled by Aggregation-Induced Emission in Precision Medicine. *Aggregate* **2025**, *6*, e70156. https://doi.org/10.1002/agt2.70156.
53. Cai, Y.; Chai, T.; Nguyen, W.; Liu, J.; Xiao, E.; Ran, X.; Ran, Y.; Du, D.; Chen, W.; Chen, X. Phototherapy in Cancer Treatment: Strategies and Challenges. *Signal Transduct. Target. Ther.* **2025**, *10*, 115. https://doi.org/10.1038/s41392-025-02140-y.
54. Tao, J.; Yuan, Z.; Zhou, M. Targeted Photodynamic Therapy: Enhancing Efficacy through Specific Organelle Engagement. *Front. Pharmacol.* **2025**, *16*, 1667812.
55. O'Neill, J. *Tackling Drug-Resistant Infections Globally: Final Report and Recommendations*; Government of the United Kingdom: London, UK, 2016.
56. GBD 2021 Antimicrobial Resistance Collaborators. Global Burden of Bacterial Antimicrobial Resistance 1990–2021: A Systematic Analysis with Forecasts to 2050. *Lancet* **2024**, *404*, 1199–1226. https://doi.org/10.1016/S0140-6736(24)01867-1.
57. Tan, B.W.H.; Lee, P.F.P. Metal-Based Complexes, a Promising Solution to Antimicrobial Resistance. *Lett. Drug Des. Discov.* **2026**, *22*, 100257. https://doi.org/10.1016/j.lddd.2025.100257.
58. Sanz del Olmo, N.; Carloni, R.; Ortega, P.; García-Gallego, S.; de la Mata, F.J. Chapter One—Metallodendrimers as a Promising Tool in the Biomedical Field: An Overview. In *Advances in Organometallic Chemistry*; Pérez, P.J., Ed.; Academic Press: Cambridge, MA, USA, 2020; Volume 74, pp. 1–52.
59. Staneva, D.; Grabchev, I. Chapter 20—Dendrimer as Antimicrobial Agents. In *Dendrimer-Based Nanotherapeutics*; Kesharwani, P., Ed.; Academic Press: Cambridge, MA, USA, 2021; pp. 363–384. ISBN 978-0-12-821250-9.
60. Liang, J.; Sun, D.; Yang, Y.; Li, M.; Li, H.; Chen, L. Discovery of Metal-Based Complexes as Promising Antimicrobial Agents. *Eur. J. Med. Chem.* **2021**, *224*, 113696. https://doi.org/10.1016/j.ejmech.2021.113696.
61. Abd-El-Aziz, A.S.; Agatemor, C.; Etkin, N. Antimicrobial Resistance Challenged with Metal-Based Antimicrobial Macromolecules. *Biomaterials* **2017**, *118*, 27–50. https://doi.org/10.1016/j.biomaterials.2016.12.002.
62. Govender, P.; Therrien, B.; Smith, G.S. Bio-Metallodendrimers—Emerging Strategies in Metal-Based Drug Design. *Eur. J. Inorg. Chem.* **2012**, *2012*, 2853–2862. https://doi.org/10.1002/ejic.201200161.
63. Tang, Y.-H.; Huang, A.Y.-T.; Chen, P.-Y.; Chen, H.-T.; Kao, C.-L. Metallodendrimers and Dendrimer Nanocomposites. *Curr. Pharm. Des.* **2011**, *17*, 2308–2330. https://doi.org/10.2174/138161211797052367.
64. Astruc, D.; Boisselier, E.; Ornelas, C. Dendrimers Designed for Functions: From Physical, Photophysical, and Supramolecular Properties to Applications in Sensing, Catalysis, Molecular Electronics, Photonics, and Nanomedicine. *Chem. Rev.* **2010**, *110*, 1857–1959. https://doi.org/10.1021/cr900327d.
65. Abd-El-Aziz, A.S.; Agatemor, C.; Etkin, N.; Overy, D.P.; Kerr, R.G. Redox-Active Cationic Organoiron Complex: A Promising Lead Structure for Developing Antimicrobial Agents with Activity against Gram-Positive Pathogens Including Methicillin-Resistant Staphylococcus Aureus and Vancomycin-Resistant Enterococcus Faecium. *RSC Adv.* **2015**, *5*, 86421–86427. https://doi.org/10.1039/C5RA16613F.
66. Abd-El-Aziz, A.S.; Agatemor, C.; Etkin, N.; Bissessur, R.; Overy, D.; Lanteigne, M.; McQuillan, K.; Kerr, R.G. Quaternized and Thiazole-Functionalized Free Radical-Generating Organometallic Dendrimers as Antimicrobial Platform against Multidrug-Resistant Microorganisms. *Macromol. Biosci.* **2017**, *17*, 1700020. https://doi.org/10.1002/mabi.201700020.

67. Bizuayehu, H.M.; Ahmed, K.Y.; Kibret, G.D.; Dadi, A.F.; Belachew, S.A.; Bagade, T.; Tegegne, T.K.; Venchiarutti, R.L.; Kibret, K.T.; Hailegebireal, A.H.; Assefa, Y.; Khan, M.N.; Abajobir, A.; Alene, K.A.; Mengesha, Z.; Erku, D.; Enquobahrie, D.A.; Minas, T.Z.; Misgan, E.; Ross, A.G. Global Disparities of Cancer and Its Projected Burden in 2050. *JAMA Netw. Open* **2024**, *7*, e2443198–e2443198. https://doi.org/10.1001/jamanetworkopen.2024.43198.
68. Dilruba, S.; Kalayda, G.V. Platinum-Based Drugs: Past, Present and Future. *Cancer Chemother. Pharmacol.* **2016**, *77*, 1103–1124. https://doi.org/10.1007/s00280-016-2976-z.
69. Wheate, N.J.; Walker, S.; Craig, G.E.; Oun, R. The Status of Platinum Anticancer Drugs in the Clinic and in Clinical Trials. *Dalton Trans.* **2010**, *39*, 8113–8127. https://doi.org/10.1039/C0DT00292E.
70. Wiltshaw, E. Cisplatin in the Treatment of Cancer. *Platinum Metals Rev.* 1979, *23*, 90–98.
71. Li, S.; Zhang, C.; Xu, X.; Wang, X.; Ren, H.; Sun, B.; Zhang, Y. Metal-Based Biomaterials for Cancer Gene Therapy. *Coord. Chem. Rev.* **2025**, *538*, 216720. https://doi.org/10.1016/j.ccr.2025.216720.
72. Abd-El-Aziz, A.S.; Agatemor, C. Emerging Opportunities in the Biomedical Applications of Dendrimers. *J. Inorg. Organomet. Polym. Mater.* **2018**, *28*, 369–382. https://doi.org/10.1007/s10904-017-0768-5.
73. Lahoti, H.S.; Jogdand, S.D. Bioimaging: Evolution, Significance, and Deficit. *Cureus* **2022**, *14*, e28923. https://doi.org/10.7759/cureus.28923.
74. Ng, C.S.; Chandler, A.G.; Chen, Y.; Wei, W.; Tannir, N.M.; Hobbs, B.P. Effect of Scan Duration on CT Perfusion Values in Metastases from Renal Cell Carcinoma. *Res. Diagn. Interv. Imaging* **2023**, *6*, 100028. https://doi.org/10.1016/j.redii.2023.100028.
75. Schilling, K.G.; Palombo, M.; Witt, A.A.; O'Grady, K.P.; Pizzolato, M.; Landman, B.A.; Smith, S.A. Characterization of Neurite and Soma Organization in the Brain and Spinal Cord with Diffusion MRI. *Imaging Neurosci.* **2025**, *3*, IMAG.a.111. https://doi.org/10.1162/IMAG.a.111.
76. Crișan, G.; Moldovean-Cioroianu, N.S.; Timaru, D.-G.; Andrieș, G.; Căinap, C.; Chiș, V. Radiopharmaceuticals for PET and SPECT Imaging: A Literature Review over the Last Decade. *Int. J. Mol. Sci.* **2022**, *23*, 5023. https://doi.org/10.3390/ijms23095023.
77. Gupta, A.; Adarsh, T.; Manchanda, V.; Sasmal, P.K.; Gupta, S. COVID-19 Detection Using AIE-Active Iridium Complexes. *Dalton Trans.* **2023**, *52*, 1188–1192. https://doi.org/10.1039/D2DT03554E.
78. Zou, Z.; Liu, D.; Wan, J.; Zhang, K.; Liu, M.; Huang, S.; Tian, J.; Zhang, X.; Wei, Y. Molecular Design of NIR Type I Phenothiazine-Based Photosensitizers with Aggregation-Enhanced ROS Generation for Effective Photodynamic Therapy Applications. *Chem. Commun.* **2025**, *61*, 13189–13192. https://doi.org/10.1039/D5CC03925H.
79. Buiel, J.; Robert, J.; Mekhjian, D.; Chauhan, D.S.; Banquy, X. Photothermal Therapy: From Encouraging Lab Results to Lackluster Clinical Translation. *Adv. Ther.* **2025**, *8*, 2400347. https://doi.org/10.1002/adtp.202400347.
80. Pitchumony, T.S.; Banevicius, L.; Janzen, N.; Zubieta, J.; Valliant, J.F. Isostructural Nuclear and Luminescent Probes Derived from Stabilized [2 + 1] Rhenium(I)/Technetium(I) Organometallic Complexes. *Inorg. Chem.* **2013**, *52*, 13521–13528. https://doi.org/10.1021/ic401972g.
81. Hungnes, I.N.; Al-Salemee, F.; Gawne, P.J.; Eykyn, T.; Atkinson, R.A.; Terry, S.Y.A.; Clarke, F.; Blower, P.J.; Pringle, P.G.; Ma, M.T. One-Step, Kit-Based Radiopharmaceuticals for Molecular SPECT Imaging: A Versatile Diphosphine Chelator for 99mTc Radiolabelling of Peptides. *Dalton Trans.* **2021**, *50*, 16156–16165. https://doi.org/10.1039/D1DT03177E.
82. Wu, C.-H.; Kisel, K.S.; Thangavel, M.K.; Chen, Y.-T.; Chang, K.-H.; Tsai, M.-R.; Chu, C.-Y.; Shen, Y.-F.; Wu, P.-C.; Zhang, Z.; Liu, T.-M. Functionalizing Collagen with Vessel-Penetrating Two-Photon Phosphorescence Probes: A New In Vivo Strategy to Map Oxygen Concentration in Tumor Microenvironment and Tissue Ischemia. *Adv. Sci.* **2021**, *8*, 2102788. https://doi.org/10.1002/advs.202102788.
83. Fredericks, S.M.; Luong, J.C.; Wrighton, M.S. Multiple Emissions from Rhenium(I) Complexes: Intraligand and Charge-Transfer Emission from Substituted Metal Carbonyl Cations. *J. Am. Chem. Soc.* **1979**, *101*, 7415–7417. https://doi.org/10.1021/ja00518a054.
84. Figueroa-Figueroa, D.I.; Hernández-Luis, F. Advances in Ferrocene Photosensitizers: Illuminating New Avenues in the Medicinal Chemistry of Cancer. *Med. Chem. Res.* **2025**, *34*, 1480–1495. https://doi.org/10.1007/s00044-025-03432-2.
85. Klarek, M.; Gautam, A.; Kowalski, K. Ferrocenyl Ferroptosis Inducers as an Emerging Class of Anticancer Agents: A Mini Review. *RSC Med. Chem.* **2026**, *17*, 1252–1270. https://doi.org/10.1039/D5MD00935A.
86. Yuan, H.; Pei, M.; Lv, B.; Mei, D.; Zhou, Y.; Wang, L.; Pu, X.; Zhao, T. 2-Nitroethenyl Ferrocene as a Photosensitizer: Evaluation of Its Photodynamic Antitumor Properties. *J. Organomet. Chem.* **2026**, *1044*, 123952. https://doi.org/10.1016/j.jorganchem.2025.123952.
87. Balaji, B.; Balakrishnan, B.; Perumalla, S.; Karande, A.A.; Chakravarty, A.R. Mitochondria-Targeting Photocytotoxic Ferrocenyl Conjugates of N-Alkylpyridinium Salts. *Eur. J. Inorg. Chem.* **2015**, *2015*, 1398–1407. https://doi.org/10.1002/ejic.201403118.

88. Lin, J.; Yang, H.; Zou, Z.; Deng, L.; Cai, X.; Chen, M.; Xu, J.; Yin, W.; Wen, B.; Xie, W.; Xu, Q.; Zhong, G.; Wu, Z.; Chen, Y.; Zhang, R.; Tian, W.; Zhang, Y.; Long, Y.; Li, Y.; Han, Z.; Liang, Y.; Ye, J.; Lu, J.; Liang, Y.; Dai, Q.; Zou, F.; He, H.; Zhong, W.; Zhuo, Y. Chemo-Photothermal Synergy Ignites Antitumor Immunity via Ferroptosis. *Signal Transduct. Target. Ther.* **2026**, *11*, 98. https://doi.org/10.1038/s41392-026-02608-5.
89. Bhattacharya, S.; Adon, T.; Dsouza, K.; Kumar, H.Y. Exploring the Future of Metal-Based Anticancer Agents: A Comprehensive Review of Ruthenium-Based Complexes. *ChemistrySelect* **2025**, *10*, e202404147. https://doi.org/10.1002/slct.202404147.
90. Pitto-Barry, A. Polymeric Nanoparticles Containing Ruthenium Complexes for Biomedical Applications: A Mini-Review on Recent Developments. *ACS Appl. Polym. Mater.* **2024**, *6*, 14133–14147. https://doi.org/10.1021/acsapm.4c00494.
91. Conti, L.; Macedi, E.; Giorgi, C.; Valtancoli, B.; Fusi, V. Combination of Light and Ru(II) Polypyridyl Complexes: Recent Advances in the Development of New Anticancer Drugs. *Coord. Chem. Rev.* **2022**, *469*, 214656. https://doi.org/10.1016/j.ccr.2022.214656.
92. Pragti; Kundu, B.K.; Mukhopadhyay, S. Target Based Chemotherapeutic Advancement of Ruthenium Complexes. *Coord. Chem. Rev.* **2021**, *448*, 214169. https://doi.org/10.1016/j.ccr.2021.214169.
93. Brabec, V.; Kasparkova, J. Ruthenium Coordination Compounds of Biological and Biomedical Significance. DNA Binding Agents. *Coord. Chem. Rev.* **2018**, *376*, 75–94. https://doi.org/10.1016/j.ccr.2018.07.012.
94. Elsayed, S.A.; Harrypersad, S.; Sahyon, H.A.; El-Magd, M.A.; Walsby, C.J. Ruthenium(II)/(III) DMSO-Based Complexes of 2-Aminophenyl Benzimidazole with In vitro and In Vivo Anticancer Activity. *Molecules* **2020**, *25*, 4284. https://doi.org/10.3390/molecules25184284.
95. Oszajca, M.; Flejszar, M.; Szura, A.; Dróżdż, P.; Brindell, M.; Kurpiewska, K. Exploring the Coordination Chemistry of Ruthenium Complexes with Lysozymes: Structural and in-Solution Studies. *Front. Chem.* **2024**, *12*, 1371637.
96. Banneville, A.-S.; Ferraro, G.; D'Elia, R.; Cornaciu-Hoffmann, I.; Pica, A.; Merlino, A. Ru and Rh Binding Sites in the Structure of Human Serum Transferrin with Fe^{3+} Bound at the C-Lobe. *Dalton Trans.* **2026**, *55*, 4051–4056. https://doi.org/10.1039/D6DT00205F.
97. Wang, M.; Wang, H.; Xu, X.; Lai, T.-P.; Zhou, Y.; Hao, Q.; Li, H.; Sun, H. Binding of Ruthenium and Osmium at Non-iron Sites of Transferrin Accounts for Their Iron-Independent Cellular Uptake. *J. Inorg. Biochem.* **2022**, *234*, 111885. https://doi.org/10.1016/j.jinorgbio.2022.111885.
98. Srivastava, P.; Verma, M.; Kumar, A.; Srivastava, P.; Mishra, R.; Sivakumar, S.; Patra, A.K. Luminescent Naphthalimide-Tagged Ruthenium(Ii)–Arene Complexes: Cellular Imaging, Photocytotoxicity and Transferrin Binding. *Dalton Trans.* **2021**, *50*, 3629–3640. https://doi.org/10.1039/D0DT02967J.
99. Bisceglie, F.; Pelosi, G.; Orsoni, N.; Pioli, M.; Carcelli, M.; Pelagatti, P.; Pinelli, S.; Sadler, P.J. Light Triggers the Antiproliferative Activity of Naphthalimide-Conjugated (H6-Arene)Ruthenium(II) Complexes. *Int. J. Mol. Sci.* **2022**, *23*, 7624. https://doi.org/10.3390/ijms23147624.
100. Xu, G.; Li, C.; Chi, C.; Wu, L.; Sun, Y.; Zhao, J.; Xia, X.-H.; Gou, S. A Supramolecular Photosensitizer Derived from an Arene-Ru(II) Complex Self-Assembly for NIR Activated Photodynamic and Photothermal Therapy. *Nat. Commun.* **2022**, *13*, 3064. https://doi.org/10.1038/s41467-022-30721-w.
101. Michlewska, S.; Kubczak, M.; Maroto-Díaz, M.; Sanz del Olmo, N.; Ortega, P.; Shcharbin, D.; Gomez Ramirez, R.; Javier de la Mata, F.; Ionov, M.; Bryszewska, M. Synthesis and Characterization of FITC Labelled Ruthenium Dendrimer as a Prospective Anticancer Drug. *Biomolecules* **2019**, *9*, 411. https://doi.org/10.3390/biom9090411.
102. Jing, S.; Wu, X.; Niu, D.; Wang, J.; Leung, C.-H.; Wang, W. Recent Advances in Organometallic NIR Iridium(III) Complexes for Detection and Therapy. *Molecules* **2024**, *29*, 256. https://doi.org/10.3390/molecules29010256.
103. Alkhaibari, I.S.; Horton, P.N.; Coles, S.J.; Buurma, N.J.; Pope, S.J.A. DNA-Binding Properties of Non-Intercalating Water-Soluble Organometallic Ir(III) Luminophores. *Chem. Eur. J.* **2025**, *31*, e202500290. https://doi.org/10.1002/chem.202500290.
104. Das, B.; Gupta, S.; Mondal, A.; Kalita, K.J.; Mallick, A.I.; Gupta, P. Tuning the Organelle-Specific Imaging and Photodynamic Therapeutic Efficacy of Theranostic Mono- and Trinuclear Organometallic Iridium(III) Complexes. *J. Med. Chem.* **2023**, *66*, 15550–15563. https://doi.org/10.1021/acs.jmedchem.3c01875.
105. Zhou, L.; Wei, F.; Xiang, J.; Li, H.; Li, C.; Zhang, P.; Liu, C.; Gong, P.; Cai, L.; Wong, K.M.-C. Enhancing the ROS Generation Ability of a Rhodamine-Decorated Iridium(Iii) Complex by Ligand Regulation for Endoplasmic Reticulum-Targeted Photodynamic Therapy. *Chem. Sci.* **2020**, *11*, 12212–12220. https://doi.org/10.1039/D0SC04751A.
106. Liu, J.; Zhang, J.; Zheng, Q.; Li, M.-J. AIEgen-Type Near-Infrared Phosphorescent Ir(III) Complex Enables Mitochondrial GSH Depletion-Amplified Photodynamic Therapy. *Inorg. Chem.* **2026**, *65*, 8376–8388. https://doi.org/10.1021/acs.inorgchem.5c05682.
107. Gupta, A.; Gautam, A.; Gandhi, H.A.; Chauhan, D.; Rabbani, M.M.; Bhattacharya, J.; Sasmal, P.K. Design of Cyclometalated Iridium(III) Complexes with Tailored Ancillary Ligands for Mitochondria-Targeted Dual Chemo-Phototherapy. *Inorg. Chem.* **2026**, *65*, 834–846. https://doi.org/10.1021/acs.inorgchem.5c05154.

108. Jones, C.; Martinez-Alonso, M.; Gagg, H.; Kirby, L.; Weinstein, J.A.; Bryant, H.E. Photostable Iridium(III) Cyclometallated Complex Is an Efficient Photosensitizer for Killing Multiple Cancer Cell Lines and 3D Models under Low Doses of Visible Light. *J. Med. Chem.* **2024**, *67*, 16157–16164. https://doi.org/10.1021/acs.jmedchem.4c00869.
109. Linero-Artiaga, A.; Svitelova, M.; Novohradský, V.; Rodríguez, V.; Markova, L.; Kasparkova, J.; Janiak, C.; Ruiz, J.; Brabec, V. Novel 2-(2′-Benzothiazolyl)-Benzimidazole-Based Iridium(III) Photocatalysts Exhibit Antiproliferative Effects in 2D and 3D Cancer Cells to Bypass Hypoxia-Induced Resistance. *J. Med. Chem.* **2026**, *69*, 6991–7011. https://doi.org/10.1021/acs.jmedchem.5c03280.
110. Shee, M.; Deepak, K.; Chatterjee, S.; Mandal, M.; Singh, N.D.P. Targeted Chemo-Photodynamic Therapy in Pancreatic Cancer: Influence of Ir(Iii)-Complex and Ion Chelating N^N-Ancillary Ligand on Cell Death Mechanism. *J. Mater. Chem. B* **2025**, *13*, 15544–15555. https://doi.org/10.1039/D5TB01855B.
111. Zhao, J.; Zhang, X.; Fang, L.; Gao, C.; Xu, C.; Gou, S. Iridium(III) Complex–Derived Polymeric Micelles with Low Dark Toxicity and Strong NIR Excitation for Phototherapy and Chemotherapy. *Small* **2020**, *16*, 2000363. https://doi.org/10.1002/smll.202000363.
112. Ke, L.; Wei, F.; Xie, L.; Karges, J.; Chen, Y.; Ji, L.; Chao, H. A Biodegradable Iridium(III) Coordination Polymer for Enhanced Two-Photon Photodynamic Therapy Using an Apoptosis–Ferroptosis Hybrid Pathway. *Angew. Chem., Int. Ed.* **2022**, *61*, e202205429. https://doi.org/10.1002/anie.202205429.
113. Romano-deGea, J.; Chen, Z.; Abhyankar, K.A.; Scopelliti, R.; Fadaei-Tirani, F.; Cariou, K.; Gasser, G.; Dyson, P.J. Azide as a Photolabile Ligand in Gold(I) Therapeutics. *J. Organomet. Chem.* **2025**, *1037*, 123724. https://doi.org/10.1016/j.jorganchem.2025.123724.
114. Massoud, J.; Pinon, A.; Gallardo-Villagrán, M.; Paulus, L.; Ouk, C.; Carrion, C.; Antoun, S.; Diab-Assaf, M.; Therrien, B.; Liagre, B. A Combination of Ruthenium Complexes and Photosensitizers to Treat Colorectal Cancer. *Inorganics* **2023**, *11*, 451. https://doi.org/10.3390/inorganics11120451.
115. Shi, H.; Carter, O.W.L.; Ponte, F.; Imberti, C.; Gomez-Gonzalez, M.A.; Cacho-Nerin, F.; Quinn, P.D.; Parker, J.E.; Sicilia, E.; Huang, H.; Sadler, P.J. A Photodynamic and Photochemotherapeutic Platinum-Iridium Charge-Transfer Conjugate for Anticancer Therapy. *Angew. Chem., Int. Ed.* **2024**, *63*, e202400476. https://doi.org/10.1002/anie.202400476.
116. Bray, F.; Laversanne, M.; Sung, H.; Ferlay, J.; Siegel, R.L.; Soerjomataram, I.; Jemal, A. Global Cancer Statistics 2022: GLOBOCAN Estimates of Incidence and Mortality Worldwide for 36 Cancers in 185 Countries. *Ca-Cancer J. Clin.* **2024**, *74*, 229–263. https://doi.org/10.3322/caac.21834.
117. Fink, H.; Langselius, O.; Vignat, J.; Rumgay, H.; Rehm, J.; Martinez, R.X.; Santero, M.; Lopez-Perez, L.; Inoue, M.; Zeng, H.; Shield, K.; Morgan, E.; Ilbawi, A.; Soerjomataram, I. Global and Regional Cancer Burden Attributable to Modifiable Risk Factors to Inform Prevention. *Nat. Med.* **2026**, *32*, 1306–1315. https://doi.org/10.1038/s41591-026-04219-7.
118. WHO. Noncommunicable Diseases and Mental Health Team. In *Global Status Report on Cancer 2026: The Future We Choose Together*; World Health Organization: Geneva, Switzerland, 2026; p. 280.
119. Arun, P.P.; Patel, R.R.; Singh, S.K.; Parmar, K.; Singh, M. Exploring Metal Complexes for Cancer Treatment: Mechanistic Insights and Therapeutic Potential. *J. Organomet. Chem.* **2025**, *1035*, 123682. https://doi.org/10.1016/j.jorganchem.2025.123682.
120. Hartinger, C.G. A Multifaceted Approach towards Organometallic Anticancer Agent Development. *J. Organomet. Chem.* **2024**, *1012*, 123144. https://doi.org/10.1016/j.jorganchem.2024.123144.
121. Köpf, H.; Köpf-Maier, P. Titanocen-Dichlorid—Das Erste Metallocen Mit Cancerostatischer Wirksamkeit. *Angew. Chem.* **1979**, *91*, 509. https://doi.org/10.1002/ange.19790910620.
122. Yashchenko, G.N.; Shashmurina, A.A.; Anoshina, G.M.; Gorelova, L.A.; Evstigneeva, N.G.; Alekseeva, L.V.; Radina, L.B. Synthesis and Study of Anti-Tumor Activity of Ferrocene-Containing Alkylating Compounds. *Khim. Farm.* **1978**, *12*, 68–72.
123. Wenzel, M.; S chneider, M.; Liss, E. Synthese, Organ-Verteilung Und Cytostatische Wirkung Der N-Methyl-N-β-Chloräthyl-Hydrazone von Metallocen-Aldehyden / Synthesis, Biochemistry and Cytostatic Effects of N-Methyl-N-β-Chlorethyl-Hydrazones of Metallocene Aldehydes. **1979**, *34*, 670–676. https://doi.org/10.1515/znc-1979-9-1003.
124. Köpf-Maier, P.; Köpf, H.; Neuse, E.W. Ferricenium Complexes: A New Type of Water-Soluble Antitumor Agent. *J. Cancer Res. Clin. Oncol.* **1984**, *108*, 336–340. https://doi.org/10.1007/BF00390468.
125. Guk, D.A.; Gibadullina, K.R.; Moiseeva, A.A.; Grishin, Y.K.; Roznyatovsky, V.A.; Prosuntsova, D.S.; Ananieva, I.A.; Gandalipov, E.R.; Shtil, A.A.; Beloglazkina, E.K. Conjugates of Titanocene with Non-Steroidal Anti-Inflammatory Drugs: Synthesis, Unusual NMR Characteristics, Stability and Cytotoxicity. *New J. Chem.* **2024**, *48*, 1650–1660. https://doi.org/10.1039/D3NJ04845D.
126. Landini, I.; Massai, L.; Cirri, D.; Gamberi, T.; Paoli, P.; Messori, L.; Mini, E.; Nobili, S. Structure-Activity Relationships in a Series of Auranofin Analogues Showing Remarkable Antiproliferative Properties. *J. Inorg. Biochem.* **2020**, *208*, 111079. https://doi.org/10.1016/j.jinorgbio.2020.111079.

127. Ellahioui, Y.; Prashar, S.; Gómez-Ruiz, S. Anticancer Applications and Recent Investigations of Metallodrugs Based on Gallium, Tin and Titanium. *Inorganics* **2017**, *5*, 4. https://doi.org/10.3390/inorganics5010004.
128. Guk, D.A.; Gibadullina, K.R.; Burlutskiy, R.O.; Pavlov, K.G.; Moiseeva, A.A.; Tafeenko, V.A.; Lyssenko, K.A.; Gandalipov, E.R.; Shtil, A.A.; Beloglazkina, E.K. New Titanocene (IV) Dicarboxylates with Potential Cytotoxicity: Synthesis, Structure, Stability and Electrochemistry. *Int. J. Mol. Sci.* **2023**, *24*, 3340. https://doi.org/10.3390/ijms24043340.
129. de la Cueva-Alique, I.; Muñoz-Moreno, L.; Benabdelouahab, Y.; Elie, B.T.; El Amrani, M.A.; Mosquera, M.E.G.; Contel, M.; Bajo, A.M.; Cuenca, T.; Royo, E. Novel Enantiopure Cyclopentadienyl Ti(IV) Oximato Compounds as Potential Anticancer Agents. *J. Inorg. Biochem.* **2016**, *156*, 22–34. https://doi.org/10.1016/j.jinorgbio.2015.12.002.
130. Carraher, C.E.; Truong, N.T.C.; Roner, M.R.; Moric, A.; Trang, N.T. Synthesis of Organoarsenic, Organoantimony, and Organobismuth Poly(Ether Esters) from Reaction with Glycyrrhetinic Acid and Their Preliminary Activity against Pancreatic Cancer Cell Lines. *J. Chin. Adv. Mater. Soc.* **2013**, *1*, 134–150. https://doi.org/10.1080/22243682.2013.812281.
131. Carraher, C.E.; Roner, M.R.; Slawek, P.; Mosca, F. Group 4 Metallocene Polymers—Selected Properties and Applications. *Inorganics* **2018**, *6*, 65. https://doi.org/10.3390/inorganics6030065.
132. Hu, W.; Hoyer, J.; Neundorf, I.; Govender, P.; Smith, G.S.; Schatzschneider, U. Synthesis of CpM(CO)3–DAB and –PAMAM Dendrimer Conjugates and Preliminary Evaluation of Their Biological Activity. *Euro. J. Inorg. Chem.* **2015**, *2015*, 1505–1510. https://doi.org/10.1002/ejic.201403060.
133. Šuta, E.; Zahirović, A.; Tešević, V.; Grgurić-Šipka, S.; Arañđelović, S.; Ljubijankić, S.; Ljujić, J.; Balaban, M.; Hrnjić, A.; Višnjevac, A.; Ljubijankić, N. Rare Examples of Rhenium(I) Tricarbonyl Iodido Complexes with Unsymmetrical Bipyridines Featuring Distinguishable Rotamers: From Synthesis and Solid-State/Solution-Phase Isomerism to Biological Activity. *J. Inorg. Biochem.* **2026**, *276*, 113167. https://doi.org/10.1016/j.jinorgbio.2025.113167.
134. Piškor, M.; Ćorić, I.; Perić, B.; Špoljarić, K.M.; Kirin, S.I.; Glavaš-Obrovac, L.; Raić-Malić, S. Quinoline- and Coumarin-Based Ligands and Their Rhenium(I) Tricarbonyl Complexes: Synthesis, Spectral Characterization and Antiproliferative Activity on T-Cell Lymphoma. *J. Inorg. Biochem.* **2025**, *262*, 112770. https://doi.org/10.1016/j.jinorgbio.2024.112770.
135. Towett, E.K.; Tembu, V.J.; Kemboi, D.; Langat, M.K.; Manicum, A.-L.E. Review of Recent Medicinal Applications of Rhenium(I) Tricarbonyl Complexes. *Int. J. Mol. Sci.* **2025**, *26*, 7005. https://doi.org/10.3390/ijms26147005.
136. Das, A.; Guha, S.; Halder, A.; Gharami, S.; Naskar, R.; Das, G.; Mondal, T.K. Synthesis, Characterization, DNA/Protein-Binding Study and Anticancer Activity of Novel Tricarbonyl Re(i) Complexes with an ONS Donor Azo-Thioether Pincer Ligand. *New J. Chem.* **2025**, *49*, 559–571. https://doi.org/10.1039/D4NJ03255A.
137. Abo-Elfadl, M.T.; Mansour, A.M. Cytotoxic Properties of Fac-Re(CO)3 Complexes with Quinoline Coligands: Insights on the Mode of Cell Death and DNA Fragmentation. *Inorganica Chim. Acta* **2023**, *553*, 121521. https://doi.org/10.1016/j.ica.2023.121521.
138. Lu, J.-J.; Ma, X.-R.; Xie, K.; Yang, P.-X.; Li, R.-T.; Ye, R.-R. Novel Heterobimetallic Ir(Iii)–Re(i) Complexes: Design, Synthesis and Antitumor Mechanism Investigation. *Dalton Trans.* **2022**, *51*, 7907–7917. https://doi.org/10.1039/D2DT00719C.
139. Konkankit, C.C.; King, A.P.; Knopf, K.M.; Southard, T.L.; Wilson, J.J. In Vivo Anticancer Activity of a Rhenium(I) Tricarbonyl Complex. *ACS Med. Chem. Lett.* **2019**, *10*, 822–827. https://doi.org/10.1021/acsmedchemlett.9b00128.
140. Marker, S.C.; King, A.P.; Granja, S.; Vaughn, B.; Woods, J.J.; Boros, E.; Wilson, J.J. Exploring the In Vivo and In vitro Anticancer Activity of Rhenium Isonitrile Complexes. *Inorg. Chem.* **2020**, *59*, 10285–10303. https://doi.org/10.1021/acs.inorgchem.0c01442.
141. Padariya, A.D.; Savaliya, N.K.; Parekh, H.M.; Bhatt, B.S.; Bhatt, V.D.; Patel, M.N. Biological and Computational Studies of Organometallic Compounds of Rhenium(I) with Substituted Phenyl(2-(Thiazol-4-Yl)-1H-Benzo[d]Imidazol-1-Yl)Methanone. *J. Organomet. Chem.* **2025**, *1036*, 123708. https://doi.org/10.1016/j.jorganchem.2025.123708.
142. Sharma, A.; Rana, R.; Kumar, N.; Jyoti; Khanna, A.; Gulati, H.K.; Pooja; Kaur, S.; Singh, J.V.; Bedi, P.M.S. Remarkable Contribution of Ferrocene as Anticancer Agent: An Updated Review (2020–2024). *Inorg. Chem. Commun.* **2025**, *175*, 114155. https://doi.org/10.1016/j.inoche.2025.114155.
143. Gupta, A.; Das, R.; Chamoli, A.; Choithramani, A.; Kumar, H.; Patel, S.; Khude, D.; Bothra, G.; Wangdale, K.; Ghosh Chowdhury, M.; Rathod, R.; Mandoli, A.; Shard, A. A Series of Ferrocene-Containing Pyrazolo [1,5-a]Pyrimidines Induce a Strong Antiproliferative Effect against Oral Cancer Cells. *Organometallics* **2022**, *41*, 2365–2378. https://doi.org/10.1021/acs.organomet.2c00348.
144. Saviozzi, C.; Biancalana, L.; Funaioli, T.; Bortoluzzi, M.; De Franco, M.; Guelfi, M.; Gandin, V.; Marchetti, F. Triiron Complex with N-Ferrocenyl Aminocarbyne Ligand Bridging a Diiron Core: DFT, Electrochemical, and Biological Insights. *Inorg. Chem.* **2024**, *63*, 1054–1067. https://doi.org/10.1021/acs.inorgchem.3c03408.
145. Woo, J.; Na, Y.; Choi, W.I.; Kim, S.; Kim, J.; Hong, J.; Sung, D. Functional Ferrocene Polymer Multilayer Coatings for Implantable Medical Devices: Biocompatible, Antifouling, and ROS-Sensitive Controlled Release of Therapeutic Drugs. *Acta Biomater.* **2021**, *125*, 242–252. https://doi.org/10.1016/j.actbio.2021.02.038.
146. Qiu, G.; Liu, X.; Wang, B.; Gu, H.; Wang, W. Ferrocene-Containing Amphiphilic Polynorbornenes as Biocompatible Drug Carriers. *Polym. Chem.* **2019**, *10*, 2527–2539. https://doi.org/10.1039/C9PY00332K.

147. Bertuzzi, D.L.; Braga, C.B.; Perli, G.; Ornelas, C. Water-Soluble Well-Defined Bifunctional Ferrocenyl Dendrimer with Anti-Cancer Activity. *Eur. J. Inorg. Chem.* **2022**, *2022*, e202101084. https://doi.org/10.1002/ejic.202101084.
148. Abd-El-Aziz, A.S.; Abdelghani, A.A.; Pearson, J.K.; Awad, M.K.; Overy, D.P.; Kerr, R.G. Design of Piperazine Organoiron Macromolecules with Antibacterial and Anticancer Activity. *Macromol. Chem. Phys.* **2016**, *217*, 987–996. https://doi.org/10.1002/macp.201500489.
149. Abd-El-Aziz, A.S.; Abdelghani, A.A.; El-Sadany, S.K.; Overy, D.P.; Kerr, R.G. Antimicrobial and Anticancer Activities of Organoiron Melamine Dendrimers Capped with Piperazine Moieties. *Eur. Polym. J.* **2016**, *82*, 307–323. https://doi.org/10.1016/j.eurpolymj.2016.04.002.
150. Singh, N.S.S.; Saleh, L.H.; PadmaPriya, G.; Ray, S.; Pal, A.; Arora, V.; Iliev, K.; Atamuratova, Z.; Yulchiev, D.; Smerat, A.; Qasim, S.M. Ruthenium-Based Anticancer Agents: Focus on Mononuclear Ru(II)–Arene Organometallic Scaffolds and Ru(III) Non-Arene Coordination Compounds as Clinical Leads. *J. Organomet. Chem.* **2026**, *1045*, 123981. https://doi.org/10.1016/j.jorganchem.2025.123981.
151. Vadakkedathu Palakkeezhillam, V.N.; Haribabu, J.; Karthik, K.S.; Suresh Kumar, V.; Manakkadan, V.; Rasin, P.; Garg, M.; Arulraj, A.; Moraga, D.; Sreekanth, A. Functionalized Nitro-Piperonal Thiosemicarbazone Based Ruthenium(Ii)–Arene Complexes for DNA Interaction, Anticancer and Flow Cytometry Studies. *New J. Chem.* **2025**, *49*, 11531–11547. https://doi.org/10.1039/D5NJ00749F.
152. Ceramella, J.; Troiano, R.; Iacopetta, D.; Mariconda, A.; Pellegrino, M.; Catalano, A.; Saturnino, C.; Aquaro, S.; Sinicropi, M.S.; Longo, P. Synthesis of Novel N-Heterocyclic Carbene-Ruthenium (II) Complexes, "Precious" Tools with Antibacterial, Anticancer and Antioxidant Properties. *Antibiotics* **2023**, *12*, 693. https://doi.org/10.3390/antibiotics12040693.
153. Golbaghi, G.; Castonguay, A. Rationally Designed Ruthenium Complexes for Breast Cancer Therapy. *Molecules* **2020**, *25*, 265. https://doi.org/10.3390/molecules25020265.
154. Domínguez-Jurado, E.; Lara-Sánchez, A.; Bravo, I.; Ocaña, A.; Alonso-Moreno, C. State of the Art in Organometallic Ruthenium Metallodrugs for Breast Cancer Treatment: Advances and Innovations. *Coord. Chem. Rev.* **2025**, *523*, 216252. https://doi.org/10.1016/j.ccr.2024.216252.
155. Kavukcu, S.B.; Vatansever, H.S.; Ilhan, S.; Türkmen, H. Naphthyl-Substituted Ruthenium(II)–Arene Complexes: Exploring the Impact of Binding Modes on Cytotoxicity in Cancer and Normal Cell Lines. *Bioinorg. Chem. Appl.* **2025**, *2025*, 5556956. https://doi.org/10.1155/bca/5556956.
156. Welsh, A.; Serala, K.; Prince, S.; Smith, G.S. Selective Targeting of Regulated Rhabdomyosarcoma Cells by Trinuclear Ruthenium(II)–Arene Complexes. *J. Med. Chem.* **2024**, *67*, 6673–6686. https://doi.org/10.1021/acs.jmedchem.4c00256.
157. Arunachalam, A.; Rengan, R.; Umapathy, D.; Arockiam, A.J.V. Impact of Biphenyl Benzhydrazone-Incorporated Arene Ru(II) Complexes on Cytotoxicity and the Cancer Cell Death Mechanism. *Organometallics* **2022**, *41*, 2474–2486. https://doi.org/10.1021/acs.organomet.2c00290.
158. Štarha, P. Anticancer Iridium(Iii) Cyclopentadienyl Complexes. *Inorg. Chem. Front.* **2025**, *12*, 897–954. https://doi.org/10.1039/D4QI02472A.
159. Kostova, I. Homo- and Hetero-Multinuclear Iridium(III) Complexes with Cytotoxic Activity. *Inorganics* **2025**, *13*, 156. https://doi.org/10.3390/inorganics13050156.
160. Lu, J.-J.; Feng, X.-S.; Liu, Y.; Cao, W.-D.; Mao, Z.-W.; Cao, Q. A Mitochondria-Targeted Iridium Complex Activates Anti-Tumour Immunity by Regulating Zinc Homeostasis in Cancer Cells and Macrophages. *Dalton Trans.* **2025**, *54*, 13642–13650. https://doi.org/10.1039/D5DT01045D.
161. Dixit, T.; Negi, M.; Viruthakasi, V. Mitochondria Localized Anticancer Iridium(III) Prodrugs for Targeted Delivery of Myeloid Cell Leukemia-1 (Mcl-1) Inhibitors and Cytotoxic Iridium(III) Complex. *Inorg. Chem.* **2024**, *63*, 24709–24723. https://doi.org/10.1021/acs.inorgchem.4c03950.
162. Sun, Q.; Wang, Y.; Fu, Q.; Ouyang, A.; Liu, S.; Wang, Z.; Su, Z.; Song, J.; Zhang, Q.; Zhang, P.; Lu, D. Sulfur-Coordinated Organoiridium(III) Complexes Exert Breast Anticancer Activity via Inhibition of Wnt/β-Catenin Signaling. *Angew. Chem. Int. Ed.* **2021**, *60*, 4841–4848. https://doi.org/10.1002/anie.202015009.
163. Xu, Z.; Yang, Y.; Jia, X.; Guo, L.; Ge, X.; Zhong, G.; Chen, S.; Liu, Z. Novel Cyclometalated Iridium(Iii) Phosphine-Imine (P^N) Complexes: Highly Efficient Anticancer and Anti-Lung Metastasis Agents in Vivo. *Inorg. Chem. Front.* **2020**, *7*, 1273–1283. https://doi.org/10.1039/C9QI01492F.
164. Kozieł, S.; Komarnicka, U.K.; Ziółkowska, A.; Skórska-Stania, A.; Pucelik, B.; Płotek, M.; Sebastian, V.; Bieńko, A.; Stochel, G.; Kyzioł, A. Anticancer Potency of Novel Organometallic Ir(Iii) Complexes with Phosphine Derivatives of Fluoroquinolones Encapsulated in Polymeric Micelles. *Inorg. Chem. Front.* **2020**, *7*, 3386–3401. https://doi.org/10.1039/D0QI00538J.
165. Cao, J.-J.; Zheng, Y.; Wu, X.-W.; Tan, C.-P.; Chen, M.-H.; Wu, N.; Ji, L.-N.; Mao, Z.-W. Anticancer Cyclometalated Iridium(III) Complexes with Planar Ligands: Mitochondrial DNA Damage and Metabolism Disturbance. *J. Med. Chem.* **2019**, *62*, 3311–3322. https://doi.org/10.1021/acs.jmedchem.8b01704.

166. Ouyang, M.; Zeng, L.; Huang, H.; Jin, C.; Liu, J.; Chen, Y.; Ji, L.; Chao, H. Fluorinated Cyclometalated Iridium(Iii) Complexes as Mitochondria-Targeted Theranostic Anticancer Agents. *Dalton Trans.* **2017**, *46*, 6734–6744. https://doi.org/10.1039/C7DT01043E.
167. Mondal, A.; Das, B.; Karmakar, S.; Pani, S.; Khan, S.; Gupta, P.; Das Sarma, J. Modulatory Role of Pantropic Cell Signaling Pathways in the Antimigratory and Antiproliferative Action of Triazole Chelated Iridium(III) Complexes in Cervical Cancer Cells. *J. Med. Chem.* **2024**, *67*, 20559–20570. https://doi.org/10.1021/acs.jmedchem.4c01997.
168. Wu, W.; Huang, J.; Li, Y.; Chen, J.; Kuang, X.; Ye, M.; Chen, R.; An, J.; Huang, Z.; Sun, J. Endoplasmic Reticulum-Targeting Iridium(III) Complexes Induce Pyroptosis and Enhance Immunogenic Cell Death in MDA-MB-231 Cells. *J. Med. Chem.* **2025**, *68*, 14727–14739.
169. Jiang, H.; Lie, Q.; Wang, F.; Zeng, J.; Yang, L.-M.; Shi, Y.-Q.; Shu, J.; Liang, J.; Huang, K.-B.; Gasser, G.; Chao, H. Organelle-Targeting Iridium(III) Benzothiazole Complexes Potently Induce Immunogenic Cell Death for Gastric Cancer Immunotherapy. *J. Med. Chem.* **2026**, *69*, 1710–1723. https://doi.org/10.1021/acs.jmedchem.5c03188.
170. Guo, J.; Yang, W.; Mai, F.; Liang, J.; Luo, J.; Zhou, M.; Yu, D.; Wang, Y.; Li, C. Unravelling Oncosis: Morphological and Molecular Insights into a Unique Cell Death Pathway. *Front. Immunol.* **2024**, *15*, 1450998.
171. Xu, C.; Lin, Y.; Huang, M.; Zhang, X.; Wang, P.; Huang, M.; Lu, J. Paraptosis: A Non-Classical Paradigm of Cell Death for Cancer Therapy. *Acta Pharmacol. Sin.* **2024**, *45*, 223–237. https://doi.org/10.1038/s41401-023-01159-7.
172. Scattolin, T.; Voloshkin, V.A.; Visentin, F.; Nolan, S.P. A Critical Review of Palladium Organometallic Anticancer Agents. *Cell Rep. Phys. Sci.* **2021**, *2*, 100446. https://doi.org/10.1016/j.xcrp.2021.100446.
173. da Silva, B.A.O.; Dias, I.S.; Sarto, L.E.; de Gois, E.P.; Torres, C.; de Almeida, E.T.; Gouvêa, C.M.C.P. Cytotoxicity Induced by Newly Synthesized Palladium (II) Complexes Lead to the Death of MCF-7 and MDA-MB-435 Cancer Cell Lines. *Adv. Pharm. Bull.* **2023**, *13*, 160–169. https://doi.org/10.34172/apb.2023.017.
174. Lighvan, Z.M.; Khonakdar, H.A.; Heydari, A.; Rafiee, M.; Jahromi, M.D.; Derakhshani, A.; Momtazi-Borojeni, A.A. Spectral and Molecular Docking Studies of Nucleic Acids/Protein Binding Interactions of a Novel Organometallic Palladium (II) Complex Containing Bioactive PTA Ligands: Its Synthesis, Anticancer Effects and Encapsulation in Albumin Nanoparticles. *Appl. Organomet. Chem.* **2020**, *34*, e5839. https://doi.org/10.1002/aoc.5839.
175. Jin, S.; Feng, C.; Wang, X. DNA or Not DNA —That Is the Question Determining the Design of Platinum Anticancer Drugs. *Eur. J. Med. Chem.* **2025**, *282*, 117077. https://doi.org/10.1016/j.ejmech.2024.117077.
176. Bauer, E.; Domingo, X.; Balcells, C.; Polat, I.H.; Crespo, M.; Quirante, J.; Badía, J.; Baldomà, L.; Font-Bardia, M.; Cascante, M. Synthesis, Characterization and Biological Activity of New Cyclometallated Platinum(Iv) Iodido Complexes. *Dalton Trans.* **2017**, *46*, 14973–14987. https://doi.org/10.1039/C7DT03448B.
177. Escolà, A.; Crespo, M.; López, C.; Quirante, J.; Jayaraman, A.; Polat, I.H.; Badía, J.; Baldomà, L.; Cascante, M. On the Stability and Biological Behavior of Cyclometallated Pt(IV) Complexes with Halido and Aryl Ligands in the Axial Positions. *Bioorganic Med. Chem.* **2016**, *24*, 5804–5815. https://doi.org/10.1016/j.bmc.2016.09.037.
178. Icsel, C.; Yilmaz, V.T.; Kaya, Y.; Samli, H.; Harrison, W.T.A.; Buyukgungor, O. New Palladium(Ii) and Platinum(Ii) 5,5-Diethylbarbiturate Complexes with 2-Phenylpyridine, 2,2′-Bipyridine and 2,2′-Dipyridylamine: Synthesis, Structures, DNA Binding, Molecular Docking, Cellular Uptake, Antioxidant Activity and Cytotoxicity. *Dalton Trans.* **2015**, *44*, 6880–6895. https://doi.org/10.1039/C5DT00728C.
179. Albert, J.; Bosque, R.; Crespo, M.; Granell, J.; López, C.; Martín, R.; González, A.; Jayaraman, A.; Quirante, J.; Calvis, C.; Badía, J.; Baldomà, L.; Font-Bardia, M.; Cascante, M.; Messeguer, R. Neutral and Ionic Platinum Compounds Containing a Cyclometallated Chiral Primary Amine: Synthesis, Antitumor Activity, DNA Interaction and Topoisomerase I–Cathepsin B Inhibition. *Dalton Trans.* **2015**, *44*, 13602–13614. https://doi.org/10.1039/C5DT01713K.
180. Vezzu, D.A.K.; Lu, Q.; Chen, Y.-H.; Huo, S. Cytotoxicity of Cyclometalated Platinum Complexes Based on Tridentate NCN and CNN-Coordinating Ligands: Remarkable Coordination Dependence. *J. Inorg. Biochem.* **2014**, *134*, 49–56. https://doi.org/10.1016/j.jinorgbio.2014.01.021.
181. Chtchigrovsky, M.; Eloy, L.; Jullien, H.; Saker, L.; Ségal-Bendirdjian, E.; Poupon, J.; Bombard, S.; Cresteil, T.; Retailleau, P.; Marinetti, A. Antitumor Trans-N-Heterocyclic Carbene–Amine–Pt(II) Complexes: Synthesis of Dinuclear Species and Exploratory Investigations of DNA Binding and Cytotoxicity Mechanisms. *J. Med. Chem.* **2013**, *56*, 2074–2086. https://doi.org/10.1021/jm301780s.
182. Su, X.; Liu, B.; Wang, W.-J.; Peng, K.; Liang, B.-B.; Zheng, Y.; Cao, Q.; Mao, Z.-W. Disruption of Zinc Homeostasis by a Novel Platinum(IV)-Terthiophene Complex for Antitumor Immunity. *Angew. Chem. Int. Ed.* **2023**, *62*, e202216917. https://doi.org/10.1002/anie.202216917.
183. Panda, T.R.; Manikandan, M.; Vaidya, S.P.; Chhatar, S.; Sinha, S.; Mehrotra, M.; Chakraborty, S.; Gadre, S.; Duari, P.; Ray, P.; Patra, M. The Power of Kinetic Inertness in Improving Platinum Anticancer Therapy by Circumventing Resistance and Ameliorating Nephrotoxicity. *Angew. Chem. Int. Ed.* **2023**, *62*, e202303958. https://doi.org/10.1002/anie.202303958.

184. Chen, C.; Zheng, Y.; Rao, H.; Huang, F.; Shen, C.; Lu, C. Copper(I) Complexes with Phenanthroline-Functionalized NHC Ligands Achieve Effective Anticancer Activity via Mitochondrial and Endoplasmic Reticulum Stress. *Appl. Organomet. Chem.* **2025**, *39*, e7756. https://doi.org/10.1002/aoc.7756.
185. Mariconda, A.; Iacopetta, D.; Sirignano, M.; Ceramella, J.; Costabile, C.; Pellegrino, M.; Rosano, C.; Catalano, A.; Saturnino, C.; El-Kashef, H.; Aquaro, S.; Sinicropi, M.S.; Longo, P. N-Heterocyclic Carbene (NHC) Silver Complexes as Versatile Chemotherapeutic Agents Targeting Human Topoisomerases and Actin. *ChemMedChem* **2022**, *17*, e202200345. https://doi.org/10.1002/cmdc.202200345.
186. Zheng, W.; Zheng, Q.; Chen, C.; Wang, H. Multinuclear Silver N-Heterocyclic Carbene Complexes Provoke Potent Anticancer Activity via Mitochondrial Dysfunction and Cell Necrosis Induction. *Appl. Organomet. Chem.* **2024**, *38*, e6544. https://doi.org/10.1002/aoc.6544.
187. Miglionico, R.; Viceconte, F.; Armentano, M.F.; Mariconda, A.; Nigro, I.; Longo, P.; Bisaccia, F. Novel Silver(I) and Gold(I) N-Heterocyclic Carbene Complexes Induce ROS-Dependent Autophagic Cell Death in Human Hepatoma Cell Line HepG2. *Chem. Biol. Drug Des.* **2026**, *107*, e70283. https://doi.org/10.1111/cbdd.70283.
188. Remadna, E.; Wilsmann, A.; Stadler, N.; Forté, J.; Hoyeau, N.; Ott, I.; Noël, J.; Caron, B.; Thorimbert, S.; Forgez, P.; Bertrand, B. Synthesis and Biological Evaluation of a New Biphenyl-Based Organogold(III) Complex with In vitro and In Vivo Anticancer Activity. *J. Med. Chem.* **2025**, *68*, 1755–1771. https://doi.org/10.1021/acs.jmedchem.4c02470.
189. Lacoma, T.; Forté, J.; Maruchenko, R.; Morichon, R.; Salmain, M.; Sobczak-Thépot, J.; Bertrand, B. Impact of Chelation on Reactivity and Cytotoxicity of Hemilabile Biphenyl Gold(III) N-Heterocyclic Carbene Complexes. *ChemMedChem* **2025**, *20*, e202500302. https://doi.org/10.1002/cmdc.202500302.
190. Steinbrueck, A.; Reback, M.L.; Rumancev, C.; Siegmund, D.; Garrevoet, J.; Falkenberg, G.; Rosenhahn, A.; Prokop, A.; Metzler-Nolte, N. Quinizarin Gold(I) N-Heterocyclic Carbene Complexes with Synergistic Activity Against Anthracycline-Resistant Leukaemia Cells: Synthesis and Biological Activity Studies. *Chem. –A Eur. J.* **2025**, *31*, e202404147. https://doi.org/10.1002/chem.202404147.
191. Tabrizi, L.; Romanova, J. Antiproliferative Activity of Gold(I) N-Heterocyclic Carbene and Triphenylphosphine Complexes with Ibuprofen Derivatives as Effective Enzyme Inhibitors. *Appl. Organomet. Chem.* **2020**, *34*, e5618. https://doi.org/10.1002/aoc.5618.
192. Tűz, B.; Correia, I.; Martinho, P.N. A Critical Analysis of the Potential of Iron Heterobimetallic Complexes in Anticancer Research. *J. Inorg. Biochem.* **2025**, *264*, 112813. https://doi.org/10.1016/j.jinorgbio.2024.112813.
193. Tran, T.B.; Sipos, É.; Bényei, A.C.; Nagy, S.; Lekli, I.; Buglyó, P. Synthesis and Characterization of Novel Co(III)/Ru(II) Heterobimetallic Complexes as Hypoxia-Activated Iron-Sequestering Anticancer Prodrugs. *Molecules* **2024**, *29*, 5967. https://doi.org/10.3390/molecules29245967.
194. Bortolamiol, E.; Dalla Pozza, M.; Demitri, N.; Rizzolio, F.; Visentin, F.; Gasser, G.; Scattolin, T. Synthesis and Anticancer Properties of Heterobimetallic Fe(II)/Pd(II) Complexes Bearing Different Butadienyl Fragments. *Eur. J. Inorg. Chem.* **2024**, *27*, e202400322. https://doi.org/10.1002/ejic.202400322.
195. Fernández-Gallardo, J.; Elie, B.T.; Sadhukha, T.; Prabha, S.; Sanaú, M.; Rotenberg, S.A.; Ramos, J.W.; Contel, M. Heterometallic Titanium–Gold Complexes Inhibit Renal Cancer Cells in vitro and in Vivo. *Chem. Sci.* **2015**, *6*, 5269–5283. https://doi.org/10.1039/C5SC01753J.
196. Dietl, M.C.; Vethacke, V.; Keshavarzi, A.; Mulks, F.F.; Rominger, F.; Rudolph, M.; Mkhalid, I.A.I.; Hashmi, A.S.K. Synthesis of Heterobimetallic Gold(I) Palladium(II) Bis(Acyclic Diaminocarbene) Complexes via the Isonitrile Route. *Organometallics* **2022**, *41*, 802–810. https://doi.org/10.1021/acs.organomet.2c00021.
197. Dietl, M.C.; Maag, M.; Ber, S.; Rominger, F.; Rudolph, M.; Caligiuri, I.; Andele, P.K.; Mkhalid, I.A.I.; Rizzolio, F.; Nogara, P.A.; Orian, L.; Scattolin, T.; Hashmi, A.S.K. Comparative Study of the Antiproliferative Activity of Heterometallic Carbene Gold(i)–Platinum(Ii) and Gold(i)–Palladium(Ii) Complexes in Cancer Cell Lines. *Chem. Sci.* **2024**, *15*, 15291–15298. https://doi.org/10.1039/D4SC04585H.
198. Chhabra, S.; Taksande, A.B.; Munjewar, P. The Penicillin Pioneer: Alexander Fleming's Journey to a Medical Breakthrough. *Cureus* **2024**, *16*, e65179. https://doi.org/10.7759/cureus.65179.
199. Ahmed, S.K.; Hussein, S.; Qurbani, K.; Ibrahim, R.H.; Fareeq, A.; Mahmood, K.A.; Mohamed, M.G. Antimicrobial Resistance: Impacts, Challenges, and Future Prospects. *J. Med. Surg. Public. Health* **2024**, *2*, 100081. https://doi.org/10.1016/j.glmedi.2024.100081.
200. World Health Organization. *WHO Releases New Reports on New Tests and Treatments in Development for Bacterial Infections*; World Health Organization: Geneva, Switzerland, 2025.
201. Ho, C.S.; Wong, C.T.H.; Aung, T.T.; Lakshminarayanan, R.; Mehta, J.S.; Rauz, S.; McNally, A.; Kintses, B.; Peacock, S.J.; de la Fuente-Nunez, C.; Hancock, R.E.W.; Ting, D.S.J. Antimicrobial Resistance: A Concise Update. *Lancet Microbe* **2025**, *6*, 100947. https://doi.org/10.1016/j.lanmic.2024.07.010.
202. Lucero-Prisno, D.E.; Okesanya, O.J.; Agboola, A.O.; Adebayo, U.O.; Adigun, O.A.; Ahmed, M.M.; Olaleke, N.O.; Oso, T.A.; Tan, M.I.R.S.; Ogaya, J.B.; Ayelaagbe, O.B.; Olawade, D.B. Emerging Technologies and Innovative Approaches

to Combat Antimicrobial Resistance: A Narrative Review of next-Generation Therapeutic Strategies. *Next Bioengin.* **2025**, *1*, 100003. https://doi.org/10.1016/j.nxbio.2025.100003.

203. Behera, B.; Singh, R.; Sharma, K.; Rai, A.; Singh, S.; Balan, B. A Comprehensive Review of Advanced Strategies to Combat Antimicrobial Resistance. *Arch. Microbiol.* **2025**, *207*, 281. https://doi.org/10.1007/s00203-025-04464-3.
204. Soundarya, V.; Nagasathya, A.; Subashchandhiran, M.; Kavitha, T.; Karthikeyan, V.; Vijay, K.; Ranjith, R.; Gokul, M.; Karmegam, N. Biosynthesis and Characterization of Bimetallic Ag-Cu Nanoparticles from Tinospora Cordifolia Aerial Roots and Their Biomedical Applications. *ChemistrySelect* **2025**, *10*, e02813. https://doi.org/10.1002/slct.202502813.
205. Akhtar, W.; Hamza, M.I.; Qayyum, S.; Khan, M.A.; Mukhtar, N.; Kamal, A.; Sarwar, R.; Nazish, M.; Alrefae, A.F.; Almutairi, M.H.; Naseem, M.T. Phyto-Synthesis, Characterization of Silver Nanoparticles from Mint Leaf Extract and Its Evaluation in Antimicrobial and Pharmacological Applications. *BMC Plant Biol.* **2025**, *25*, 1072. https://doi.org/10.1186/s12870-025-07043-2.
206. Samhitha, S.S.; Surabhi, S.; Saireddy, S.K.; Santhosh, G. Platinum Nanoparticles in Biomedical Applications: Antibacterial and Antiviral Perspectives. In *Nanoparticles in Modern Antimicrobial and Antiviral Applications*; Kokkarachedu, V., Sadiku, R., Eds.; Springer International Publishing: Cham, Switzerland, 2024; pp. 47–64. ISBN 978-3-031-50093-0.
207. Kaiser, K.G.; Delattre, V.; Frost, V.J.; Buck, G.W.; Phu, J.V.; Fernandez, T.G.; Pavel, I.E. Nanosilver: An Old Antibacterial Agent with Great Promise in the Fight against Antibiotic Resistance. *Antibiotics* **2023**, *12*, 1264. https://doi.org/10.3390/antibiotics12081264.
208. Sakthi Devi, R.; Girigoswami, A.; Siddharth, M.; Girigoswami, K. Applications of Gold and Silver Nanoparticles in Theranostics. *Appl. Biochem. Biotechnol.* **2022**, *194*, 4187–4219. https://doi.org/10.1007/s12010-022-03963-z.
209. Turner, R.J. The Good, the Bad, and the Ugly of Metals as Antimicrobials. *BioMetals* **2024**, *37*, 545–559. https://doi.org/10.1007/s10534-023-00565-y.
210. Biegański, P.; Szczupak, Ł.; Arruebo, M.; Kowalski, K. Brief Survey on Organometalated Antibacterial Drugs and Metal-Based Materials with Antibacterial Activity. *RSC Chem. Biol.* **2021**, *2*, 368–386. https://doi.org/10.1039/D0CB00218F.
211. Dzhardimalieva, G.I.; Rabinskiy, L.N.; Kydralieva, K.A.; Uflyand, I.E. Recent Advances in Metallopolymer-Based Drug Delivery Systems. *RSC Adv.* **2019**, *9*, 37009–37051. https://doi.org/10.1039/C9RA06678K.
212. Casali, E.; Gandini, A.; Merlo, G.; Carli, L.; Weigand, J.J.; Porta, A.; Zanoni, G. Titanocenes Functionalization with High Chemical Diversity via Titanium Protecting Groups. *Commun. Chem.* **2025**, *8*, 221. https://doi.org/10.1038/s42004-025-01624-w.
213. Tornieporth-Oetting, I.C.; White, P.S. Ionic Titanocene(IV). Alpha.-Amino Acid Complexes of DL-Phenylalanine and DL-4-Fluorophenylalanine: Synthesis, Characterization, and Investigation of the Antimicrobial Behavior toward Escherichia Coli. *Organometallics* **1995**, *14*, 1632–1636. https://doi.org/10.1021/om00004a017.
214. Srivastava, A.; Srivastava, A.K.; Vishwkarma, A.; Pandey, O.P.; Sengupta, S.K. Synthesis, Spectroscopic Studies and Biological Aspects of Bis(Cyclopentadienyl)Titanium(IV) Complexes with 4-Amino-5-(Nicotinic/Picolinic/Ison Icotinic/Indole-3-Propyl/Indole-3-Ethyl)-3- Mercapto-1,2,4-Triazole. *J. Ind. Chem. Soc.* **2020**, *97*, 2363–2371. https://doi.org/10.5281/zenodo.5656098.
215. Scaccaglia, M.; Birbaumer, M.P.; Pinelli, S.; Pelosi, G.; Frei, A. Discovery of Antibacterial Manganese(i) Tricarbonyl Complexes through Combinatorial Chemistry. *Chem. Sci.* **2024**, *15*, 3907–3919. https://doi.org/10.1039/D3SC05326A.
216. Friães, S.; Trigueiros, C.; Gomes, C.S.B.; Fernandes, A.R.; Lenis-Rojas, O.A.; Martins, M.; Royo, B. Antimicrobial Activity of Manganese(I) Tricarbonyl Complexes Bearing 1,2,3-Triazole Ligands. *Molecules* **2023**, *28*, 7453. https://doi.org/10.3390/molecules28217453.
217. Jančić, A.M.; Katanić Stanković, J.S.; Srećković, N.; Mihailović, V.; Komatina, D.I.; Stevanović, D. Ferrocene-Containing Tetrahydropyrimidin-2(1H)-Ones: Antioxidant and Antimicrobial Activity. *J. Organomet. Chem.* **2022**, *967*, 122335. https://doi.org/10.1016/j.jorganchem.2022.122335.
218. dos Santos Filho, J.M.; de Souza Castro, M.V.B. Synthesis, Structural Characterization, and Antimicrobial Activity of Novel Ferrocene-N-Acyl Hydrazones Designed by Means of Molecular Simplification Strategy Celebrating the 100th Anniversary of the Birth of Professor Paulo Freire. *J. Organomet. Chem.* **2022**, *979*, 122488. https://doi.org/10.1016/j.jorganchem.2022.122488.
219. Peter, S.; Morifi, E.; Nwamadi, M.; Oselusi, S.O.; Tantoh, A.L.; Fonkui, T.Y.; Ndinteh, D.T.; Aderibigbe, B.A. Ferrocene-Based Hybrid Drugs as Potential Anticancer and Antibacterial Therapeutic Agents for Incorporation into Nanocarriers: In Silico, In vitro, Molecular Docking Evaluations. *Pharmaceutics* **2025**, *17*, 722. https://doi.org/10.3390/pharmaceutics17060722.
220. Anusionwu, C.G.; Fonkui, T.Y.; Oselusi, S.O.; Egieyeh, S.A.; Aderibigbe, B.A.; Mbianda, X.Y. Ferrocene-Bisphosphonates Hybrid Drug Molecules: In vitro Antibacterial and Antifungal, in Silico ADME, Drug-Likeness, and Molecular Docking Studies. *Res. Chem.* **2024**, *7*, 101278. https://doi.org/10.1016/j.rechem.2023.101278.

221. Kovačević, M.; Roca, S.; Jadreško, D.; Mrvčić, J.; Hanousek Čiča, K.; Čakić Semenčić, M.; Barišić, L. Conformational, Electrochemical, and Antioxidative Properties of Conjugates of Different Ferrocene Turn-Inducing Scaffolds with Hydrophobic Amino Acids. *Inorganics* **2024**, *12*, 195. https://doi.org/10.3390/inorganics12070195.
222. Bugarinović, J.P.; Pešić, M.S.; Minić, A.; Katanić, J.; Ilić-Komatina, D.; Pejović, A.; Mihailović, V.; Stevanović, D.; Nastasijević, B.; Damljanović, I. Ferrocene-Containing Tetrahydropyrazolopyrazolones: Antioxidant and Antimicrobial Activity. *J. Inorg. Biochem.* **2018**, *189*, 134–142. https://doi.org/10.1016/j.jinorgbio.2018.09.015.
223. Abd-El-Aziz, A.S.; Agatemor, C.; Etkin, N.; Overy, D.P.; Lanteigne, M.; McQuillan, K.; Kerr, R.G. Antimicrobial Organometallic Dendrimers with Tunable Activity against Multidrug-Resistant Bacteria. *Biomacromolecules* **2015**, *16*, 3694–3703. https://doi.org/10.1021/acs.biomac.5b01207.
224. Grzechnik, E.; Mierzejewska, J.; Drężek, K.; Tomaszewski, W.; Górski, Ł.; Jańczewski, D. Ferrocene-Grafted Polyethyleneimines, Stimuli Responsive Macromolecules with Antimicrobial Properties. *Macromol. Chem. Phys.* **2025**, *226*, e00219. https://doi.org/10.1002/macp.202500219.
225. Mu, S.; Liu, W.; Zhao, L.; Long, Y.; Gu, H. Antimicrobial AgNPs Composites of Gelatin Hydrogels Crosslinked by Ferrocene-Containing Tetrablock Terpolymer. *Polymer* **2019**, *169*, 80–94. https://doi.org/10.1016/j.polymer.2019.02.047.
226. Bhunya, D.; Datta, R.; Maity, R.; Saha, A.; Sen, S.; Brandao, P.; Pattanayak, S.; Maity, T.; Sarkar, K.; Samanta, B.C. Design and Synthesis of Bioactive Ru(Ii) Complexes: Antibacterial Activity, Biocompatibility and Biomolecular Binding. *RSC Adv.* **2025**, *15*, 42573–42587. https://doi.org/10.1039/D5RA05336F.
227. Ren, L.; Zhang, J.; Bai, X.; Hardy, C.G.; Shimizu, K.D.; Tang, C. Preparation of Cationic Cobaltocenium Polymers and Block Copolymers by "Living" Ring-Opening Metathesis Polymerization. *Chem. Sci.* **2012**, *3*, 580–583. https://doi.org/10.1039/C1SC00783A.
228. Yang, P.; Bam, M.; Pageni, P.; Zhu, T.; Chen, Y. P.; Nagarkatti, M.; Decho A.W.; Tang, C. Trio Act of Boronolectin with Antibiotic-Metal Complexed Macromolecules toward Broad-Spectrum Antimicrobial Efficacy. *ACS Infect. Dis.* **2017,** *3*, 845–853. https://doi.org/10.1021/acsinfecdis.7b00132
229. Pageni, P.; Yang, P.; Bam, M.; Zhu, T.; Chen, Y.P.; Decho, A.W.; Nagarkatti, M.; Tang, C. Recyclable Magnetic Nanoparticles Grafted with Antimicrobial Metallopolymer-Antibiotic Bioconjugates. *Biomaterials* **2018**, *178*, 363–372. https://doi.org/10.1016/j.biomaterials.2018.05.007.
230. Yang, P.; Luo, Y.; Kurnaz, L.B.; Bam, M.; Yang, X.; Decho, A.W.; Nagarkatti, M.; Tang, C. Biodegradable Polycaprolactone Metallopolymer–Antibiotic Bioconjugates Containing Phenylboronic Acid and Cobaltocenium for Antimicrobial Application. *Biomater. Sci.* **2021**, *9*, 7237–7246. https://doi.org/10.1039/D1BM00970B.
231. Hwang, J.; Barman, S.; Gao, R.; Yang, X.; O'Malley, A.; Nagarkatti, P.; Nagarkatti, M.; Chruszcz, M.; Tang, C. Membrane-Active Metallopolymers: Repurposing and Rehabilitating Antibiotics to Gram-Negative Superbugs. *Adv. Healthc. Mater.* **2023**, *12*, 2301764. https://doi.org/10.1002/adhm.202301764.
232. Hossain, M.W.; Brand, I.; Barman, S.; Abidoun, A.; Hwang, J.; Parris, A.; Yang, X.; Nagarkatti, P.; Nagarkatti, M.; Tang, C. Antimicrobial Cobaltocenium Copolymers: Tuning Amphiphilicity against NDM-1 Bacteria. *Biomater. Sci.* **2025**, *13*, 4232–4244. https://doi.org/10.1039/D5BM00497G.
233. Turcio-García, L.Á.; Parra-Unda, R.; Valdés, H.; Hernández-Ortega, S.; Valenzuela-Ramirez, G.G.; Ahumada-Santos, Y.P.; Sánchez-Lugo, Y.; Reyes-Márquez, V.; Morales-Morales, D. Fluorinated Rh(I)–NHC Compounds as Potential Antibacterials Against Multidrug-Resistant Klebsiella Pneumoniae Clinical Isolates Producing ESBL. *Pharmaceutics* **2025**, *17*, 973. https://doi.org/10.3390/pharmaceutics17080973.
234. Ott, I. Recent Developments on Gold N-Heterocyclic Carbene Complexes as Antibacterial Tool Compounds and Potential Antibiotics. *J. Organomet. Chem.* **2026**, *1048*, 124041. https://doi.org/10.1016/j.jorganchem.2026.124041.
235. Isbel, S.R.; Patil, S.A.; Bugarin, A. NHCs Silver Complexes as Potential Antimicrobial Agents. *Inorganica Chim. Acta* **2024**, *563*, 121899. https://doi.org/10.1016/j.ica.2023.121899.
236. Melaiye, A.; Sun, Z.; Hindi, K.; Milsted, A.; Ely, D.; Reneker, D.H.; Tessier, C.A.; Youngs, W.J. Silver(I)−Imidazole Cyclophane Gem-Diol Complexes Encapsulated by Electrospun Tecophilic Nanofibers: Formation of Nanosilver Particles and Antimicrobial Activity. *J. Am. Chem. Soc.* **2005**, *127*, 2285–2291. https://doi.org/10.1021/ja040226s.
237. Melaiye, A.; Simons, R.S.; Milsted, A.; Pingitore, F.; Wesdemiotis, C.; Tessier, C.A.; Youngs, W.J. Formation of Water-Soluble Pincer Silver(I)−Carbene Complexes: A Novel Antimicrobial Agent. *J. Med. Chem.* **2004**, *47*, 973–977. https://doi.org/10.1021/jm030262m.
238. Özdemir, İ.; Denizci, A.; Öztürk, H.T.; Çetinkaya, B. Synthetic and Antimicrobial Studies on New Gold(I) Complexes of Imidazolidin-2-Ylidenes. *Appl. Organomet. Chem.* **2004**, *18*, 318–322. https://doi.org/10.1002/aoc.668.
239. Prencipe, F.; Zanfardino, A.; Di Napoli, M.; Rossi, F.; D'Errico, S.; Piccialli, G.; Mangiatordi, G.F.; Saviano, M.; Ronga, L.; Varcamonti, M.; Tesauro, D. Silver (I) N-Heterocyclic Carbene Complexes: A Winning and Broad Spectrum of Antimicrobial Properties. *Int. J. Mol. Sci.* **2021**, *22*, 2497. https://doi.org/10.3390/ijms22052497.
240. Ashraf, R.; Javed, M.; Taskin-Tok, T.; Nadeem, R.; Javaid, M.K.; El-Naggar, M.; Alzahrani, O.M.; Mahmoud, S.F. Design, DFT Studies, Antimicrobial and Antioxidant Potential of Binuclear N-Heterocyclic Carbene (NHCs) Complexes,

Probing the Aspect of DNA Interaction through In-Vitro and In-Silico Approach. *Comput. Biol. Chem.* **2021**, *95*, 107591. https://doi.org/10.1016/j.compbiolchem.2021.107591.

241. Büssing, R.; Bublitz, A.; Karge, B.; Brönstrup, M.; Strowig, T.; Ott, I. An Organometallic Hybrid Antibiotic of Metronidazole with a Gold(I) N-Heterocyclic Carbene Overcomes Metronidazole Resistance in Clostridioides Difficile. *JBIC J. Biol. Inorg. Chem.* **2024**, *29*, 511–518. https://doi.org/10.1007/s00775-024-02064-y.
242. Mármol, I.; Quero, J.; Azcárate, P.; Atrián-Blasco, E.; Ramos, C.; Santos, J.; Gimeno, M.C.; Rodríguez-Yoldi, M.J.; Cerrada, E. Biological Activity of NHC-Gold-Alkynyl Complexes Derived from 3-Hydroxyflavones. *Pharmaceutics* **2022**, *14*, 2064. https://doi.org/10.3390/pharmaceutics14102064.
243. Mather, J.C.; Wyllie, J.A.; Hamilton, A.; Soares da Costa, T.P.; Barnard, P.J. Antibacterial Silver and Gold Complexes of Imidazole and 1,2,4-Triazole Derived N-Heterocyclic Carbenes. *Dalton Trans.* **2022**, *51*, 12056–12070. https://doi.org/10.1039/D2DT01657E.
244. Rodríguez-Prieto, T.; Popp, P.F.; Copa-Patiño, J.L.; Mata, F.J.; Cano, J.; Mascher, T.; Gómez, R. Silver (I) N-Heterocyclic Carbenes Carbosilane Dendritic Systems and Their Imidazolium-Terminated Analogues as Antibacterial Agents: Study of Their Mode of Action. *Pharmaceutics* **2020**, *12*, 968. https://doi.org/10.3390/pharmaceutics12100968.
245. Rodríguez-Prieto, T.; Fattori, A.; Camejo, C.; Javier de la Mata, F.; Cano, J.; Francesca Ottaviani, M.; Gómez, R. Synthesis of Imidazolium-Terminated Carbosilane Dendrimers and Dendrons and Study of Their Interactions with a Cell Membrane Model. *Eur. Polym. J.* **2020**, *133*, 109748. https://doi.org/10.1016/j.eurpolymj.2020.109748.
246. Lach, K.; Skrzyniarz, K.; Takvor-Mena, S.; Łysek-Gładysińska, M.; Furmańczyk, P.; Barrios-Gumiel, O.; Sanchez-Nieves, J.; Ciepluch, K. Endolysin CHAP Domain-Carbosilane Metallodendrimer Complexes with Triple Action on Gram-Negative Bacteria: Membrane Destabilization, Reactive Oxygen Species Production and Peptidoglycan Degradation. *Int. J. Biol. Macromol.* **2024**, *278*, 134634. https://doi.org/10.1016/j.ijbiomac.2024.134634.
247. Chakraborty, P.; Oosterhuis, D.; Bonsignore, R.; Casini, A.; Olinga, P.; Scheffers, D.-J. An Organogold Compound as Potential Antimicrobial Agent against Drug-Resistant Bacteria: Initial Mechanistic Insights. *ChemMedChem* **2021**, *16*, 3060–3070. https://doi.org/10.1002/cmdc.202100342.
248. Ratia, C.; Cepas, V.; Soengas, R.; Navarro, Y.; Velasco de Andres, M.; Iglesias, M.; Lozano, F.; López-Ortiz, F.; Soto, S. A C∧S-Cyclometallated Gold(III) Complex as a Novel Antibacterial Candidate Against Drug-Resistant Bacteria. *Front. Microbiol.* **2022**, *13*, 815622. https://doi.org/10.3389/fmicb.2022.815622.
249. Ratia, C.; Sueiro, S.; Soengas, R.G.; Iglesias, M.J.; López-Ortiz, F.; Soto, S.M. Gold(III) Complexes Activity against Multidrug-Resistant Bacteria of Veterinary Significance. *Antibiotics* **2022**, *11*, 1728. https://doi.org/10.3390/antibiotics11121728.
250. Uvarova, M.A.; Shmelev, M.A.; Bekker, O.B.; Lutsenko, I.A.; Nefedov, S.E.; Eremenko, I.L. Targeted Design of Heterotrimetallic 1-D Coordination Polymers Based on Functionalized Metallocenes Featuring Antibacterial Activity. *New J. Chem.* **2024**, *48*, 17391–17395. https://doi.org/10.1039/D4NJ03598D.
251. Wojtala, D.; Kozieł, S.; Łoś, J.; Guz-Regner, K.; Lesiów, M.K.; Szmitka, M.; Kardas, K.; Bajkowski, M.; Bugla-Płoskońska, G.; Komarnicka, U.K. Antibacterial Potential of Mono- Ru(II) and Bi-Metallic Ru(II)-Mn(II) Inorganic Compounds with Phosphino-Fluoroquinolone Conjugates. *Front. Chem. Biol.* **2026**, *5*, 1746130.
252. Li, Z.; Mackie, E.R.R.; Ramkissoon, P.; Mather, J.C.; Wiratpruk, N.; Soares da Costa, T.P.; Barnard, P.J. Synthesis, Conformational Analysis and Antibacterial Activity of Au(i)–Ag(i) and Au(i)–Hg(Ii) Heterobimetallic N-Heterocyclic Carbene Complexes. *Dalton Trans.* **2020**, *49*, 12820–12834. https://doi.org/10.1039/D0DT02225J.
253. Kaminsky, R.; Mäser, P. Global Impact of Parasitic Infections and the Importance of Parasite Control. *Front. Parasitol.* **2025**, *4*, 1546195.
254. Giannelli, A.; Schnyder, M.; Wright, I.; Charlier, J. Control of Companion Animal Parasites and Impact on One Health. *One Health* **2024**, *18*, 100679. https://doi.org/10.1016/j.onehlt.2024.100679.
255. Sargsyan, T.; Stepanyan, L.; Tsaturyan, A.; Palumbo, R.; Vicidomini, C.; Roviello, G.N. Intracellular Parasitic Infections Caused by Plasmodium Falciparum, Leishmania Spp., Toxoplasma Gondii, Echinococcus Multilocularis, Among Key Pathogens: Global Burden, Transmission Dynamics, and Vaccine Advances—A Narrative Review with Contextual Insights from Armenia. *Vaccines* **2025**, *13*, 1082. https://doi.org/10.3390/vaccines13111082.
256. Chen, J.; Zhou, J.; Pan, W. Immunometabolism: Towards a Better Understanding the Mechanism of Parasitic Infection and Immunity. *Front. Immunol.* **2021**, *12*, 661241.
257. Pink, R.; Hudson, A.; Mouriès, M.-A.; Bendig, M. Opportunities and Challenges in Antiparasitic Drug Discovery. *Nat. Rev. Drug Discov.* **2005**, *4*, 727–740. https://doi.org/10.1038/nrd1824.
258. Scalese, G.; Kostenkova, K.; Crans, D.C.; Gambino, D. Metallomics and Other Omics Approaches in Antiparasitic Metal-Based Drug Research. *Curr. Opin. Chem. Biol.* **2022**, *67*, 102127. https://doi.org/10.1016/j.cbpa.2022.102127.
259. Gambino, D.; Otero, L. Design of Prospective Antiparasitic Metal-Based Compounds Including Selected Organometallic Cores. *Inorganica Chim. Acta* **2018**, *472*, 58–75. https://doi.org/10.1016/j.ica.2017.07.068.

260. Al Nasr, I.S.; Weise, M.; Koko, W.S.; Khan, T.A.; Schobert, R.; Biersack, B. Antiparasitic Activities of Bimetallic N-Heterocyclic Carbene Gold(I) Complexes with Ferrocene Ligands: Relevance of Chlorido and Phosphino Ligands. *Appl. Organomet. Chem.* **2023**, *37*, e6952. https://doi.org/10.1002/aoc.6952.
261. Toro, P.M.; Peralta, F.; Oyarzo, J.; Wilkinson, S.R.; Zavala, M.; Arancibia, R.; Moncada-Basualto, M.; Brito, I.; Cisterna, J.; Klahn, A.H.; López, C. Evaluation of Trypanocidal Properties of Ferrocenyl and Cyrhetrenyl N-Acylhydrazones with Pendant 5-Nitrofuryl Group. *J. Inorg. Biochem.* **2021**, *219*, 111428. https://doi.org/10.1016/j.jinorgbio.2021.111428.
262. Saldías, M.; Acuña, A.; Mellado, M.; Wilkinson, S.R.; Moncada-Basualto, M.; Artigas, V.; Fuentealba, M.; Lucero, A.; Oyarzo, J.; Toro, P.M. Organometallic N-Acylhydrazones of 5-Nitrofuran and 5-Nitrothiophene Based: Synthesis, Electrochemical, Antiparasitic Evaluation, and Computational Study. *Appl. Organomet. Chem.* **2023**, *37*, e7263. https://doi.org/10.1002/aoc.7263.
263. Lucero, A.; Levín, P.; Villaman, D.; Arancibia, R.; Gallardo, M.; Wilkinson, S.R.; Toro, P.M. Synthesis, Structural Characterization and Antitrypanosomal Activity of Ferrocenyl-Based Imines with (2 or 4)-Nitrophenyl-2-Furan Group. *Inorg. Chem. Commun.* **2024**, *167*, 112714. https://doi.org/10.1016/j.inoche.2024.112714.
264. Munnik, B.L.; Kaschula, C.H.; Harding, C.R.; Chellan, P. Investigation of New Ferrocenyl-Artesunate Derivatives as Antiparasitics. *Dalton Trans.* **2023**, *52*, 15786–15797. https://doi.org/10.1039/D3DT02254D.
265. Betts, H.D.; Ong, Y.C.; Anghel, N.; Keller, S.; Karges, J.; Voutsara, N.; Müller, J.; Manoury, E.; Blacque, O.; Cariou, K.; Hemphill, A.; Gasser, G. Organometallic Derivatives of Decoquinate Targeted toward Toxoplasma Gondii. *Organometallics* **2022**, *41*, 2035–2041. https://doi.org/10.1021/acs.organomet.2c00204.
266. Murwira, T.E.; Smith, G.S.; Hurdayal, R. Exploring Ferrocenyl-Quinoline Hybrids as in vitro Agents against Leishmania Major Promastigotes. *J. Organomet. Chem.* **2026**, *1043*, 123935. https://doi.org/10.1016/j.jorganchem.2025.123935.
267. Studer, V.; Anghel, N.; Desiatkina, O.; Felder, T.; Boubaker, G.; Amdouni, Y.; Ramseier, J.; Hungerbühler, M.; Kempf, C.; Heverhagen, J.T.; Hemphill, A.; Ruprecht, N.; Furrer, J.; Păunescu, E. Conjugates Containing Two and Three Trithiolato-Bridged Dinuclear Ruthenium(II)-Arene Units as In Vitro Antiparasitic and Anticancer Agents. *Pharmaceuticals* **2020**, *13*, 471. https://doi.org/10.3390/ph13120471.
268. Păunescu, E.; Boubaker, G.; Desiatkina, O.; Anghel, N.; Amdouni, Y.; Hemphill, A.; Furrer, J. The Quest of the Best—A SAR Study of Trithiolato-Bridged Dinuclear Ruthenium(II)-Arene Compounds Presenting Antiparasitic Properties. *Eur. J. Med. Chem.* **2021**, *222*, 113610. https://doi.org/10.1016/j.ejmech.2021.113610.
269. Desiatkina, O.; Johns, S.K.; Anghel, N.; Boubaker, G.; Hemphill, A.; Furrer, J.; Păunescu, E. Synthesis and Antiparasitic Activity of New Conjugates—Organic Drugs Tethered to Trithiolato-Bridged Dinuclear Ruthenium(II)–Arene Complexes. *Inorganics* **2021**, *9*, 59. https://doi.org/10.3390/inorganics9080059.
270. Desiatkina, O.; Boubaker, G.; Anghel, N.; Amdouni, Y.; Hemphill, A.; Furrer, J.; Păunescu, E. Synthesis, Photophysical Properties and Biological Evaluation of New Conjugates BODIPY: Dinuclear Trithiolato-Bridged Ruthenium(II)-Arene Complexes. *ChemBioChem* **2022**, *23*, e202200536. https://doi.org/10.1002/cbic.202200536.
271. Desiatkina, O.; Mösching, M.; Anghel, N.; Boubaker, G.; Amdouni, Y.; Hemphill, A.; Furrer, J.; Păunescu, E. New Nucleic Base-Tethered Trithiolato-Bridged Dinuclear Ruthenium(II)-Arene Compounds: Synthesis and Antiparasitic Activity. *Molecules* **2022**, *27*, 8173. https://doi.org/10.3390/molecules27238173.
272. Desiatkina, O.; Anghel, N.; Boubaker, G.; Amdouni, Y.; Hemphill, A.; Furrer, J.; Păunescu, E. Trithiolato-Bridged Dinuclear Ruthenium(II)-Arene Conjugates Tethered with Lipophilic Units: Synthesis and Toxoplasma Gondii Antiparasitic Activity. *J. Organomet. Chem.* **2023**, *986*, 122624. https://doi.org/10.1016/j.jorganchem.2023.122624.
273. Holzer, I.; Desiatkina, O.; Anghel, N.; Johns, S.K.; Boubaker, G.; Hemphill, A.; Furrer, J.; Păunescu, E. Synthesis and Antiparasitic Activity of New Trithiolato-Bridged Dinuclear Ruthenium(II)-Arene-Carbohydrate Conjugates. *Molecules* **2023**, *28*, 902. https://doi.org/10.3390/molecules28020902.
274. Basto, A.P.; Anghel, N.; Rubbiani, R.; Müller, J.; Stibal, D.; Giannini, F.; Süss-Fink, G.; Balmer, V.; Gasser, G.; Furrer, J.; Hemphill, A. Targeting of the Mitochondrion by Dinuclear Thiolato-Bridged Arene Ruthenium Complexes in Cancer Cells and in the Apicomplexan Parasite *Neospora caninum*. *Metallomics* **2019**, *11*, 462–474. https://doi.org/10.1039/c8mt00307f.
275. Anghel, N.; Müller, J.; Serricchio, M.; Jelk, J.; Bütikofer, P.; Boubaker, G.; Imhof, D.; Ramseier, J.; Desiatkina, O.; Păunescu, E.; Braga-Lagache, S.; Heller, M.; Furrer, J.; Hemphill, A. Cellular and Molecular Targets of Nucleotide-Tagged Trithiolato-Bridged Arene Ruthenium Complexes in the Protozoan Parasites *Toxoplasma gondii* and *Trypanosoma brucei*. *Int. J. Mol. Sci.* **2021**, *22*, 10787. https://doi.org/10.3390/ijms221910787.
276. Boubaker, G.; Bernal, A.; Vigneswaran, A.; Imhof, D.; de Sousa, M.C.F.; Hänggeli, K.P.A.; Haudenschild, N.; Furrer, J.; Păunescu, E.; Desiatkina, O.; Hemphill, A. In vitro and in Vivo Activities of a Trithiolato-diRuthenium Complex Conjugated with Sulfadoxine against the Apicomplexan Parasite *Toxoplasma gondii*. *Int. J. Parasitol. Drugs Drug Resist.* **2024**, *25*, 100544. https://doi.org/10.1016/j.ijpddr.2024.100544.
277. Lin, Y.; Scalese, G.; Bulman, C.A.; Vinck, R.; Blacque, O.; Paulino, M.; Ballesteros-Casallas, A.; Pérez Díaz, L.; Salinas, G.; Mitreva, M.; Weil, T.; Cariou, K.; Sakanari, J.A.; Gambino, D.; Gasser, G. Antifungal and Antiparasitic Activities of

Metallocene-Containing Fluconazole Derivatives. *ACS Infect. Dis.* **2024**, *10*, 938–950. https://doi.org/10.1021/acsinfecdis.3c00577.

278. Yagmurlu, A.; Buğday, N.; Yaşar, Ş.; Boulebd, H.; Mansour, L.; Koko, W.S.; Hamdi, N.; Yaşar, S. Synthesis, DFT Calculations, and Investigation of Catalytic and Biological Activities of Back-Bond Functionalized Re-NHC-Cu Complexes. *Appl. Organomet. Chem.* **2024**, *38*, e7545. https://doi.org/10.1002/aoc.7545.
279. Pérez-Ramos, P.; Gomez-Escobedo, R.; Nogueda-Torres, B.; Moreno-Rodriguez, A.; Llamedo, A.; Rodríguez-Solla, H.; Soto, S.M.; Rivera, G.; Soengas, R.G. Organometallic Gold(III) (C^S)-Cyclometallated Complexes as Candidates to New Drugs against Chagas Disease. *Bioorganic Med. Chem. Lett.* **2026**, *134*, 130559. https://doi.org/10.1016/j.bmcl.2026.130559.
280. Belmonte Sánchez, E.; Iglesias, M.J.; el Hajjouji, H.; Roces, L.; García-Granda, S.; Villuendas, P.; Urriolabeitia, E.P.; López Ortiz, F. Cycloaurated Phosphinothioic Amide Complex as a Precursor of Gold(I) Nanoparticles: Efficient Catalysts for A3 Synthesis of Propargylamines under Solvent-Free Conditions. *Organometallics* **2017**, *36*, 1962–1973. https://doi.org/10.1021/acs.organomet.7b00102.
281. Feng, L.; Pomel, S.; Latre de Late, P.; Taravaud, A.; Loiseau, P.M.; Maes, L.; Cho-Ngwa, F.; Bulman, C.A.; Fischer, C.; Sakanari, J.A.; Ziniel, P.D.; Williams, D.L.; Davioud-Charvet, E. Repurposing Auranofin and Evaluation of a New Gold(I) Compound for the Search of Treatment of Human and Cattle Parasitic Diseases: From Protozoa to Helminth Infections. *Molecules* **2020**, *25*, 5075. https://doi.org/10.3390/molecules25215075.
282. Khanye, S.D.; Gut, J.; Rosenthal, P.J.; Chibale, K.; Smith, G.S. Ferrocenylthiosemicarbazones Conjugated to a Poly(Propyleneimine) Dendrimer Scaffold: Synthesis and in vitro Antimalarial Activity. *J. Organomet. Chem.* **2011**, *696*, 3296–3300. https://doi.org/10.1016/j.jorganchem.2011.07.028.
283. Tompa, D.R.; Immanuel, A.; Srikanth, S.; Kadhirvel, S. Trends and Strategies to Combat Viral Infections: A Review on FDA Approved Antiviral Drugs. *Int. J. Biol. Macromol.* **2021**, *172*, 524–541. https://doi.org/10.1016/j.ijbiomac.2021.01.076.
284. Ma, X.; Allahou, L.W.; Yang, R.; Ma, Y.; Dimoula, M.; Chau, D.Y.S.; Williams, G.R.; Knowles, J.C.; Poma, A. Antiviral Molecularly Imprinted Polymers: Engineered Precision for Multifunctional Therapeutic Strategies. *Mater. Sci. Eng. R: Rep.* **2026**, *167*, 101099. https://doi.org/10.1016/j.mser.2025.101099.
285. Mehrotra, R.; Shukla, S.N.; Gaur, P. Metallo-Antiviral Aspirants: Answer to the Upcoming Virus Outbreak. *Eur. J. Med. Chem. Rep.* **2023**, *8*, 100104. https://doi.org/10.1016/j.ejmcr.2023.100104.
286. Anthony, E.J.; Bolitho, E.M.; Bridgewater, H.E.; Carter, O.W.L.; Donnelly, J.M.; Imberti, C.; Lant, E.C.; Lermyte, F.; Needham, R.J.; Palau, M.; Sadler, P.J.; Shi, H.; Wang, F.-X.; Zhang, W.-Y.; Zhang, Z. Metallodrugs Are Unique: Opportunities and Challenges of Discovery and development†. *Chem. Sci.* **2020**, *11*, 12888–12917. https://doi.org/10.1039/d0sc04082g.
287. Karges, J.; Kalaj, M.; Gembicky, M.; Cohen, S.M. ReI Tricarbonyl Complexes as Coordinate Covalent Inhibitors for the SARS-CoV-2 Main Cysteine Protease. *Angew. Chem. Int. Ed.* **2021**, *60*, 10716–10723. https://doi.org/10.1002/anie.202016768.
288. Chuong, C.; DuChane, C.M.; Webb, E.M.; Rai, P.; Marano, J.M.; Bernier, C.M.; Merola, J.S.; Weger-Lucarelli, J. Noble Metal Organometallic Complexes Display Antiviral Activity against SARS-CoV-2. *Viruses* **2021**, *13*, 980. https://doi.org/10.3390/v13060980.
289. Janković, N.; Milović, E.; Jovanović, J.Đ.; Marković, Z.; Vraneš, M.; Stanojković, T.; Matić, I.; Crnogorac, M.Đ.; Klisurić, O.; Cvetinov, M.; Bukhari, S.N.A. A New Class of Half-Sandwich Ruthenium Complexes Containing Biginelli Hybrids: Anticancer and Anti-SARS-CoV-2 Activities. *Chem. -Biol. Interact.* **2022**, *363*, 110025. https://doi.org/10.1016/j.cbi.2022.110025.
290. Üstün, E.; Düşünceli, S.D.; Coşkun, F.; Özdemir, İ. Molybdenum Carbonyl Complexes with Benzimidazole Derivatives Against SARS-CoV-2 by Molecular Docking and DFT/TDDFT Methods. *J. Comput. Biophys. Chem.* **2021**, *20*, 815–827. https://doi.org/10.1142/S2737416521500502.
291. Rapuš, U.; Pivarcsik, T.; Mitrović, A.; Kljun, J.; Bogdanov, A.; Spengler, G.; Meden, A.; Gobec, S.; Kos, J.; Enyedy, É.A.; Turel, I. Synthesis of a Fac-Tricarbonylrhenium(I) Complex with Pyrithione, Its Physicochemical Characterization, and Assessment of Biological Effects. *ACS Omega* **2025**, *10*, 38272–38291. https://doi.org/10.1021/acsomega.5c06647.
292. Kowalski, K. A Brief Survey on the Application of Metal-Catalyzed Azide–Alkyne Cycloaddition Reactions to the Synthesis of Ferrocenyl-x-1,2,3-Triazolyl-R (x = None or a Linker and R = Organic Entity) Compounds with Anticancer Activity. *Coord. Chem. Rev.* **2023**, *479*, 214996. https://doi.org/10.1016/j.ccr.2022.214996.
293. Karpowicz, R.; Steverding, D.; Füllborn-Ott, J.; Ott, I.; Dhital, S.; Albrecht, T.; Kowalski, K. Ferrocene Bridged Nucleosides: Synthesis, Electrochemistry, Antitrypanosomal and Antiviral Activity Studies. *J. Organomet. Chem.* **2026**, *1050*, 124081. https://doi.org/10.1016/j.jorganchem.2026.124081.
294. Fontes, J.V.; Agnoli, M.E.F.; Clauss, G.; Garcia, M.S.A.; Ferreira, A.V.P.; Antoniucci, G.A.; Costa-Oliveira, A.L.; Jardim, A.C.G.; Miguel, D.C.; Abbehausen, C. The Halogen Effect in [Cu(NHC)X] Compounds: A Case Study on the Anti-Leishmania and Antiviral Activity of [Cu(IPr)X]. *ChemistrySelect* **2025**, *10*, e02039. https://doi.org/10.1002/slct.202502039.

295. Gil-Moles, M.; Türck, S.; Basu, U.; Pettenuzzo, A.; Bhattacharya, S.; Rajan, A.; Ma, X.; Büssing, R.; Wölker, J.; Burmeister, H.; Hoffmeister, H.; Schneeberg, P.; Prause, A.; Lippmann, P.; Kusi-Nimarko, J.; Hassell-Hart, S.; McGown, A.; Guest, D.; Lin, Y.; Notaro, A.; Vinck, R.; Karges, J.; Cariou, K.; Peng, K.; Qin, X.; Wang, X.; Skiba, J.; Szczupak, Ł.; Kowalski, K.; Schatzschneider, U.; Hemmert, C.; Gornitzka, H.; Milaeva, E.R.; Nazarov, A.A.; Gasser, G.; Spencer, J.; Ronconi, L.; Kortz, U.; Cinatl, J.; Bojkova, D.; Ott, I. Metallodrug Profiling against SARS-CoV-2 Target Proteins Identifies Highly Potent Inhibitors of the S/ACE2 Interaction and the Papain-like Protease PL(Pro). *Chemistry* **2021**, *27*, 17928–17940. https://doi.org/10.1002/chem.202103258.
296. Skiba, J.; Hirschfeld, M.; Lang, H.; Trzybiński, D.; Woźniak, K.; Gazecka, M.; Zmora, P.; Kowalski, K. Click—Ferrocenyl Nucleotides—Synthesis, Electrochemistry, and Antiproliferative Activity Studies. *J. Organomet. Chem.* **2024**, *1016*, 123242. https://doi.org/10.1016/j.jorganchem.2024.123242.
297. Kowalski, K.; Szczupak, Ł.; Saloman, S.; Steverding, D.; Jabłoński, A.; Vrček, V.; Hildebrandt, A.; Lang, H.; Rybarczyk-Pirek, A. Cymantrene, Cyrhetrene and Ferrocene Nucleobase Conjugates: Synthesis, Structure, Computational Study, Electrochemistry and Antitrypanosomal Activity. *ChemPlusChem* **2016**, *82*, 303–314. https://doi.org/10.1002/cplu.201600462.
298. Santoro, O.; Collado, A.; Slawin, A.M.Z.; Nolan, S.P.; Cazin, C.S.J. A General Synthetic Route to [Cu(X)(NHC)] (NHC = N-Heterocyclic Carbene, X = Cl, Br, I) Complexes. *Chem. Commun.* **2013**, *49*, 10483–10485. https://doi.org/10.1039/C3CC45488F.
299. Santos, I.A.; Fontes, J.V.; Rodrigues, G.C.; de Godoy, M.O.; Oliva, G.; Guido, R.V.C.; Merits, A.; Abbehausen, C.; Harris, M.; Jardim, A.C.G. Cu(I)-N-Heterocyclic Carbenes as Potent Inhibitors of SARS-CoV-2 Replication. *BioMetals* **2026**, *39*, 681–699. https://doi.org/10.1007/s10534-025-00775-6.
300. Gil-Moles, M.; Basu, U.; Büssing, R.; Hoffmeister, H.; Türck, S.; Varchmin, A.; Ott, I. Gold Metallodrugs to Target Coronavirus Proteins: Inhibitory Effects on the Spike-ACE2 Interaction and on PLpro Protease Activity by Auranofin and Gold Organometallics. *Chem.–A Eur. J.* **2020**, *26*, 15140–15144. https://doi.org/10.1002/chem.202004112.
301. Bennett, J.M.; Reeves, G.; Billman, G.E.; Sturmberg, J.P. Inflammation–Nature's Way to Efficiently Respond to All Types of Challenges: Implications for Understanding and Managing "the Epidemic" of Chronic Diseases. *Front. Med.* **2018**, *5*, 316.
302. Bender, E.C.; Tareq, H.S.; Suggs, L.J. Inflammation: A Matter of Immune Cell Life and Death. *npj Biomed. Innov.* **2025**, *2*, 7. https://doi.org/10.1038/s44385-025-00010-4.
303. Zhang, J.; Pitto-Barry, A.; Shang, L.; Barry, N.P.E. Anti-Inflammatory Activity of Electron-Deficient Organometallics. *R. Soc. Open Sci.* **2017**, *4*, 170786. https://doi.org/10.1098/rsos.170786.
304. Jayakumar, T.; Huang, H.-C.; Hsia, C.-W.; Fong, T.-H.; Khamrang, T.; Velusamy, M.; Manubolu, M.; Sheu, J.-R.; Hsia, C.-H. Ruthenium Derivatives Attenuate LPS-Induced Inflammatory Responses and Liver Injury via Suppressing NF-κB Signaling and Free Radical Production. *Bioorganic Chem.* **2020**, *96*, 103639. https://doi.org/10.1016/j.bioorg.2020.103639.
305. Trommenschlager, A.; Chotard, F.; Bertrand, B.; Amor, S.; Richard, P.; Bettaïeb, A.; Paul, C.; Connat, J.-L.; Le Gendre, P.; Bodio, E. Gold(I)–Coumarin–Caffeine-Based Complexes as New Potential Anti-Inflammatory and Anticancer Trackable Agents. *ChemMedChem* **2018**, *13*, 2408–2414. https://doi.org/10.1002/cmdc.201800474.
306. Panchal, N.K.; Prince Sabina, E. Non-Steroidal Anti-Inflammatory Drugs (NSAIDs): A Current Insight into Its Molecular Mechanism Eliciting Organ Toxicities. *Food Chem. Toxicol.* **2023**, *172*, 113598. https://doi.org/10.1016/j.fct.2022.113598.
307. Abd-El-Aziz, A.S.; Benaaisha, M.R.; Abdelghani, A.A.; Bissessur, R.; Abdel-Rahman, L.H.; Fayez, A.M.; El-ezz, D.A. Aspirin-Based Organoiron Dendrimers as Promising Anti-Inflammatory, Anticancer, and Antimicrobial Drugs. *Biomolecules* **2021**, *11*, 1568. https://doi.org/10.3390/biom11111568.
308. Abd-El-Aziz, A.S.; Abdelghani, A.A.; El-Ghezlani, E.G.; Abou El-ezz, D.; Abdel-Rahman, L.H. Pharmacological Evaluation of Novel Organoiron Dendrimers as Antimicrobial and Anti-Inflammatory Agents. *Macromol. Biosci.* **2021**, *21*, 2000242. https://doi.org/10.1002/mabi.202000242.
309. D'Amato, A.; Iacopetta, D.; Ceramella, J.; Troiano, R.; Mariconda, A.; Catalano, A.; Marra, M.; Saturnino, C.; Rosano, C.; Sinicropi, M.S.; Longo, P. Design, Synthesis and Biological Evaluation of Multitarget Hybrid Molecules Containing NHC-Au(I) Complexes and Carbazole Moieties. *Eur. J. Med. Chem.* **2024**, *277*, 116757. https://doi.org/10.1016/j.ejmech.2024.116757.
310. Jiang, Q.; Liu, J.; Huang, S.; Wang, X.-Y.; Chen, X.; Liu, G.-H.; Ye, K.; Song, W.; Masters, C.L.; Wang, J.; Wang, Y.J. Antiageing Strategy for Neurodegenerative Diseases: From Mechanisms to Clinical Advances. *Signal Transduct. Target. Ther.* **2025**, *10*, 76. https://doi.org/10.1038/s41392-025-02145-7.
311. Gadhave, D.G.; Sugandhi, V.V.; Jha, S.K.; Nangare, S.N.; Gupta, G.; Singh, S.K.; Dua, K.; Cho, H.; Hansbro, P.M.; Paudel, K.R. Neurodegenerative Disorders: Mechanisms of Degeneration and Therapeutic Approaches with Their Clinical Relevance. *Ageing Res. Rev.* **2024**, *99*, 102357. https://doi.org/10.1016/j.arr.2024.102357.
312. Liu, Y.; Ma, J.; Zhang, Q.; Wang, Y.; Sun, Q. Mechanism of Metal Complexes in Alzheimer's Disease. *Int. J. Mol. Sci.* **2024**, *25*, 11873. https://doi.org/10.3390/ijms252211873.

313. Sagnou, M.; Mavroidi, B.; Shegani, A.; Paravatou-Petsotas, M.; Raptopoulou, C.; Psycharis, V.; Pirmettis, I.; Papadopoulos, M.S.; Pelecanou, M. Remarkable Brain Penetration of Cyclopentadienyl M(CO)3+ (M = 99mTc, Re) Derivatives of Benzothiazole and Benzimidazole Paves the Way for Their Application as Diagnostic, with Single-Photon-Emission Computed Tomography (SPECT), and Therapeutic Agents for Alzheimer's Disease. *J. Med. Chem.* **2019**, *62*, 2638–2650. https://doi.org/10.1021/acs.jmedchem.8b01949.
314. Hacker, R.M.; Grimard, D.M.; Morgan, K.A.; Saleh, E.; Wrublik, M.M.; Meiss, C.J.; Kant, C.C.; Jones, M.A.; Brennessel, W.W.; Webb, M.I. Ru(Ii)–Arene Azole Complexes as Anti-Amyloid-β Agents. *Dalton Trans.* **2024**, *53*, 18845–18855. https://doi.org/10.1039/D4DT01740D.
315. Ceramella, J.; D'Amato, A.; Procopio, F.; Mariconda, A.; Chavarria, D.; Iacopetta, D.; Ortuso, F.; Longo, P.; Borges, F.; Sinicropi, M.S. Novel Au(I)- and Ag(I)-NHC Complexes with N-Boc-Protected Proline as Potential Candidates for Neurodegenerative Disorders. *Int. J. Mol. Sci.* **2025**, *26*, 6116. https://doi.org/10.3390/ijms26136116.